NANOPORE ANALYSIS OF PEPTIDES AND PROTEINS

A Thesis Submitted to the College of Graduate Studies and Research
In Partial Fulfillment of the Requirements for the
Degree of Doctor of Philosophy
In the Department of Biochemistry
University of Saskatchewan
Saskatoon

By

Radu Ioan Stefureac

PERMISSION TO USE

In presenting this thesis in partial fulfillment of the requirements for a postgraduate degree from the University of Saskatchewan, I agree that the Libraries of this University may make it freely available for inspection. I further agree that permission for copying of this thesis in any manner, in whole or in part, for scholarly purposes may be granted by the professors who supervised my thesis work, or in their absence, by the Head of the Department or the Dean of the College in which my thesis work was done. It is understood that any copying or publication or use of this thesis or parts thereof for financial gain shall not be allowed without my written permission. It is also understood that due recognition shall be given to me and to the University of Saskatchewan in any scholarly use which may be made of any materials in my thesis.

Requests for permission to copy or make other use of material in this thesis in whole or in part should be addressed to:

Head of the Department of Biochemistry
University of Saskatchewan
Saskatoon, Saskatchewan S7N 0W0

ABSTRACT

Nanopore sensing is a single-molecule technique capable of detecting peptide and protein molecules by monitoring the change in current generated by their interaction with protein or solid-state nanopores in an applied electric field.

The interaction of a small globular protein HPr and two of its mutants, with the aerolysin nanopore were analyzed and compared with earlier results obtained with the α-hemolysin nanopore. The HPr molecules interact differently with the two nanopores while the anatomy and net charge of the pores affect their translocation parameters.

Cleavage of insulin's disulfide bonds with the reducing agent TCEP and the release of the component polypeptides could also be detected by nanopore analysis.

An alternating current field superimposed on the direct current field inhibited the translocation of a peptide with a permanent dipole moment, while another peptide with no dipole moment was less affected.

The detection of conformational changes in peptides and small proteins caused by metal ion binding also proved possible. A Zn-finger protein was able to translocate the α-hemolysin pore in the absence of Zn(II), while mostly bumping events were observed when Zn(II) was added. By comparison, the FSD-1 protein, which folds into a Zn-finger motif by hydrophobic interactions alone, was not able to translocate. The metal binding ability of three prion peptides was studied with an α-hemolysin pore. The results clearly indicated that Cu(II) and Zn(II) bound to all three peptides and caused conformational changes reflected in their interaction parameters with the α-hemolysin pore.

The interaction of HPr, calmodulin and maltose binding protein with 7 nm and 5 nm diameter silicon nitride (Si_xN_y) pores indicated that protein molecules with dimensions comparable to, or larger than the pore diameter do not translocate. However, smaller proteins are able to translocate in a folded conformation.

Finally, the formation of prion/antibody complexes was successfully detected with an 11 nm Si_xN_y pore but not with a 19 nm pore. The results underline the importance of choosing a pore with a suitable diameter in relation to the size of the analytes.

PUBLISHED WORKS

Articles in refereed journals resulting from work presented in this thesis:

Stefureac, R. I., Kachayev, A. and Lee, J. S. (2012). Modulation of the translocation of peptides through nanopores by the application of an AC electric field. Chem Commun *48*, 1928-1930.

Stefureac, R. I., Trivedi, D., Marziali, A., and Lee, J. S. (2010). Evidence that small proteins translocate through silicon nitride pores in a folded conformation. J Phys Condens Matter *22*, 454133 (10pp).

Stefureac, R. I., Madampage, C. A., Andrievskaia, O., and Lee, J. S. (2010). Nanopore analysis of the interaction of metal ions with prion proteins and peptides. Biochem Cell Biol *88*, 347-358.

Stefureac, R. I., and Lee, J. S. (2008). Nanopore analysis of the folding of zinc fingers. Small *4*, 1646-1650.

Stefureac, R., Waldner, L., Howard, P., and Lee, J. S. (2008). Nanopore analysis of a small 86-residue protein. Small *4*, 59-63.

Articles in refereed journals resulting from work performed in Prof. Jeremy S. Lee lab:

Christensen, C., Baran, C., Krasniqi, B., Stefureac, R. I., Nokhrin, S., and Lee, J. S. (2011). Effect of charge, topology and orientation of the electric field on the interaction of peptides with the alpha-hemolysin pore. J Pept Sci *17*, 726-734.

Meng, H., Detillieux, D., Baran, C., Krasniqi, B., Christensen, C., Madampage, C., Stefureac, R. I., and Lee, J. S. (2010). Nanopore analysis of tethered peptides. J Pept Sci *16*, 701-708.

Stefureac, R., Long, Y., Kraatz, H.B., Howard, P., and Lee, J. S. (2006). Transport of α-helical peptides through α-hemolysin and aerolysin pores. Biochemistry *45*, 9172-9179.

Sutherland, T. C., Long, Y. T., Stefureac, R. I., Bediako-Amoa, I., Kraatz, H. B., and Lee, J. S. (2004). Structure of peptides investigated by nanopore analysis. Nano Lett *4*, 1273-1277.

ACKNOWLEDGEMENTS

First and foremost I would like to sincerely thank my supervisor Prof. Jeremy S. Lee for giving me the opportunity of working on such an exciting and novel research area. Your knowledge, brilliant ideas, enthusiastic imagination and passion for scientific discovery have made this project a journey to remember. I am also very grateful for the freedom and trust you bestowed on me during my program, which made me feel more like a scientific collaborator than a graduate student. Also the support and generosity shown towards me and the project made me confident to pursue this academic endeavor.

I would also like to acknowledge the members of my graduate advisory committee for the stimulating questions, constructive critiques, expert advice and endless patience.

The completion of my PhD project would not have proven possible without the generous support of Prof. Andre Marziali's lab from the Department of Physics and Astronomy at the University of British Columbia. My training session in Vancouver was a wonderful experience which taught me the way a great collaboration should work. Special thanks go to Ms. Dhruti Trivedi for her expert advice in handling, mounting and fabrication of solid-state nanopores. Your help and easy-going personality were greatly appreciated.

I cannot forget Prof. Todd Sutherland's contribution to my initial training in everything that concerned the nanopore analysis technique. I would also like to thank Prof. Oleg Dmitriev, Dr. Sergiy Nokhrin and Mr. Anton Kachayev for their illuminating discussions and helpful suggestions.

My time as a graduate student at the University of Saskatchewan would have been a lonely experience without the friends I made in the lab along the way: Mr. Besnik Krasniqi, Dr. Claudia Madampage, Dr. Michael Dinsmore and Dr. Michael Lane. Thanks also go to past and present lab-mates including: Carla Thiessen, Dielle Detillieux, Christian Baran, Christopher Christensen, Meena Kumari and Omid Tavassoly.

Gratitude belongs to the staff of the Biochemistry student lab: Mr. Jeff Hilchey, Dr. Tricia Ulmer, Maureen Sinclair, Cindy Farrar and James (JT) Talbot for their unconditional and complete support and for the surprise birthday party. I will miss you!

Working as a teaching assistant for the Biochemistry 212 class was one of the most rewarding experiences of my program and stirred my passion for teaching.

A heart-felt thank you to Åsa Almstedt, my good friend and companion during the past 3 years, for putting up with me, for the fantastic road trips and for the great times spent together.

Enormous thanks are due to my parents and family back in Romania, France and the USA for believing in me and taking pride in my accomplishments.

Finally, to all my Romanian, Ukrainian and Canadian friends I thank you for welcoming me into your homes and hearts, for all your help, traditional suppers, trips and donations.

Financial support for these studies was provided by scholarships from the Department of Biochemistry, the College of Medicine, the College of Graduate Studies and Research at the University of Saskatchewan as well as from the Natural Science and Engineering Research Council of Canada (NSERC) and research grants to Prof. Jeremy Lee.

DEDICATION

I dedicate this thesis to my family:
To my paternal grandparents for bringing out and cultivating my love for science;
To my maternal grandparents for showing me how to be a gentleman;
To my mother for teaching me foreign languages and how to live a rich spiritual life;
And to my father for teaching me that life is like a match of tennis.

I love you all!

TABLE OF CONTENTS

LIST OF TABLES

LIST OF FIGURES

LIST OF ABBREVIATIONS

A10	Fmoc-$D_2A_{10}K_2$ peptide
AC	alternating current
AFM	atomic force microscopy
ag	atto grams (10^{-18} g)
bPrP	bovine prion protein
BSA	bovine serum albumin
BSE	bovine spongiform encephalopathy
CD	circular dichroism
CDI	conformational-dependent immunoassay
CJD	Creutzfeld-Jakob disease
CWD	chronic wasting disease
DC	direct current
DNA	deoxyribonucleic acid
EDTA	ethylenediaminetetraacetic acid
ELISA	enzyme-linked immunosorbent assay
F	Farad
FFI	fatal familial insomnia
FSE	feline spongiform encephalopathy
Fmoc	N-(9-fluorenyl)methoxycarbonyl
FRET	fluorescence resonance energy transfer
Gdm-HCl	guanidium chloride
GPI	glycosyl phosphatidyl inositol
GSS	Gerstmann-Sträussler-Scheinker syndrome
HPr	histidine-containing phosphocarrier protein
LIA	luminescent immunoassay
MBP	maltose binding protein
mer	base-pair suffix

NMR	nuclear magnetic resonance
nN	nano Newton (10^{-9} N)
nS	nano Siemens (10^{-9} S)
Ω	Ohm
PC	polycarbonate
PCR	polymerase chain reaction
PEG	polyethylene glycol
PET	poly(ethyleneterephtalate)
pH	negative logarithm of the hydrogen ion concentration
PI	polyimide
PMCA	prion misfolding cyclic amplification
poly[A]	polyadenylic acid
poly[C]	polycytidylic acid
poly[U]	polyuridylic acid
poly[dC]	polydeoxycytidylic acid
PrP^{C}	cellular prion protein
PrP^{Sc}	scrapie prion protein
PTS	phosphoenolpyruvate:sugar phosphotransferase system
PTFE	polytetrafluoroethylene
QUIC	quaking-induced conversion
RNA	ribonucleic acid
RNase A	ribonuclease A
SDS	sodium dodecyl sulfate
SEM	scanning electron microscopy
Si_xN_y	silicon nitride (non-stoichiometric)
TCEP	tris(2-carboxyethyl)phosphine
TEM	transmission electron microscope
TME	transmissible mink encephalopathy
Tris	tris-[hydroxymethyl]aminomethane

TSE	transmissible spongiform encephalopathy
UV	ultraviolet
wt	wild-type prefix

1.0 INTRODUCTION

One of the central dogmas of biochemistry was that protein function was determined by the specific three-dimensional folding of the protein molecule and consequently, denatured or unfolded proteins were considered to be non-functional or inactive. However, recent progress in proteomics and genomics research suggest that as many as 30 % of eukaryotic proteins are unfolded or contain significant disordered regions (Uversky, 2002; Fink, 2005; Uversky *et al.*, 2008). This type of protein belongs to the group of natively-unfolded or intrinsically-disordered proteins. More than 30 different functions have so far been identified for the intrinsically-disordered proteins, mostly related to cell cycle control as well as transcriptional and translational regulation (Vucetic *et al.*, 2003). Many of these proteins become folded upon interaction with DNA, other proteins, or metal ions, and have also been implicated in disease pathogenesis. Examples include p53 and cancer, α-synuclein and Parkinson's disease, huntingtin and Huntington's disease, Aβ peptide and Alzheimer's disease as well as PrP and prion diseases (Friedler *et al.*, 2003; Binolfi *et al.*, 2006; Chiti and Dobson, 2006). Needless to say, disordered proteins have proven difficult to study by conventional techniques such as X-ray crystallography or NMR, because multiple conformations coexist. Single molecule techniques may be used to overcome this problem as they can examine a single conformation.

During the past 25 years, several single-molecule analysis methods such as atomic force microscopy (AFM), video fluorescence microscopy, fluorescence correlation spectroscopy (FCS), fluorescence resonance energy transfer (FRET) and optical or magnetic tweezers have been developed (Magde *et al.*, 1972; Binnig *et al.*, 1986; Kron and Spudich, 1986; Brion *et al.*, 1990; Ha *et al.*, 1996; Strick *et al.*, 1996). All these analytical techniques require that the molecules be either specifically labeled or immobilized before they can be probed.

Nanopore analysis is a relatively new and versatile method that permits continuous single-molecule detection in solution without the need for substrate labeling or immobilization.

This method, also known as “resistive-pulse sensing” or “nanopore sensing”, unites elements from four different scientific areas: microbiology, electrophysiology, electronics and more recently, nanofabrication. Important advances in all these fields were required for single-molecule analysis with nanopores to become possible.

The focus of this thesis is to further the understanding of peptide and protein folding and dynamics in solution at the single molecule level with the aid of nanopore sensing. Protein-protein complex formation and interaction with nanopores was also studied with the goal of developing a diagnostic tool for protein misfolding diseases.

1.1 Nanopore detection and analysis

The idea of using nanopores inserted in lipid membranes as a tool for the analysis of single molecules was inspired by the very intense molecular transport activity between the intracellular and the extracellular media as well as between different cellular organelles. Molecular transport across the naturally-impermeable membranous structures of cells occurs through a variety of protein channels incorporated into the fluid mosaic of the lipid bilayers. These channels or pores act as gates through which a wide variety of molecules such as ions, sugars, nucleic acids and proteins can pass during their transport from one organelle to another, or from the cytoplasm to the outside of the cell. The ability of the pores to allow the passage of ions and larger molecules suggested that the ions could be used to carry an electric current which in turn could drive larger polar molecules through the channels. The change in the ionic flow through the channel due to the transit of the macromolecule would depend on the structure of the particular translocating molecule.

1.1.1 Principles of nanopore detection

Similar to the natural molecular translocation mechanism through protein channels, the nanopore detection method utilizes a nanopore inserted into an insulating membrane

separating two chambers filled with a buffer/electrolyte solution. The principle for nanopore detection is similar to the Coulter counter used for counting and sizing particles and is presented in Figure 1.1 (Coulter, 1953). An electric potential is applied across the membrane via two Ag/AgCl electrodes and the ionic current through the open pore is monitored with a patch-clamp amplifier. The patch-clamp amplifier is a very sensitive feedback amplifier capable of maintaining a constant command voltage (clamp) while measuring pA currents flowing between the two electrodes. When a charged molecule (in the illustrated case an α-helical peptide) is driven into and through the nanopore (here α-hemolysin) by the electric potential, it causes a drop in the ionic current as electrolyte solution is displaced from the pore by the translocating molecule. The ionic current drop has a characteristic amplitude (I_{block}) and duration (T_{block}) reflecting the particular structure of that molecule. The amplitudes and durations of the current blockade are measured by the patch-clamp amplifier, converted into digital data by a digitizer and finally sent to a computer for analysis. For a constant electrolyte concentration, pH value (typically 1 M KCl and pH 7.8), temperature and applied potential the amplitudes are related to the volume of the molecule while the durations depend mainly on its length and charge. Furthermore, changes in the volume and length of the molecule are reflected in the two parameters mentioned above which are connected to the particular structure adopted in solution. Thus, in principle, nanopore detection could be used to distinguish between identical molecules adopting different conformations. As will be discussed later, this feature could prove useful for the investigation of protein misfolding diseases.

1.1.2 Types of nanopores

Currently, there are two types of pores used for the nanopore detection method: protein pores and solid-state pores.

The protein pores belong to the group of pore-forming toxins produced by bacteria with damaging effects on the cytoplasmic phospholipid bilayer of human and animal cells. Their innate property of auto-insertion into lipid bilayers played a crucial part in establishing this group of proteins as sensors.

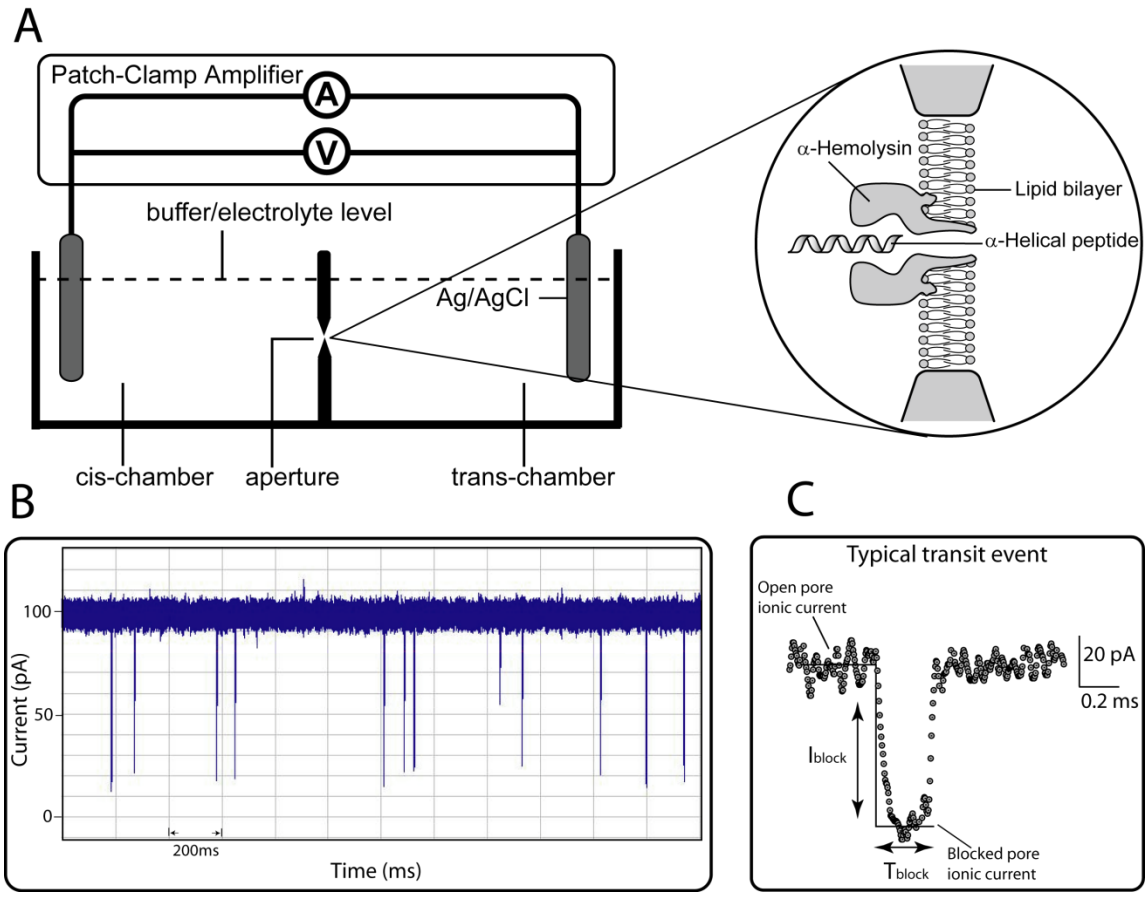

Figure 1.1. Scheme of principle for nanopore sensing. Panel (A) presents a schematic diagram of the perfusion unit setup with the Ag/AgCl electrodes and the patch-clamp amplifier connected. The blown-up section illustrates the lipid bilayer formed on the perfusion cup aperture with an α-hemolysin pore inserted and an α-helical peptide translocating. Panel (B) shows a screen-shot of the current trace through an α-hemolysin pore with molecules translocating. Panel (C) presents the enlarged profile of a typical transit event. The intensity (I_{block}) and duration (T_{block}) of the current blockade correlate with the particular structure of the analyte.

Solid-state pores have been developed with the goal of improving the life span of the nanopore setup by using synthetic membranes, the range of molecules that can be analyzed by controlling the pore diameter as well as the range of experimental conditions that can be used (pH, temperature, ionic strength, applied potentials, etc.).

1.1.2.1 Protein pores

α-hemolysin from *Staphylococcus aureus* has been the most widely used pore since the inception of this method of analysis in 1996 (Kasianowicz *et al.*, 1996). This nanopore proved to have appropriate dimensions for single-molecule sensing as well as excellent stability, reproducibility and electric properties. The toxin is secreted as a 293 amino acid water-soluble monomer and has a molecular weight of 33.2 kDa (Bhakdi *et al.*, 1981; Fussle *et al.*, 1981). The monomer binds to phospholipid bilayers and oligomerizes into a stable heptameric water-filled pore that subsequently auto-inserts into the structure of the bilayer (Gouaux *et al.*, 1994; Bayley, 1995). When assembled, the α-hemolysin pore adopts a mushroom shape approximately 100 Å in length and up to 100 Å in diameter with a hydrophilic interior and a hydrophobic exterior (Song *et al.*, 1996). The extra-membrane cap domain (Figure 1.2) forms a funnel-like vestibule with a maximum diameter of 46 Å and is connected with the stem domain through a 14 Å constriction. The transmembrane stem domain is formed of 14 antiparallel β-strands grouped in a right-handed β-barrel with a height of 52 Å and an intracellular end diameter of 20 Å. Being in direct contact with the membrane, the rim domain is involved in the stability of the pore within the lipid bilayer (Song *et al.*, 1996; Kasianowicz *et al.*, 1999). Channel formation by α-hemolysin in reconstituted planar lipid bilayers was detected with patch-clamp instrumentation as discrete increasing steps in the membrane current, with each step corresponding to the insertion of a new pore (Menestrina, 1986). The resultant current under an applied potential of 100 mV has a value of 100 pA for each channel inserted, conferring to α-hemolysin a conductance of 1 nS in 1 M KCl at 22˚C (Akeson *et al.*, 1999; Dekker, 2007). The conductance, noise and ionic selectivity of the pore are sensitive to the pH and the electrolyte concentration with a minimum level of noise at pH values between 7.5 and 8.0 (Bezrukov and Kasianowicz, 1993; Kasianowicz and Bezrukov, 1995). Although the preference of α-hemolysin for anions,

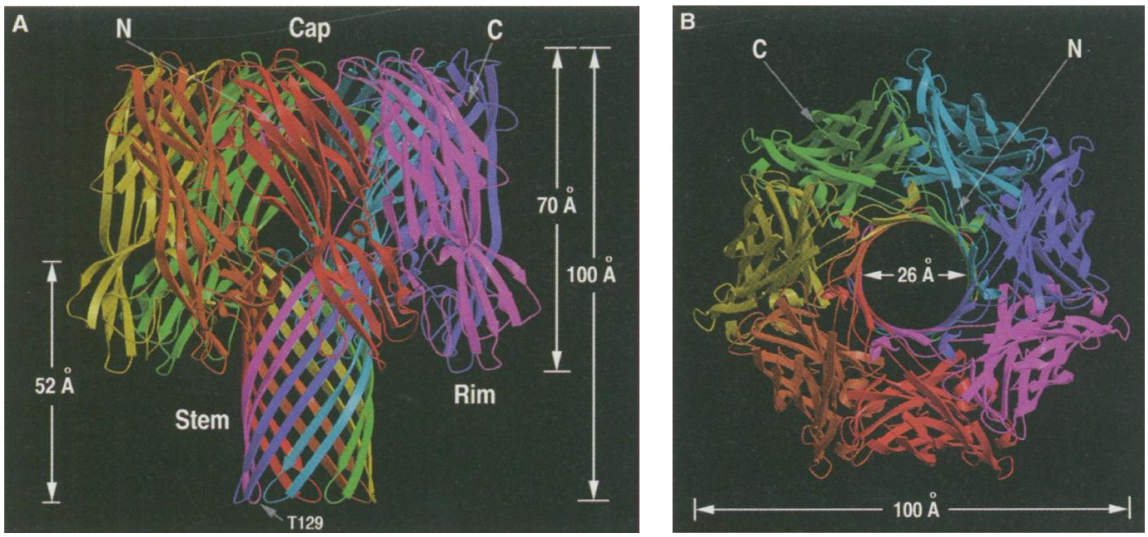

Figure 1.2. Ribbon diagram of the α-hemolysin pore showing the heptameric structure and dimensions. Image A shows the side view and image B shows the top view. The monomers are represented in different colors. (Reprinted by permission from Song *et al.*, 1996. Copyright 1996 AAAS).

due to the charged amino acids lining the inside walls, drops with increasing electrolyte concentrations, the pore maintains a slight anion-selective character even at high molar concentration of electrolyte (4 M KCl) (Misakian and Kasianowicz, 2003; Merzlyak *et al.*, 2005). Once inserted into the lipd bilayer, the channels maintain a stable open state for hours in concentrated KCl solution and only in the presence of milimolar concentrations of divalent and trivalent cations undergoes a pH and voltage-dependent inactivation (Menestrina, 1986; Korchev *et al.*, 1995; Bashford *et al.*, 1996). α-hemolysin has secondary and tertiary structural similarities with aerolysin, a toxin from *Aeromonas hydrophila* which has also been used in nanopore analysis.

Aerolysin was identified in 1975 and later purified and sequenced by Buckley, Howard and coworkers (Bernheimer *et al.*, 1975; Buckley *et al.*, 1981; Howard *et al.*, 1987). Secreted as proaerolysin, a 470 amino acid inactive precursor with a molecular weight of 52 kDa, aerolysin becomes activated by proteolytic removal of a 25 amino acid C-terminal peptide (Howard and Buckley, 1985; van der Goot *et al.*, 1993). The activated aerolysin monomer concentrates at the membrane surface before it auto-inserts as a heptameric aqueous pore complex (Garland and Buckley, 1988; Moniatte *et al.*, 1996; Fivaz *et al.*, 1999). Although a crystal structure of the assembled aerolysin pore is not yet available, the electron microscopy image available shows that aerolysin is formed of a disk-shaped cap domain lacking the vestibule area present in α-hemolysin and a β-barrel transmembrane domain (Figure 1.3) (Parker *et al.*, 1994). The transmembrane channel is approximately 80 Å in length and has an estimated diameter between 10 Å and 17 Å (Wilmsen *et al.*, 1992; Parker *et al.*, 1994). Although the ability of aerolysin to form channels in planar lipid bilayers was reported for the first time in 1990, this nanopore was not used for nanopore detection until 2006 (Wilmsen *et al.*, 1990; Wilmsen *et al.*, 1991; Stefureac *et al.*, 2006). Discrete increasing steps in the transmembrane current of 21 pA under an applied potential of 50 mV indicated a channel conductance of 0.42 nS for aerolysin (Wilmsen *et al.*, 1990). Because aerolysin lacks the vestibule domain, its effective length is greater than that of α-hemolysin (10 nm). For ohmic behavior, the current through the nanopore is inversely proportional to its length, which explains the lower conductance of aerolysin compared to α-hemolysin despite a similar diameter. Furthermore, due to the lack of the bulky vestibule, aerolysin

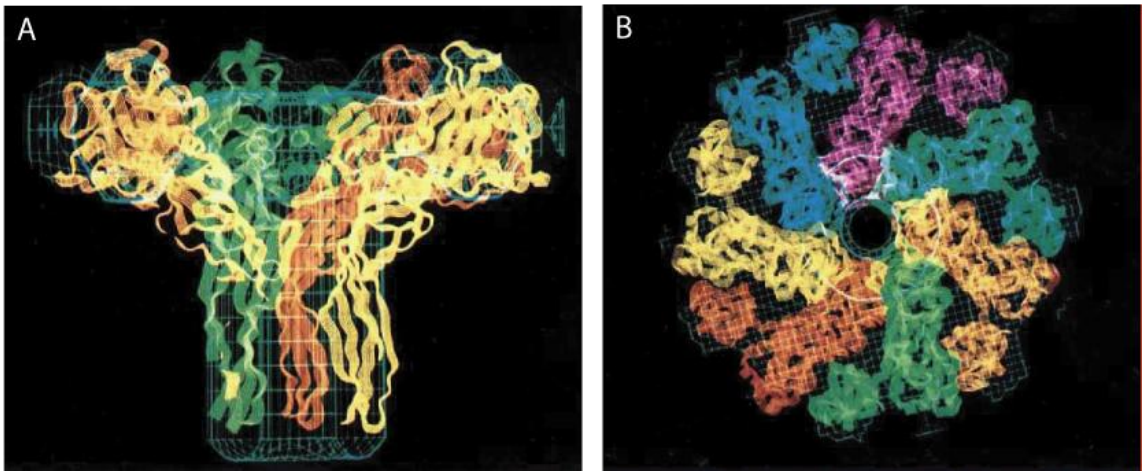

Figure 1.3. Structure of the aerolysin channel derived from electron microscopy. A side view of the channel is presented in image **A** and a top view in image **B**. Each monomer is represented in a different color. (Reprinted by permission from Parker *et al.*, 1994. Copyright Macmillan Publishers Ltd. 1994).

proved more resistant to urea denaturation than α-hemolysin and also presented a lower geometric and current asymmetry (Pastoriza-Gallego *et al.*, 2007; Pastoriza-Gallego *et al.*, 2011).

MspA represents the main hydrophilic pathway across the cell wall of *Mycobacterium smegmatis* (Stahl *et al.*, 2001). The mature MspA porin results after the cleavage of a 27 amino acids signal peptide and contains 184 amino acids with a molecular mass of 19.4 kDa (Niederweis *et al.*, 1999). The crystal structure of the porin was solved in 2004 and revealed a homooctameric goblet-like conformation with a central channel containing a 5 Å long, 12 Å wide constriction towards the periplasmic end (Figure 1.4) (Faller *et al.*, 2004). The porin is 96 Å long and 88 Å wide at the extracellular end while the internal diameter varies from 48 Å at the extracellular end to 10 Å at the periplasmic constriction. The large diameter of MspA accounts for the channel's high conductance values of 4.9 nS in 1.0 M KCl solution at 20 ˚C because the conductance is proportional to the diameter of the channel for ohmic behavior. MspA readily inserts into lipid bilayers presenting high thermal and chemical stability while being a cation-selective porin (Niederweis *et al.*, 1999; Butler *et al.*, 2008).

The protein pores have the advantage of self-assembly and excellent pore-to-pore reproducibility in terms of electrical properties. They are also easy to engineer and have appropriate diameters for the detection of small molecules such as nucleic acids, peptides and small proteins (Kasianowicz *et al.*, 1996; Sutherland *et al.*, 2004; Stefureac *et al.*, 2008). On the other hand, protein pores have significant limitations: being assembled in fragile lipid bilayers it is uncertain if they could be incorporated into portable sensing devices. They also have a limited life span, a fixed diameter and only a limited number of experimental conditions can be tested without damaging either the bilayers or the pores. To overcome these limitations, several groups have developed synthetic or solid-state nanopores.

1.1.2.2 Solid-state pores

During the past 10 years solid-state nanopore fabrication has seen major developments and currently such structures are starting to become commercially available. Depending on the material used, three main methodologies are commonly

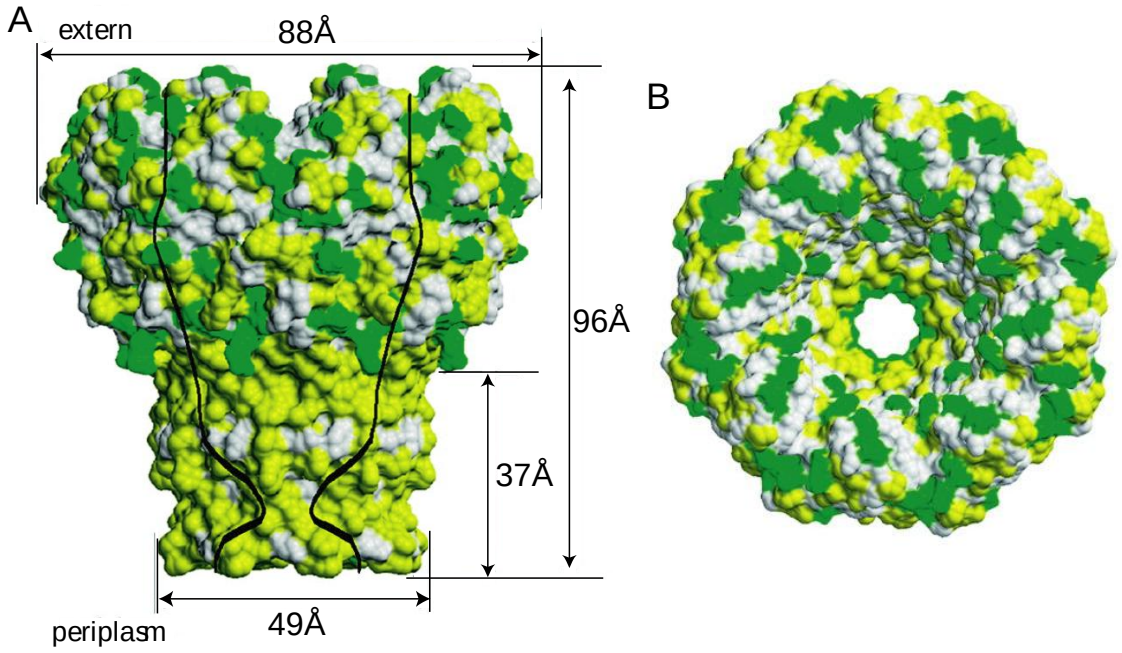

Figure 1.4. Structure and hydrophobicity map of the MspA porin. A side view of the channel is presented in image **A** and a top view in image **B**. Polar amino acids are depicted in green and nonpolar amino acids in yellow. (Reprinted by permission from Faller *et al.*, 2004. Copyright 2004 AAAS).

used for solid-state nanopore fabrication in insulating membranes: focused ion-beam drilling (in silicon nitride Si_xN_y), focused electron-beam drilling (in SiO_2, Si_xN_y and graphene) and chemical track-etching (in polymeric films) (Figure 1.5).

The first solid-state nanopore used in single-molecule detection was generated in Si_xN_y membranes using the ion-beam drilling technique (Li *et al.*, 2001). At the beginning of the process, this method uses a focused ion beam (Ar^+) with energies of several thousand electron-volts (KeV) which removes layers of the material via sputtering (atomic scale erosion process) until it connects with a conical cavity preformed on the opposite side yielding a large pore (50 nm-100 nm) (Figure 1.5A). A diffuse ion beam is used during the second step of the procedure to narrow the pore down to the required diameter with a precision of ~1 nm via matter transport due to surface diffusion, viscous flow and redeposition (Stein *et al.*, 2002; Mitsui *et al.*, 2006). The control over the pore formation is maintained through a feedback system using an ion detector situated below the membrane which triggers the deactivation of the ion beam when the desired pore size is reached (Figure 1.5A). The pores fabricated with this method were asymmetrical in terms of geometry and electrical properties exhibiting a high preference for the transport of cations. This current rectification was successfully corrected and thus the pores were rendered non-rectifying by an atomic layer deposition of an Al_2O_3 film (Chen *et al.*, 2004). Besides Si_xN_y, other materials such as silica, SiO_2, Cr, Al, poly(methyl methacrylate) and polyimide could be milled and shrunk in a similar way (Stein *et al.*, 2004).

A different approach was tested by Cees Dekker's group at the Delft University of Technology which initially used electron beam lithography from a transmission electron microscope (TEM) and KOH etching to drill a larger pore (20 nm) in SiO_2 membrane which was successively shrunk to the desired diameter by a diffuse electron beam following thermal oxidation (Figure 1.5B) (Storm *et al.*, 2003). A major advantage of this technique is that direct visual feedback is possible through the TEM which allows controlling the pore diameter with single nanometer precision. A variation of this method uses a highly focused electron beam which can drill holes in free-standing SiO_2 membranes without the need of electron beam lithography. The diameter of the hole is fine-tuned with a diffuse electron beam as described above. Several groups have adopted

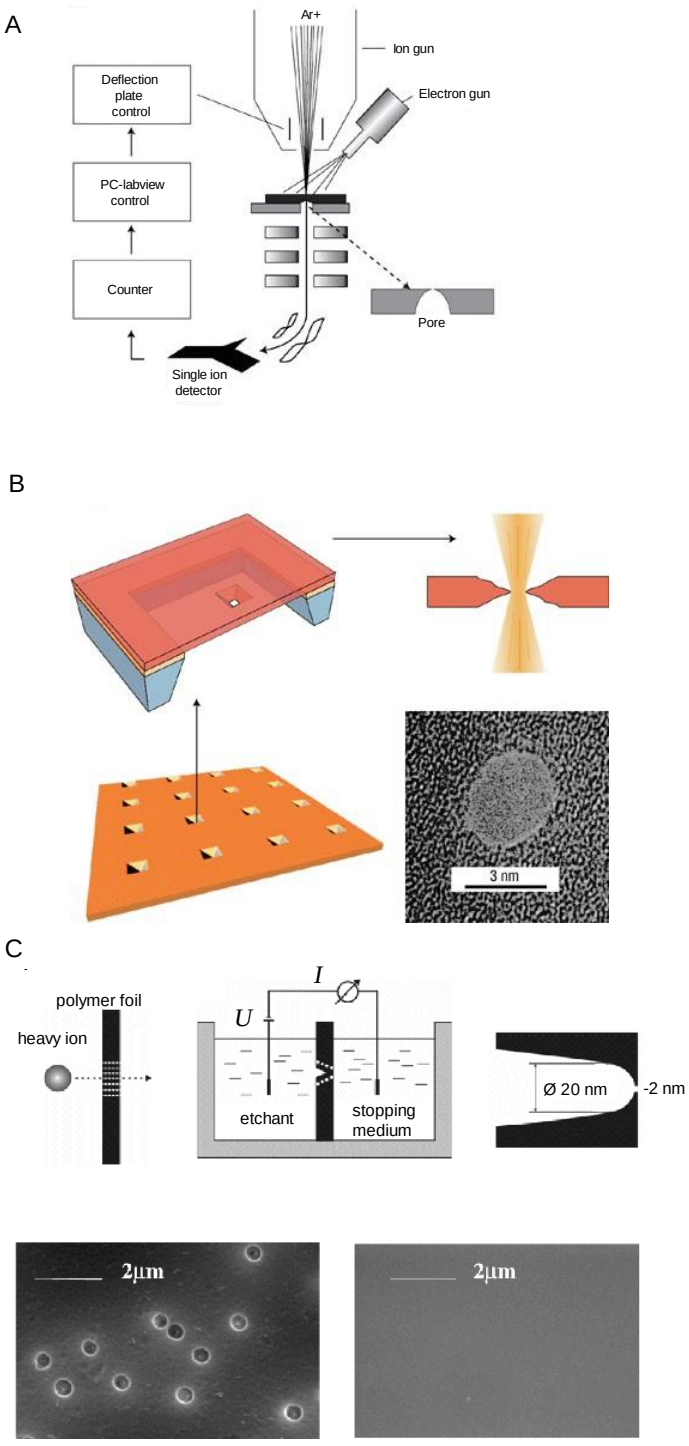

Figure 1.5. Fabrication methods for solid-state nanopores. Panel (A) presents the ion-beam drilling method, panel (B) shows electron beam lithography and panel (C) illustrates the ion-track etching technique. (Reprinted by permission from Dekker, 2007 Copyright Macmillan Publishers Ltd. 2007 and Siwy *et al.*, 2002. Copyright 2002).

the direct drilling approach to create pores (3 nm-30 nm) in Si_xN_y membranes with accuracies of 0.5 nm, while others have designed nanopore arrays for parallelized single-molecule detection (Figure 1.5B) (Kim *et al.*, 2006; Kim *et al.*, 2007; Tabard-Cossa *et al.*, 2007). More importantly, here the shrinking process mechanism is different than the one reported for the ion beam drilling method. The electron beam appears to melt the SiO_2 and Si_xN_y membranes and due to the local surface tension the resultant pore adopts a symmetrical double cone structure which confers a non-rectifying electrical behavior to these pores (Figure 1.5B). The solid-state nanopores used in the last part of the results section of this thesis were fabricated in Si_xN_y using this methodology (Tabard-Cossa *et al.*, 2007). Electron beam-drilled pores (5 nm-25 nm) have also been fabricated in atomically-thin graphene membranes (Garaj *et al.*, 2010; Merchant *et al.*, 2010; Schneider *et al.*, 2010).

Ion-track etching is the oldest fabrication method for synthetic pores and has been used and improved since the 1960's (Fleischer and Price, 1963; DeBlois and Bean, 1970). The method uses heavy ions (Xe, Pb, Au or U) accelerated at very high kinetic energies (GeV) which allow the ions to penetrate layers of poly(ethyleneterephtalate) (PET), polycarbonate (PC) and polyimide (PI) leaving tracks into the material (Figure 1.5C). These individual tracks are then isolated and chemically etched with a concentrated NaOH or NaOCl solution to generate pores down to 2 nm in diameter (Apel *et al.*, 2001; Siwy *et al.*, 2002; Siwy *et al.*, 2003b). The etching process is stopped by neutralizing the basic solution with an acidic solution situated on the opposite side of the film immediately after penetration. The concentration and temperature of the etchant, as well as the duration of the process, are used to control the pore diameter, which is monitored either by scanning electron microscopy (SEM) or by conductivity measurements (Siwy *et al.*, 2003a; Siwy *et al.*, 2003b; Wharton *et al.*, 2007). The pores resulting from this technique have conical shapes with transport properties dependent on the material and can be used for nanopore detection as well as ionic devices such as ionic diodes and ionic transistors (Daiguji *et al.*, 2005; Siwy, 2006).

Although replacing the fragile lipid bilayer with a non-biological membrane improved the stability and the life span of the nanopore setup, other problems became apparent with these synthetic nanopores. One major problem arises from the relatively

high capacitance of the Si_xN_y material which is reflected in a much higher current noise and thus a lower signal-to-noise ratio than its biological counterpart (Tabard-Cossa and *et al.*, 2007). More importantly, the analytes tend to adhere to the pore walls and cause the pores to become permanently blocked, making single-molecule detection impossible. Another common problem with the solid-state nanopores is the poor pore-to-pore fabrication reproducibility with strong variations of the conductance and noise values between pores with the same nominal diameters (Smeets *et al.*, 2006b).

Atomic layer deposition of alumina, polydimethylsiloxane curing on the Si_xN_y membrane surrounding the nanopore, coating with organosilanes, polyethylene glycol (PEG) or complete lipid coatings of the pores are the main strategies used to improve the signal-to-noise ratio and to minimize the non-specific binding of molecules to the walls of the synthetic nanopores (Chen *et al.*, 2004; Sexton *et al.*, 2007; Tabard-Cossa *et al.*, 2007; Wanunu and Meller, 2007; Yusko *et al.*, 2011). For a more detailed discussion of the solid-state nanopores shortcomings as experienced during the experimental part of this project please refer to section 2.5 and section 4.6.

1.1.3 Sensing with nanopores

Initially intended as a tool for DNA and RNA analysis with the long term goal of rapid nucleic acid sequencing, the method of sensing with nanopores was later extended for investigating a broad spectrum of molecules ranging from metal ions, small organic compunds and short peptides to chemical warfare agents, proteins and biomolecular complexes. In this section, the most significant advances in nucleic acid as well as in peptide and protein detection with nanopores will be presented.

1.1.3.1 Sensing of nucleic acids with protein pores

The first report of single-molecule detection using nanopores was published in 1996 by Kasianowicz *et al.* and set the foundation of the nanopore sensing field. In their pioneering paper, the authors witnessed the translocation of individual single-stranded RNA and DNA molecules through the α-hemolysin pore as the ionic current through the pore was reduced by 85 % to 100 % (Kasianowicz *et al.*, 1996). The events histograms

of poly[U] for instance, revealed three peaks with characteristic time values ranging from 0.095 ms to 1.288 ms under an applied potential of 120 mV. The duration of the faster events was found to be independent of the polymer length and the applied voltage and was thus ascribed to molecules colliding with the pore. The rest of the events had lifetimes proportional to their length and inversely proportional to the applied voltage indicating complete translocations through the pore. However, these events were grouped in two distinct peaks probably due to their different translocation orientation (3′ to 5′ vs. 5′ to 3′). The larger diameter of double-stranded DNA (~22 Å) did not allow for translocation, generating events with similar characteristics to the colliding or bumping molecules mentioned above. In a separate experiment, addition of ribonuclease A (RNase A) to the *cis* chamber resulted in a sudden increase in the frequency of the current blockade as poly[U] molecules were sequentially cut by the enzyme into smaller segments. This result showed that the frequency of events was proportional to the analyte concentration and also proved possible the detection of enzymatic activity. The presence of single-stranded DNA molecules in the *trans* chamber was demonstrated by the polymerase chain reaction (PCR) (Kasianowicz *et al.*, 1996).

More detailed studies of RNA and DNA translocation through α-hemolysin followed. Akeson and colleagues demonstrated that 130 – 150 nucleotide-long individual RNA molecules of poly[C], poly[A], poly[U] and poly[dC] can be distinguished from each other as the current blockade amplitudes and translocation times correlated to their individual secondary structures (Akeson *et al.*, 1999). By examining the shapes of individual events of co-polymeric poly[A] and poly[C] molecules, a bi-level blockade was recorded corresponding to the translocation of the individual components. Besides being able to distinguish segments of different nucleotides within the same strand, these experiments also helped determine the orientation of the molecules during translocation. A preference for 3′ to 5′ translocation was found. The bi-level blockades disappeared upon digestion with RNase A which cleaves 3′ pyrimidine residues. Furthermore, experiments conducted by Meller and coworkers distinguished between DNA molecules of similar length such as poly[dC]$_{100}$, poly[dA]$_{100}$, poly[dA$_{50}$dC$_{50}$], poly[dC$_{50}$dT$_{50}$] and poly[dAdC]$_{50}$ (Meller *et al.*, 2000). On one hand, the fact that sequence-specific information could be obtained from the current signatures

suggested that the nanopore method of analysis could be developed into a high-speed sequencing tool for RNA and DNA. On the other hand, due to the very fast translocation speeds (1-20 μs/nucleotide) compared to the rise time of the instrumentation (33 μs), it was concluded that to achieve single purine and pyrimidine nucleotide detection, increased resolution was needed (Akeson *et al.*, 1999).

One way to increase the time resolution was to lower the experimental temperature (Meller *et al.*, 2000). Experiments conducted at temperatures ranging from 15˚C to 40˚C showed a pronounced decrease in translocation times at low temperature values. A translocation duration dependence on the temperature of $\sim T^{-2}$ was found for all DNA molecules tested. The separation of the peaks in the current blockade amplitude histograms proved to be best at low temperature values, suggesting that even lower temperatures would optimize the identification of individual polymers in mixed samples. Using this strategy, the authors were able to distinguish differences in sequences between same-length polymers down to 10 nucleotides (Meller *et al.*, 2000).

Another way to increase the time resolution was to use single-stranded DNA molecules which formed hairpin structures with 2 to 10 base pairs stems (Vercoutere *et al.*, 2001; Vercoutere *et al.*, 2003; Winters-Hilt *et al.*, 2003). In these experiments it was found that the hairpin molecules had to unzip to translocate the pore and that the transit time increased with the number of base pairs forming the stems of the hairpins. Further studies done on DNA hairpins demonstrated that the unzipping times decreased exponentially with the applied voltage (Mathe *et al.*, 2004). The resolution was successfully improved while single nucleotide and single base pair differences in the loop and/or the stem of the hairpin respectively could be detected with this strategy (Vercoutere *et al.*, 2001; Vercoutere *et al.*, 2003; Winters-Hilt *et al.*, 2003).

Furthermore, unzipping with nanopores proved useful for the detection of single-point mutations in mismatched DNA duplexes (Nakane *et al.*, 2004). A long biotinylated single-stranded DNA bound to streptavidin was not able to pass through the α-hemolysin pore but the single-stranded end can thread through to the *trans* side where it binds complementary DNA strands. The reversed applied potential value required for unzipping the double-stranded segment was inversely proportional to the number of mismatched bases present (Nakane *et al.*, 2004). This ingenious experiment marked the

starting point of the single-molecule force spectroscopy method. An offspring technique of nanopore sensing, this method studies the forces involved in the interactions between different biological molecules without the need for immobilization on solid supports as is required with molecular tweezers or atomic force microscopy (Nakane *et al.*, 2004).

It was also reported that chemically-tagged bases within a single-stranded DNA molecule slowed down the translocation and a characteristic current signal was obtained based on the modified/unmodified pattern (Mitchell and Howorka, 2008). This approach allowed the discrimination between single nucleotide polymorphisms (Borsenberger *et al.*, 2009). Recent results showed that single-stranded DNA translocation through α-hemolysin could be significantly decreased to about 4.1 ms for $(dA)_{20}$ by using electrolyte solutions containing organic salts and/or by introducing positive charges inside the lumen of the pore by site-directed mutagenesis (de Zoysa *et al.*, 2009; Rincon-Restrepo *et al.*, 2011).

Other important results include the fact that the blockade frequency was proportional to the polymer concentration and that it increased exponentially with the applied potential. Single-stranded DNA molecules showed a higher propensity for translocation from the vestibule side of the α-hemolysin pore than from the stem side and their translocation in the 3′ to 5′ direction caused larger current blockades with faster durations than the 5′ to 3′ direction (Henrickson *et al.*, 2000; Mathe *et al.*, 2005; Butler *et al.*, 2006).

Despite the richness of knowledge about DNA translocation behavior through α-hemolysin, a DNA sequencing device based on nanopore sensing would not be possible without significant improvements in time sensitivity. The major obstacle in detecting individual nucleotides with α-hemolysin is the 5 nm long beta barrel domain which accommodates between 10-15 nucleotides at a given time which collectively affect the ionic current (Meller *et al.*, 2001; Dekker, 2007; Branton *et al.*, 2008). Since the residence time of each nucleotide inside this region is between 1-20 μs, it leaves only about 100 ions to mark the difference between two consecutive bases (a current of 2 pA). This cannot be resolved from the open pore noise unless the bases enter the pore separately or the thickness of the beta-barrel is similar to the thickness of one nucleobase (Dekker, 2007).

Recent studies revealed that such a tool requires a much more complex setup. By using protein engineering, an α-hemolysin mutant pore $(M113R)_7$ was created (Astier *et al.*, 2006). The mutant was designed to have high affinity for heptakis-(6-deoxy-6-amino)-β-cyclodextrin which was inserted through the stem end of the α-hemolysin pore and served as a molecular adapter with a smaller diameter for the sensing of 2′-deoxyribonucleoside 5′-monophosphates. The interaction between the nucleobases and the adaptor generated distinct current blockade values for each of the four nucleobases so that they could be identified with 93-98% accuracy (Astier *et al.*, 2006). The blockade durations were very similar and could not be used for individual base identification. The method was further improved by covalently attaching the molecular adapter to the inside of the β-barrel which enabled the continuous identification of nucleoside 5′-monophosphate molecules with 99.8% accuracy. The experimental conditions were adjusted to permit the activity of an exonuclease which sequentially digested single-stranded DNA molecules while the individual bases were successfully identified by the pore-adapter complex (Clarke *et al.*, 2009). This experiment suggested that the nanopore-based DNA sequencing tool will include an exonuclease genetically fused to the α-hemolysin pore in such a position that will allow the sequential capture of each cut nucleotide by the pore vestibule followed by translocation through the molecular adapter thus prohibiting the multiple detection of the same base. In another experiment, Cockroft *et al.* were able to identify each of the four nucleotides as they were added to an α-hemolysin-tethered DNA strand by an attached DNA polymerase (Cockroft *et al.*, 2008). Similar experiments were conducted with a variety of polymerases and were used to optimize the detection process (Gyarfas *et al.*, 2009; Hurt *et al.*, 2009; Wilson *et al.*, 2009; Chu *et al.*, 2010; Lieberman *et al.*, 2010; Olasagasti *et al.*, 2010; Garalde *et al.*, 2011). In a different approach, Stoddart *et al.* succeeded in identifying three regions within the α-hemolysin pore capable of interacting with a DNA strand in a base-specific manner (recognition points). Using poly[dC] strands immobilized inside the α-hemolysin pore through a streptavidin-biotin complex fused to the strand and containing $poly[dA]_5$ blocks at different positions, the authors located the recognition points R_1 (at the pore constriction), R_2 and R_3 within the β-barrel domain (Stoddart *et al.*, 2009; Stoddart *et al.*, 2010). Comparing the blockade current generated by poly[dC] strands

containing only one A base at different positions with that of poly[dC] of the same length, the single base difference could be recognized as long as the A base fell within one of the three recognition points. Furthermore, only R_2 and R_3 were able to distinguish between all four nucleobases during similar experiments (Stoddart *et al.*, 2009; Stoddart *et al.*, 2010). In the follow-up article, modified bases such as 5-methylcytosine and 5-hydroxy-methylcytosine could be distinguished in the same manner, which suggested that this approach could be used to identify epigenetic modifications in genomic DNA (Wallace *et al.*, 2010).

The single nucleotide sensitivity problem of α-hemolysin could also be overcome by using the channel protein MspA from *Mycobacterium smegmatis*. This octameric protein presents an ideal anatomy for single base identification with a single constriction of ~12 Å in diameter and ~5 Å in thickness (Faller *et al.*, 2004). By using a mutated version of MspA and slowing down the DNA strand translocation with double-stranded sections between each nucleotide of the strand to be sequenced, Derrington and coworkers were able to successfully identify each of the four deoxyribonucleotides (Derrington *et al.*, 2010).

1.1.3.2 Sensing of nucleic acids with solid-state nanopores

Until 2001 only single-stranded and partially double-stranded nucleic acid molecules were tested in nanopore experiments. With the advent of the solid-state pores, double-stranded DNA molecules could be studied at last. While the detection principle remained the same, the effects of double-stranded DNA concentration, length and applied potential on the translocation signatures were systematically investigated with Si_xN_y, SiO_2 and polymeric nanopores of various diameters.

The first molecule to be detected with solid state nanopores was a 500 base pair (bp) double-stranded DNA which generated blockades of 12% of the ionic current through a 5 nm diameter Si_xN_y pore (Li *et al.*, 2001). Further experiments showed that Si_xN_y pores could detect different levels of folding of double-stranded DNA molecules (Li *et al.*, 2003). Comparing the event profiles, blockade amplitudes and durations obtained for translocations through a 3 nm pore with those through a 10 nm diameter pore, it was concluded that double-stranded DNA molecules with a diameter of 2.2 nm translocated

the 3 nm pore in a linear conformation, whereas the much larger 10 nm pore allowed some of them to adopt a hairpin conformation during transit (Li *et al.*, 2003). The linear DNA molecules generated classic one-step current blockade profiles, while the folded DNA molecules had two and even three-stepped profiles, depending on their conformation (Figure 1.6). Later it was found that using voltages higher than 200 mV decreased the number of hairpin conformations by linearizing the molecules (Chen *et al.*, 2004). Similar results were reported by several other groups who were also able to separately identify DNA strands of different lengths from a solution mixture (Fologea *et al.*, 2005a; Storm *et al.*, 2005b; Fologea *et al.*, 2007a; Wanunu *et al.*, 2008). Besides indicating the folding of double-stranded DNA molecules, larger synthetic nanopores were able to detect the translocation of paired molecules (Li *et al.*, 2003).

Furthermore, denaturation of DNA at high pH values was observed on an 8 nm diameter pore while at the same time double-stranded DNA and single-stranded DNA could be distinguished based on their translocation signatures (Fologea *et al.*, 2005a). The translocation velocity of double-stranded DNA molecules through Si_xN_y pores proved to be two orders of magnitude faster than that of single-stranded DNA through α-hemolysin, a very important set-back for the use of solid-state pores in DNA sequencing devices (Chen *et al.*, 2004). However, one order of magnitude improvement in time resolution was achieved by increasing the electrolyte viscosity (using 50 % glycerol), lowering the experimental temperature to 4 ˚C and decreasing the applied potential to 20 mV (Fologea *et al.*, 2005b). In contrast to the experiments performed with α-hemolysin, which showed a linear dependence between the translocation time and DNA length, solid-state pores confer a power law between the two parameters (Storm *et al.*, 2005a; Storm *et al.*, 2005b; Wanunu *et al.*, 2008). The power exponent differs for shorter and longer DNA strands. This relationship was explained by the presence of a hydrodynamic drag that molecules transiting the larger solid-state pores experience with more pronounced effects on longer DNA molecules. Since the width of single-stranded DNA molecules is very similar to the diameter of α-hemolysin, hydrodynamic drag is not present when using biological pores. The blockade current varied linearly with the applied potential and the translocation times decreased with increasing applied voltage (Storm *et al.*, 2005a; Storm *et al.*, 2005b; Wanunu *et al.*, 2008). Moreover, lowering the

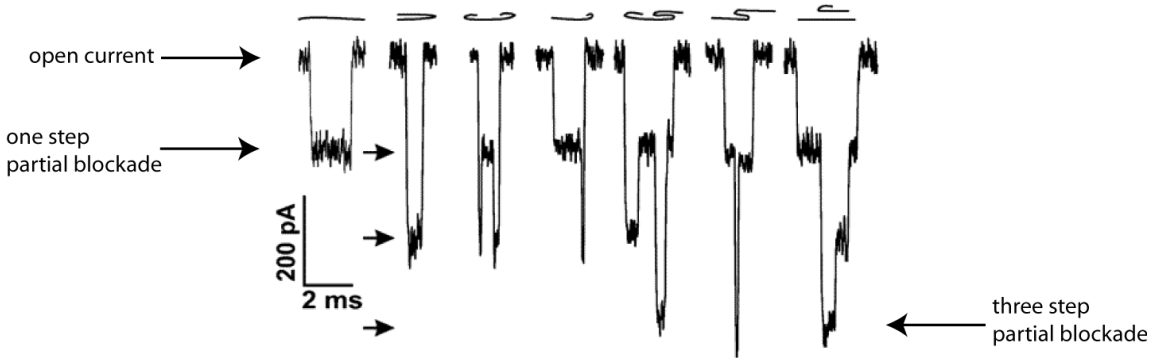

Figure 1.6. Profiles of different translocation events through solid-state nanopores. Each profile reflects a particular conformation of the molecules during their passage through the pores (shown above each profile). (Reprinted by permission from Chen *et al.*, 2004. Copyright American Chemical Society 2004).

temperature and the pore diameter resulted in an increase of the translocation times of one order of magnitude (Wanunu *et al.*, 2008). Similarly to α-hemolysin experiments, Si_xN_y pores with diameters less than 2 nm were used to forcibly unzip double-stranded DNA segments by driving them into the pore by an applied potential of 300 mV. The degree of complementarity between the two strands of the duplex DNA was reflected in the time required for the unzipping process, with slower times needed to unzip perfectly complementary duplexes and faster times when mismatches were present (McNally *et al.*, 2008). In a similar experiment, single-stranded DNA hairpins needed less force to be unzipped in pores with diameters below 1.5 nm than in pores with larger diameters (Zhao *et al.*, 2008a).

To date, solid state pores have proved useful for detection, sizing and determination of strand complementarity of DNA molecules but have been unable to distinguish between homopolymeric segments within individual strands or to identify single nucleotides. An ingenious advancement towards fast sequencing with solid state nanopores uses an extra pair of electrodes incorporated into the membrane structure in the vicinity of the nanopore. This approach promises to distinguish between individual nucleotides by tunneling currents through the bases and measuring their unique transverse current distributions with a scanning tunneling microscope or by perturbations in capacitance (Zwolak and Di Ventra, 2005; Gracheva *et al.*, 2006; Lagerqvist *et al.*, 2006, 2007; Liang and Chou, 2008; Tsutsui *et al.*, 2009). However, the fabrication of such nanopores is an extremely challenging task and so is the task of minimizing the noise and controlling the orientation of the bases inside the nanopore to allow proper contact with the embedded electrodes (Zwolak and Di Ventra, 2005). Recently, an optical recognition method has been proposed by McNally and colleagues. In this approach, the target DNA is first converted according to a binary code established by molecular beacons carrying two different fluorophores (yellow and red). When the beacons are stripped off by electrically driving the molecules through sub-2 nm diameter solid-state pores, photon bursts are detected by a total internal reflection imaging system. The color sequence generated reflects the sequence of the target DNA (McNally *et al.*, 2010). Although the method presents promise for high throughput parallelization,

the steps required for sample preparation, labeling and code conversion represent a serious draw-back.

In conclusion, the results reported to date show clearly that DNA detection and sequencing with both biological pores and solid-state pores have significant limitations. On one hand, there is the instability of the lipid bilayer in which the biological pores are inserted and on the other hand the challenge of solid-state nanopore fabrication with precise dimensions. These limitations may be overcome by integrating biological pores into solid state membranes resulting in hybrid nanopores as recently reported (Hall *et al.*, 2010; Venkatesan *et al.*, 2011). Such a setup would provide a highly reproducible and indefinitely stable nanopore that will facilitate the process of DNA sequencing in the near future (Branton *et al.*, 2008). The newly-emerged graphene nanopores may represent a second approach to overcome the above-mentioned limitations. Being atomically-thin, these nanopores may prove advantageous for single-base identification either by ionic-current or tunneling current measurements (Garaj *et al.*, 2010; Merchant *et al.*, 2010; Schneider *et al.*, 2010).

1.1.3.3 Sensing of peptides and proteins with protein pores

In parallel with the nanopore analysis of DNA, several groups have reported that peptide and protein molecules could be analyzed the same way. Based on the idea proposed by Singer that polypeptides translocate through channels *in vivo*, our lab was the first one to report the transit of a series of peptides, containing repeats of the sequence (Gly-Pro-Pro), through α-hemolysin nanopores in 2004 (Singer *et al.*, 1987; Sutherland *et al.*, 2004). These collagen-like peptides existed as mixtures of single, double or collagen-like triple helices and their particular level of folding was successfully distinguished and identified based on their translocation signatures. At the same time, an increase in both the current blockade and translocation time with the peptide length was observed. This breakthrough indicated that nanopore sensing could be used to conduct structural and conformational studies of peptides and proteins, enabling the collection of results difficult to obtain by bulk spectroscopic techniques such as circular dichroism (CD) or nuclear magnetic resonance (NMR). Furthermore, the peptides had much lower charge densities than DNA which was reflected in transit times

of 1 to 2 orders of magnitude longer, resulting in increased signal resolution compared to nucleic acids. The electrically-driven passage of cationic α-helical peptides through α-hemolysin from the stem side to the vestibule side was analyzed by Movileanu *et al.* and the effect of peptide charge and peptide length on the energy barrier for transport through the pore was measured. It was found that the number of events per time increased with the applied electric potential and decreased with the peptide length (Movileanu *et al.*, 2005). Since α-hemolysin is a slightly anion-selective channel, the energy barrier that positively-charged peptides encounter as they transit the β-barrel domain could be lowered by placing negatively-charged amino acid residues inside this domain by mutagenesis, as reported by Wolfe *et al.*, or by using anionic α-helical peptides as performed by our laboratory (Stefureac *et al.*, 2006; Wolfe *et al.*, 2007). In the latter study the authors show that the net charge of the peptides affects their interaction with the nanopore and so a more negatively-charged peptide will translocate faster and will generate more events than a less negatively-charged or neutral peptide. Also, the peptide dipole moment plays an important part in the orientation of the peptide under the applied electric field facilitating translocation. The same molecules were also analyzed on a second biological nanopore called aerolysin from *Aeromonas hydrophila*, a nanopore lacking the vestibule domain present in α-hemolysin. The translocation signatures and the frequency of events recorded reflected the anatomical characteristics of the two pores and pointed out that the vestibule domain promoted translocation while at the same time the translocation durations were affected by specific interactions between the peptides and the amino acids lining the inside walls of the pore (Stefureac *et al.*, 2006). This paper constituted the first report of peptide translocation through the aerolysin nanopore.

The study of the electrophoretic translocation of peptides through α-hemolysin continued with the analysis of a series of β-hairpin peptides with different levels of folding (Goodrich *et al.*, 2007). It was found that both partially and fully-folded β-hairpins were able to pass through the nanopore with translocation features depending on their individual degree of folding; that is longer times were needed for folded molecules to transit the nanopore than for unfolded molecules because folded polypeptides have a greater energetic penalty than unfolded polypeptides (Movileanu,

2009). The frequency of events increased with the applied voltage while the transit times decreased, as was the case for α-helical peptide studies indicative of translocations. The authors also reported that a part of the molecules generated very fast interaction durations with the nanopore which were ascribed to either collisions with the stem entrance or translocations in completely extended conformations (Goodrich *et al.*, 2007). To have a complete picture of the translocation signatures of various peptide conformations, our laboratory has investigated two short polypeptides which adopted α-helical hairpin folds. One peptide contained a disulfide bond which enforced the α-helical hairpin fold while the second peptide lacked the disulfide bond, adopting a more relaxed hairpin conformation. The results obtained for both α-helical hairpin peptides indicated that most of the interactions with the α-hemolysin channel resulted in translocations while at the same time some molecules just collided with the nanopore, failing to cross to the opposite side (Madampage, 2011).

Since polypeptide translocation through β-barrel pores is a wide-spread process in cell biology, which in some cases takes place without ATP consumption, questions about the kinetics of the peptide translocations through nanopores were raised and the interactions between the peptides and the nanopore during translocation were investigated (Krantz *et al.*, 2005; Movileanu, 2008). It was found that the transit of positively-charged polypeptides is facilitated by replacing the positively-charged amino acid residues with negatively-charged amino acid residues at different positions within the α-hemolysin's β-barrel domain. The frequency of events and blockade durations were dependent on the position and number of mutations, with fastest translocation times through pores containing the most negatively-charged residues situated around the stem entrance. The blockade durations of the translocating molecules were independent of the polypeptide concentration while the frequency of events varied linearly with the concentration. At the same time, the hydrophobic peptides generated fewer events than the hydrophilic peptides due to the hydrophilic character of the pore interior. Bumping events were reported only with the wild-type α-hemolysin and one of the mutants (Mohammad and Movileanu, 2008; Bikwemu *et al.*, 2010).

Beside the electrostatic interaction between charged peptides and charged nanopores, aromatic interactions were also examined. The transport of neutral peptides, with lengths

between 2 to 11 amino acids containing mostly aromatic amino acids through α-hemolysin mutant pores engineered with aromatic binding sites, was tested in similar experiments by Zhao and coworkers (Zhao *et al.*, 2009b). The aromatic amino acids present inside the nanopores caused an increase in the translocation times of the aromatic peptides. The increase in translocation times became more pronounced as more aromatic binding sites were placed inside the pore, indicating a stronger binding affinity between the peptides and the pores. The longer interaction times generated an increased signal resolution which enabled the successful differentiation and quantification of the individual peptides contained in a solution mixture, some peptides differing only by a single amino acid in sequence. Another important finding of this work was that an appropriately modified nanopore can be used to determine peptide sequences since the authors were able to distinguish between peptides with the same length and composition but with different sequences based on their different translocation signatures (Zhao *et al.*, 2009b). Furthermore, the same authors also show that increasing the ionic strength increases the aromatic interactions between the peptides and the pores and influences the sensitivity of the detection, which is particularly useful for the case of peptide identification in mixtures (Zhao *et al.*, 2008b). The above studies provide evidence that noncovalent interactions that can either promote or inhibit the translocation of molecules are taking place inside the nanopore and can be used for peptide identification and sequencing. This approach shows promise towards label-free protein sequencing by using a protease such as trypsin to digest the proteins into peptides followed by nanopore analysis of the resulting peptides as recently reported (Zhao *et al.*, 2009a). At the same time, the sequencing procedure could be accelerated by using a nanopore array, allowing the simultaneous analysis of peptides resulting from several digestion reactions (Zhao *et al.*, 2008b).

Recently, α-hemolysin was used to detect peptide conformational changes. β-amyloid 42 (Aβ42) is a peptide found in the plaques formed inside the brains of Alzheimer's patients. The ability of this peptide to aggregate was tested in the presence of an aggregation promoter as well as of an aggregation inhibitor (Wang *et al.*, 2011). It was reported that the translocation of Aβ42 was abolished in the presence of the aggregation promoter due to the formation of protofibrils, while the binding of the

aggregation inhibitor to either Aβ42 or the protofibrils increased the number of translocations (Wang *et al.,* 2011). This result confirms that nanopore sensing can be used to detect pathological conformational changes in proteins with potential applications in diagnosis of protein misfolding diseases, as will be discussed in Chapter 3 of the present thesis.

The richness of information obtained from the nanopore analysis of peptides proved that different secondary and tertiary structures can be individually identified and distinguished, suggesting that nanopore sensing could be used to help elucidate one of the most intriguing problems of modern biochemistry: the folding mechanism of proteins (Nicholson and Scholtz, 1996). Similar to the DNA nanopore analysis performed by Akeson and Meller, which showed that polyadenylic acid gives a different current blockade than polyuridylic acid, our lab anticipated the ability of the nanopores to distinguish between the transit of an α-helical segment and a β-sheet segment present within the same protein molecule (Figure 1.7). To determine if small protein molecules can be detected and separately identified we have examined the interactions of a small globular protein, HPr, together with two of its mutants with α-hemolysin and aerolysin pores (Stefureac *et al.,* 2008). Even though HPr contains only 85 amino acids, it is too large to translocate through either pore in a folded conformation. The protein is able to transit the pores by partially unfolding under the applied transmembrane potential. Besides the electric force acting on the protein, the presence of the vestibule domain of α-hemolysin together with HPr's low activation energy of unfolding contributed to the unfolding of the protein and explained the higher proportion of translocations through α-hemolysin as compared to aerolysin. Although the experiments proved that both α-hemolysin and aerolysin pores are sensitive to single mutations that alter the overall folding state and net charge of HPr, identification of the passage of individual α-helical or β-sheet segments within the protein was not possible due to the low resolution time (Stefureac *et al.,* 2008). This paper was the first to report the translocation of partially folded proteins through the aerolysin nanopore. The unfolding properties of a much larger protein, maltose binding protein (MBP), were investigated with the α-hemolysin nanopore by incubating MBP with increasing concentrations of denaturing agent guanidium chloride (Gdm-HCl) which generated partly and completely unfolded

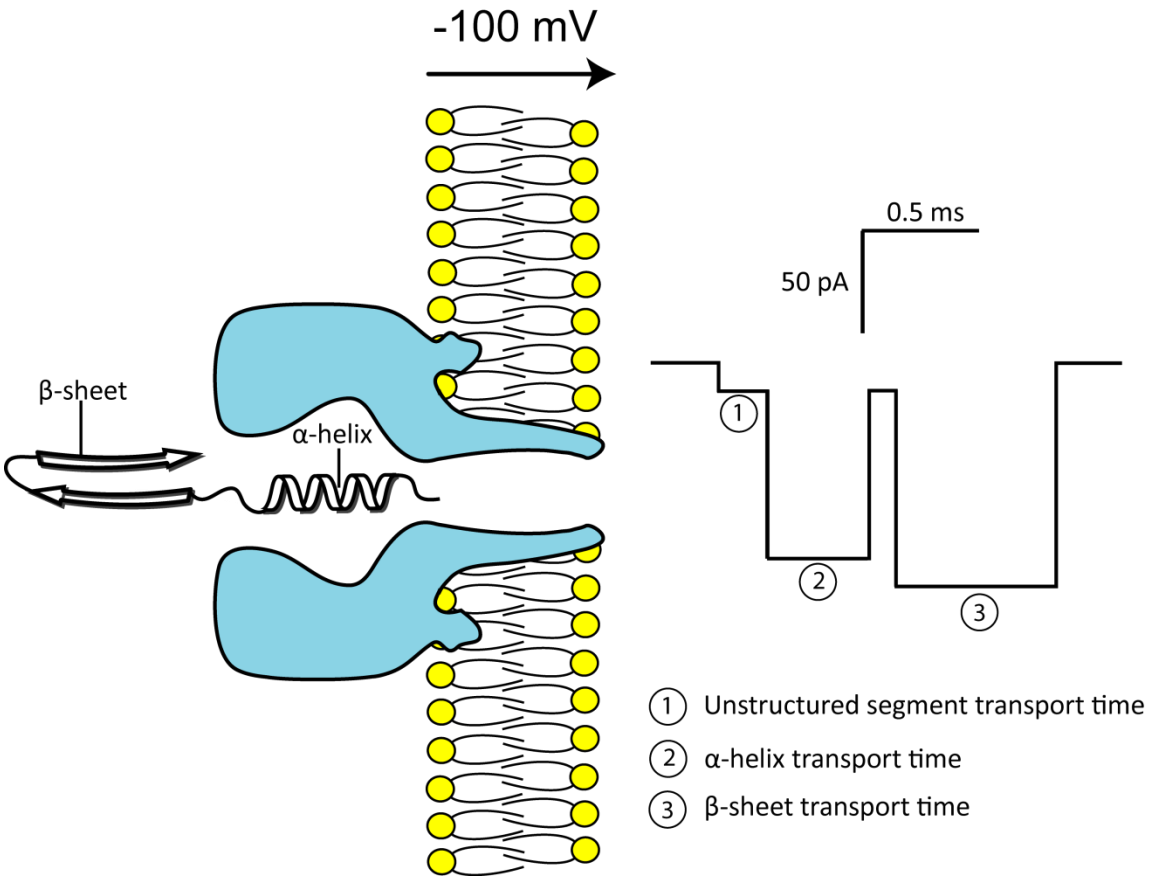

Figure 1.7. Schematic representation of the α-hemolysin pore inserted into a lipid bilayer with α-helical and β-sheet segments of a protein ready for translocation. The transit of differently folded segments should be reflected within the translocation profile of each protein molecule. (Sutherland and Lee, 2004 personal communication).

proteins (Oukhaled *et al.*, 2007). Short and long current blockades were recorded, with the short blockades being ascribed to completely unfolded molecules while the long blockades belonged to partially unfolded conformations.

The frequency of the short current blockades increased with the Gdm-HCl concentration and all molecules in solution became completely unfolded at a concentration of 1.35 M. In the absence of denaturant, the interaction of MBP with the nanopore could not be detected. The frequency of events was proportional to the protein concentration and increased exponentially with the applied potential while the blockade times decreased as the potential was increased (Oukhaled *et al.*, 2007). These experiments highlighted the fact that the translocation of MBP through the nanopore depended on the level of folding of the protein and supported complete translocation of denatured protein molecules. The authors continued the analysis of MBP interaction with α-hemolysin in a new article reporting a preference for translocation through the vestibule side as compared to the stem side (Pastoriza-Gallego *et al.*, 2009).

Furthermore, the vestibule domain of α-hemolysin was successfully denatured in the presence of 4 M urea while still inserted into the lipid bilayer. In this pore conformation, the probability for translocation through the denatured end decreased and approached the value obtained for the stem side of the nanopore while the current blockade duration increased considerably (Pastoriza-Gallego *et al.*, 2009). These results confirmed the important role that the vestibule domain plays in facilitating the orientation and translocation of proteins through α-hemolysin.

Using a special protein-protein construct and an α-hemolysin pore engineered with electrostatic traps, Mohammad *et al.* brought more insights about the mechanism of protein translocation and unfolding through nanopores. The authors found that to initiate the translocation, a protein requires a leading sequence containing appropriately charged amino acid residues to enter the nanopore and interact with oppositely-charged electrostatic traps within the pore lumen (Mohammad *et al.*, 2008). Repulsion, driving and electrostatic forces play important roles in the steps following the initiation of the protein translocation and are expected in some cases to be large enough to mechanically unfold the protein domains residing outside the nanopore as was previously observed with the HPr protein (Mohammad *et al.*, 2008; Stefureac *et al.*, 2008).

The entry and transport of unfolded proteins through the aerolysin nanopore has recently been investigated in a similar way as previously performed with α-hemolysin. The translocation parameters of MBP together with a destabilized mutant and two MBP molecules fused together head to tail under denaturing conditions were studied as a function of applied voltage, protein concentration and channel side entry (Pastoriza-Gallego *et al.*, 2011). Similar to the α-hemolysin analysis, the ionic current blockades determined by all the analyte molecules were grouped into two types of interactions with different blockade currents and blockade times: bumping and translocation. The proportion of bumping events decreased as the applied potential was increased and the frequency of events generated was higher for the stem side. Furthermore, the translocation blockade current for MBP and the double construct stayed the same while the blockade time was twice as long for the double construct as for MBP. This finding again supports the protein translocation through aerolysin as was shown for the transport of α-helical peptides of increasing lengths through α-hemolysin and aerolysin pores (Stefureac *et al.*, 2006; Pastoriza-Gallego *et al.*, 2011). By comparison to the α-hemolysin MBP translocation experiments, the translocation times through aerolysin were up to one order of magnitude longer which recommends aerolysin as a good candidate for further protein unfolding studies and protein sequencing.

1.1.3.4 Sensing of peptides and proteins with solid-state nanopores

Solid-state nanopores with wider diameters than α-hemolysin have been used to detect the translocation of large proteins in their native or unfolded state as well as of free or immobilized protein-antibody complexes. In a first paper, bovine serum albumin (BSA) was able to translocate through a 55 nm diameter Si_xN_y nanopore and the magnitude of the blockade current correlated well with the dimensions of the BSA molecules transiting the pore. Current blockades were observed only when a positive potential was applied which was in agreement with an electrophoretic transport of the negatively-charged BSA molecules through the nanopore. The authors reported that BSA molecules adhered for longer times to the inner walls of the pore, causing occasional drops of 100 mV to 200 mV in the open pore current value. The variation in the current drop value was recently identified as being due to changes in BSA

conformation caused by the applied electric potential (Han *et al.*, 2006; Niedzwiecki *et al.*, 2010). With smaller diameter Si_xN_y nanopores (16-18 nm), Fologea and colleagues were able to differentiate between the transits of two proteins of different sizes: BSA and fibrinogen. Being a larger protein than BSA, fibrinogen generated larger blockade currents and longer blockade times. Changing the pH of the buffer solution affected the net charge of the protein and consequently its behavior under the applied electric potential. More importantly, the authors managed for the first time to translocate enough BSA molecules to directly prove their presence on the *trans* side of the solid-state membrane by an immunosorbent assay. These results also demonstrated that the relative charge and size of unknown protein molecules could be estimated from their translocation parameters (Fologea *et al.*, 2007b). An increased resolution of translocation events determined for four different protein molecules was reported by conducting the recordings in buffers with pH values near the isoelectric point of each respective protein which reduced their electrophoretic mobility (Han *et al.*, 2008). The authors were able to identify the transit of BSA, ovalbumin, streptavidin and avidin through Si_xN_y nanopores (diameter 28 nm) based on their individual physicochemical properties such as size, charge and pH-dependent migration.

Talaga and Li reported that by using different urea concentrations, several degrees of unfolding of β-lactoglobulin could be detected as the molecules transited Si_xN_y nanopores (Talaga and Li, 2009). Furthermore, in 8 M urea both β-lactoglobulin and HPr proteins were completely unfolded and their interaction with the nanopore could be compared. Since β-lactoglobulin is twice as long as HPr, it needed twice the time to translocate a 4 nm diameter pore whereas the blockade current was similar for both molecules because their excluded volumes were comparable. The authors concluded that even in the absence of the denaturant, the majority of β-lactoglobulin molecules were linearized or looped during translocation by the high electrical forces acting on them (Talaga and Li, 2009). However, this finding contrasted with the results obtained by Firnkes and coworkers which did not report such behavior for the translocation of avidin through 20 nm diameter Si_xN_y pores (Firnkes *et al.*, 2010). In the latter article, the authors present an in-depth systematic study of the electrokinetic effects that govern protein translocation across solid-state pores: electrophoresis and electroosmosis. These

two effects are additive if the charge of the protein has the same sign as the charge of the pore walls, and subtractive if the charges have opposite signs. The effective velocity of the protein molecules during translocation depends on the applied electric potential as well as on the values of the zeta potential of the protein and of the pore which are pH-dependent in their turn. It is thus possible for electroosmosis to enhance or counteract electrophoresis, promoting or inhibiting translocation. When the two electrokinetic forces cancel each other out, the translocation of proteins becomes diffusion-controlled. It becomes obvious that for an accurate interpretation of protein-pore interactions, it is imperative to consider the relative charged states of both the protein and the pore (Firnkes *et al.*, 2010).

To complete the analysis of native and unfolded MBP through nanopores, Oukhaled and colleagues have recently investigated its interaction with two Si_xN_y nanopores with diameters of 4 nm and 20 nm (Oukhaled *et al.*, 2011). The results showed that the native MBP generates higher event frequency, as well as larger blockade currents and durations, than the unfolded MBP. Furthermore, the percentage current blockade stays constant with increasing voltage for the native proteins while it decreases for unfolded proteins. These findings suggested that the unfolded proteins occupy smaller volumes inside the nanopore than native proteins and that their conformation, and hence their volume, is affected by the applied potential which stretches the molecules. The blockade durations of both the native and unfolded proteins decreased with increasing voltage, indicating an electrophoretic-dominant transport through the pores. Moreover, the percentage current blockade determined by protein translocation through the 4 nm pore was larger than through the 20 nm pore. The authors also reported complications determined by the protein adsorbtion to the nanopore's surface (Oukhaled *et al.*, 2011). This phenomenon has been recently investigated by Sexton and coworkers in a comparative study of the interaction of BSA, phosphorylase B and β-galactosidase with gold-coated conical nanotubes. It was observed that smaller proteins have a higher propensity of adhering to the pore walls, although for shorter times than larger proteins and that the difference in protein size had a more significant effect on the blockade durations than on the blockade current amplitudes (Sexton *et al.*, 2010).

The problem of non-specific protein adsorbtion and clogging of solid-state nanopores has been addressed and successfully eliminated by coating the Si_xN_y nanopores with fluid lipid bilayers (Yusko *et al.*, 2011). Various types of lipids can be used to directly control the thickness as well as the surface chemistry of the coating and indirectly the final diameter and length of the nanopore. By introducing lipids with a biotinyl cap into the structure of the lipid coating, it was possible to observe the translocation of streptavidin-biotin, polyclonal anti-biotin Fab-biotin and monoclonal anti-biotin IgG-biotin complexes through the nanopore. In the absence of the biotinylated lipids, the frequency of events was found to be 500-fold lower than in the presence of the capture sites. This original approach suggested that such a strategy could prove useful for the detection and analysis of proteins from dilute solutions, and also could be used to slow down the molecular transit through the nanopore in order to obtain information about the affinity of proteins to different ligands based on the frequency of events generated. Finally, the analysis of molecules known to aggregate and adhere to solid-state surfaces such as the amyloid-beta (Aβ) peptides related to Alzheimer's disease was possible with the lipid-coated nanopores. This finding will likely prove useful for the future study of real-time aggregation of other amyloidogenic peptides involved in protein misfolding diseases (Yusko *et al.*, 2011).

1.1.3.5 Nanopore sensing of protein-antibody complexes

Differentiation between the transit of proteins and that of protein-antibody complexes through synthetic pores was possible based on the same principles of detection. Colloid particles decorated with streptavidin generated larger blockade currents when translocating micrometer polydimethylsiloxane pores in the presence of specific monoclonal antibodies than in their absence, indicating the concentration-dependent formation of protein-antibody complexes on the surface of the colloidal particles (Saleh and Sohn, 2003). Siwy *et al.* demonstrated that the ionic flow through gold-plated poly(ethyleneterephtalate) (PET) conical nanopores fabricated through the track-etch method is permanently stopped if molecular recognition agents such as protein G, ricin or biotin immobilized on the pore's wall surface are exposed to a solution of IgG, antiricin antibody, and streptavidin, respectively (Siwy *et al.*, 2005).

More recently, in a similar approach using glass nanopipettes functionalized with covalently-attached IgG molecules, Umehara *et al.* successfully detected the specific binding of cancer biomarker proteins (Umehara *et al.*, 2009). With sub-micrometer glass pores, Uram *et al.* were able to determine the number of antibodies bound to viral particles without immobilization by observing the change in particle volume upon antibody binding as reflected in the translocation parameters (Uram *et al.*, 2006). The binding of BSA to a Fab fragment from a BSA-binding antibody was detected with gold-plated PET conical nanopores (diameter 9-27 nm). The current blockade signatures generated by the translocation of the BSA-Fab complex could be easily distinguished from those of the free Fab and also from signatures of a control protein which did not bind the Fab fragment. Details about the size and stoichiometry of the complex could also be obtained. An important discovery of this research was that the complex generated smaller blockade currents than BSA. This is explained by the fact that the change in size of the complex is compensated by the change in charge, in agreement with observations from DNA translocation experiments (Smeets *et al.*, 2006a; Sexton *et al.*, 2007). The authors concluded that to detect current blockades, the size of the narrow tip diameter of the conical pore must be comparable to the diameter of the analyzed species (Sexton *et al.*, 2007). Furthermore, the specific interaction between the β-human chorionic gonadotropin hormone with its specific monoclonal IgG in a dose-dependent way was also demonstrated. The resulting hormone-antibody complex's electrophoretic mobility proved to be higher than that of the individual components which explained the lack of events upon addition of the hormone to the antibody solution (Han *et al.*, 2008). These findings supported the fact that sensing with solid-state nanopores can be successfully employed for immunoassays without the need for specific labeling, immobilization, or amplification steps required in traditional approaches.

1.1.3.6 The effect of alternating current on nanopore sensing

Until recently, the nanopore sensing experiments have been conducted almost exclusively using direct current (DC) measurements. A few groups have looked at the effects of alternating current (AC) on nanopore conductance and on the interaction of different analytes with the nanopore, suggesting significant advantages over the DC

approach. By superimposing a 25 Hz, 20 mV sine wave on the applied DC bias, Wilk and coworkers were able to measure the AC conductance of the OmpF porin of *E. coli* and found a linear dependence of the pore conductance on the electrolyte concentration (Wilk *et al.*, 2006). Ervin *et al.* confirmed the AC conductance values of OmpF obtained by Wilk *et al.* and also successfully measured the AC conductance value of the α-hemolysin channel during similar experiments (Ervin *et al.*, 2007). α-hemolysin's AC and DC conductance values in 1.0 M KCl and 10 mM phosphate buffer (pH 7.4) were found to be very similar (0.95 ± 0.08 nS and 0.89 ± 0.09 nS, respectively). Furthermore, the conductance of both channels for infinite electrolyte dilutions revealed non-zero values which indicated that only three mobile counterions contribute to the net conductivity of the α-hemolysin nanopore (Ervin *et al.*, 2007).

There is a twofold advantage of using a low AC voltage (10-20 mV rms) superimposed on a low DC voltage (10-50 mV) instead of unique large DC voltage (50-100 mV). First, the electrostatic interference on binding kinetics and deformations of the molecules are reduced. Second, the electroosmotic and electrophoretic effects of the high electric field on the molecular and ionic transport through the nanopores are minimized (Ervin *et al.*, 2007). These effects enable a more accurate measurement which was observed during the reversible binding of heptakis-(6-O-sulfo)-β-cyclodextrin and of a nine base pair DNA hairpin molecule to the α-hemolysin nanopore (Ervin *et al.*, 2008). Increasing the number of inserted α-hemolysin nanopores from 1 to 26 resulted in a significant increase in sensitivity without the generation of highly complex current traces because simultaneous events proved to be highly improbable (Ervin *et al.*, 2009).

More importantly, the effect of alternating electric fields on DNA interaction with nanopores may prove useful for the development of the future DNA sequencer as observed in molecular dynamics simulations experiments (Sigalov *et al.*, 2008). In these simulations, a nanopore fabricated in a silicon-based membrane was designed to function as a capacitor with two conductive layers separated by an insulator layer (Figure 1.8). The alternating potential which drove single-stranded DNA molecules back and forth inside the nanopore was applied through one pair of electrodes (V_{ext}) while the sequence-specific electric potentials generated by the DNA movement were measured

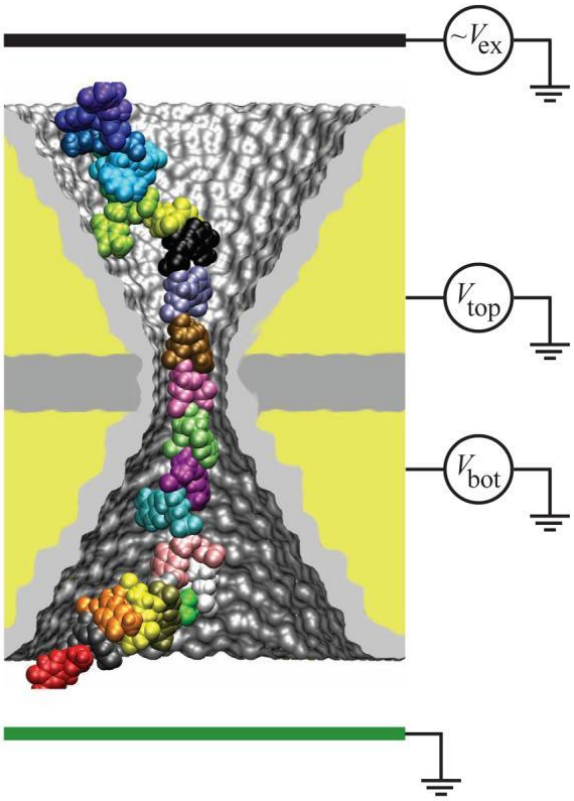

Figure 1.8. Design of a synthetic nanopore for DNA sequencing. The single DNA molecule is driven back and forth inside the nanopore by an applied alternating potential V_{ex}. An insulating SiO_2 membrane (grey) separates two conductive plates (yellow) which act as electrodes (V_{top} and V_{bot}) and measure the electrostatic potentials determined by the motion of DNA. (Reprinted by permission from Sigalov *et al.*, 2008. Copyright American Chemical Society 2008).

by the two conductive membrane layers acting as a second set of electrodes (V_{top} and V_{bottom}) (Sigalov *et al.*, 2008).

Experiments combining AC and DC measurements have been recently reported (Lathrop *et al.*, 2010). A DC voltage was used to drive a 12 base pair DNA hairpin with a 50 nucleotide poly-A tail into the α-hemolysin pore followed by the deactivation of the DC voltage and monitoring of the channel conductance only with an AC voltage applied. The time required for the DNA hairpin to exit the nanopore was found to be dependent on the DC and AC voltages applied (0-100 mV_{dc} and 20-250 mV_{ac}), AC frequency (60-200 kHz) and temperature (-10 to +20˚C). In this way, the activation enthalpy energy and the asymmetry factor associated with the DNA hairpin escape from the nanopore could be directly determined. The authors showed an improved signal-to-noise ratio of the current traces when AC rather than DC voltages were used and anticipated that at frequencies higher than 200 kHz the AC field variation may become faster than the response time of the DNA molecules. In this situation, the effect of the AC field on the molecular interactions with the nanopore would be diminished (Lathrop *et al.*, 2010).

1.2 Bioanalytical applications of single-molecule nanopore sensing

The array of nanopore sensing experiments indicates a wide range of possible bioanalytical applications for this single-molecule analysis technique. The DNA and RNA sensing experiments show potential for the development of a high throughput sequencing method, while the nanopore force spectroscopy approach could prove useful as a rapid clinical genotyping technique (Nakane *et al.*, 2004; Tropini and Marziali, 2007; Zhao *et al.*, 2007). In this way the identification of single nucleotide polymorphisms (SNP) will allow the study of disease genetics and pharmacogenomics (Mirsaidov *et al.*, 2010). Epigenetic modifications detected in the manner reported by Stoddart and coworkers may play an important role in the early detection of cancer and at the same time in the development of personalized genomic medicine (Stoddart *et al.*, 2009; Mirsaidov *et al.*, 2010; Stoddart *et al.*, 2010).

On the other hand, the ability of nanopore sensing to detect different degrees of protein folding/unfolding or aggregation and to distinguish between different protein

conformations without the need of substrate labeling or immobilization, may make this method of analysis a tool for the understanding of protein misfolding diseases such as prion diseases, Alzheimer's and Parkinson's disease (Stefureac *et al.*, 2010a).

Besides these mainstream applications, nanopore sensing with genetically engineered pores has shown promise as a detection tool for dangerous molecules such as 2,4,6-trinitrotoluene (TNT), liquid explosives, organoarsenic compounds, organophosphorous nerve agents and nitrogen mustards which could be used in terrorist warfare (Shin *et al.*, 2002; Guan *et al.*, 2005; Jayawardhana *et al.*, 2009; Wang *et al.*, 2009). Furthermore, while some groups have employed nanopores as molecular biosensors for biological toxins such as ricin and anthrax with the aid of specific antibodies, others have coupled pores with molecular adapters to detect therapeutic drugs in solution (Gu *et al.*, 1999; Halverson *et al.*, 2005; Siwy *et al.*, 2005).

1.3 Other single-molecule techniques

Besides nanopore sensing, other techniques that allow the study of individual molecules have been developed. Four of the most common of these analytical methods together with their applications are briefly presented here.

A technique capable of determining intra- or intermolecular distances is fluorescence resonance energy transfer (FRET). The method can determine distances ranging from 2-8 nm by measuring the efficiency of energy transfer between a donor and an acceptor fluorophore attached to the molecules of interest (Ha, 2001). The variation in the distance between the two fluorophores as reflected in the efficiency of energy transfer indicates a conformational change of a molecule or its movement relative to another (Selvin, 2000). FRET has been extensively used to study nucleic acid folding and dynamics, conformational changes of proteins, protein-protein interaction within cell membranes and movement of large macromolecular complexes (Deniz *et al.*, 2000; Sako *et al.*, 2000; Zhuang *et al.*, 2000; Sako and Yanagida, 2003; Diez *et al.*, 2004; Ha, 2004; van Holde and Zlatanova, 2006).

Optical tweezers represent the most sensitive single-molecule technique for measuring linear force and motion (Walter *et al.*, 2008). This method uses a highly-focused light beam capable of levitating a micrometer-size polystyrene bead to which

single molecules can be attached. If the bead is moved from the beam's center of focus by an external force, the light beam will respond with a proportional opposing force which is measured by interferometry (Bustamante *et al.*, 2008; Spudich *et al.*, 2008). Individual molecules can be tethered between one optical tweezer and a fixed surface or between two optical tweezers and be pulled mechanically to unravel the force needed to unfold proteins or RNA molecules as well as the interaction force between two proteins (Williams and Rouzina, 2002; Abbondanzieri *et al.*, 2005; Bechtluft *et al.*, 2007). Interaction forces between 0.1-300 pN can be measured with this analytical technique (Walter *et al.*, 2008). The coupling of optical tweezers with nanopore sensing proved to be an advantageous combination for measuring the electric force acting on translocating DNA molecules (Keyser *et al.*, 2006; Dekker, 2007). In these experiments, the polystyrene bead of the optical tweezers was coated with λ-DNA molecules and was placed in the proximity of a solid-state nanopore in an electrolyte solution. An applied voltage drove the λ-DNA molecule into the nanopore exerting a force on the attached polystyrene bead which moved out of the focus center of the optical tweezers until the electric and optical forces were balanced. With this ingenious setup, the authors observed that the force acting on the DNA molecule increased linearly with the applied voltage at a value of 0.24 pN/mV (Keyser *et al.*, 2006).

Magnetic tweezers have similar applications as optical tweezers but with a different functional principle. In this case a magnetic microbead is suspended in an external magnetic field and can be used to measure both force and torque by rotating or pulling the magnet (Lionnet *et al.*, 2008; Walter *et al.*, 2008). This method proved useful for studying DNA elasticity and protein-DNA interactions (Strick *et al.*, 1996; Charvin *et al.*, 2005; Gore *et al.*, 2006).

Atomic force microscopy (AFM) is a single-molecule technique which can be used for imaging and force measurement. Briefly, a very sharp tip is mounted at the end of a flexible cantilever. A laser beam is shone onto the cantilever and its reflection is detected by a photo diode. The change in the position of the cantilever is detected as a variation in the position of the reflected beam on the photo diode. Moving the cantilever across different surfaces generates an AFM map or image of the respective surface. In this way, the morphology of single molecules such as membrane proteins, nuclear pore

complexes or bacterial porins can be determined (Muller *et al.*, 1996; Stoffler *et al.*, 1999; Jaroslawski *et al.*, 2007). The method is also a force spectroscopy tool allowing higher force measurements (10-10,000 pN) than the molecular tweezers. Mechanical properties of single molecules can be measured with subnanometer and pN resolution by attaching one end of the molecule to the tip of the cantilever and the other to a movable flat plane. Cell adhesion, protein folding and protein-protein interactions can be investigated with AFM (Rabbi and Marszalek, 2008).

Although these methods of analysis are extremely sensitive and are successfully employed in single-molecule studies, they require substrate immobilization and/or labeling which slows down the speed of detection by increasing the preparation times and costs of operation.

1.4 Prions

Prions are very small infectious pathogens of proteinaceous nature responsible for a fatal neurodegenerative group of diseases called transmissible spongiform encephalopathies (TSEs) or prion diseases (Prusiner, 1982). Prion diseases are caused by the conformational conversion of the cellular prion protein (PrP^{C}), a normal component of the central nervous and lymphatic systems, into the infectious scrapie isoform (PrP^{Sc}) under the influence of the exogenous PrP^{Sc} through a domino-like mechanism (Prusiner, 1991, 1998). Fourier-transform infrared spectroscopy measurements of the two PrP isoforms showed an α-helical content of 42% and 3% β-sheet for PrP^{C}, whereas PrP^{Sc} had 30% α-helical and 43% β-sheet content (Pan *et al.*, 1993). The misfolded proteins aggregate, forming amyloid fibrils and plaques in the neuronal tissue, which in turn lead to neuronal apoptosis and death of the subject. Since both prion proteins have the same sequence, TSEs are the only known diseases in which the target and the infectious agent are the same (Prusiner, 2001).

1.4.1 Structure and function of the prion protein

PrP^{C} is encoded by a small, single copy gene called *Prnp* present on chromosome 20. PrP^{C} is normally expressed at the presynaptic membrane of neurons, glia cells,

lymphoid tissues, gastroepithelial cells, heart, kidney and muscle (Brown *et al.*, 1998a; Sales *et al.*, 1998). PrP^{C} involvement in the central nervous system explains the neurodegenerative effects determined by the newly-formed PrP^{Sc} aggregates (Kretzschmar *et al.*, 1986). The human PrP^{C} is synthesized and released into the endoplasmic reticulum (ER) lumen as a 253 amino acid polypeptide chain. In the ER lumen, the N-terminal signal peptide (amino acids 1-22) is cleaved and two N-linked carbohydrate moieties are attached at positions N181 and N197 (Figure 1.9a) (Gaggelli *et al.*, 2006). The carbohydrate moieties have the role of stabilizing the structured parts of the protein (Zuegg and Gready, 2000). The protein is linked to the outer cell membrane through a glycosylphosphatidylinositol anchor (GPI anchor) that is synthesized in the endoplasmic reticulum and attaches at position 230 (Caughey, 1993) (Figure 1.9). The GPI anchor enables the protein to be cycled back and forth from the endosome by exocytosis and maintains the protein at 0.9-1.3 nm from the membrane surface (Shyng *et al.*, 1995; Caughey and Chesebro, 1997; Zuegg and Gready, 2000). The mature PrP^{C} is 208-209 amino acids long with a molecular weight of ~35 kDa (Hegde *et al.*, 1998; Aguzzi and Calella, 2009).

The structural analysis of recombinant PrP^{C} from various species confirmed that the overall structure of the protein is globular (Riek *et al.*, 1996; Viles *et al.*, 2001; Kuwata *et al.*, 2004; Calzolai *et al.*, 2005). Moreover, a high level of structural homology between bovine and human PrP^{C} has been found and both proteins have the same global architecture (López García *et al.*, 2000). The NMR structural studies of recombinant PrP^{C} from all species revealed the presence of three α-helices, a short antiparallel β-sheet segment and a flexible disordered N-terminal region (López García *et al.*, 2000) (Figure 1.9b). In the bovine prion protein, for example, residues 144-154 form Helix 1, residues 173-194 form Helix 2 and residues 200-226 form Helix 3. It is worth mentioning here that Helix 2 and Helix 3 are connected by a disulphide bond between residues 179 and 214, the only one present in the structure of the prion protein. The short β-sheet segment comprises the residues 128-131 and 161-164 (López García *et al.*, 2000). The disordered N-terminal region extends over 108 residues and contains four identical glycine-rich octapeptide repeats (residues 51-91 PHGGGWGQ) that can bind preferentially up to

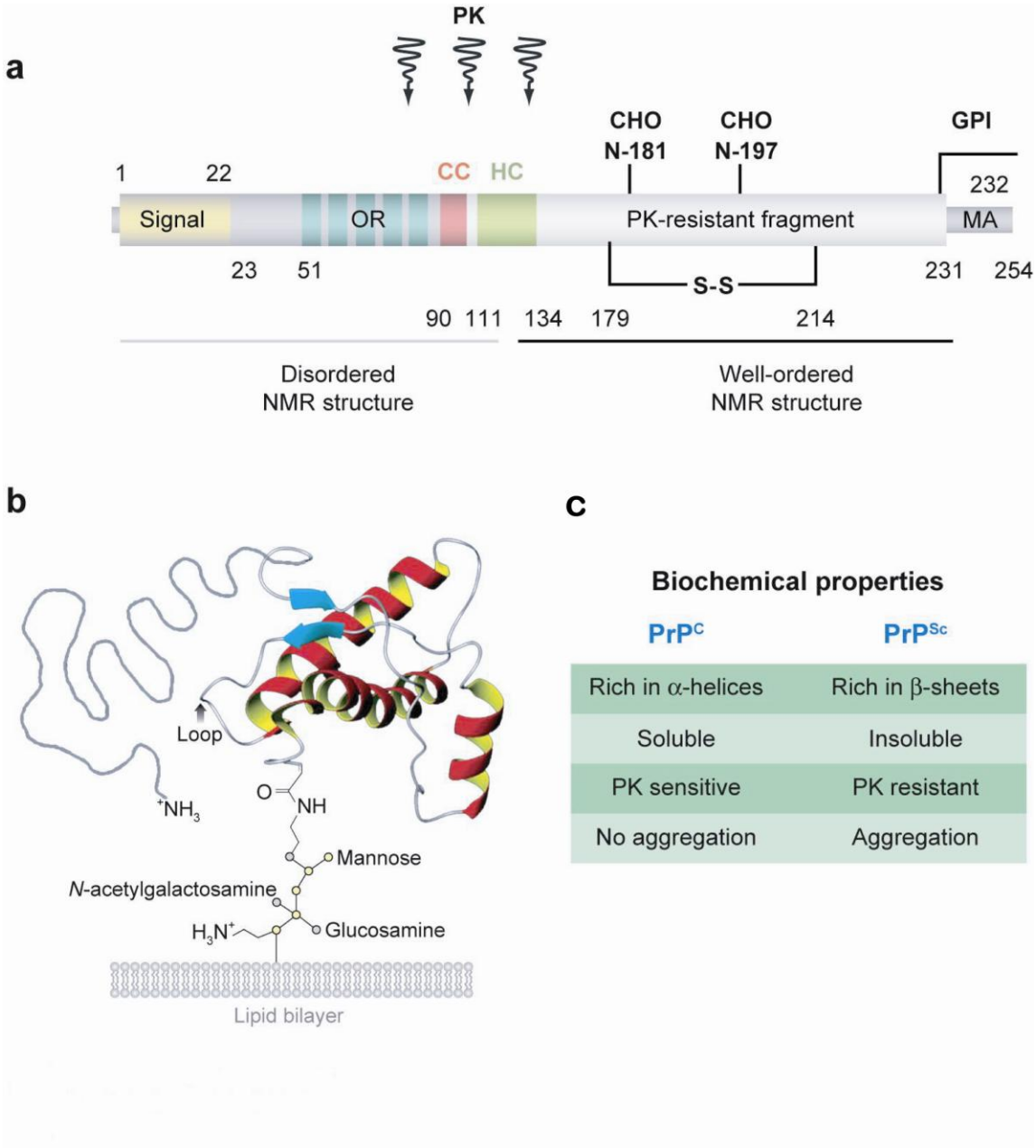

Figure 1.9. The structure of PrP^{C} and biochemical properties of PrP^{C} and PrP^{Sc}. Panel (a) illustrates the primary structure and posttranslational modifications of PrP^{C}. The secretory signal peptide situated at the N-terminus (yellow), the octarepeat region (OC) (blue), the charged cluster (CC)(pink), the hydrophobic core (HC)(green), the glycosylation sites (CHO), the disulfide bond (S-S), the proteinase K digestion sites (PK), the membrane anchor (MA) and glycosylphosphatidylinositol (GPI). Panel (b) shows the tertiary structure of PrP^{C} inserted in a lipid bilayer as obtained by NMR and panel (c) the biochemical properties of PrP^{C} and PrP^{Sc}. (Reprinted by permission from Aguzzi *et al.*, (2008). Copyright 2008 by Annual Reviews).

four divalent copper atoms (Pan *et al.*, 1992; Hornshaw *et al.*, 1995; Brown *et al.*, 1997; Viles *et al.*, 1999; Brown *et al.*, 2001a) (Figure 1.9).

There are continuing discussions about the normal physiological function of the PrP^{C}. One of the most important is that the protein is a mediator in copper transport and homeostasis in the brain. It has been shown that copper binding to the octapeptide repeat region of PrP is a pH-dependent process starting at pH 6, reaching a maximum at pH 7.8 and decreasing drastically at acidic pH values (Viles *et al.*, 1999; Whittal *et al.*, 2000). This discovery suggested a pH-dependent molecular mechanism by which PrP binds Cu^{2+} in the extracellular matrix and releases it within the endosome. The shuffling movement between the synaptic space and the endosome suggested that PrP^{C} may have a role in the synaptic transduction of the nervous signal (Mouillet-Richard *et al.*, 2000; Lee *et al.*, 2001). Furthermore, addition of Cu^{2+} to PrP^{C} causes the protein to become protease-resistant and detergent insoluble, properties characteristic of PrP^{Sc} (Quaglio *et al.*, 2001). Another important function of PrP^{C} is its antioxidant activity and it has been shown that the protein can act as a copper-based superoxide dismutase, protecting the neuronal cells against reactive oxygen species (Brown *et al.*, 1997; Brown *et al.*, 1999; Vassallo and Herms, 2003). The superoxide dismutase activity ceases when the N-terminal part of PrP^{C} comprising the octapeptide repeats is removed (Sakudo *et al.*, 2003). Studies of PrP^{C}-deficient cerebellar cells from mice showed that the nervous cells were more sensitive to oxidative stress than the wild-type cells, indicating a very important role in neuroprotection and even memory formation (Martins and Brentani, 2002; Coitinho *et al.*, 2006). Furthermore, PrP^{C} has been shown to interact with a variety of proteins, as well as with DNA and RNA, suggesting a cell signaling or protein modulation role (Nandi, 1997; Deleault *et al.*, 2003; Caughey and Baron, 2006; Lima *et al.*, 2006; Marc *et al.*, 2007; Aguzzi *et al.*, 2008).

Although PrP-null mice (*Prnp*$^{0/0}$) develop normally and are resistant to prion inoculation, subtle abnormalities in circadian rhythm regulation, neuronal myelination and olfaction have been reported (Bueler *et al.*, 1992; Collinge *et al.*, 1994; Tobler *et al.*, 1996; Nishida *et al.*, 1999). On the other hand, *Prnp* knockout mice (*Prnp*$^{-/-}$), with the exception of Zurich I mice, presented ataxia and loss of Purkinje cells towards the end of their lives (Sakaguchi *et al.*, 1996; Rossi *et al.*, 2001).

The conversion mechanism of the normal PrP^{C} protein into the pathogenic PrP^{Sc} is not completely elucidated. What is certain is that PrP^{C} is converted into PrP^{Sc} under the catalytic effect of exogenous PrP^{Sc} which acts as a template for changing the native PrP^{C} folding (Borchelt *et al.*, 1992; Aguzzi and Polymenidou, 2004). Currently, the template-directed refolding and the seeded nucleation are the two generally accepted models for the conformational conversion of PrP^{C} into PrP^{Sc} (Aguzzi and Calella, 2009). Recent studies have revealed that *de novo* formation of PrP^{Sc} is not physiologically favored and other accessory proteins may be involved (Telling *et al.*, 1995; Wong *et al.*, 2001).

Unlike the normal isoform, PrP^{Sc} is resistant to protease K digestion, forms aggregates and does not bind copper (McKinley *et al.*, 1983; Meyer *et al.*, 1986; Hope *et al.*, 1988; Shaked *et al.*, 2001). The lack of copper binding indicates that structural modifications in the octapeptide repeat regions of the N-terminal domain of the protein take place in PrP^{Sc}. Optical spectroscopy measurements confirmed the refolding of the residues situated between positions 90 and 140 into β-sheets in PrP^{Sc} (Huang *et al.*, 1996). In other words, both the octapeptide repeat and helix 1 are transformed into a left-handed β-helix that becomes the N-terminal part of PrP^{Sc} (Ziegler *et al.*, 2003) (Figure 1.10). On the other hand, electron-crystallographic data showed that the helical subdomain formed by helices 2 and 3 remains unchanged, being held in place by the disulphide bond which is required for PrP^{Sc} formation (Muramoto *et al.*, 1996; Wille *et al.*, 2002). Both PrP^{Sc} and the PrP 27-30 fragment (residues 90 to 231) that results after protease K digestion of PrP^{Sc} have been found to contain the β-sheet helix and to have the ability to polymerize into amyloid fibrils (Prusiner *et al.*, 1983; Caughey *et al.*, 1991).

Interestingly, recent experiments showed the formation of β-sheet fibrils when stoichiometrically-mixing two synthetic short peptides belonging to the unstructured N-terminal end of bovine PrP. Addition to the mix of a third peptide derived from Helix 1 abolished the formation of the fibrils, underlining the important role of Helix 1 in preventing aggregation (Tahiri-Alaoui *et al.*, 2003). Synthetic peptides were further used to identify the amino acid sequences that could be involved in PrP fibrillogenesis and toxicity. In 1993, Forloni *et al.* determined that the peptide comprising residues 106 to 126 has a high propensity for fibril formation and induces cell death in neuronal cultures

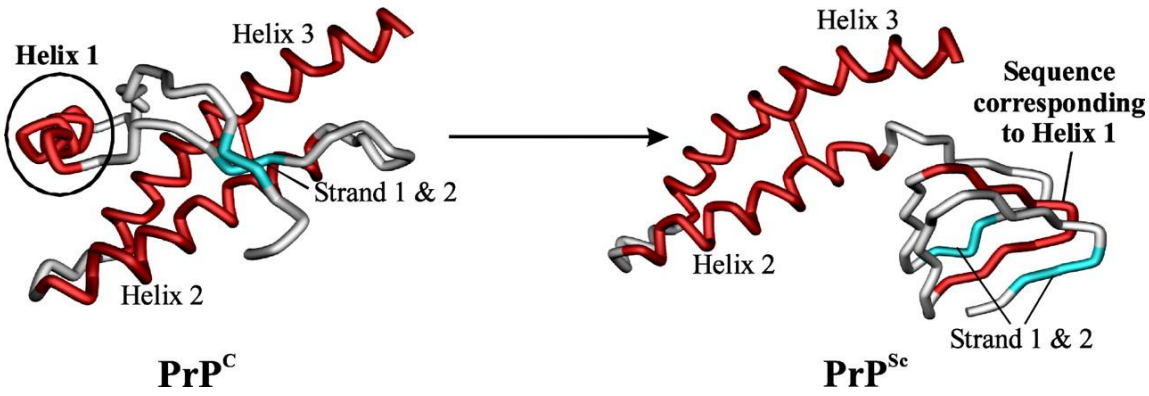

Figure 1.10. Schematic view of the structural conversion of PrP^{C} into PrP^{Sc}. The octapeptide repeat and helix 1 are transformed into a left-handed β-helix that becomes the N-terminal part of PrP^{Sc} while helices 2 and 3 are maintained in both isoforms. (Reprinted by permission from Ziegler *et al.*, 2003. Copyright American Society for Biochemistry and Molecular Biology 2003).

(Forloni *et al.*, 1993). The authors showed that the palindromic region AGAAAAGA (residues 113 to 120) is particularly important for the toxicity when PrP^{C} is expressed (Brown *et al.*, 1994). The fact that this particular region of the protein can acquire different secondary structures depending on the pH, the bound metal ions and the presence of lipids suggested that it could represent the site where the conformational change of PrP^{C} to PrP^{Sc} initiates (Muramoto *et al.*, 1996; Jobling *et al.*, 2001; Grasso *et al.*, 2004; Di Natale *et al.*, 2005).

1.4.2 Prion diseases

Prion diseases were originally identified as scrapie disease in sheep and later as bovine spongiform encephalopathy (BSE) in cattle, chronic wasting disease (CWD) in mule deer and elk, transmissible mink encephalopathy (TME) in mink and feline spongiform encephalopathy (FSE) in cats (Klatzo *et al.*, 1959; Hartsough and Burger, 1965; Roos *et al.*, 1973; Williams and Young, 1980; Wells *et al.*, 1987). In humans, prion diseases can be genetic such as familial Creutzfeld-Jakob disease (fCJD), fatal familial insomnia (FFI) and Gerstmann-Sträussler-Scheinker syndrome (GSS), infectious such as Kuru and the variant Creutzfeld-Jakob disease (vCJD), or sporadic such as sporadic Creutzfeld-Jakob disease (sCJD) (Gambetti *et al.*, 1995; Ghetti *et al.*, 1995; Wood *et al.*, 1997; Lezmi *et al.*, 2003; Lysek *et al.*, 2005). Although prion diseases share a variety of clinical symptoms such as dementia, myoclonus, ataxia, paralysis, insomnia and wasting syndrome, the speed of progression differs from one disease to another (Weissmann, 1996; Zahn *et al.*, 2000).

The first reports of scrapie date back to 1732 in England while its etiology remained unclear for the following 250 years (Prusiner, 1982). The transmission mechanism in sheep is still not well understood although the general consensus is that it occurs orally, maternally or through tissue scarification (Hadlow *et al.*, 1982; Taylor *et al.*, 1996; Hunter *et al.*, 1997; Ligios *et al.*, 2005). Polymorphisms at three different codons in the PrP gene indicate a relationship between the host genotype and the prion strain conferring different degrees of susceptibility to scrapie (Westaway *et al.*, 1994).

The BSE or “mad cow’ disease epidemic in England during the second half of the 1980s was probably caused by contamination of the meat and bone nutritional

supplement fed to cattle which contained sheep prions (Wilesmith *et al.*, 1991). More importantly, BSE prions could be transmitted to humans through meat consumption and the disease was identified as vCJD in 1996 (Will and Zeidler, 1996). Although the incidence of BSE has been kept under control by ending the practice of feeding cattle prion-contaminated meals, the disease has not completely disappeared. The 2003 BSE outbreak in Canada has had a huge negative impact on the country's beef industry and the search for a *pre-mortem* detection method continues.

CWD is the only prion disease naturally occurring in free ranging wild animals and was first described in captive mule deer in Colorado, USA in 1967 (Gilch *et al.*, 2011). The disease is horizontally transmitted to cattle and sheep through environmental contamination and possibly to humans through deer or elk meet consumption (Miller *et al.*, 1998; Gross and Miller, 2001). The infectious agent of CWD has been detected in lymphoid tissues, saliva, urine and feces of contaminated animals. Immunohistochemical testing of cervid tonsils is used to monitor the spreading of the disease throughout North America and a wild-life vaccine is currently in the making for therapy (Wild *et al.*, 2002; Wolfe *et al.*, 2002; Gilch *et al.*, 2011).

TME is a sporadic disease with a rapid incubation period of 7-12 months (Marsh, 1976). Identified in 1947 in Wisconsin and Minnesota and described in 1965, TME is believed to originate from oral consumption of scrapie or BSE contaminated feed (Hartsough and Burger, 1965; Marsh *et al.*, 1991; Liberski *et al.*, 2009). The fact that the TME agent previously passed through cattle showed high infectivity in mink represents a clue for the existence of strain variation (Marsh and Bessen, 1994; Bartz *et al.*, 2002).

FSE has been reported in the United Kingdom since the 1990s in domestic cats as well as other feline species in zoos around the world. Studies of FSE cases in captive cheetahs reported a concomitant lymphatic and neural spread of the FSE agent through the body as well as maternal and hematogenous transmission of infectivity (Lezmi *et al.*, 2003; Bencsik *et al.*, 2009; Eiden *et al.*, 2010).

In humans, Kuru was first discovered in the Fore tribe of Papua New Guinea, an isolated community that practiced cannibalistic rituals (Gajdusek and Zigas, 1957). The transmission of the disease occurred through the consumption of contaminated brain of deceased relatives and spread throughout the families (Klitzman *et al.*, 1984). A decline

in incidence was observed once the cannibalistic rituals ceased and presently the disease is disappearing. The long incubation times observed for Kuru and other CJD cases were found to be dependent on a polymorphism at PrP codon 129. Heterozygosity (methionine/valine) at this codon increased the incubation time and resistance to prion diseases (Collinge *et al.*, 2006).

Several types of CJD have been described and classified based on their etiology. For example sporadic CJD (sCJD), which accounts for about 85 % of human TSEs, appears in the absence of infective or genetic factors (Aguzzi and Calella, 2009). Homozygosity at PrP codon 129 seems to be a predisposing factor for the disease (Palmer *et al.*, 1991). Although the source of sCJD remains unknown, the iatrogenic form (iCJD) of the disease is transmitted through contaminated neurosurgical instruments, grafts, contaminated human pituitary hormone solutions and EEG electrodes (Nevin *et al.*, 1960; Koch *et al.*, 1985; Brown, 2000). Familial TSEs such as fCJD, GSS and FFI are caused by a number of autosomal dominant pathogenic mutations in the *Prnp* gene. In fCJD, besides a large number of reported point mutations, there can also be an increase in the number of N-terminal octapeptide repeats which are involved in causing the disease (Owen *et al.*, 1989). Clinically, there is a rapid development of dementia and myoclonus unlike GSS which is characterized by a later onset of dementia (Hainfellner *et al.*, 1995). GSS is a very rare inherited prion disease due to point mutations at PrP codons 102, 117 and 198 among others (Hsiao *et al.*, 1989; Prusiner, 1989). In FFI, thalamo-limbic dysfunctions determined by a single point mutation (D178N) coupled with the polymorphism of codon 129 were manifested through complete loss of sleep, somato-motor abnormalities and sterility (Gambetti *et al.*, 1995; Montagna, 2005, 2011).

The major international concern is the transmission of BSE to humans as the new variant CJD (vCJD) through contaminated meat consumption (Collinge and Rossor, 1996; Will and Zeidler, 1996). The disease is characterized by an early onset age with distinct clinico-pathological manifestations and long duration. Interestingly, recent studies report that disease transmission has only occurred in individuals who were methionine homozygous at PrP codon 129 (Haik and Brandel, 2011). Although the incidence of the disease has markedly decreased since 2004, new cases caused by contaminated blood transfusions have been confirmed (Peden *et al.*, 2004). These

reports again underline the acute need of a sensitive prion detector for blood supply screening in hospitals.

1.4.3 Prion strains

The phenotypic diversity observed both in animal and human prion diseases, as well as the species barrier, can be explained through the existence of prion strains. These strains were observed initially in goats with scrapie which developed two distinct clinical syndromes termed "hyper" and "drowsy" according to their respective manifestations (Pattison and Millson, 1961). Furthermore, it was demonstrated that inoculations with isolates of each prion strain successfully transmitted their respective syndrome to the recipients. Later, strains started to be identified based on the difference in incubation times and neuropathologic profiles, while it was discovered that new strains can result upon passage from one species to another (Fraser and Dickinson, 1973; Kimberlin *et al.*, 1987). Generally the different prion strains were proved to be produced by the existence of several PrP^{Sc} isoforms that could be distinguished based on their conformation, glycosylation state and size of the fragment generated by proteinase K digestion (Figure 1.11B) (Bessen and Marsh, 1992; Medori *et al.*, 1992; Parchi *et al.*, 1996). A brief description of the strain mechanism is that one or more of the PrP^{Sc} isoforms from the mixture combine with the host PrP^{C} into distinct misfolded PrP polymers during the prion infectious cycle and continues to propagate, causing a specific prion disease characteristic of the respective prion strain (Figure 1.11) (Collinge and Clarke, 2007). Thus, the existence of strains in prion diseases is intimately linked to the individual conformations of the original exogenous PrP^{Sc} molecules and is not due to modifications in the DNA coding sequence (Halfmann and Lindquist, 2010). The selection of a particular prion strain from the mixture to propagate in a given host is directed by the structural compatibility between PrP^{Sc} and the host PrP^{C}, which in turn depends on the amino acid sequence of the host PrP^{C} (Collinge, 2010). This conclusion also explains the species barrier, by facilitating the transmission of prions between species with high degrees of similarity in the primary structure of PrP^{C} and prohibiting the transmission in species with low degrees of structure similarity. Furthermore, the presence of PrP^{C} polymorphisms lowers the susceptibility of transmission even within

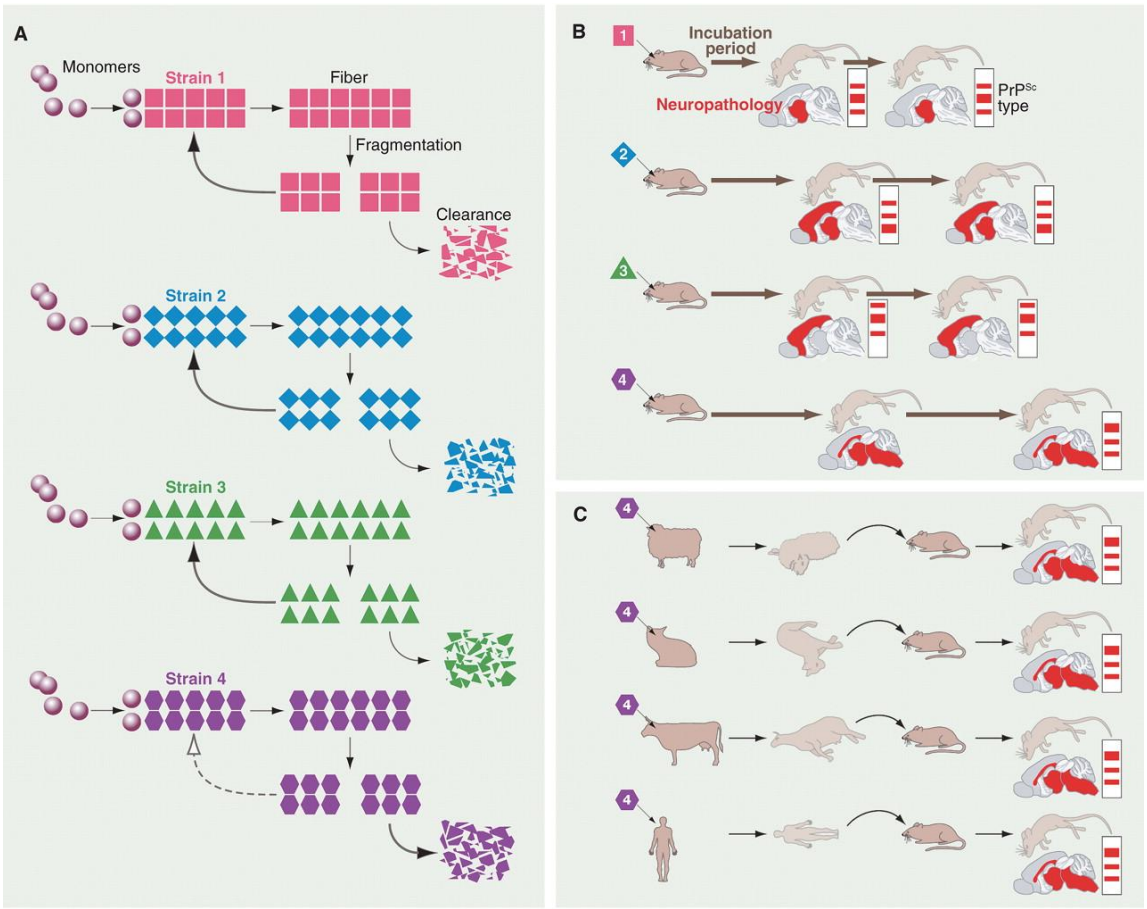

Figure 1.11. Prion strain propagation. Panel (A) shows the propagation of different prion strains by the template-directed refolding mechanism during which PrP^{C} molecules are recruited by the PrP^{Sc} polymer and converted to PrP^{Sc} by autocatalysis. The PrP^{Sc} fibers fragment to generate more infectious templates. Panel (B) shows that strains can be differentiated based on their incubation times (arrow lengths), neuropathology (brain areas affected) and PrP^{Sc} fragments (western blots). Panel (C) shows that strains may maintain their properties even after passages in several other species with distinct PrP^{C} sequences. (Reprinted by permission from Collinge and Clark, 2007. Copyright 2007 AAAS).

the same species as was reported for the PrP codon 129 polymorphism (Collinge *et al.*, 2006). When such a transmission barrier exists, the prion propagation can either be stopped, necessitate longer incubation times, or the prion strain may mutate into a new strain which will be able to accommodate that particular PrP^C conformation breaking the transmission barrier. The resulting new strain may be more or less infective than the original strain which is a situation of great concern for public health especially in the case of potential CWD transmission to humans (Angers *et al.*, 2010).

1.4.4 Metal affinity of the prion protein

The normal function of PrP^C appears to be intimately related to its ability to bind metal ions. Although PrP^C binds preferentially to redox-active metals such as Cu(II) and Fe(II), it was showen to also bind Zn(II), Mn(II) and Ni(II), albeit with much lower affinities (Brown *et al.*, 1997; Brown *et al.*, 2000; Jackson *et al.*, 2001; Millhauser, 2004; Basu *et al.*, 2007; Walter *et al.*, 2007; Brazier *et al.*, 2008). Cu(II) and Zn(II) bind within the N-terminal octapeptide repeat region. The normal PrP^C contains four PHGGGWGQ octapeptide repeats which can bind up to four Cu(II) or Zn(II) atoms (Figure 1.12). Crystallographic and spectroscopic studies confirmed the octarepeat binding units and the coordination partners of the Cu(II) at full occupancy involving the histidine imidazole, two deprotonated glycine amides, the glycine carbonyl and a water molecule forming a square pyramidal complex (Figure 1.12A) (Burns *et al.*, 2003). Two aditional Cu(II) binding sites involving His 96 and 111 have also been identified together with three probable sites within the globular C-terminal domain of the PrP^C (Walter *et al.*, 2009). Multiple coordination modes with variable neurotoxic activities have been proposed to exist as a function of the degree of metal ion occupancy (Pushie and Vogel, 2009). Cu(II) binding to PrP^C starts at His 96 and His 111 and subsequently continues in the octapeptide repeat region (Klewpatinond *et al.*, 2008). Interestingly, Cu(II) and Zn(II) binding to the octapeptide repeat region caused conformational changes dependent on the number of atoms bound, triggering PrP endocytosis and aggregation as well as fibril formation inhibition (Figure 1.12B) (Burns *et al.*, 2003; Klewpatinond and Viles, 2007; Millhauser, 2007; Walter *et al.*, 2007; Stevens *et al.*, 2009). Addition of a large excess of Zn(II) (>1 mM) to Cu(II)-bound PrP^C molecules did

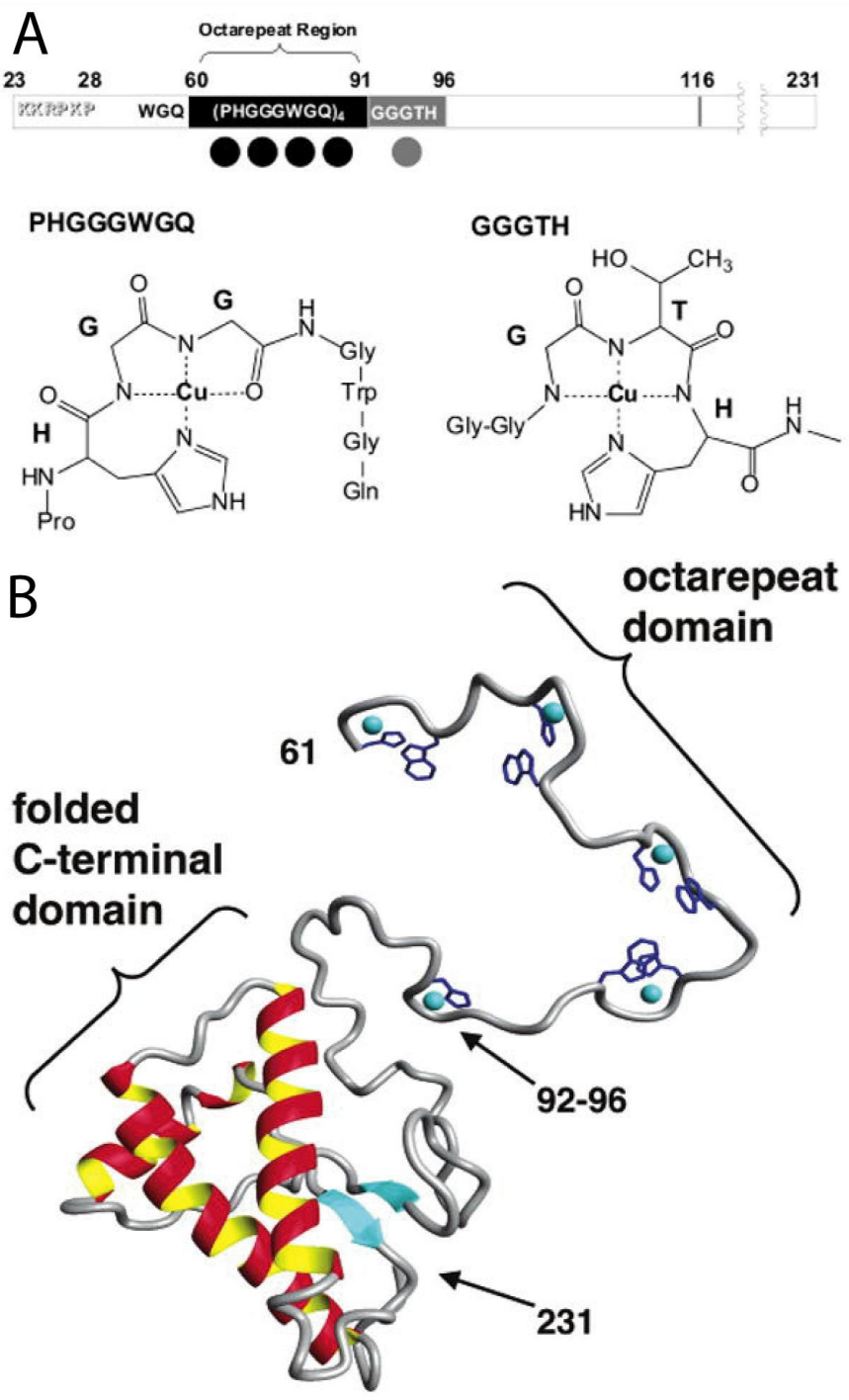

Figure 1.12. Cu(II) coordination of PrP^C. Panel (A) presents the location of the Cu(II) binding sites along the PrP^C sequence and the two Cu(II) coordination modes. Panel (B) presents the three-dimensional conformation of the PrP^C molecule with five Cu(II) bound. (Reprinted by permission from Burns *et al.*, 2003. Copyright American Chemical Society 2003).

not displace the bound Cu(II), confirming the higher affinity of PrP^C for Cu(II) (~10 nM) as compared to Zn(II) (~200 µM) (Walter *et al.*, 2007; Viles *et al.*, 2008; Nadal *et al.*, 2009). The increase in the number of octapeptide repeats by up to five additional inserts has been associated with the pathology of CJD by creating a Cu(II) imbalance in the brain which increased the neurotoxicity and decreased the onset age of the disease in humans from over 60 years to about 30-40 years of age (Goldfarb *et al.*, 1991; Krasemann *et al.*, 1995; Stevens *et al.*, 2009).

PrP^C appears to play an important part in the cellular uptake and transport of iron through a yet-unknown mechanism (Singh *et al.*, 2009a; Singh *et al.*, 2009b). Although the exact location of the binding sites of iron to PrP^C has not been identified, experiments showed that iron binding is dependent on the protein's secondary or tertiary structure since complete PrP^C denaturation results in the release of all bound iron (Singh *et al.*, 2010). However, PrP^C affinity for iron is low in comparison to other iron binding proteins such as ferritin or transferrin which regulate iron metabolism in the cells (Singh *et al.*, 2010; Brown, 2011a).

A Mn(II) bound form of the prion protein was isolated from experimentally-infected mice brains and it has been shown to promote and initiate prion aggregation (Thackray *et al.*, 2002; Giese *et al.*, 2004; Brazier *et al.*, 2008). Isothermal titration calorimetry measurements have identified a low affinity Mn(II) binding site (~200 µM) within the octapeptide repeat region and a high affinity Mn(II) binding site (~ 63 µM) located around His 95 (Brazier *et al.*, 2008). While the coordination mode of Mn(II) is currently unknown, recent studies show that it most probably differs from that of Cu(II), causing the prion protein to adopt a structurally distinct conformation as indicated by circular dichroism measurements (Thompsett and Brown, 2007; Zhu *et al.*, 2008; Brown, 2011b).

1.4.5 Inactivation, therapeutics and treatment of prion diseases

It is a well-known fact that prions are resistant to disinfectants and heat as well as to ionizing and UV radiation (Alper *et al.*, 1966, 1978). Prion inactivation methods include autoclaving at 134˚C for 5 hours, treatment with concentrated NaOH and NaOCl solutions for 2 hours at room temperature, or with a H_2O_2/alkaline detergent mixture at

55˚C for 10 minutes or a combination of these methods (Prusiner *et al.*, 1983; Fichet *et al.*, 2004; Schmitt *et al.*, 2010). Gas plasma sterilization has recently proved effective for the decontamination of sensitive medical instruments infected with prions (Fichet *et al.*, 2004; Okpara-Hofmann *et al.*, 2005).

As far as antiprion therapeutics are concerned, a very large number of molecules have been tested as potential antiprion agents both in cell culture as well as in animal model systems. A variety of polyamine dendrimers such as polypropyleneimine, polyethyleneimine, polyamidoamine and lipopolyamines were successfully used to eliminate the detection of PrP^{Sc} in previously PrP^{Sc} infected neuroblastoma cells (ScN2a) (Supattapone *et al.*, 1999; Winklhofer and Tatzelt, 2000; Supattapone *et al.*, 2001; Solassol *et al.*, 2004). Sulfated polyanionic glycans (pentosan polysulfate and dextran sulfate) proved effective in inhibiting PrP^{Sc} formation and accumulation in scrapie infected cells probably by affecting the attachment of glycosaminoglycans to the prion protein which is required for prion infectivity (Caughey and Raymond, 1993). Phosphorothioate oligonucleotides were found to share common binding sites with the sulfated glycans on the PrP^{Sc} molecule and increased survival times if added at the same time with the scrapie inoculums (Kocisko *et al.*, 1994). The dye Congo red, a disulfated molecule, destabilizes PrP^{Sc} amyloids and inhibits their formation through a similar mechanism in cells (Caughey *et al.*, 1993). Although intracerebral and subcutaneous administration of Congo red and some of its derivatives to animal models slowed down prion disease progression in scrapie infected hamsters, these compounds failed to completely cure the disease (Poli *et al.*, 2004). Heparin sulfate and suramin (polysulfonated nafthyl urea) also had PrP^{Sc} formation inhibitory activities in ScN2a cells as well as in scrapie-infected hamster models by promoting misfolding of PrP^{C} before reaching its conversion site into PrP^{Sc} (Gabizon *et al.*, 1993; Nunziante *et al.*, 2005). Other molecules investigated included porphyrin, phtalocyanine and amphotericin B which prevented PrP^{Sc} accumulation and increased the survival rate in scrapie-infected cells and/or animals (Tagliavini *et al.*, 1997; Caughey *et al.*, 1998).

Generally, the antiprion agents proved to be more effective in cellular studies than in animal models, probably because of the existence of the blood-brain barrier which protects the central nervous system against a wide range of chemical molecules. Thus,

compounds known to readily cross this barrier were further tested for antiprion activity. Of several tricyclic acridine and phenothiazine derivatives, quinacrine showed great promise as an antiprion therapeutic agent in neuroblastoma cells and were tested even on human subjects with terminal CJD. The drug was unsuccessful in human studies and had hepatotoxic effects in some patients, underlining the acute need for a *pre-mortem* prion disease diagnosis method for humans before such treatment is commenced (Korth *et al.*, 2001; Prusiner *et al.*, 2004).

Immunotherapy for prion diseases was investigated in parallel with the prion chemotherapy. A variety of monoclonal and polyclonal anti-PrP antibodies were generated in transgenic or *Prnp*$^{0/0}$ mice and their inhibitory effects on PrP^{Sc} propagation have been proven in different cell lines (Korth *et al.*, 1997; Enari *et al.*, 2001; Peretz *et al.*, 2001; Gilch *et al.*, 2003). One of the most effective antibody fragments proved to be Fab D18 which was able to not only stop prion replication, but also successfully eliminated previously existing PrP^{Sc} (Enari *et al.*, 2001). The results indicated that the antibodies bind to the PrP^{C} molecules present on the cell surface, thus blocking the access of the infective PrP^{Sc} molecules to PrP^{C} molecules (Kim *et al.*, 2004). Passive immunization with monoclonal antibodies of scrapie-infected mice had inhibitory effects on PrP^{Sc} propagation only in cases of peripheral infection and when applied before the onset of the clinical symptoms. This happened most probably because the antibodies were not able to cross the blood-brain barrier and reach the central nervous system (Heppner *et al.*, 2001; White *et al.*, 2003; Li *et al.*, 2010). Active immunization with full-length recombinant PrP^{C}, as well as with different PrP^{C} peptides, was able only to delay the onset of the disease and mice tested eventually died. It was reported that only antibodies with affinity for PrP^{C} regions 105-125 and 144-152 showed antiprion activities (Schwarz *et al.*, 2003; Magri *et al.*, 2005). Recent investigations show great promise towards the development of a potent anti-PrP^{Sc} vaccine through the study of different epitopes and delivery options (Hedlin *et al.*, 2010).

In summary, the above therapeutic approaches extend the incubation times and slow down the progression of the disease by inhibiting the accumulation of PrP^{Sc}, destabilizing PrP^{Sc} amyloids and limiting the availability of PrP^{C} for pathogenic conversion. However, prion diseases remain incurable to the present day.

1.4.6 Diagnostic methods for prion diseases

To date, an approved presymptomatic diagnosis method of the prion diseases has remained elusive. Infectivity bioassays in mice require very long incubation times and are affected by the species barrier (Ingrosso *et al.*, 1995; Brown *et al.*, 1998b; Brown, 2001). Thus, definitive diagnosis of most TSEs relies on the detection of the proteinase K resistant form of the prion protein (PrP 27-30) in *post-mortem* brain tissue of infected individuals (McKinley *et al.*, 1983; Meyer *et al.*, 1986). Only five diagnostic tests have been approved by the European Commission and assay kits are commercially available. The *Prionics-Check Western Test* comprises SDS-PAGE separation of PrP 27-30 fragment resulted after PrP^{Sc} proteinase K digestion followed by Western blot analysis with the monoclonal antibody 6H4 which binds to the DYEDRYYRE epitope. The detection limit was determined to be between 5.0-20.0 pmol with good reproducibility (Schaller *et al.*, 1999; Oesch *et al.*, 2000; Soto, 2004). The *CEA/Biorad test* uses two different monoclonal antibodies in a sandwiched enzyme-linked immunosorbent assay (ELISA). One antibody is immobilized onto a solid surface plate and binds the PrP 27-30 contained in the brain homogenate/lysate. The second PrP 27-30 specific antibody coupled to an enzyme (peroxidase) is added to the plate and its binding to PrP 27-30 is indicated by the presence of enzyme activity in the ELISA test. This test has high sensitivity with detection limits of 0.5-2.0 pmol but requires much longer preparatory steps (Moynagh and Schimmel, 1999; Grassi *et al.*, 2001; Bennion and Daggett, 2002; Soto, 2004). A similar two antibody (one for capture and another for detection) approach is used for PrP 27-30 detection in the *Prionics-Check luminescent immunoassay (LIA) test* with the distinction that the proteinase K digested samples are first mixed with the antibody-peroxidase complex and then are transferred to the immobilized antibody plate. A chemiluminescence-producing peroxidase substrate is added during the last step of the assay, which indicates the presence of PrP 27-30 with 97.9% sensitivity (1.0-5.0 pmol) (Biffiger *et al.*, 2002; Soto, 2004). A chemiluminescence ELISA method is also used for PrP 27-30 detection in the *Enfer test*, with detection limits ranging from 1.0 pmol to 10.0 pmol (Moynagh and Schimmel, 1999; Soto, 2004).

The conformational-dependent immunoassay (CDI) developed by Stanley Prusiner's group at the University of California in San Francisco is capable of detecting the presence of both PrP^{C} and PrP^{Sc} proteins individually without the need for protease digestion (Safar *et al.*, 1998). This assay is basically a sandwich immunoassay, employing a capture antibody and a fluorescently-labeled antibody for detection. The detection antibody binds a PrP conformational epitope accessible only in the PrP^{C} conformation and not in the PrP^{Sc} conformation. Specific antibody binding to the native and denatured PrP form is measured by dividing the sample into two aliquots, one of which is treated with 4 M guanidium hydrochloride while the other one is left untouched. After both aliquots are fixed on capture antibody-coated plates, the labeled detection antibody is added and fluorescence is detected for both aliquots. The difference in fluorescence between the native and denatured reactions correlates with the amount of PrP^{Sc} in the sample. The method has been subsequently improved to detect prion protein concentrations as low as 0.5-5.0 pmol during an 8 hour procedure (Perrier *et al.*, 2002; Safar *et al.*, 2002; Bellon *et al.*, 2003; Soto, 2004).

The detection methods presented above are generally used to identify the presence of PrP^{Sc} in brain tissue, which is known to have the highest PrP^{Sc} concentration. However, brain biopsy can only be done *post-mortem*. The search for a less invasive prion detection method continues, although the past years have brought a few significant advances. Besides the brain tissue, PrP^{Sc} has been identified during the biopsy of lymphoid tissues such as tonsils, appendices, spleens as well as in skeletal muscle and olfactory epithelium of patients with sporadic CJD (Hill *et al.*, 1997; Hilton *et al.*, 1998; Glatzel *et al.*, 2003; Zanusso *et al.*, 2003). These findings showed some promise for the development of a less invasive prion disease diagnosis method; however, the best option for the patient would be a prion blood detector. The biggest challenge for such a method is the extremely low PrP^{Sc} concentration in blood. For example, in the buffy coat fraction of blood from scrapie-infected rodent models, the concentration of PrP^{Sc} is estimated to be $\sim 3 \times 10^{-14}$ M during the symptomatic phase and about 10 fold lower during the incubation period. In human and cattle blood it is expected to be even lower, making its detection impossible without PrP^{Sc} amplification or concentration techniques (Brown *et al.*, 1998b; Brown, 2001; Brown *et al.*, 2001b).

The prion misfolding cyclic amplification (PMCA) was developed as a rapid *in vitro* prion replication method aimed at increasing the PrP^{Sc} concentration in diluted samples and serves as the foundation of the most sensitive method of prion detection (Saborio *et al.*, 2001). Briefly, the samples containing undetectable amounts of PrP^{Sc} are incubated with excess quantities of PrP^{C} from brain homogenate, which results in the formation of new PrP^{Sc} aggregates. Sonication of the aggregates following the incubation step disrupts the growing aggregates and fragments them into smaller PrP^{Sc} converting units. The cycle is repeated until a detectable amount of PrP^{Sc} is generated (Figure 1.13) (Saborio *et al.*, 2001; Soto *et al.*, 2005). This approach resulted in a several million fold increase in sensitivity compared to the standard Western blot assay and was successfully used to detect the presence of PrP^{Sc} in hamster and sheep blood during the presymptomatic and symptomatic phase of the prion disease with detection limits of ~1 ag of PrP^{Sc} in approximately 3 weeks (Saa *et al.*, 2006; Thorne and Terry, 2008). Furthermore, PrP^{Sc} was also identified in urine and cerebral spinal fluid by using an improved version of the PMCA technique called quaking-induced conversion (QUIC) which uses recombinant PrP^{C} instead of brain homogenate and replaces the sonication step with automated shaking to fragment the PrP^{Sc} aggregates (Murayama *et al.*, 2007; Atarashi *et al.*, 2008; Atarashi *et al.*, 2011; Orru *et al.*, 2011).

PrP conformation-specific antibodies have been developed for each prion protein isoform and have been used in the sandwich ELISA methods (Korth *et al.*, 1997; Paramithiotis *et al.*, 2003; Andrievskaia *et al.*, 2006; Polymenidou *et al.*, 2008). Latest advances in prion detection methods combine the QUIC amplification method with immunoprecipitation. The use of PrP^{Sc} specific IgM monoclonal antibody 15B3 obtained by Korth and coworkers brings the detection limit down to ~1 fg of prion in blood plasma within 48 hours, making this combined technique the most sensitive available to date (Atarashi *et al.*, 2011; Orru *et al.*, 2011).

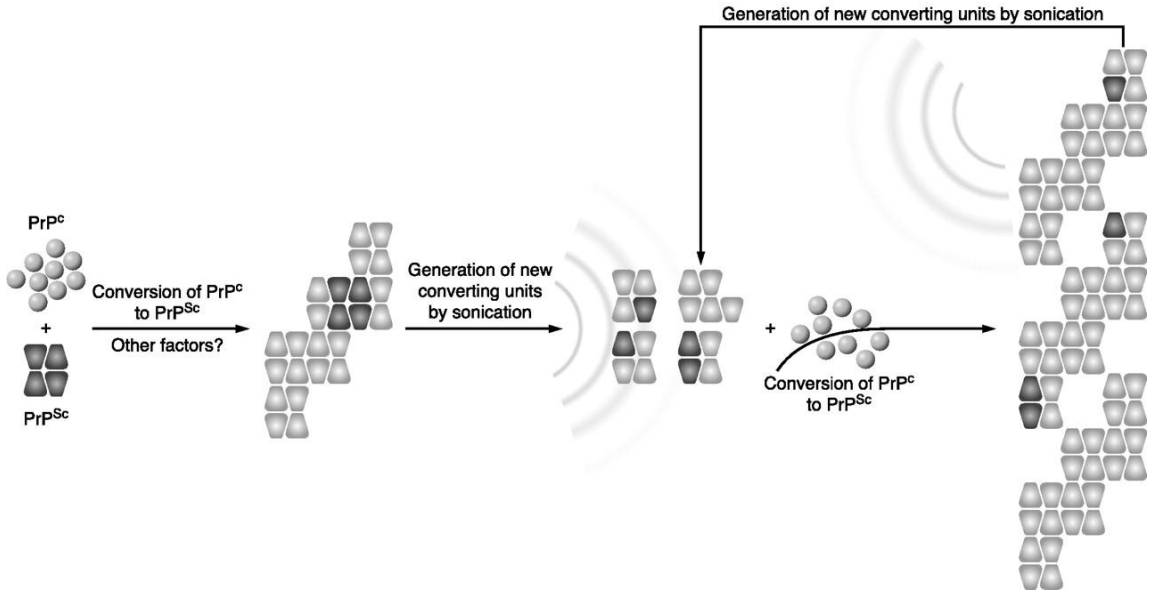

Figure 1.13. The protein misfolding cyclic amplification (PMCA). PrP^{C} molecules are recruited by PrP^{Sc} seeds, converted to PrP^{Sc} and incorporated into aggregates. The PrP^{Sc} aggregates are subsequently fragmented by rounds of sonication thus generating an increasing number of PrP^{Sc} converting units. The procedure is repeated until the required quantity of prion protein is obtained. (Reprinted from Aguzzi and Calella, 2009. Copyright American Physiological Society 2009).

1.5 Thesis objectives

The nanopore sensing method of analysis represents a powerful single-molecule technique with great potential for the study of protein folding and protein-protein interaction. The experimental part of this thesis represents a natural continuation of previous peptide and protein nanopore investigations done by our laboratory and is aimed at gaining a better understanding of the folding/unfolding mechanism of peptides and proteins during their dynamic interaction with different types of nanopores. Furthermore, the potential application of nanopore sensing as a diagnostic tool for protein misfolding diseases in general, and prion diseases in particular, is assessed.

Experiments previously peformed in our lab with the α-hemolysin pore have shown that small protein molecules, such as the histidine-containing phosphocarrier protein (HPr), can unfold to translocate the nanopore and different folding states determined by mutations can be detected (Stefureac *et al.*, 2008). To find out how the anatomy of the nanopore affects the translocation signatures of these proteins and their unfolding, a similar analysis was performed with the aerolysin pore at the very beginning of this project.

The next objective was to determine if and how protein conformational changes due to disulfide bond cleavage are reflected in their interaction parameters with the α-hemolysin pore. For this set of experiments, insulin was used since this protein contains a number of disulfide bonds which are readily cleaved by tris(2-carboxyethyl)phosphine (TCEP).

Another objective of this work was to investigate the effects of alternating current rather than direct current on the translocation of peptides and proteins through α-hemolysin nanopores. It was hypothesized that molecules of different lengths and dipole moments will resonate at different frequencies of the applied electric field which will improve their separation from complex mixtures.

The conformational study of protein folding continued with the nanopore analysis of Zn-finger peptides in the presence and absence of different metal ions. The purpose of this set of experiments was to determine if metal-induced folding of peptides can be detected by this analytical method.

The effect that metal ion binding to proteins exerts on their conformation immediately suggested that nanopore sensing could prove useful for distinguishing between the two prion protein isoforms based on their different affinities for Cu(II), as well as for studying metal binding to proteins. To test this hypothesis, nanopore analysis of synthetic peptides mimicking the metal-binding sequences of PrP^{C} was performed with the α-hemolysin pore, and their affinity for different metal ions was investigated.

The next objective of this project was to determine if nanopore sensing can be developed into a real-time live animal and human TSE detector. With this goal in mind and considering the dimensions of the full-length prion protein and its aggregates, it became obvious that solid-state nanopores accommodating the passage of such large molecules were needed. The first experiments done after the characterization of the solid-state nanopores concentrated on the sensitivity of the method by determining if proteins of different sizes could be distinguished with this type of pore as well as elucidating whether proteins transit the solid-state pores in a folded or unfolded conformation.

Since the specificity of the future nanopore prion detector is to be conferred by PrP-specific antibodies, the next objective was to test if the formation of the PrP-antibody complex can be detected by the solid-state nanopore analysis method. Other questions that needed to be answered here concerned whether or not the molecular complex needs to translocate the nanopores in order for its formation to be detected, what would the optimal nanopore diameter be for such a task, and if results obtained on different pores correlate.

These sets of experiments lay the foundation for the development of the electrophoretic nanopore prion detector with single-molecule sensitivity. In the long run, the prion detector will rely on solid-state nanopores engineered with specific antibodies and will prove useful for the real-time detection and discrimination of the normal as well as the infectious prion proteins.

2.0 MATERIALS AND METHODS

2.1 Reagents, supplies and equipment

Table 2.1 presents all the chemical and biological reagents, equipment and supplies used for the experiments performed in this research. Table 2.2 shows the names of the manufacturing companies and their addresses.

2.2 Analysis of protein molecules using nanopore detection

2.2.1 Analysis of wild type and mutant HPr with aerolysin pores

The wild type *E.coli* HPr together with the T34N and S46D mutants were generous gifts from Dr. Bruce Waygood from the Department of Biochemistry, University of Saskatchewan, and were over 99% pure (Waygood and Steeves, 1980; Sharma *et al.*, 1991; Napper *et al.*, 1996). 10 mg/mL HPr solutions in 10 mM potassium phosphate buffer with 1.0 M KCl at pH 7.8 were prepared fresh daily for the nanopore experiment.

The aerolysin nanopore was received as a kind gift from Dr. Peter Howard, Department of Microbiology and Immunology, University of Saskatchewan. The stock aerolysin solution concentration was 1.5 μg/mL, and contained 0.1 μM trypsin required for activation. A 1000x diluted aerolysin solution in 10 mM potassium phosphate buffer/1.0 M KCl at pH 7.8 was used in the patch-clamp experiments. All aerolysin solutions were stored at -20 °C.

The stock lipid solution used in all the experiments performed in this thesis was 20 mg/mL 1,2-diphytanoyl-sn-glycero-3-phosphocholine in $CHCl_3$, purchased from Avanti Polar Lipids Inc. was aliquoted in several 75μL Kimble vials and stored at -20°C. Before each experiment, one aliquot was dried under vacuum for 4 hours with a Welch Vacuum pump (Thomas Industries) and then re-disolved in decane to a final concentration of 30 mg/mL.

Table 2.1. Chemical and biological reagents, equipment and supplies

Item	Supplier
Chemical and biological reagents	
1,2-diphytanoyl-sn-glycero-3-phosphocholine in $CHCl_3$	Avanti Polar Lipids
16.5% Tris-Tricine precast SDS-PAGE gel	BIO-RAD
Argon (gaseous)	Praxair
Bromophenol blue	BIO-RAD
Cobalt chloride ($CoCl_2$)	Sigma-Aldrich
Control peptide (hairpin): Ac-SESYINPDGTWTVTE-NH_2	Sigma-Genosys
Copper sulfate ($Cu_2SO_4 \cdot 5H_2O$)	Sigma-Aldrich
Decane (anhydrous)	Sigma-Aldrich
Ethanol	EMD
Ethylenediaminetetraacetic acid (EDTA)	BDH
Fmoc-$D_2A_{10}K_2$ (A10)	Sigma-Genosys
FSD-1: QQYTAKIKGRTFRNEKELRDFIEKFKGR	Sigma-Genosys
Guanidine hydrochloride (Gdn-HCl)	EM Science
Hydrochloric acid (HCl)	BDH
Hydrogen peroxide (H_2O_2)	EMD
Insulin from bovine pancreas	Sigma-Aldrich
Insulin chain A from bovine pancreas	Sigma-Aldrich
Insulin chain B from bovine pancreas	Sigma-Aldrich
Magnesium chloride ($MgCl_2$)	BDH
Manganese chloride ($MnCl_2 \cdot 4H_2O$)	Fisher Scientific
Maltose binding protein	VLI Research Inc.
Nitric acid (HNO_3)	EMD
Nitrogen (gaseous)	Praxair
Octa2: PHGGGWGQ PHGGGWGQ	Sigma-Genosys
Octa4: PHGGGWGQ PHGGGWGQ PHGGGWGQ PHGGGWGQ	Sigma-Genosys
Potassium chloride (KCl)	Sigma-Aldrich
Protein molecular weight markers	Boehringer Mannheim, Promega

PrP106-126: KTNMKHMAGAAAAGAVVGGLG	AnaSpec
Potassium phosphate, dibasic (Na_2HPO_4)	Sigma-Aldrich
Potassium phosphate, monobasic (NaH_2PO_4)	Sigma-Aldrich
Ribonuclease A (RNase A)	MP Biomedicals
Silver wire	Alfa Aesar
Sodium dodecyl sulfate (SDS)	Sigma-Aldrich
Sulfuric acid (H_2SO_4)	EMD
N-tris-hydroxymethyl-methyl glycine (Tricine)	Sigma-Aldrich
Tris-[hydroxymethyl] aminomethane (Tris)	Sigma-Aldrich
Tris-2-carboxyethyl-phosphine hydrochloride (TCEP)	Fluka Biochemika
Zinc chloride ($ZnCl_2$)	BDH
Zif268: KPFQCRICMRNFSRSDHLTTHIRTHTGD	Sigma-Genosys
α-hemolysin	Sigma-Aldrich

Equipment and supplies

Active-air floating table	Kinetic Systems
Automatic Pipettes and tips	Eppendorf , VWR
Axopatch 200B amplifier	Axon Instruments
Basic pH meter	Fischer
BC-535 amplifier	Warner Instruments
DigiData 1322A digitizer	Axon Instruments
DigiData 1440A digitizer	Axon Instruments
Falcon tubes	VWR
Faraday cage	Warner Instruments
Filters (0.2 μm)	Sarstedt
Glass vials and plastic caps	Kimble-Kontes, VWR
Headstage model BC-535	Warner Instruments
Headstage model CV203BU	Axon Instruments
HP 8662A signal generator	Hewlett Packard
LPF-8 eight-pole low pass Bessel filter	Warner Instruments
Microcentrifuge tubes	VWR
Microliter syringes	Hamilton
Mini-PROTEAN® electrophoresis cells	BIO-RAD

Nitrile gloves (large)	VWR
ONEAC PC750A power supply	ONEAC
Parafilm	VWR
Pasteur pipettes and rubber bulbs	VWR
pClamp 9.0 and 10.1 software	Axon Instruments
Perfusion bilayer chamber and cup	Warner Instruments
Petri dishes (glass)	VWR
Silicone elastomer sheet	McMaster-Carr
Size 000 paintbrushes	Island Blue
Syringes and needles	Becton Dickinson
Tektronix® TDS220 digital oscilloscope	Tektronix
Tubes (various diameters)	Small parts Inc.
Vacuum jars	Bel-Art Products
Welch vacuum pump	Thomas Industries

Table 2.2. Companies and addresses

Company	Address
AnaSpec	AnaSpec, Fremont, CA, USA.
Avanti Polar Lipids	Avanti Polar Lipids, Alabaster, AL, USA.
Axon Instruments	Axon Instruments, Foster City, CA, USA.
BDH	British Drug House, Saskatoon, SK, Canada.
Becton Dickinson	Becton Dickinson, Franklin Lakes, NJ, USA.
Bel-Art Products	Bel-Art Products, Pequannock, NJ, USA.
BIO-RAD	BIO-RAD Laboratories, Mississauga, ON, Canada.
Boehringer Mannheim	Boehringer Mannheim Canada, Laval, PQ, Canada.
EMD	EMD Biosciences, San Diego, CA, USA.
Eppendorf	Eppendorf AG, Hamburg, Germany.
Fischer	Fischer Scientific, Winnipeg, MB, Canada.
Fluka Biochemika	Fluka Biochemika, Buchs, Swizerland.
GIBCO/BRL	Bethesda Research Laboratories, Burlington, ON, Canada.
Hamilton	Hamilton, Reno, NV, USA.
Island Blue	Island Blue Art Supplies, Victoria, BC, Canada.
Kimble-Kontes	Kimble-Kontes, Vineland, NJ, USA.
Kinetic Systems	Kinetic Systems, Boston, MA, USA.
McMaster-Carr	McMaster-Carr, Santa Fe Springs, CA, USA.
ONEAC	ONEAC, Libertyville, IL, USA.
Praxair	Praxair, Inc., Saskatoon, SK, Canada.
Promega	Promega, Madison, WI, USA.
Sarstedt	Sarstedt, Montreal, QC, Canada.
Sigma	Sigma Chemical Company, St.Louis, MO, USA.
Sigma-Aldrich	Sigma-Aldrich Canada Ltd., Oakville, ON, Canada.
Sigma-Genosys	Sigma-Genosys, The Woodlands, TX, USA.
Tektronix	Tektronix, Beaverton, OR, USA.
Thomas Industries	Thomas Industries Inc., Louisville, KY, USA.
VWR	VWR, Mississauga, ON, Canada.
Warner Instruments	Warner Instruments, Hamden, CT, USA.

The electrolyte solution used for the measurements was 1.0 M KCl in 10 mM KH_2PO_4/K_2HPO_4 buffer (pH 7.8). Millipore water (18 MΩ·cm) was used for all solutions.

A transmembrane potential of 100 mV which drove anions from the *cis* to the *trans* chamber was applied through Ag/AgCl electrodes and the experiments were performed as described in section 2.6.

2.2.2 Analysis of Insulin with α-hemolysin pores in the presence of TCEP

Highly pure insulin from bovine pancreas (≥27 USP units/mg) was procured from Sigma-Aldrich together with the oxidized ammonium salts of chain A (90% pure) and chain B (85% pure) peptides.

The reducing agent tris-2-carboxyethyl-phosphine hydrochloride (TCEP) was ordered from Fluka Biochemika and used without purification. Since TCEP is known to oxidize over time, fresh solutions were made before each experiment.

The final concentration of insulin in the perfusion cup was 174 µM, and that of TCEP was 1.74 mM to give an overall 10-fold TCEP excess.

This set of experiments was done in 1.0 M KCl with 10 mM KH_2PO_4/K_2HPO_4 buffer (pH 7.0) and contained 5 mM EDTA in order to avoid insulin's propensity for multimerization in the presence of metal ions. The pH value was lowered to 7.0 to confer all insulin molecules a common net charge of -2e, taking into account the pKa value of 8.0 for the sidechain of cysteine residues. The same applied potential as in section 2.2.1 was used.

α-hemolysin was purchased from Sigma-Aldrich and used without purification. The α-hemolysin solution was made up to a final concentration of 1.25 µg/mL in 1.0 M KCl with 10 mM KH_2PO_4/K_2HPO_4 buffer (pH 7.0) and was stored at 4 °C.

The sodium dodecyl sulfate polyacrylamide gel electrophoresis (SDS-PAGE) experiment, which confirmed the cleavage of insulin's disulfide bonds by TCEP, was performed on a 16.5% Tris-Tricine precast gel from Bio-Rad in Mini-PROTEAN® electrophoresis cells. Tris-Tricine-SDS cathode buffer pH 8.2 and Tris-HCl anode buffer pH 8.9 were used. The experiment was run at 50 mV for the first 10 minutes and at 100

mV until the tracking dye reached the end of the gel. The gel was then removed from the cell and placed in a silver-stain solution for visualization.

2.3 The alternating current (AC) experiments

The Fmoc-protected α-helical A10 peptide (Fmoc-$D_2A_{10}K_2$) was purchased from Sigma-Genosys and was over 90% pure. A stock solution of 2 mg/mL was prepared in 10 mM KH_2PO_4/K_2HPO_4 buffer with 1 M KCl at pH 7.8.

The α-hemolysin solution was made up to a final concentration of 1.25 µg/mL in 1.0 M KCl with 10 mM KH_2PO_4/K_2HPO_4 buffer (pH 7.8) and was stored at 4 °C. The same buffer/electrolyte was also used as the working buffer during the experiments.

The AC voltage was applied to the perfusion cell by an HP 8662A signal generator (Hewlett Packard) connected to the BC-535 amplifier headstage (Warner Instruments). The amplitude and frequency of the sine-wave was checked with a Tektronix® TDS220 digital oscilloscope (Tektronix) before recording of data was commenced. The overall transmembrane potential was 60 mV with an AC amplitude of 200 mV for all five frequencies investigated (10 MHz, 20 MHz, 50 MHz, 100 MHz and 500 MHz).

2.4 Analysis of peptide molecules in the presence of metal ions using nanopore detection

2.4.1 The Zn-finger peptides

The Zn-finger peptides were synthesized by solid-phase synthesis and purified by preparative reverse-phase high performance liquid chromatography (Sigma-Genosys). The products were characterized by time-of-flight mass spectrometry and the measured masses were within ± 1 mass units of their calculated values for both peptides. The amino acid sequences of the two peptides were as follows:

Zif268: KPFQCRICMRNFSRSDHLTTHIRTHTGD;

FSD-1: QQYTAKIKGRTFRNEKELRDFIEKFKGR.

Peptide solutions (2.0 mg/mL) in potassium phosphate buffer (10 mM) with 1.0 M KCl (pH 7.8) were prepared fresh daily for the nanopore experiment. Aliquots of the peptides (10 µL) were incubated with $ZnCl_2$, $CoCl_2$ or $MgCl_2$ (Sigma-Aldrich) and then were added to the *cis* side of the perfusion chamber. All experiments were performed under an applied potential of 100 mV driving anions from the *cis* side to the *trans* side of the α-hemolysin pore. All other methods were performed as described in section 2.6.

2.4.2 The prion peptides

The control hairpin peptide as well as Octa2 and Octa4 peptides used in this set of experiments were purchased from Sigma-Genosys and were ≥70% pure. PrP106-126 was purchased from AnaSpec Inc. and was ≥95% pure. The peptides had the following sequences:

Control peptide (hairpin): Ac-SESYINPDGTWTVTE-NH2;
Octa2: PHGGGWGQ PHGGGWGQ;
Octa4: PHGGGWGQ PHGGGWGQ PHGGGWGQ PHGGGWGQ;
PrP106–126: KTNMKHMAGAAAAGAVVGGLG.

All samples tested were dissolved at 1–2 mg/mL in 10 mM Tris–HCl, pH 7.8. Aliquots of the peptides were incubated for 30 min with the appropriate metal chloride or sulphate before addition to the perfusion cup at the ratios presented in Chapter 3.3.3.

The electrolyte solution used was 1.0 M KCl in 10 mM Tris–HCl buffer (pH 7.8). The transmembrane potential used was 100 mV and the *trans* chamber was kept positive while the *cis* chamber was grounded. The experiments were carried out at 22 ± 1 ˚C as outlined in section 2.6.

2.5 Analysis of protein molecules using solid-state nanopores

The Si_xN_y nanopores were obtained through collaboration with Dr. André Marziali laboratory from the Department of Physics and Astronomy at the University of British Columbia. These solid-state nanopores were all fabricated through the focused electron

beam technique using a 200 kV transmission electron microscope (Storm *et al.*, 2003; Smeets *et al.*, 2006; Kim *et al.*, 2007; Tabard-Cossa *et al.*, 2007).

With the model reported by Deblois and Bean for cylindrical pores with diameters comparable in size to their lengths, it is possible to calculate the theoretical value of the solid-state pore conductance as follows:

$$G = \frac{k\pi d_p^2}{4(h_p + 0.8d_p)} \qquad \text{Equation 2.1}$$

where G is the pore conductance, k is the buffer conductivity, h_p is the thickness of the pore and d_p is the diameter of the pore (DeBlois and Bean, 1970). The pore conductance values were experimentally obtained by calculating the slope of the open pore current versus applied voltage curve (I/V curve) (Figure 3.19 and 3.26). These measurements were performed before each experiment since it was observed that the open pore current increased slightly with time. Solving equation 2.1 for d_p, an approximate value of the pore diameter is obtained. The pores used in the experiments were tested after mounting on the experimental setup to insure that their conductivity had the correct value for that particular diameter (within the error of the pore thickness). This also confirmed that the measured currents were indeed through the nanopore and not the result of a leakage in the setup. All pores presented stable conductances during an individual experiment.

For the experiments presented in Section 3.4, a total of 36 solid-state pores were tested. Out of these 36 pores only 17 pores were able to detect events. 8 pores out of the 17 pores had correct conductance values and finally only 4 pores lasted long enough to collect complete data sets. Other shortcomings of the nanopores included poor pore-to-pore reproducibility, large open pore current noise (50-100 pA compared to 2-5 pA for α-hemolysin), unexpected sensitivity to certain chemicals such as potassium phosphate buffer, irreversible clogging, very clean and delicate manipulation required and expensive fabrication equipment.

2.5.1 Analysis of maltose binding protein, calmodulin and HPr

All proteins tested were negatively charged at the experimental pH value of 7.3. Highly pure (99.9%) maltose binding protein (MBP) was obtained from VLI Research Inc. Calmodulin (CaM) and the histidine-containing phosphocarrier protein (HPr) were

provided by Drs. E. B. Waygood and L. T. J. Delbaere of the Department of Biochemistry, University of Saskatchewan and were used without any further purification. The physical and chemical characteristics of the proteins are listed in Table 3.10.

Nanopore diameters were nominally 7 nm and 5 nm and had a calculated effective pore length of ~15 nm. Their initial conductance values are shown in Table 3.9.

The electrolyte/buffer solution used for all experiments consisted of 1.0 M KCl / 10 mM Tris-HCl pH 7.3. Deionized ultra pure water with resistivity of 18 MΩ•cm was used for all solutions. Protein interaction with the 7 nm diameter Si_xN_y pore was investigated under 50 mV, 100 mV and 200 mV applied potential and under 50 mV, 100 mV and 150 mV applied potential for the 5 nm pore experiments. The proteins were added on the *cis* side of the perfusion cell since the applied potentials carried the anions from the *cis* side to the *trans* side. The final protein concentration in the experimental cup was 4 μM and the experiments were carried out at 22 ± 1 ºC.

2.5.2 Analysis of bPrP(25-242) interaction with monoclonal antibody M2188

All proteins tested were positively charged at pH values above 7.0. Highly pure (70 Kunitz units/mg protein) ribonuclease A (RNase A) was purchased from MP Biomedicals. The monoclonal antibody M2188 was developed against recombinant bovine prion protein bPrP residues 25-242 with a C-terminal His5 tag in mice and subsequently extracted and purified as described previously (Andrievskaia *et al.* 2006). bPrP(25-242) and M2188 were received as gifts from Dr. Olga Andrievskaia from the Canadian Food Inspection Agency, Nepean , Ontario, Canada. Protein stock solutions of 2 mg/mL, 1 mg/mL and 2.44 mg/mL of RNase A, bPrP and M2188 respectively were made in 1.0 M KCl /10 mM Tris-HCl pH 7.8 which was also used as working buffer. Aliquots of bPrP(25-242) and RNase A were incubated with M2188 at the desired ratio for 1h before they were added to the experimental setup. Deionized ultrapure water with resistivity of 18 MΩ·cm was used for all solutions. Protein interaction with the 11 nm diameter Si_xN_y pore was investigated under 50 mV, 100 mV and 150 mV applied potential and under 80 mV applied potential for the 19 nm pore experiments. The proteins were added on the *trans* side of the perfusion cell to facilitate their

electrophoretic transport with the applied potentials. The experiments were carried out at 22 ± 2 ºC. The physical and chemical characteristics of the proteins are listed in Table 3.16. The pI values of RNase A and bPrP were calculated with the Innovagen Peptide Property Calculator (Lund, Sweden) and their dimensions were estimated from the X-Ray and NMR structures respectively (Joseph-McCarthy *et al.*, 1996; López García *et al.*, 2000). The volumes were calculated assuming the proteins were regular ellipsoids except for the antibody where the volume was calculated based on the individual volumes of the Fab and Fc fragments (Pilz *et al.*, 1975; Pilz *et al.*, 1976).

Two synthetic nanopores with nominal diameters of 11 nm and 19 nm were used. After mounting the pores on the experimental setup, their conductivity was determined by calculating the slope of the open pore current versus applied voltage curve (I/V curve) (Figure 3.26) as presented by Stefureac *et al.* (Stefureac *et al.*, 2010b). From the conductivity values an effective pore length of ~ 6 nm was calculated. Both pores showed stable conductances throughout the duration of each experiment and their initial values are listed in Table 3.17.

2.6 The patch-clamp experimental setup, data collection and processing

2.6.1 The hardware

For the investigation of individual molecules with protein pores and solid-state pores a patch-clamp apparatus was used. Figure 2.1E shows a photograph of the instrumental setup. The patch-clamp instrument consists of four main components connected to a personal computer: the perfusion unit, the electrodes, the amplifier and the digitizer.

The hardware description will begin with the perfusion unit. For the experiments utilizing protein pores, the perfusion unit is formed of a Teflon perfusion bilayer chamber (black) and a Delrin perfusion bilayer cup (white) with a 150 μm aperture on one side (Figure 2.1A). The two components separate the perfusion unit into two compartments, *cis* and *trans*, each with an approximate volume of 1.0 mL. Both compartments were filled with the same electrolyte solution. The perfusion unit was encased in a block of solid copper that rested on an active-air floating table (Kinetic Systems) to reduce the vibrational interference of the signal. For the solid-state pore experiments, the perfusion unit consists of a two-piece poly-tetra-fluoro-ethylene

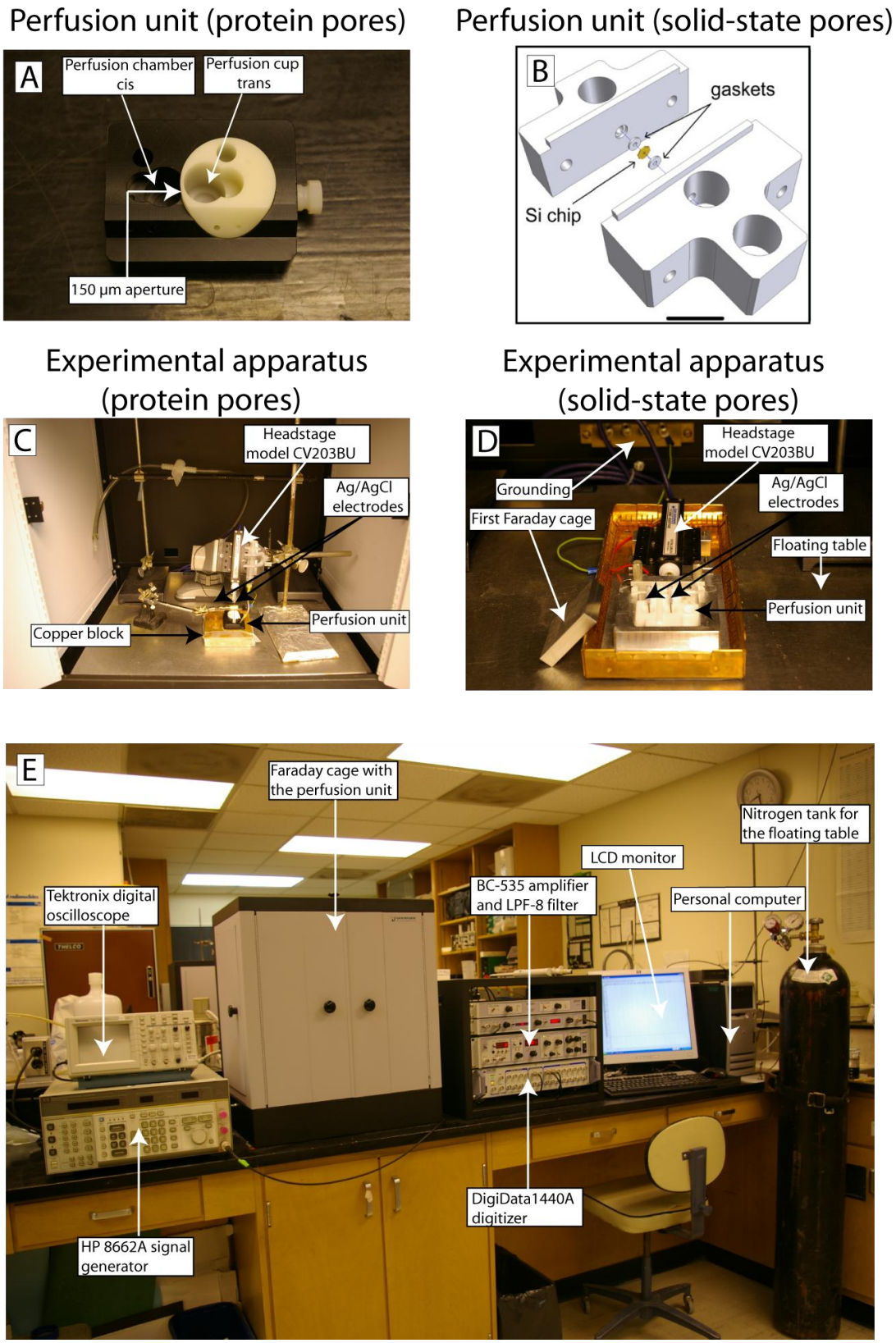

Figure 2.1. Images of the instrumental setup. Panel B reprinted by permission from Tabard-Cossa *et al.*, 2007. Copyright 2007.

(PTFE) cell with three liquid reservoirs of 0.5 ml volume each (Figure 2.1B) (Tabard-Cossa *et al.*, 2007). The solid-state nanopore support chip was interposed between two silicone elastomer gaskets which ensured the gigaohm-seal between the first two electrolyte-filled reservoirs of the cell, allowing the passage of ions only through the nanopore. The third reservoir is usually filled with water to minimize the evaporation of the electrolyte during the experiment and is not connected to any of the other reservoirs. The whole cell assembly was tightened together by two stainless steel bolts with nuts and was placed inside an aluminum housing unit which attenuated the electromagnetic noise. A first small Faraday cage enclosing both the electrodes and the perfusion unit was also added at this point. The solid-state apparatus in Figure 2.1D was designed and fabricated at the University of British Columbia under the supervision of Dr. André Marziali.

The electric potential across the perfusion units is applied via two Ag/AgCl electrodes that had been sanded with sand paper and kept in bleach for about 2 hours prior to each experiment to allow for plating.

The perfusion units and the electrodes were placed inside a large Faraday cage (Warner Instruments) that protected the signal against external electric noise. The two electrodes transmitted the signals through an integrating headstage (model CV203BU, with internal cooling unit, Axon Instruments or model BC-535, Warner Instruments) to the patch-clamp amplifier (Axopatch 200B, Axon Instruments or BC-535, Warner Instruments) which converted the voltage to current. The measuring electrode with the low-noise integrating headstage was connected to the *trans* compartment and the reference electrode was connected to the *cis* compartment. The signal was further transmitted to the analog-to-digital converter (DigiData 1322A or DigiData 1440A, Axon Instruments) where it was electronically filtered and digitized. We controlled the membrane potential and the current needed to maintain the potential using the voltage clamp recording mode of the amplifier. All components inside the Faraday cage were grounded to a copper rod at the back of the metal cover of the cage and then connected to the amplifier's signal ground. During the AC experiments, an HP 8662A (Hewlett Packard) sine-wave generator was employed to apply an AC voltage on top of the DC voltage generated by the amplifier. Furthermore, all the patch-clamp instrument

components and the sine-wave generator were powered through a conditioned power supply (ONEAC) and were not connected directly to the wall outlet.

The patch-clamp instrument was connected to a personal computer running the Clampex software included in the pClamp 9.0 and 10.1 packages (Axon Instruments), which enabled us to adjust other very important experimental parameters such as the filter used and the level of signal amplification.

2.6.2 The lipid bilayer setup and pore insertion

Before bilayer formation, the lipid/decane solution was applied on the 150 μm aperture of the perfusion cup with a size 000 paintbrush. The lipid excess was dried under a jet of argon. The *cis* and *trans* compartments of the perfusion unit were filled with the same electrolyte/buffer solution. A lipid multilayer film was formed by dipping the paintbrush into the lipid solution and painting across the aperture while in the electrolyte solution. The multilayer needed to be thinned to a bilayer with repeated brush strokes, until capacitance values allowing pore insertion were obtained. To make sure the bilayer was formed, a transmembrane potential of 100 mV was applied through the Ag/AgCl electrodes. If the bilayer was created, there was no electrical current traveling between the *cis* and *trans* compartments. The bilayer quality was monitored using capacitance measurements performed by pClamp 9.0 or 10.1 software. After a good lipid bilayer was formed, 5μL of nanopore solution (α-hemolysin or aerolysin) was injected adjacent to the aperture in the *cis* chamber. The nanopores self-assembled and inserted into the lipid bilayer. Nanopore insertions were detected by characteristic increases in the current values. In 1M KCl/10 mM phosphate buffer at pH 7.8 under an applied potential of 100 mV, the open current for a single pore insertion was 100 pA and 50 pA for α-hemolysin and aerolysin, respectively. Once a stable single-pore insertion was detected, 10-50 μL of the solution of the compound to be analyzed was added to the *cis* chamber, proximal to the aperture. For the vast majority of our studied molecules, current blockade events appeared immediately after their addition to the *cis* chamber and data recording was commenced. The experiments were carried out at 22 ± 2°C.

2.6.3 The solid-state nanopore setup

The nanopore chips were subjected to piranha cleaning (H_2O_2:H_2SO_4 1:3) at 95˚C for 30 minutes before mounting on the PTFE cell. The piranha solution treatment was used to remove all impurities and render the Si_xN_y surface hydrophilic (Smeets *et al.*, 2003). Following piranha treatment, the chip was rinsed with distilled water and dried under a current of nitrogen.

The two halves of the experimental cell were boiled first in 20% HNO_3 for 10 minutes and then two more times in distilled water for 10 minutes each time. Finally, the two cell components were dried under compressed air and were then ready for the chip mounting procedure.

During the mounting procedure, the nanopore chip was sandwiched between two silicone elastomer gaskets and was positioned in the 2.032 mm indentation performed on one part of the electrolytic cell (Figure 2.1B). The other part of the cell was then added and the assembly locked in position with two bolts and nuts.

The two reservoirs connected through the nanopore were initially filled with degassed ethanol and the whole cell was placed under vacuum (from a water-based vacuum pump) in order to achieve proper wetting of the nanopore and to remove any residual air bubbles from the assembly. During the last step, the ethanol was exchanged by perfusion with degassed electrolyte/buffer solution and the experimental cell was positioned inside the Faraday cage to be connected to the electrodes.

2.6.4 Data collection

In patch-clamp experiments, the raw signal-to-noise ratio is usually low. Thus, to increase the voltage-clamp recording quality, the current needs to be subjected to a level of amplification and electronic filtration before it is digitized and recorded (Sherman-Gold, 2008). Initially, the current measured as a voltage undergoes a level of pre-amplification in the headstage before passing through a low pass filter in the Axopatch 200B or through a separate LPF-8 eight-pole Bessel filter (Warner Instruments). After the signal is filtered, it goes through another amplification step in the digitizer. Finally, the properly amplified and filtered signal is digitized by the analog-to-digital converter and is recorded as current in picoamperes through Clampex software, part of the pClamp

9.0 or 10.1 package from Axon Instruments. The recorded files are saved in a compact binary format specific to Axon Instruments (PClamp, 2005).

For all experiments presented in this thesis, a fixed-length event acquisition mode was used. In this acquisition mode, data was acquired for same-length sweeps whenever an input signal crossed the preset threshold level. This mode of data acquisition has proven to optimize the usage of the hard disk space especially when recording events that alternated with long periods of inactivity (Sherman-Gold, 2008).

The filtering, amplification and sampling rate of the signal are the most important factors for a good quality recording and can be adjusted through the software. To maximize the quality of the signal to be digitized, it must be first filtered and then amplified enough for the signal to occupy the complete range of the digitizer (Heinemann, 1995). Filters are used to reduce the background noise, to avoid aliasing and to improve the signal-to-noise ratio. In all experiments performed throughout this research, a 10 kHz low-pass Bessel filter was used.

The Axopatch 200B amplifier, for example, has a variable gain ranging from 0.5x to 500x. In our experiments with the protein nanopores, we used a gain of 1x while in some solid-state nanopore experiments, especially those with very high open pore currents (larger pores), we used a gain of 0.5x in order to be able to observe the current traces on screen.

The Digidata 1322A and DigiData 1440A digitizers were set to sample the amplified analog signal at a rate of 100 kHz. Filtering at 10 kHz and sampling at 100 kHz enabled us to record good quality signals and observe the details of the signals while the data was recorded.

2.6.5 Data analysis

The recorded data analysis was done with the Clampfit software contained within the pClamp 9.0 or 10.1 packages from Axon Instruments. There are three main types of windows in Clampfit: analysis, results and layout. Recorded data was opened in the analysis window, displayed as a series of concatenated episodes of events and visualized in the browse mode so that the important features of the signals could be observed.

For our data analysis we used the single-channel analysis mode. In this method of analysis, an event is defined as a sudden change in current as the result of the ion displacement from inside the nanopore by the molecule analyzed. The events are characterized by the amplitude of the blockade current (**I**) and the blockade time or duration (**T**) of the molecules. Depending on these two parameters, the interactions with the nanopore can be of three types. The first type of interaction, also called "bumping", is characterized by a small **I** value and is caused by molecules colliding with the nanopore and then diffusing away (Sutherland *et al.*, 2004; Stefureac *et al.*, 2006). The second type of interaction is known as "translocation" and presents a larger **I** caused by molecules crossing the nanopore from the *cis* side to the *trans* side. Provided that the applied voltages are of opposite sign compared to the net charge of the analyte, translocation events have blockade times which decrease with increasing applied voltages (Akeson *et al.*, 1999; Sutherland *et al.*, 2004; Stefureac *et al.*, 2006). Recently, a third type of interaction, namely "intercalation", was identified (Meng *et al.*, 2010). This type of interaction can generate large **I** values similar to translocations but their **T** values in fact increase with increasing applied voltages. In this situation, the molecules enter the nanopore temporarily and then diffuse back out exiting on the same side they entered. Translocations and intercalations can only be distinguished through nanopore sensing experiments carried out under a range of increasing applied voltages while monitoring the blockade duration variation.

Once a zone of interest on the displayed data was identified, the next step was to select this segment for the Clampfit analysis. For the event detection step, one or two detection thresholds were used. On one hand, if the acquired data was formed of only one type of event, then a single detection threshold was sufficient. On the other hand, if two distinctive populations of events belonging to two different blockade amplitudes and times were identified, using two detection thresholds enhanced the separation and ease of analysis. After the segment to be analyzed was selected and the thresholds placed, the program scanned through the data approximating the amplitude and calculating the duration of each event crossing the thresholds using a non-stop level detection mode. In our protein pore experiments, any event with current blockade amplitude at least three times larger than the membrane noise was recorded. Once the event detection session for

the selected segment was complete, the features of each event could be observed in the event viewer window. There it was much easier to notice the presence of one or more populations of events belonging to different blockade amplitudes and durations or identifying and rejecting unwanted signals from the analyzed data.

The time it takes for the instrument to respond to a signal is called the rise time of the instrument ($\mathbf{T}_R$) and determines the minimum duration of a transition that can still be accurately measured in a signal. The rise time depends on the low pass filter cut-off frequency (f_c) applied during data collection and the standard deviation of the signal. It has been shown that $\mathbf{T}_R$ is approximately $0.33/f_c$ and so the rise time for data collected at 10 kHz is about 33 μs (Colquhoun and Sigworth, 1995). Furthermore, Colquhoun and Sigworth suggest that the amplitude of a channel blockade can be measured accurately only if the event duration is twice the rise time of the recording system (Colquhoun and Sigworth, 1995). In our experiments we considered any transition 50 μs or less to be too fast to be correctly measured and the events were not included in our calculations.

Resolution of the amplitude is determined by the filter frequency and the sampling rate. Clampfit calculates the amplitude by averaging the data points in the level after dropping the first and last points to eliminate interference from filter attenuation (PClamp, 2005).

After the analysis was finished, the individual characteristics of each event were found in the results window as a spreadsheet of all durations and amplitudes listed in sequence by their start time in the original file. Further on, we examined the results spreadsheet in Clampfit and imported it into Origin 7.0 graphing software (OriginLab Corporation). The imported data was organized in histograms of current blockade amplitudes and blockade durations versus the number of events. The amplitude of the blockade current populations was determined by fitting each blockade current distribution with the Gaussian function. The lifetime data was obtained by fitting each blockade duration distribution with a single exponential decay function. Curve fitting was done using Lavenberg-Marquardt method (Levenberg, 1944; Marquardt, 1963). The standard deviation of the function was used to evaluate the goodness of the fit.

3.0 RESULTS

3.1 Analysis of protein molecules using nanopore detection

3.1.1 Introduction

Earlier results from our laboratory revealed that the α-hemolysin nanopore can be used as a sensor for the study of protein folding/unfolding in solution (Stefureac *et al.*, 2008). The major finding of this work was that the histidine-containing phosphocarrier protein (HPr) from *Escherichia coli* was able to unfold under the applied electrical force and the conformational differences between the wild-type protein (wtHPr) and two of its mutants (S46D and T34N) could be detected with the α-hemolysin nanopore.

The first objective of my project was to elucidate the role that the vestibule domain of α-hemolysin plays in the protein unfolding and orientation of proteins for translocation. For this purpose, the interaction of wtHPr together and its two mutants S46D and T34N with the aerolysin nanopore which lacks the vestibule domain was investigated.

As a second objective, we were interested in testing whether the conformational changes determined by disulfide bond cleavage of proteins can be detected with the nanopore sensing method of analysis. The protein insulin was chosen to test the proof of principle for this kind of detection with the α-hemolysin nanopore.

3.1.1.1 The structure of HPr

The histidine-containing phosphocarrier protein, HPr, of the phosphoenolpyruvate:sugar phosphotransferase system (PTS) is a monomeric 85 amino acid, globular, soluble, pH and heat-stable protein with a molecular weight of about 9.5 kDa (Anderson *et al.*, 1971) (Figure 3.1). The protein is also stable over a wide interval of pH values ranging from 3.6 to 9.0 and has no net charge at physiological pH (Waygood *et al.*, 1985).

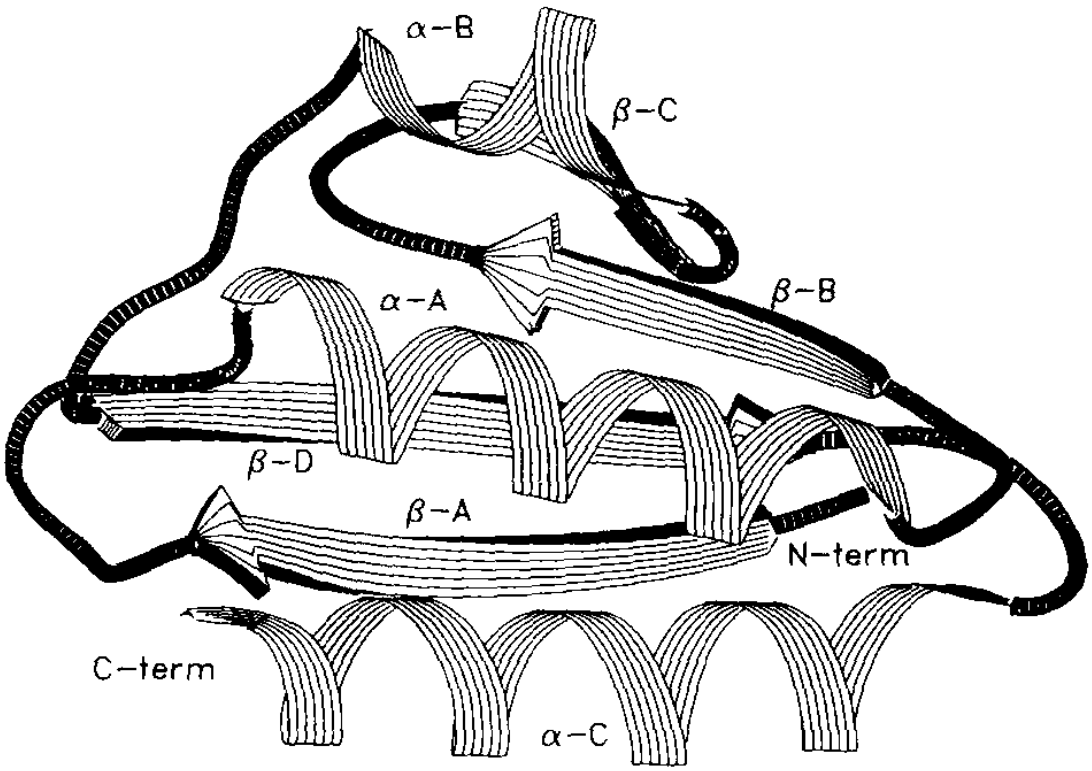

Figure 3.1. A ribbon diagram of the HPr model highlighting the secondary structure. Helices are presented as coils, and strands are depicted as flat arrows. Each of the α-helices and β-sheets are labeled. The N terminus and C terminus are also indicated. The helical face is in front and the β-sheet is in back (Reprinted by permission from Jia *et al.*, 1993. Copyright American Society for Biochemistry and Molecular Biology 1993).

HPr does not contain disulfide bonds or other prosthetic groups (Waygood *et al.*, 1985; Klevit and Waygood, 1986; Smallshaw *et al.*, 1998). The overall folding topology is βαββαβα (Figure 3.1), forming an open-faced β-sandwich**.** The three α-helices overlay the four β-stands that form an antiparallel β-sheet. The β-sheet and the α-helical faces pack against one another, forming a well defined hydrophobic core. The overall shape of *E. coli* HPr is ellipsoidal, having approximate dimensions of 21 x 27 x 38 Å (Jia *et al.*, 1993). The structure is compact and regular which may, in part, account for the thermal stability of HPr (Kundig *et al.*, 1965; Anderson *et al.*, 1971).

The X-ray structure of S46D mutant at 1.5 Å has been determined (Napper *et al.*, 1996). The conformational changes of S46D compared to wtHPr are modest, consisting in a tightening of the α-B helix. The principal effect of the alteration of S46D is a 40% decrease in the PTS activity (Sharma *et al.*, 1991). The mutant carries a formal negative charge at physiological pH.

So far, no three dimensional structure of the T34N mutant has been reported. wtHPr specific antibodies do not bind T34N and the mutant completely lacks PTS activity. These reports suggested the adoption of a disrupted structure (Sharma *et al.*, 1991; Prasad *et al.*, 1998). Moreover, T34N is uncharged at physiological pH.

3.1.1.2 The structure of insulin

Insulin is a protein hormone produced exclusively by the pancreatic β cells with a compact three-dimensional structure consisting of two polypeptide chains connected by two inter-chain disulfide bridges (Adams *et al.*, 1969; Blundell *et al.*, 1971). The A chain (21 amino acids and 2.5 kDa) contains an intra-chain disulfide bridge which stabilizes the hairpin structure of the N-terminal helix linked to the C-terminal helix. The B chain (30 amino acids and 3.5 kDa) has a three-turn central helix flanked by two extended amino acid strands (Figure 3.2) (Adams *et al.*, 1969). In the body, insulin is stored as hexameric complexes with Zn(II) but can also exist as dimers, tetramers or multimers depending on concentration, pH, metal ions and solvent composition while only the monomeric form of insulin is biochemically active (Brange *et al.*, 1997; Chang *et al.*, 1997).

Insulin has low solubility at neutral pH and it can only be dissolved up to 1 mg/mL in phosphate buffer solutions (Lakhiari and Muller, 2004). Alkaline stock solutions are not

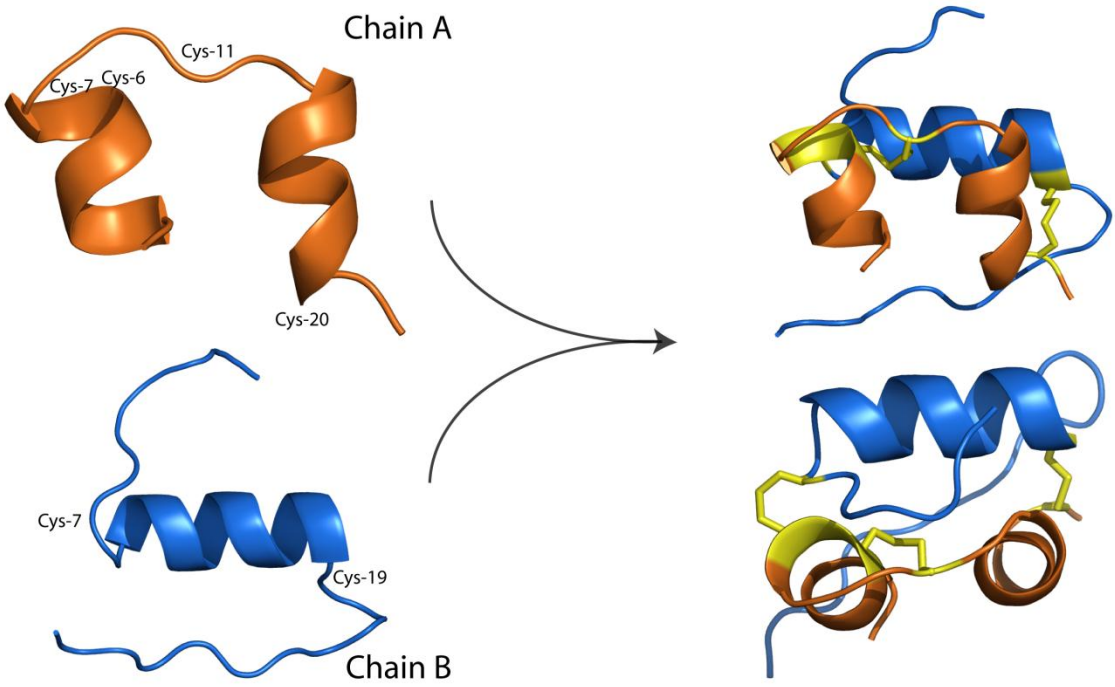

Figure 3.2. The quaternary structure of insulin. Chain A and chain B are assembled through the post-translational formation of two inter-chain disulfide bridges and the cleavage of the C-terminal peptide (not shown). The positions of the Cys involved in disulfide bond formation are indicated. (Based on the 2HIU structure and adapted from Beta Cell Biology Consortium, Copyright 2005).

recommended since high pH increases the rate of deamidation and aggregation. The insulin monomer has an ellipsoidal shape with dimensions of 31 Å x 18 Å x 27 Å and has a net charge of -2e at neutral pH (Hua *et al.*, 1995). Upon treatment with reducing agents, such as TCEP, the disulfide bonds are cleaved and the two insulin polypeptide chains are released. Chain A taken separately has a -2e net charge at pH 7.0 and is water soluble whereas chain B is neutral and precipitates over time (Hong *et al.*, 2006).

3.1.2 Analysis of wild type and mutant HPr with aerolysin pores

The transport of wild type HPr (wtHPr) protein together with the two mutants, S46D and T34N, through aerolysin pores was investigated by measuring the current blockade (**I**) and the blockade duration (**T**). The setting for the experiments and the analysis of the acquired data are described in greater detail in the materials and methods. The current blockade analysis is presented as a histogram where the number of events for each 1 pA increment in **I** is counted. Similarly, the blockade duration analysis histogram counted the number of events for each 0.05 ms increment in **T**. The intensity of the current blockade histograms for wtHPr and the two mutants are shown in Figure 3.3. The histograms of the current blockade duration are presented in Figure 3.4. The calculated parameters are listed in Table 3.1 for easier reference.

The experiments performed with wtHPr revealed, after processing, that the events fell into two distinct types describing two populations (Figure 3.3a). The first population had a Gaussian-fitted peak situated at -21 pA and had a wider distribution of events than the second population centered at a value of -43 pA. The current blockade duration values were obtained by fitting each distribution with a single exponential function. For the first population peak of the wtHPr a blockade lifetime value ($\mathbf{T}_1$) of 0.36 ms was obtained whereas the second population peak was characterized by a $\mathbf{T}_2$ value of 0.19 ms (Table 3.1). Thus the events belonging to the first population had current blockade amplitudes almost two times smaller and current blockade durations two times longer than the events forming the second population. There were also more events forming the first population than the second population.

The current blockade distribution of the S46D mutant looked very similar to that of the wtHPr, in terms of number of populations and in the value of the blockade current (Figure 3.3c).

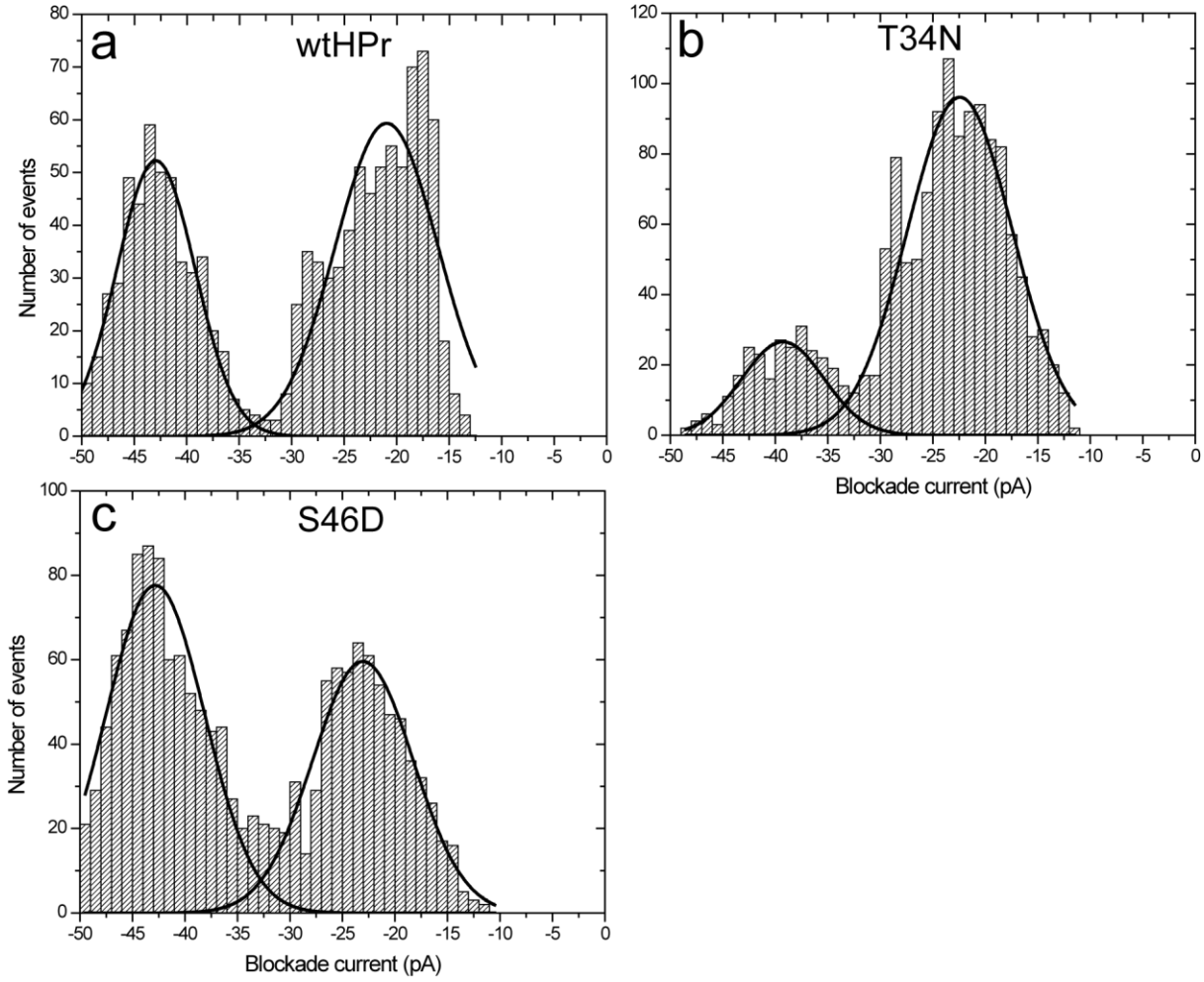

Figure 3.3. Blockade current histograms of the interactions of wtHPr and the HPr mutants T34N and S46D with the aerolysin nanopore. The peak current values were obtained by fitting the event populations with the Gaussian function.

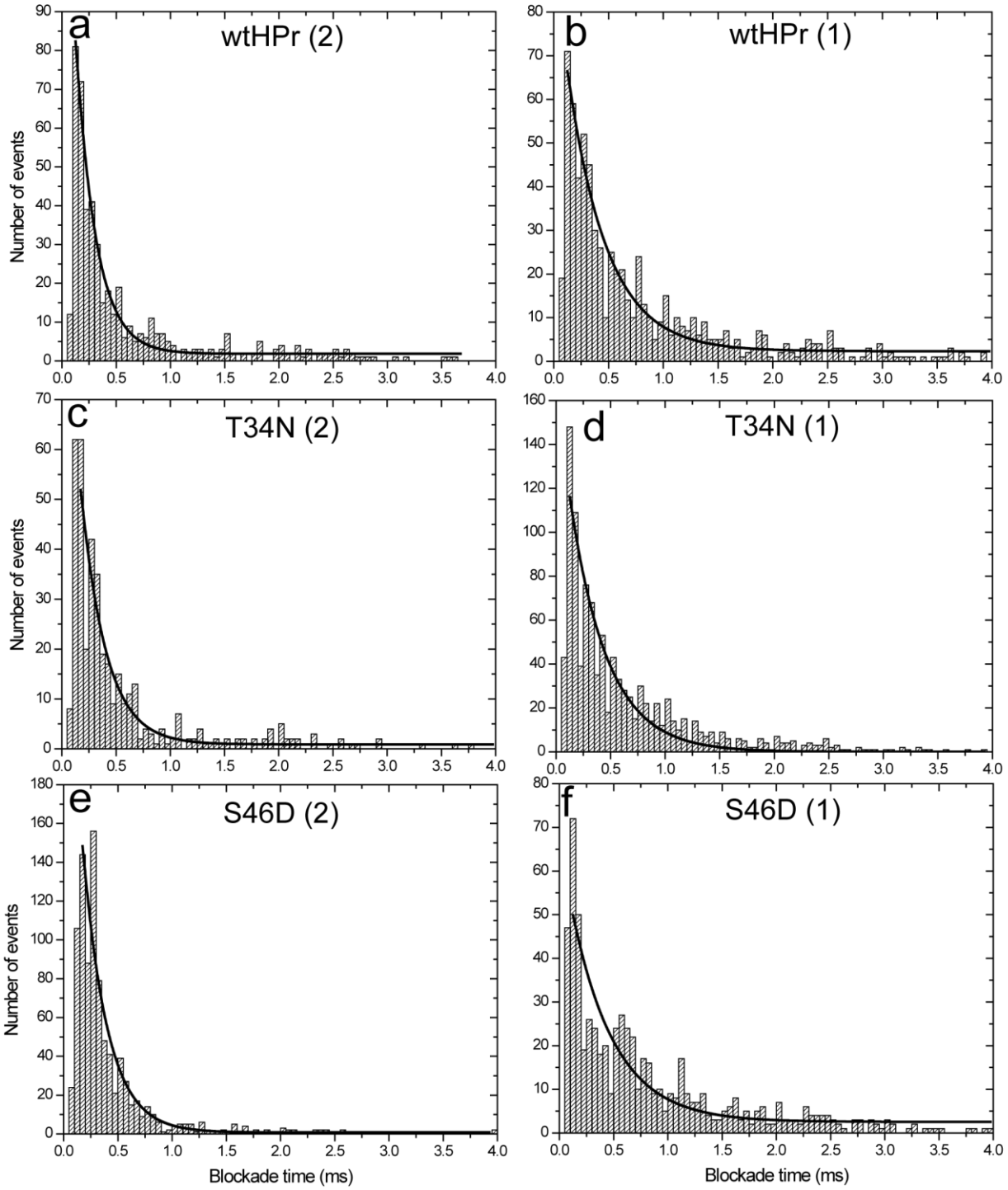

Figure 3.4. Blockade time histograms of the individual population of events generated by the interactions of wtHPr, T34N and S46D molecules with the α-hemolysin pores. Panels a, c and e show the lifetimes of the events forming the second populations while panels b, d and f show the lifetimes of the events forming the first populations. The event distributions were fitted with a single exponential decay function.

Table 3.1. Interaction parameters of the wtHPr together with the T34N and S46D mutants with the aerolysin pores[a].

Compound	I_1 (pA)	I_2 (pA)	T_1 (ms)	T_2 (ms)	A_1	A_2	A_2/A_1	W_1	W_2
wtHPr	-21	-43	0.36	0.19	692	485	0.7	9.8	7.4
T34N	-22	-39	0.29	0.23	1048	397	0.4	9.9	7.8
S46D	-23	-43	0.40	0.22	643	926	1.4	9.5	9.3

[a] **I_1**, **I_2**, **T_1** and **T_2** represent the intensities and the durations of the current blockades of the respective event populations presented in Figure 3.3. The number of events (**A_1** and **A_2**) forming the populations and their widths at half their heights (**W_1** and **W_2**) are also presented here. (The error is estimated to be ±1 pA for **I** and ±10% for **T**).

The first population had a peak at -23 pA while the second population had a blockade current of -43 pA. The blockade time histograms in Figure 3.4c showed a time of 0.40 ms for the first population and 0.22 ms for the second population. There were however more events belonging to the second population than the first population in the ratio of 1.4:1 (Table 3.1).

The second mutant tested was T34N which also showed a two population current blockade histogram (Figure 3.3b). The $\mathbf{I}_1$ value was found to be -22 pA while the $\mathbf{I}_2$ value was -39 pA. The analysis of the blockade durations revealed similar time values of 0.29 ms and 0.23 ms for the first and second event populations respectively. This mutant showed the least number of events forming the second population of all three molecules tested indicating a greater preference for collision events than for translocations.

From the results obtained so far it is apparent that single mutations in the structure of a protein are reflected in the protein-nanopore interaction. Although the blockade current values of the three molecules tested differed only slightly, important differences in the proportion of events between the two populations indicated a clear preference for translocation in the case of the S46D mutant.

3.1.3 Analysis of insulin with α-hemolysin pores in the presence of TCEP

The interaction between bovine insulin and the α-hemolysin pore in the presence and absence of 10-fold excess TCEP was analyzed using a similar experimental setup as for the experiments performed with the HPr proteins. The same parameters **I** and **T** were monitored. TCEP is a very stable, odorless, water-soluble, thiol-free reducing agent with a broad application to protein research involving reduction of disulphide bonds over a wide pH range (Burns *et al.*, 1991). Furthermore, nanopore analysis of the individual insulin chains was performed as a control. The current blockade histograms for all molecules are presented in Figure 3.5 while the blockade duration histograms are grouped in Figure 3.6. All calculated parameters are summarized in Table 3.2.

A dramatic difference is apparent between the first two histograms in Figure 3.5a and Figure 3.5b. For insulin without TCEP the histogram presents a low total number of events (515) spread along the blockade current axis between -20 pA and -85 pA forming a profile difficult to interpret with several possible populations of events (Figure 3.5a). In the presence of TCEP, the number of events increases 10-fold reaching a value of 5188 during the same 30

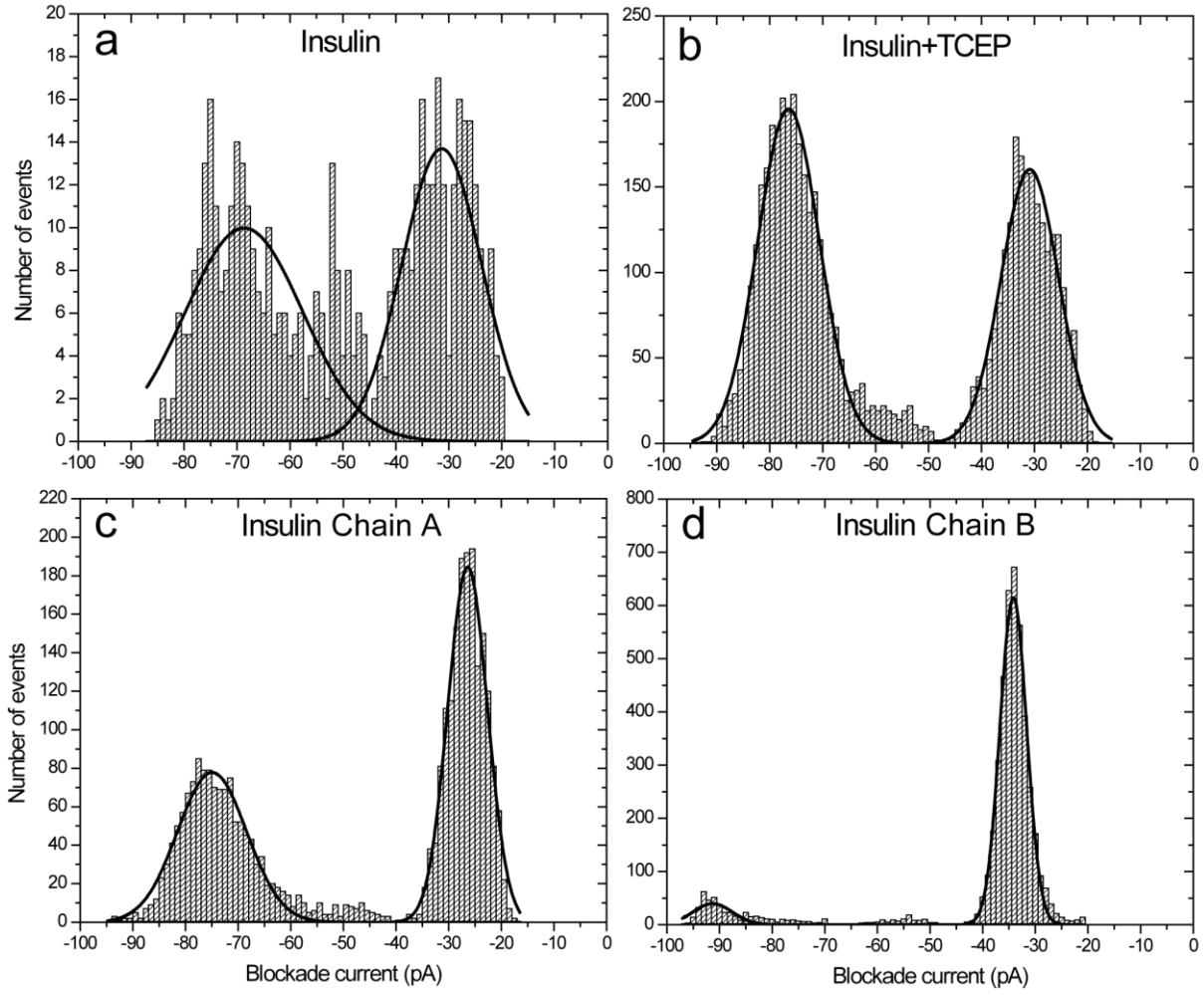

Figure 3.5. Blockade current histograms of the interactions of insulin in the absence of TCEP (a), insulin in the presence of TCEP (b) and of insulin chain A (c) and chain B (d) with α-hemolysin nanopores. The peak current values were obtained by fitting the event populations with the Gaussian function.

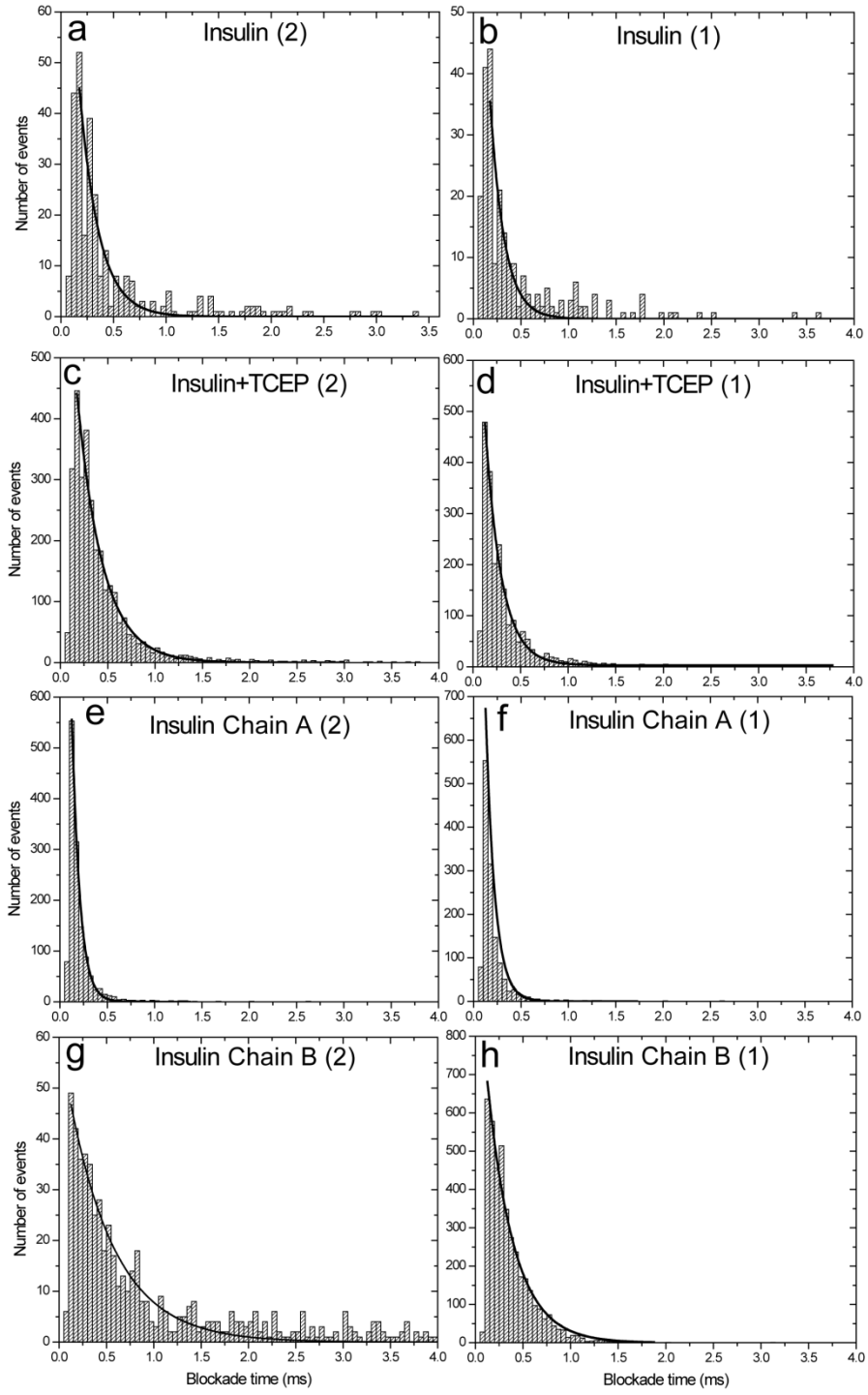

Figure 3.6. Blockade time histograms of the individual population of events generated by the interactions of insulin in the absence of TCEP (a, b), insulin in the presence of TCEP (c, d) and of insulin chain A (e, f) and chain B (g, h) with α-hemolysin nanopores. Panels a, c, e and g show the lifetimes of the events forming the second populations while panels b, d, f and h show the lifetimes of the events forming the first populations. The event distributions were fitted with a single exponential decay function.

Table 3.2. Interaction parameters of the insulin in the absence of TCEP, insulin in the presence of TCEP and of insulin chain A and chain B with the α-hemolysin pores[a].

Compound	I_1 (pA)	I_2 (pA)	T_1 (ms)	T_2 (ms)	A_1	A_2	A_2/A_1	W_1	W_2
Insulin	-31	-69	0.15	0.18	232	283	0.82	15.0	22.2
Insulin+TCEP	-31	-76	0.17	0.27	2150	3038	0.71	10.7	11.6
Insulin Chain A	-26	-75	0.10	0.08	1739	1359	0.78	7.4	13.0
Insulin Chain B	-34	-94	0.28	0.49	4084	588	0.14	4.8	7.4

[a] $\mathbf{I}_1$, $\mathbf{I}_2$, $\mathbf{T}_1$ and $\mathbf{T}_2$ represent the intensities and the durations of the current blockades of the respective event populations presented in Figure 3.5. The number of events ($\mathbf{A}_1$ and $\mathbf{A}_2$) forming the populations and their widths at half their heights ($\mathbf{W}_1$ and $\mathbf{W}_2$) are also presented here. (The error is estimated to be ±1 pA for **I** and ±10% for **T**).

minute recording period and the event distribution becomes distinctly separated in two populations of events. Moreover, the distribution of events, as reflected in the peak width at half the maximum height (**W**), sharpens drastically indicating that the vast majority of the molecules have fallen into the two distinct types of events: bumping or translocation.

The peak values of the current distributions where calculated with a Gaussian function and the current blockade duration histograms from Figure 3.6 were fitted with an exponential decay function of first order.

From the calculated parameters listed in Table 3.2 it can be seen that insulin in the presence of TCEP had a bumping peak situated at -31 pA with a blockade time of 0.17 ms and a translocation peak with a current blockade value of -76 pA and a blockade time of 0.27 ms.

The few events determined by the interaction of insulin with the α-hemolysin pore could be formally grouped in a low current blockade peak situated at -31 pA with a blockade time of 0.15 ms and a high current blockade peak situated at -69 pA with a blockade duration of 0.18 ms. The wide distribution of the events forming these populations of events could be determined by aggregated insulin molecules unable to translocate or by partial entries of the polypeptide extremities.

Similar to insulin in the presence of TCEP, chain A of insulin alone generated a histogram of blockade current amplitudes which shows two distinct populations of events: one with a peak current value of -75 pA and a fast translocation time of 0.08 ms and another with a peak current value of -26 pA and a bumping time of 0.10 ms (Figure 3.5c, Figure 3.6e and f, Table 3.2). Furthermore, it must be noted that insulin in the presence of TCEP and insulin's chain A histograms present a very similar ratio of translocations to bumpings 0.71 and 0.78 respectively (Table 3.2).

About 85% of the interactions between chain B and α-hemolysin generated the formation of the large peak situated at -34 pA with a blockade duration of 0.28 ms (Figure 3.5d, Figure 3.6h, Table 3.2). The remainder 15% of the events recorded are grouped in a small peak situated at -94 pA with a blockade duration of 0.49 ms (Figure 3.5d, Figure 3.6h, Table 3.2).

The results presented above indicate significant changes in both the blockade current and the blockade time histograms upon addition of TCEP reducing agent to insulin as compared to native insulin. These changes support the cleavage of the disulfide bonds present in the structure of insulin and the release of the component polypeptides.

3.2 The alternating current effect on peptide interaction with α-hemolysin

3.2.1 Introduction

A modification enabling the interpolation of a sine wave generator was made to the patch-clamp headstage. This modification allowed an AC voltage to be superimposed on the DC voltage and to be delivered through the electrodes to the electrolyte/buffer solution inside the perfusion cups and finally to the molecules to be analyzed (Figure 3.7A). This set-up was thought to be useful to further the study of the effects of peptide dipole moments upon their translocation through α-hemolysin pores and could be theoretically tailored into a peptide separation method.

In our early analysis of the effect of dipole moment on the transport characteristics of α-helical peptides through protein nanopores, it was found that peptides with small dipole moments gave more bumping events. Presumably this is because they were less likely to be rotated by the electric field into an orientation which could translocate smoothly (Stefureac *et al.*, 2006). We reasoned that the discrimination of the pore might be improved by applying an AC field superimposed on the normal electrophoretic voltage. When an AC field is applied, the peptides will tend to rotate according to the frequency of the AC field and their speed of rotation will depend on the dipole moment of each particular peptide (Figure 3.7B). Peptides with a large dipole moment would be more likely to be disoriented as they approach the narrow constriction of the pore, causing an increase in the proportion of bumping events while short molecules with smaller dipole moments will rotate more slowly and will be more likely to translocate (Figure 3.7B). Furthermore, it can be hypothesized that peptides of various lengths and dipole moments will resonate at different frequencies of the applied electric field which will improve their separation from a mix.

To avoid using an AC frequency range where the AC field variation would be faster than the response time of the molecules, it was important to consider their rotational correlation time ($\boldsymbol{\tau_c}$). This parameter represents the time it takes a molecule to rotate by one radian under Brownian diffusion. $\boldsymbol{\tau_c}$ can be experimentally determined with techniques such as fluorescence spectroscopy, light scattering or NMR and can also be calculated for approximate spherical proteins with Stoke's law (Cavanagh *et al.*, 2007). For proteins, $\boldsymbol{\tau_c}$ expressed in ns can be estimated roughly as being 0.6 x Mw of the protein in kDa. Typical $\boldsymbol{\tau_c}$ values for peptides and proteins range between 1.5-10 ns but are strongly influenced by the particular level of folding

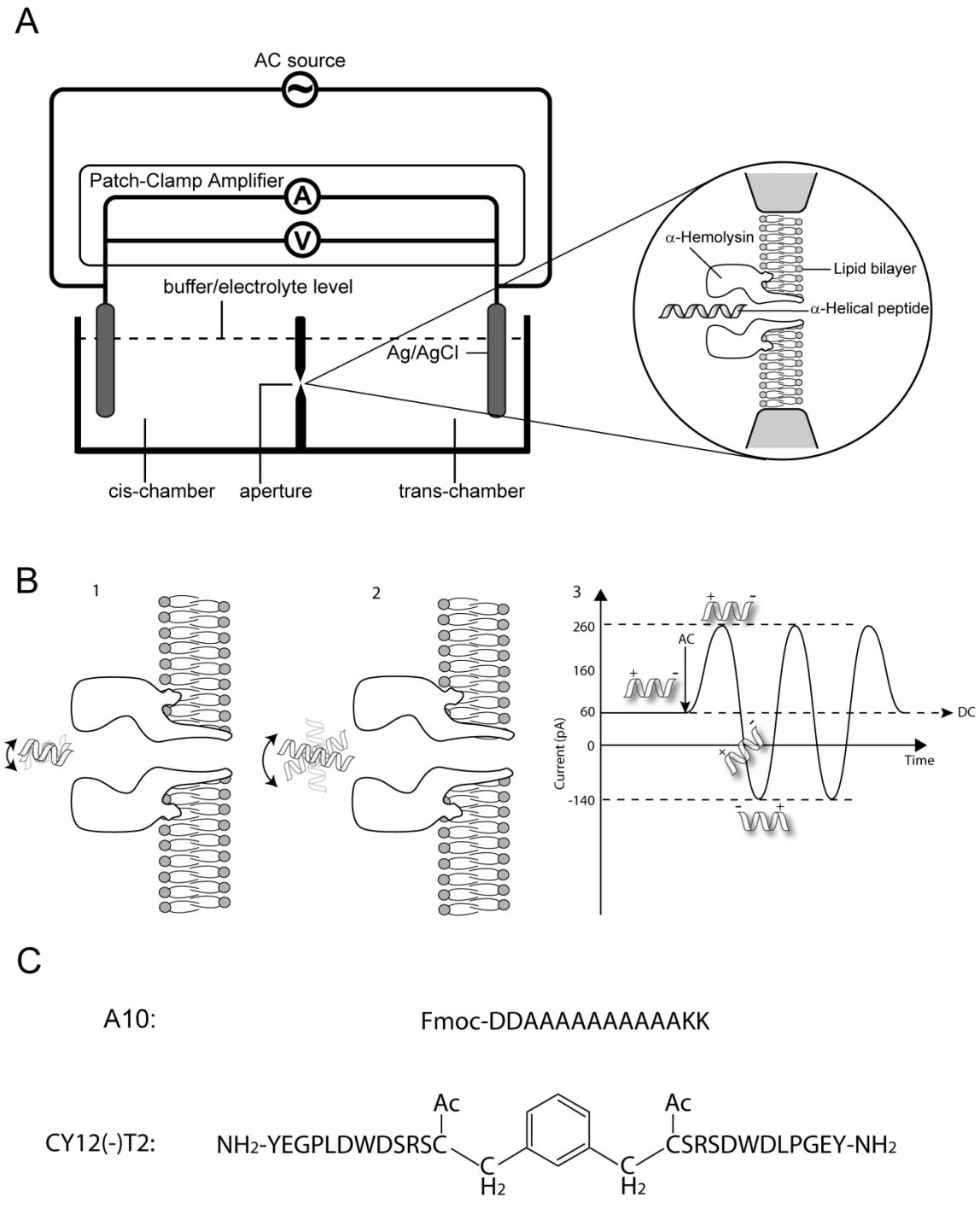

Figure 3.7. AC experiments. (A) Experimental setup. The AC voltage was applied across the two electrodes with a HP 8662A signal generator. (B) Cartoon showing that short peptides with smaller dipole moments rotate slower in an AC field (panel B1) and can enter the pore easier than long peptides with larger dipole moments which rotate faster (panel B2). The change in peptide orientation according to the AC frequency (panel B3). (C) Sequence of the peptides. A10 has a large dipole moment while CY12(-)T2 with a net charge of -4e has no permanent dipole moment in a linear conformation.

of the respective structures (Lam *et al.*, 1998; Larsen *et al.*, 2003; Cavanagh *et al.*, 2007). These values translated into a maximal frequency of 667 MHz that could be appropriately used for our experiments. Frequencies in the MHz range were chosen for the AC voltage because they were not expected to be either filtered or detected by our Axon headstage or amplifier. By trial and error, many different combinations of AC voltage amplitude with a constant DC voltage offset were tested with the α-helical peptide Fmoc-$D_2A_{10}K_2$ (A10) and CY12(-)T2 peptides before fixing these parameters as shown in Figure 3.7B. It was found that a 200 mV AC voltage superimposed on a constant 60 mV driving voltage yielded a stable membrane and consistent parameters over time for frequencies from 10-500 MHz as measured by an oscilloscope.

The reason behind choosing the two peptides was that the A10 peptide has a significant dipole moment while CY12(-)T2 in a linear conformation has no permanent dipole, thus a difference in their interaction with α-hemolysin was expected.

3.2.1.1 The α-helical peptide Fmoc-$D_2A_{10}K_2$ (A10)

The 14 amino acid α-helical peptide Fmoc-$D_2A_{10}K_2$ (A10) has been previously synthesized and analyzed through circular dichroism measurements (CD) and nanopore sensing experiments (Stefureac *et al.*, 2006). The CD spectra at pH values ranging from 3.5 to 8.3 have shown the formation of a very stable α-helical secondary structure (approximately a three-turn α-helix) with no signs of aggregation (Perutz *et al.*, 2002; Stefureac *et al.*, 2006). As an α-helix, the peptide had a length of 28.3 Å, a net charge of -1e and a dipole moment of 260 debye which made A10 the perfect study subject for our AC nanopore experiment (Stefureac *et al.*, 2006).

3.2.1.2 The CY12(-)T2 peptide

The CY12(-)T2 peptide contains two repeats of the sequence AcCSRSDWDLPGEYNH_2 attached through cysteine thiol linkages to a xylene molecule by displacement of bromide from *m*-bromoxylene (Figure 3.7C). Each of the two oligopeptide repeats attached to the xylene moiety has a net charge of -2e which confers CY12(-)T2 a net charge of -4e. The molecule does not possess a permanent dipole moment when in a linear conformation (Figure 3.7C).

3.2.2 Nanopore analysis of Fmoc-$D_2A_{10}K_2$ (A10) under an AC voltage

Figure 3.8 shows the effect of AC frequency on the current blockade histograms of A10. In the absence of any AC voltage, a single Gaussian peak is observed centered at -40 pA (67% of open pore current, OPC) which is consistent with previous results indicating translocations (Figure 3.8a) (Stefureac *et al.*, 2006). Upon applying the AC voltage a new peak appears at about -25 pA which increases in magnitude as the frequency increases from 10 MHz to 500 MHz (Figure 3.8b-f). The peak at -25 pA is almost certainly due to bumping events because a % OPC of about 40% is too small to be caused by A10 translocations. The event parameters are summarized in Table 3.3. The translocation peak had Gaussian-fitted blockade current values very similar to the blockade current value obtained in the DC experiment (-40 pA). The increase in the bumping to translocation ratios with increasing AC frequency was very reproducible with different pore/membrane preparations on different days.

3.2.3 Nanopore analysis of CY12(-)T2 under an AC voltage

CY12(-)T2 was also studied previously with a constant DC voltage (Meng *et al.*, 2010). As shown in Figure 3.9a, in the absence of an AC voltage it gives a complicated event profile because it can adopt at least two different conformations. Both Gaussian peaks at -53 and -47 pA are due to translocations because it was previously shown that the parameter, **T**, decreases with increasing voltage but there are also unassigned events at about -37 pA and a bumping peak at -17 pA (Meng *et al.*, 2010). Compared to A10, the effects of applying an AC voltage are more subtle (Figure 3.9b-f). At 10 MHz, the translocation peak at -47 pA and the events around -37 pA are diminished and the bumping peak at -28 pA becomes very broad, implying at least two types of interactions. At increased frequencies the event profiles show an increase in translocation events and a decrease in bumping events. The translocation population peaks for all frequencies are situated at blockade current values around -53 pA which are not significantly different from the blockade current value of the second translocation peak generated in the absence of the AC voltage. The event parameters are listed in Table 3.4. From the results presented above it becomes apparent that peptide molecules possessing different dipole moments indeed behave differently when in an AC environment than in an exclusively DC environment.

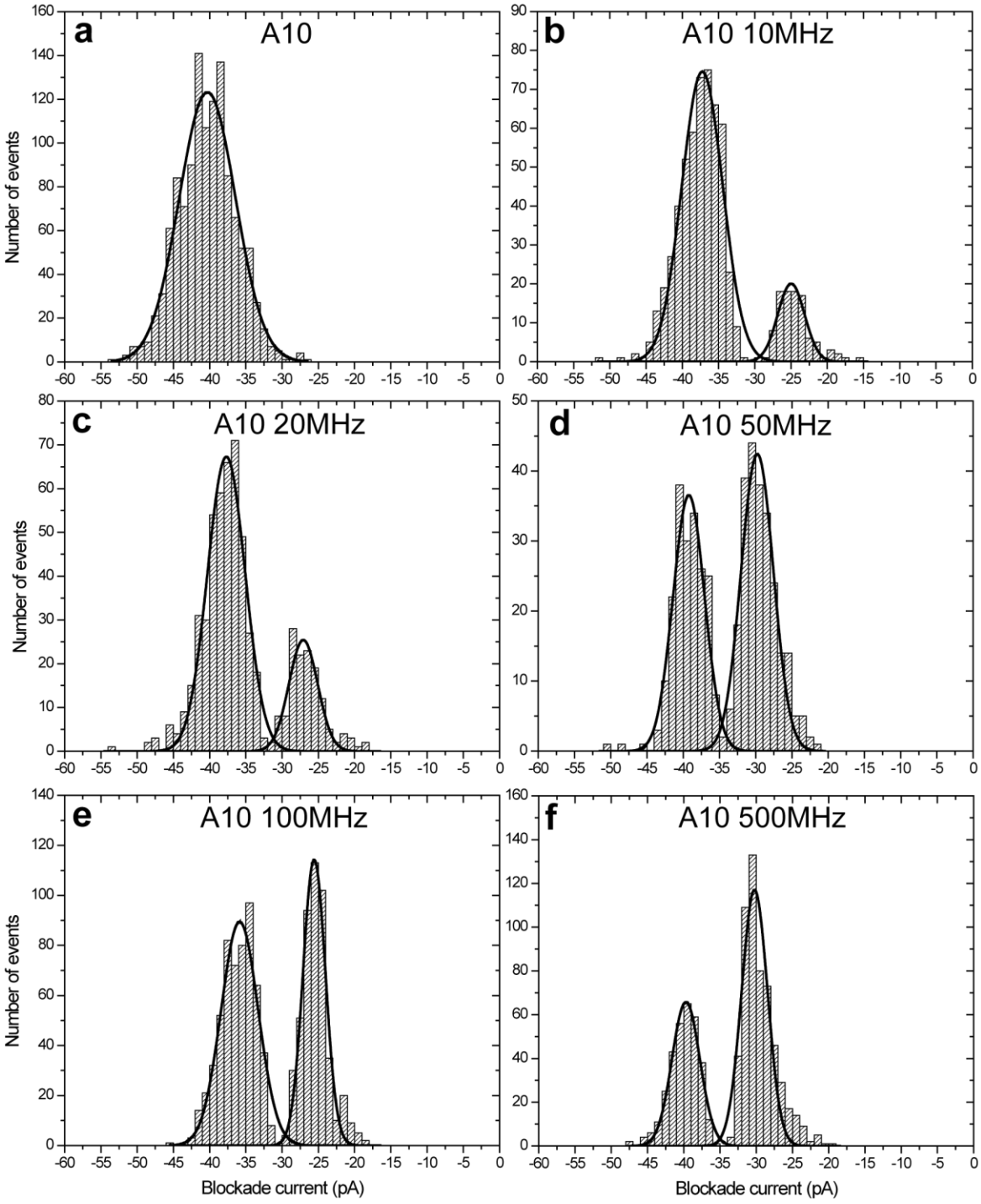

Figure 3.8. Blockade current histograms of the interactions of A10 in a DC field (a) and AC field (b-f) with α-hemolysin nanopores. The AC frequencies used were 10 MHz, 20 MHz, 50 MHz, 100 MHz and 500 MHz. The electrophoretic driving force was set at 60 mV with a superimposed AC field of 200 mV. The peak current values were obtained by fitting the event populations with the Gaussian function.

Table 3.3. The interaction parameters of the A10 peptide interaction with α-hemolysin under different AC frequencies [a].

A10/AC	I_1 (pA)	I_2 (pA)	T_1 (ms)	T_2 (ms)	A_1	A_2	A_1/A_2	W_1	W_2
No AC	-	-40	-	0.22	-	1206	-	-	7.8
10 MHz	-25	-37	0.05	0.17	100	528	0.19	3.6	5.6
20 MHz	-27	-38	0.06	0.17	139	448	0.31	3.9	5.2
50 MHz	-30	-39	0.12	0.15	244	201	1.21	4.4	4.3
100 MHz	-26	-36	0.06	0.18	475	564	0.84	3.4	5.1
500 MHz	-30	-40	0.14	0.18	564	322	1.75	3.5	3.8

[a] $\mathbf{I}_1$, $\mathbf{I}_2$, $\mathbf{T}_1$, and $\mathbf{T}_2$ represent the intensities and the durations of the current blockades of the respective event populations presented in Figure 3.8. $\mathbf{A}_1$ and $\mathbf{A}_2$ are the number of events forming the populations and $\mathbf{W}_1$ and $\mathbf{W}_2$ represent their width at half the maximum heigh. (The error is estimated to be ±1 pA for **I** and ±10% for **T**).

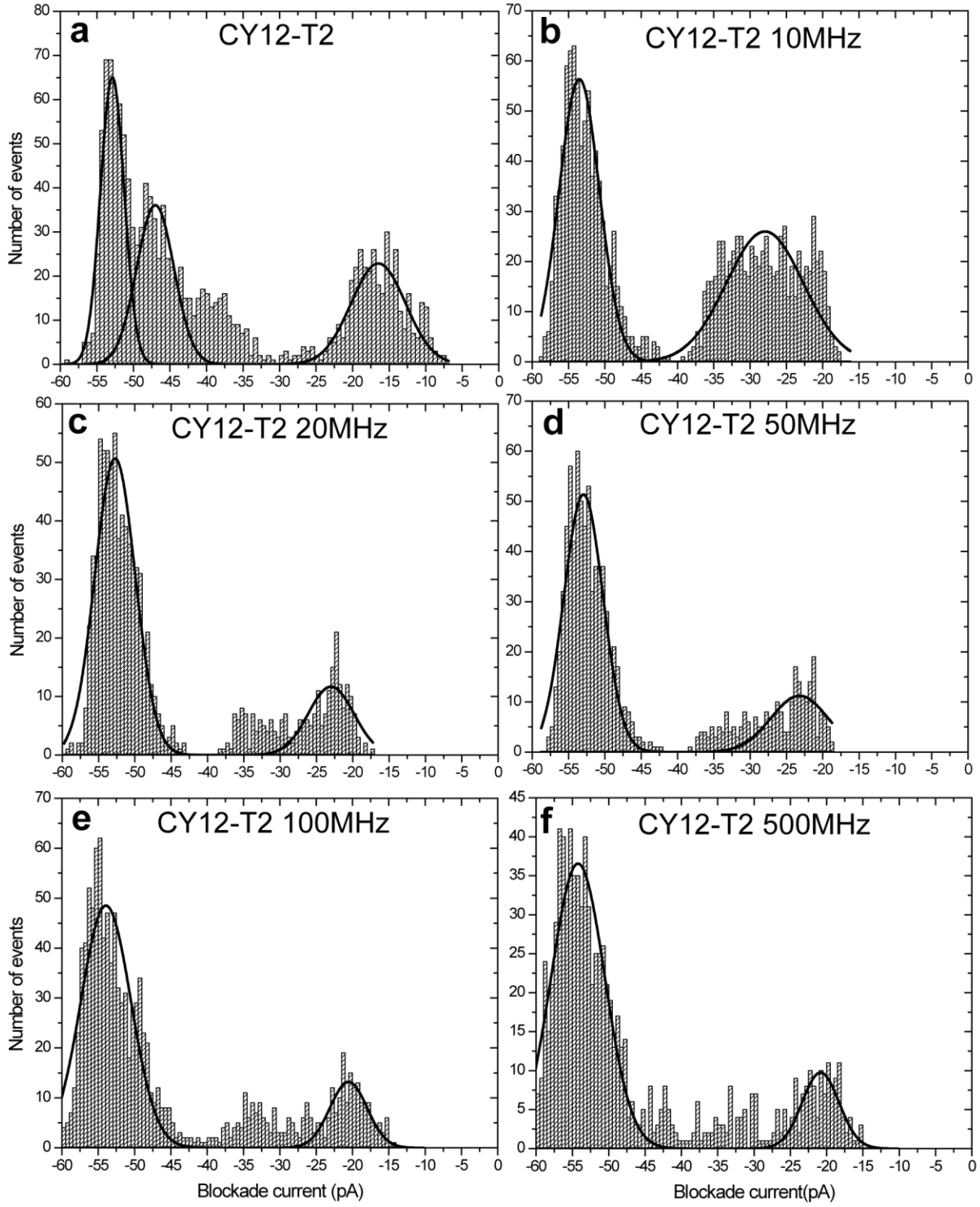

Figure 3.9. Blockade current histograms of the interactions of CY12(-)T2 in a DC field (a) and AC field (b-f) with α-hemolysin nanopores. The AC frequencies used were 10 MHz, 20 MHz, 50 MHz, 100 MHz and 500 MHz. The electrophoretic driving force was set at 60 mV with a superimposed AC field of 200 mV. The peak current values were obtained by fitting the event populations with the Gaussian function.

Table 3.4 The interaction parameters of the CY12(-)T2 peptide interaction with α-hemolysin under different AC frequencies [a].

CY12(-)T2/AC	I_1 (pA)	I_2 (pA)	T_1 (ms)	T_2 (ms)	A_1	A_2	A_1/A_2	W_1	W_2
No AC	-17	-53/-47	0.06	1.54/0.68	213	495	0.43	7.4	5.0/3.1
10 MHz	-28	-54	0.09	0.72	353	392	0.90	11.0	5.5
20 MHz	-23	-53	0.06	0.83	92	353	0.26	6.2	5.5
50 MHz	-23	-53	0.06	0.76	110	346	0.32	7.8	5.3
100 MHz	-21	-54	0.05	0.71	85	419	0.20	5.0	6.8
500 MHz	-21	-54	0.05	0.91	62	336	0.18	5.0	7.3

[a] $\mathbf{I}_1$, $\mathbf{I}_2$, $\mathbf{T}_1$, and $\mathbf{T}_2$ represent the intensities and the durations of the current blockades of the respective event populations presented in Figure 3.9. $\mathbf{A}_1$ and $\mathbf{A}_2$ are the number of events under the curve and $\mathbf{W}_1$ and $\mathbf{W}_2$ represent their width at half the maximum height. (The error is estimated to be ±1 pA for **I** and ±10% for **T**).

3.3 Analysis of peptide molecules in the presence of metal ions using nanopore detection

3.3.1 Introduction

The results presented in Chapter 3.1 confirmed the ability of nanopore sensing to detect conformational changes in proteins caused by mutations in their primary sequence as well as disulfide bond cleavage. For the next step of my project, we were interested if structural modifications to peptides due to metal ion binding could be detected by this single-molecule method of analysis. To reach this goal, we chose to start with one of the simplest models available in biochemistry, which is the Zn-finger structural motif.

The affinity of many proteins for metal ions plays a crucial role in their ability to perform biochemical functions. One such protein is PrP^C which is involved in maintaining copper homeostasis in the brain protecting neuronal cells against oxidative stress. Upon pathological conformational changes, the prion protein loses its ability to bind copper and aggregates into amyloid plaques disrupting cellular functions and eventually causing transmissible spongiform encephalopathies. The difference in copper binding affinity could be used, in principle, to identify and distinguish the two prion protein isoforms. Thus, another objective of this thesis was to demonstrate that the conformation of prion peptides can be modulated by binding divalent metal ions.

3.3.1.1 The Zn-finger peptides

The Zn-finger motif was first identified in several transcription regulatory proteins as Zn(II)-binding repeat units which fold into a nucleic acid binding domain (Klug and Rhodes, 1987; Evans and Hollenberg, 1988). The most common Zn-finger motif contains about 30 amino acids with the following sequence:

$$\underline{\text{Cys}} - X_{2,4} - \underline{\text{Cys}} - X_3 - \text{Phe} - X_5 - \text{Leu} - X_2 - \underline{\text{His}} - X_{3,4} - \underline{\text{His}}$$

This sequence can coordinate Zn(II) between the sulfur atoms of two deprotonated cysteines and the nitrogen atoms of two neutral histidines resulting in a compact folding with a β-sheet structure on the Cys side and an α-helical structure on the His side (Figure 3.10a) (Kaim and Schwederski, 1994). Although commonly encountered as strings of several Zn-finger motifs, single Zn-fingers can also function as independent structures (Parraga *et al.*, 1988).

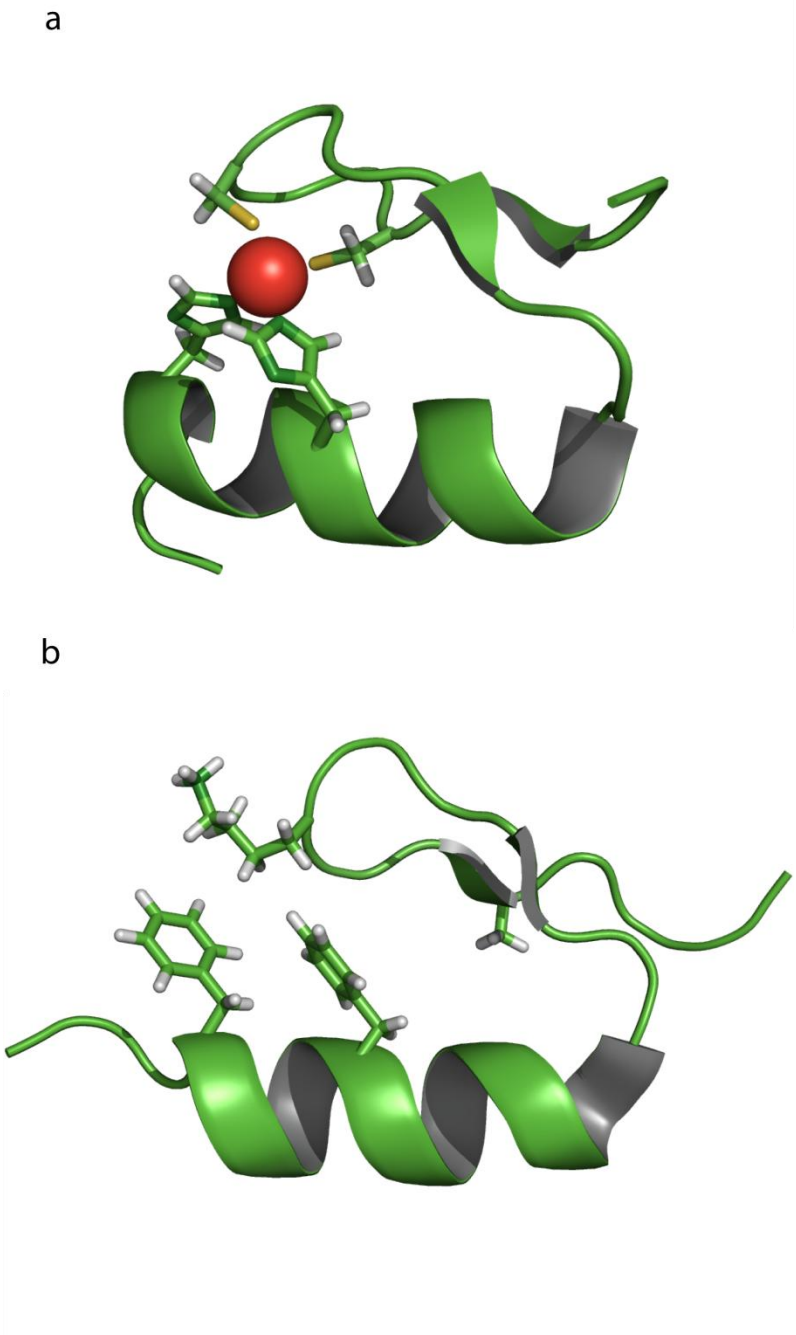

Figure 3.10. Cartoon diagram of a) Zif268 with an atom of Zn(II) bound (red) and b) FSD-1. Helices are represented as coils and strands as flat arrows. Adapted from Pavletich and Pabo, 1991 and Dahiyat and Mayo, 1997.

In our experiments, we have analyzed a 28 amino acid long single Zn-finger module (Zif268) with the typical β-sheet, α-helix and turn motifs (Figure 3.10a). In the absence of Zn(II), which clamps the α-helix onto the β-sheet, the peptide is unfolded and only binds weakly to its DNA target (Berg and Godwin, 1997). Interestingly, the Zn-finger motif was the first structure to be designed by fully automated sequence selection (Dahiyat and Mayo, 1997). The resulting protein, called FSD-1 folds into the correct structure by using hydrophobic interactions in the core in the place of Zn(II) (Figure 3.10b).

3.3.1.2 The prion peptides

The binding of metal ions to PrP^{C} has received considerable attention because there is evidence from multiple lines of research that it can cause changes in conformation (Quaglio *et al.*, 2001; Burns *et al.*, 2003; Todorova-Balvay *et al.*, 2005; Leach *et al.*, 2006). Two regions appear most important (Gaggelli *et al.*, 2006) (Figure 3.11). The octapeptide repeat (residues 60–91, human sequence) is highly conserved and contains 4 tandem sequences of PHGGGWGQ. It is found in the disordered N-terminal domain and can bind 4–5 Cu(II) ions with micromolar or sub-nanomolar dissociation constants (Walter *et al.*, 2006). The affinity for other divalent metal ions is several orders of magnitude lower (Stockel *et al.*, 1998; Millhauser, 2004). Elimination of this region does not prevent formation of PrP^{Sc}, but addition of further repeats increases the likelihood of development of spontaneous TSE, confirming the region's importance in disease pathogenesis (Goldfarb *et al.*, 1991; Leliveld *et al.*, 2006). Cu(II) binding to the octapeptide repeat may influence the folding of the C-terminal domain and cause self-association of the protein (Wells *et al.*, 2006; Thompsett and Brown, 2007; Zhu *et al.*, 2008).

The second region (residues 106–126) is at the interface between the disordered and globular domains of PrP (Figure 3.11). The peptide alone is toxic to neurons in vitro and shares many amyloidogenic properties with the β peptide of Alzheimer's disease (Jobling *et al.*, 2001; Walsh *et al.*, 2009). The PrP 106–126 peptide binds Cu(II), Zn(II), and Mn(II) and appears critical for aggregation and neurotoxicity (Gaggelli *et al.*, 2005). One model suggests that metal ion binding causes this region to adopt a β-sheet conformation that helps stabilize the β-sheet of PrP^{Sc} (Jobling *et al.* 2001). However, a direct effect of metal ions on pathogenesis has been

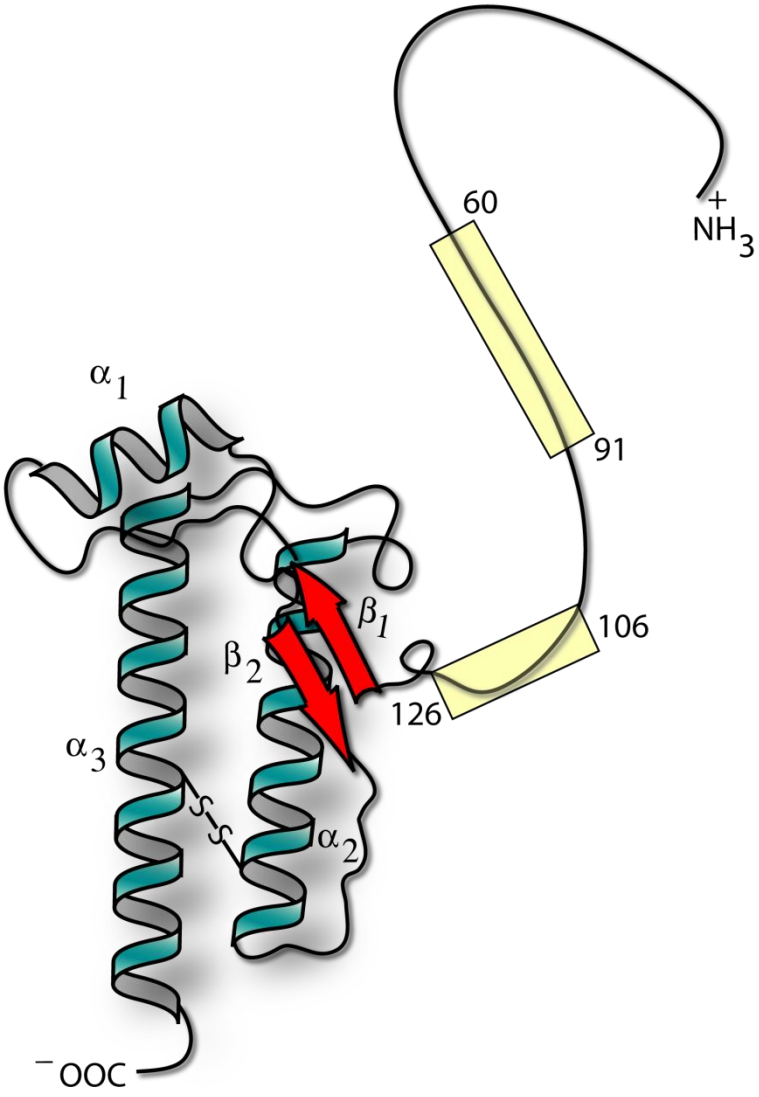

Figure 3.11. Cartoon model of the structure of the prion protein showing the Cu(II) binding regions of residues 60-91 and 106-126.

difficult to establish. Some studies suggest that Cu(II) binding causes prion diseases, whereas others suggest that a copper deficiency is responsible (Varela-Nallar *et al.*, 2006).

Although many aspects of prion biochemistry remain an enigma, misfolding and metal ion binding play a central role in the prion disease pathogenesis.

The metal ion binding to prion peptides containing two and four octapeptide repeats from the N-terminal copper-binding region of PrP^C (Octa2, $(PHGGGWGQ)_2$ and Octa 4, $(PHGGGWGQ)_4$) as well as residues 106–126 (PrP106–126) was studied with α-hemolysin nanopores.

3.3.2 Nanopore analysis of the folding of Zn-fingers

The magnitude and duration of the blockade currents caused by Zif268 and FSD-1 with the α-hemolysin pore were measured and analyzed by curve fitting as described in the materials and methods chapter. The blockade current histograms for Zif268 in the absence and in the presence of increasing concentrations of Zn(II) are shown in Figure 3.12a, b and c while the current blockade duration histograms appear in Figure 3.13. The corresponding **I** and **T** values extracted from the histograms are listed in Table 3.5. In the absence of metal ions, Zif268 generates two distinct populations corresponding to bumping events ($\mathbf{I}_1$=-33 pA) and the more frequent translocation events ($\mathbf{I}_2$=-80 pA). The blockade times are also distinguishable with $\mathbf{T}_1$ and $\mathbf{T}_2$ having values of 0.07 and 0.30 ms respectively.

Upon addition of an equimolar concentration of Zn(II) there is a large decrease in translocation events and a corresponding increase in bumping events with the ratio $\mathbf{A}_1/\mathbf{A}_2$ increasing from 0.40 to 1.43 (Table 3.5). The simplest interpretation is that Zn(II) stabilizes the folded conformation which is too large to translocate through the pore.

In the presence of a 10-fold molar excess of Zn(II) the number of translocation events is reduced even further and the ratio $\mathbf{A}_1/\mathbf{A}_2$ increases to 3.83. As well, the distribution of blockade currents for bumping events becomes very narrow. The peak widths at half their maximum heights (**W**) are also listed in Table 3.5. In the absence of Zn(II), $\mathbf{W}_1$ is 18.8 whereas with an excess of Zn(II) it decreases to 3.7 with a significantly reduced **I** value ($\mathbf{I}_1$ =-33 and -23 pA respectively). Thus, as expected, a single folded conformation upon bumping gives essentially a single blockade current compared to the more variable blockade currents of unfolded or partially-folded molecules.

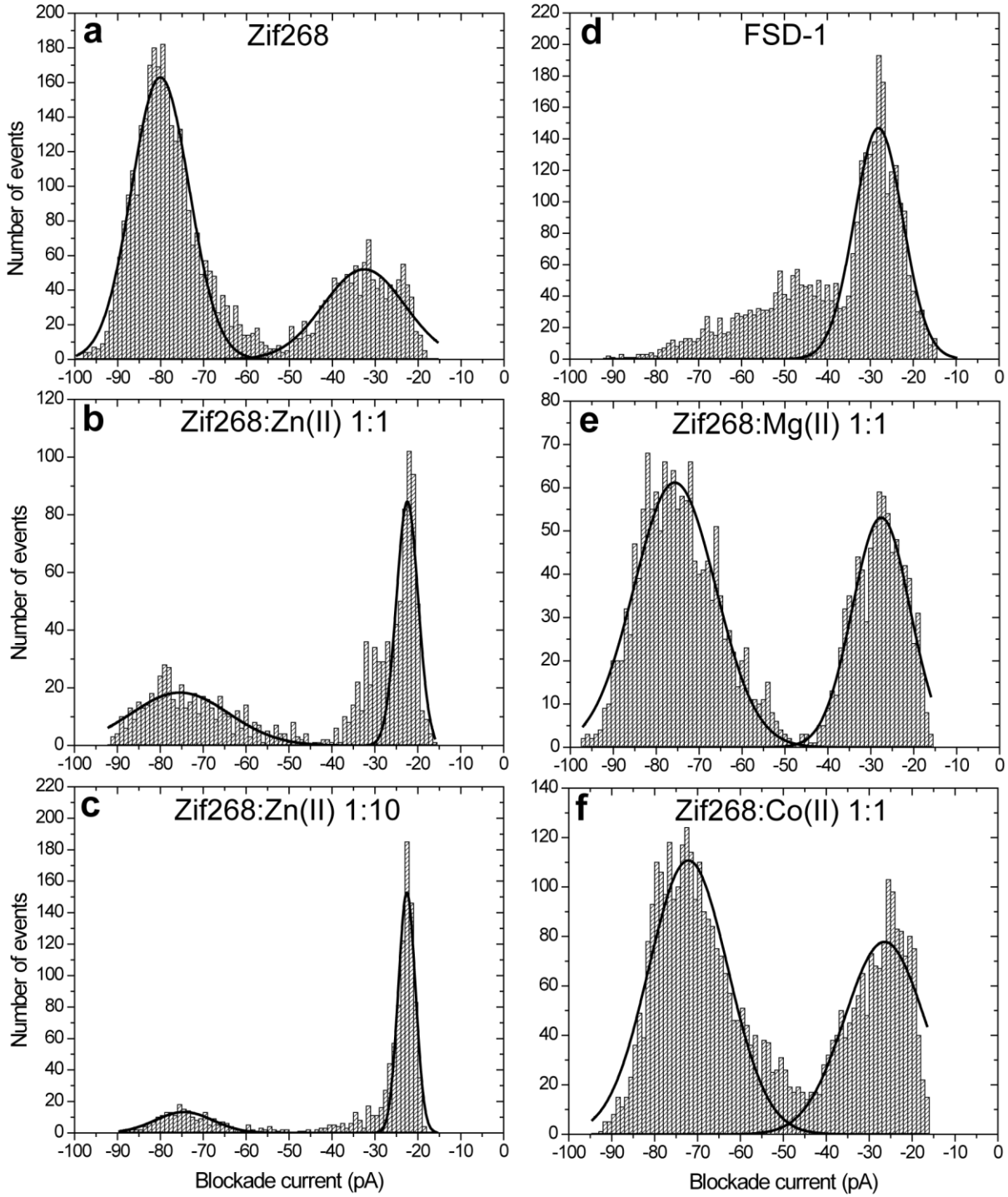

Figure 3.12. Blockade current histograms for Zif268 a) in the absence and b) in the presence of equimolar Zn(II) and c)10-fold excess of Zn(II) as well as histograms of d) FSD-1 and e) Zif268 in the presence of equimolar Mg(II) and f) Co(II).

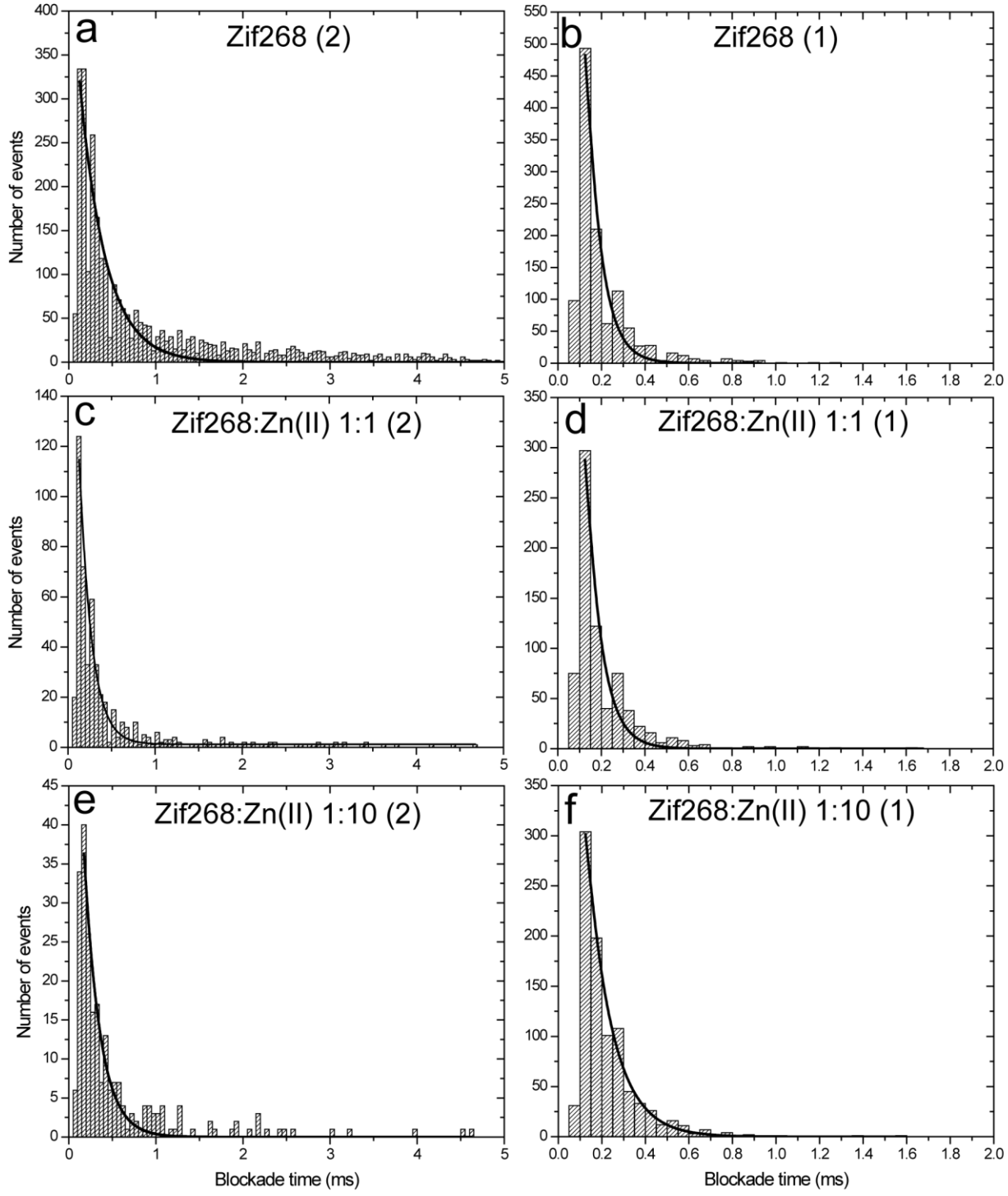

Figure 3.13. Blockade time histograms for each of the two populations of events (1 and 2) for Zif268 in the presence and in the absence of equimolar and 10-fold excess of Zn(II).

Table 3.5. The interaction parameters of the FSD-1 and Zif268 in the absence and in the presence of Zn(II), Mg(II) and Co(II)[a].

Peptide	I_1 (pA)	I_2 (pA)	T_1 (ms)	T_2 (ms)	A_1	A_2	A_1/A_2	W_1	W_2
Zif268	-33	-80	0.07	0.30	1153	2871	0.40	18.8	13.3
Zif268:Zn(II) 1:1	-22	-75	0.07	0.14	729	508	1.43	4.82	22.7
Zif268:Zn(II) 1:10	-23	-75	0.12	0.18	905	236	3.83	3.7	13.0
FSD-1	-28	-	0.03	0.15	1904	1233	1.54	11.2	-
Zif268:Mg(II) 1:1	-28	-76	0.02	0.07	795	1510	0.52	13.3	18.9
Zif268:Co(II) 1:1	-26	-72	0.03	0.12	1329	2815	0.47	18.5	18.4

[a] $\mathbf{I}_1$, $\mathbf{I}_2$, $\mathbf{T}_1$, and $\mathbf{T}_2$ represent the intensities and the durations of the current blockades of the respective event populations presented in Figure 3.12. $\mathbf{A}_1$ and $\mathbf{A}_2$ are the number of events forming the populations and $\mathbf{W}_1$ and $\mathbf{W}_2$ represent their width at half the maximum height. (The error is estimated to be ±1 pA for **I** and ±10% for **T**).

For FSD-1 the nanopore analysis reveals a majority of bumping events with a blockade current ($\mathbf{I}_1$ =-28 pA) similar to that for Zif268 (Figure 3.12a and d). There is also a broad shoulder of events with higher blockade currents which may represent the translocation of partially-folded molecules.

As a further control, the effect of Mg(II) and Co(II) on the folding of Zif 268 was studied (Figure 3.12e and f). It is clear that the majority of events remain translocations and there is no sharpening of the bumping peak as expected since the binding of other ions to Zn-fingers is at least three orders of magnitude weaker than Zn(II) (Berg and Godwin, 1997).

This set of nanopore sensing experiments proved possible the detection of conformational changes in peptides caused by metal ion binding and recommended the study of metal ion binding to prion peptides and proteins.

3.3.3 Nanopore analysis of the interaction of metal ions with prion peptides

Nanopore analysis on α-hemolysin pores was used to study the effect of Cu(II) and other divalent metals on the translocation of prion peptides. A similar experimental setup as for the experiments performed with the Zn-finger peptides was employed.

It has been previously reported that high concentrations of some divalent metal ions, including Cu(II), can cause changes to the architecture of the pore (Menestrina, 1986; Bashford *et al.*, 1988). Therefore, control experiments were performed. First, Cu(II) was added to the *cis* chamber and the open pore current was monitored. Below 0.3 mmol/L the current was steady at –100 pA, but above 0.3 mmol/L reversible blockages became apparent (data not shown). Second, a control peptide that is known to exist in 2 conformations was investigated (Xu *et al.*, 2003). The peptide adopts either a disordered random strand or an intramolecular β-sheet. Thus any non-specific binding of Cu(II) to either conformation would also be expected to effect the event parameters. A typical recording is shown in Figure 3.14 in which each spike or event represents a single molecule interacting with the pore. In general, if a molecule bumps into the pore both the current blockade and the length of the event are smaller than if the molecule translocates through the pore (Goodrich *et al.* 2007). The magnitude and duration of the blockade currents were measured and analyzed by curve fitting as described previously.

As shown in Figure 3.15, the control peptide gives two peaks in the histogram of blockade currents in the absence and presence of an excess of 0.12 mmol/L Cu(II), which is an 8-fold

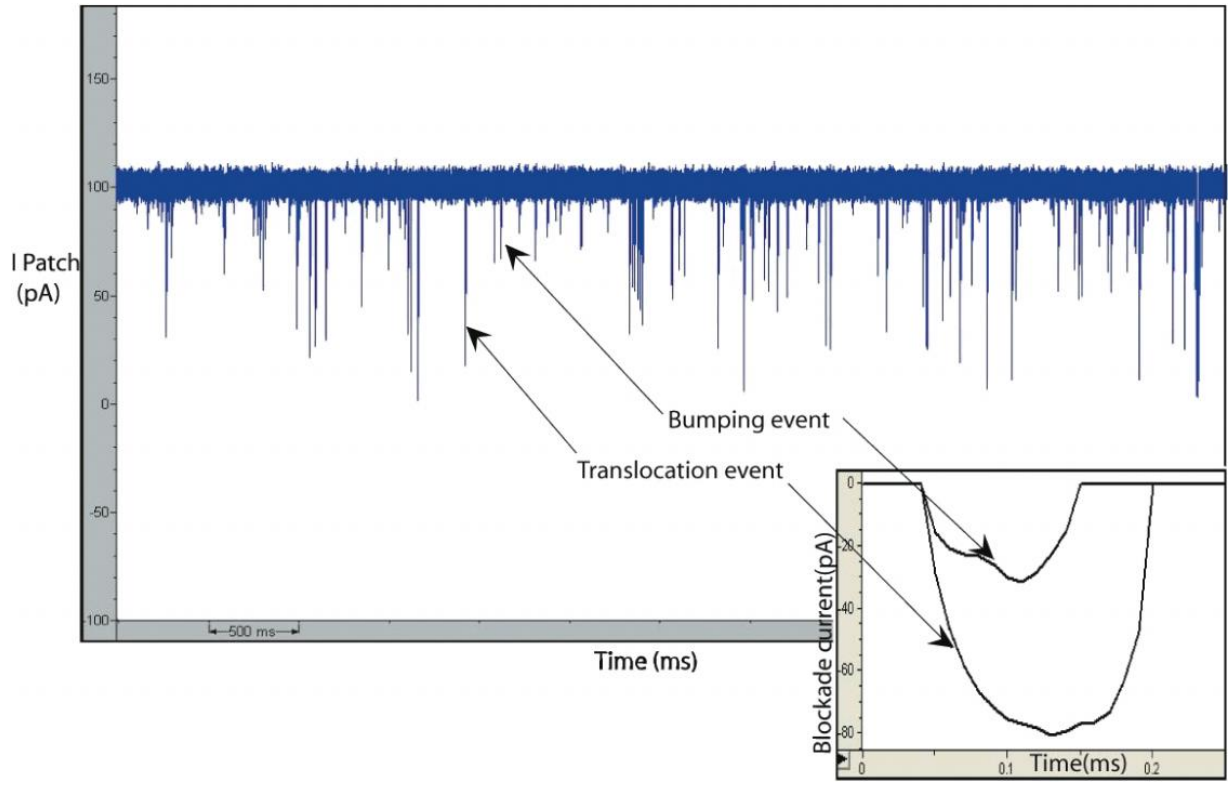

Figure 3.14. Current (pA) versus time (ms) trace for the control peptide. The inset shows an expanded view of typical bumping and translocation events.

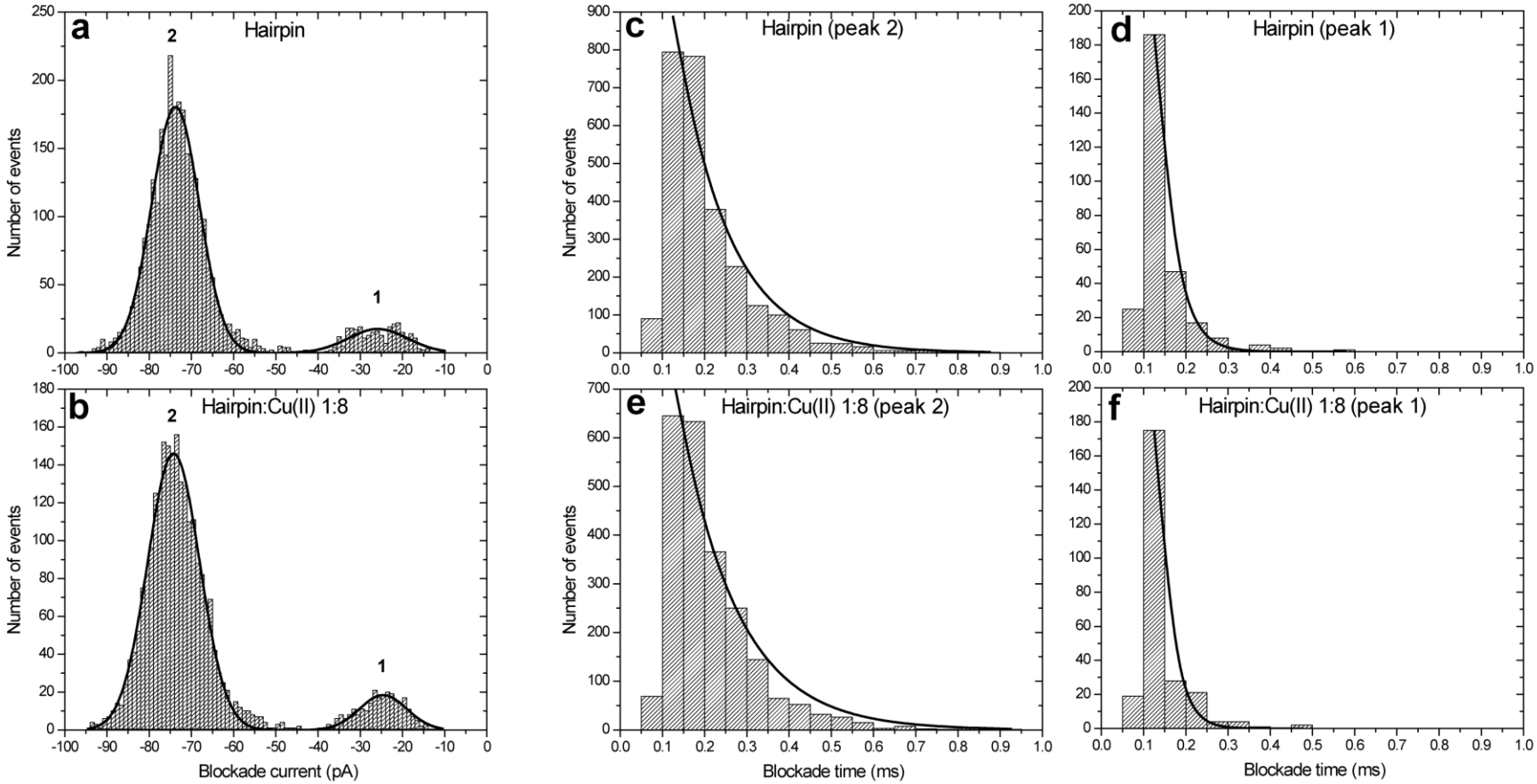

Figure 3.15. Current blockade histograms for the control peptide in the absence (a) and in the presence of Cu(II) (b). The corresponding blockade time histograms are for peak 2 (c) and peak 1 (d) without Cu(II) and for peak 2 (e) and peak 1 (f) with Cu(II).

excess over the peptide concentration. The peak at –26 pA is due to bumping events and the peak at –74 pA is due to translocation events. The histograms of blockade time for both bumping and translocation events also show no significant changes upon the addition of Cu(II) (Figure 3.15 and Table 3.6). In the experiments described below, the Cu(II) concentration was less than 0.3 mmol/L so no interference with the pore is expected.

Histograms of blockade current for Octa2 are shown in Figure 3.16 and the corresponding event parameters are summarized in Table 3.7. In the absence of metal ions there is a single population of translocation events with $\mathbf{I}_2$ = –67 pA, which is typical for a small peptide of 16 amino acids (Stefureac *et al.* 2006; Goodrich *et al.* 2007; Zhao *et al.* 2009). Upon the addition of 2 equivalents of Cu(II) (Octa2 at 20 µmol/L and Cu(II) at 40 µmol/L), the translocation peak broadens and shifts to –77 pA with a broad shoulder. (For simplicity, this feature has not been included in the analysis.) As well, a bumping peak becomes evident with $\mathbf{I}_1$ = –24 pA, and $\mathbf{T}_2$ increases from 0.16 ms to about 0.46 ms (Table 3.7). Upon addition of an 8-fold excess of Cu(II), the peak currents remain constant, but the ratio of translocation to bumping events ($\mathbf{A}_2/\mathbf{A}_1$) decreases from 2.5 to 1.8. Thus Cu(II) binds to Octa2 and causes significant conformational changes. In contrast, addition of Mg(II) or Mn(II) has no effect. As a further control, the peptide was studied in 1 mmol/L EDTA, but this too caused no change in the profile (data not shown). Zn(II) causes broadening of the translocation peak, but with a significant increase in blockade current ($\mathbf{I}_2$ = –72 pA); there is also the appearance of a small proportion of bumping events. Thus Zn(II) binds to Octa2 but more weakly than Cu(II).

For Octa4 (Figure 3.17 and Table 3.8) a similar pattern is found, although the effects of metal ions are more pronounced. In the absence of metal ions, there are few bumping events with $\mathbf{I}_1$ = –28 pA and the translocation events appear to be of two types centered around –75 and –87 pA, which may represent different orientations of the same molecule (i.e., either N-terminus or C-terminus first) or different conformations (i.e., folded or unfolded). However, for convenience, all the translocation events have been analyzed as a single Gaussian distribution. Upon addition of 16 equivalents of Cu(II) (Octa4 at 10 µmol/L and Cu(II) at 160 µmol/L) the ratio of translocation to bumping events decreases considerably, and with 64 equivalents of Cu(II) the translocation peak is further depressed and becomes much broader. As well, $\mathbf{I}_1$ for bumping events decreases by as much as –8 pA upon addition of Cu(II) and $\mathbf{T}_1$ increases from

Table 3.6. Event parameters for the control peptide [a].

Compound	I_1 (pA)	I_2 (pA)	T_1 (ms)	T_2 (ms)	A_1	A_2	A_2/A_1	W_1	W_2
Hairpin	-26	-74	0.03	0.12	291	2647	9.1	14.1	11.2
Hairpin:Cu(II) 1:8	-25	-74	0.03	0.14	255	2315	9.1	11.1	12.2

[a] $\mathbf{I}_1$, $\mathbf{I}_2$, $\mathbf{T}_1$, and $\mathbf{T}_2$ represent the intensities and the durations of the current blockades of the respective event populations presented in Figure 3.15. $\mathbf{A}_1$ and $\mathbf{A}_2$ are the number of events forming the populations and $\mathbf{W}_1$ and $\mathbf{W}_2$ represent their width at half the maximum height. (The error is estimated to be ±1 pA for **I** and ±10 % for **T)**.

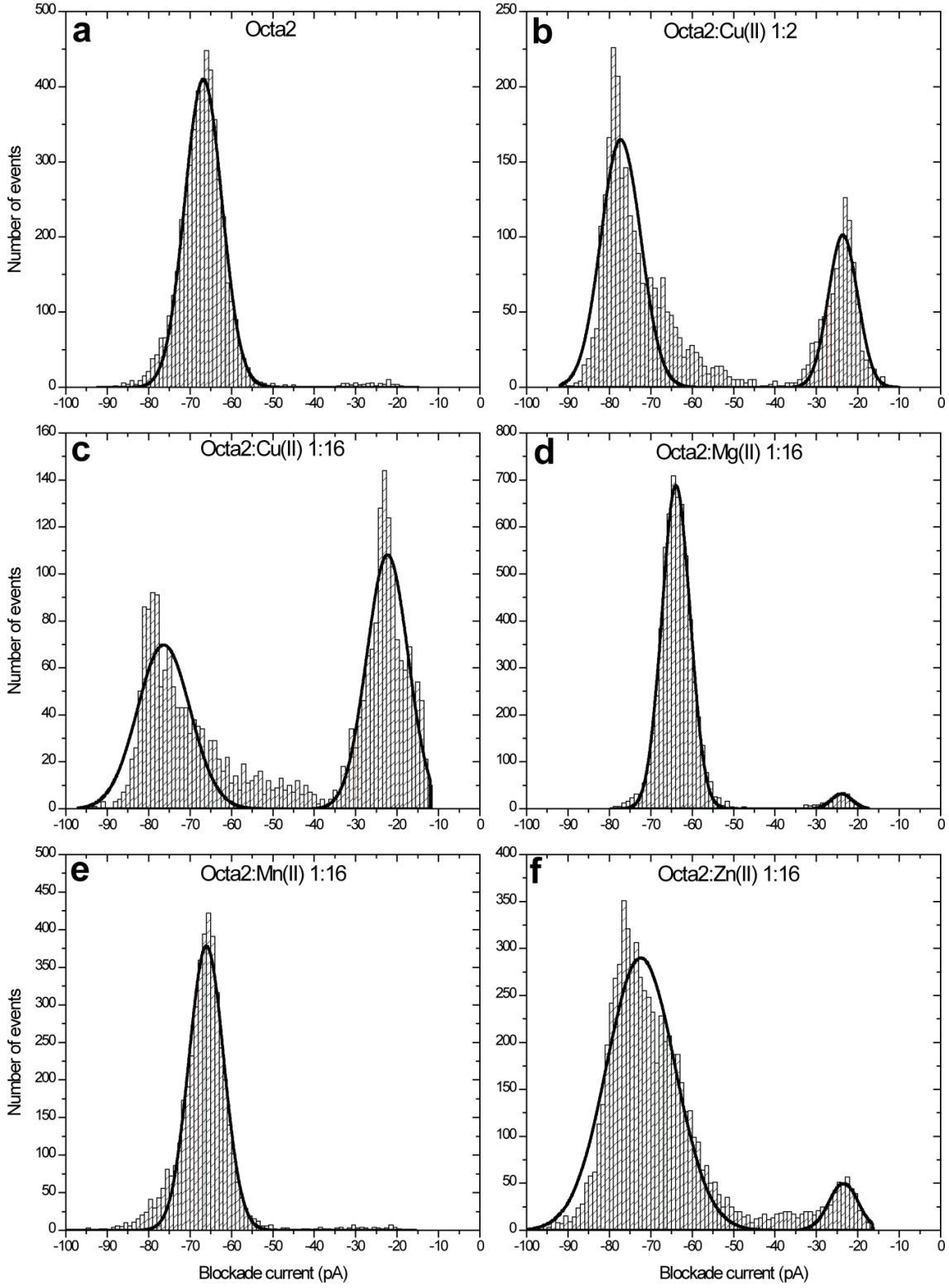

Figure 3.16. Blockade current histogram for (*a*) Octa 2, (*b*) with Cu(II) 2x, (*c*) with Cu(II) 8x, (*d*) with Mg(II) 16x, (*e*) with Mn(II) 16x, and (*f*) with Zn(II) 16x. For simplicity, the broad shoulders in (*b*) and (*c*) were not included in the analysis.

Table 3.7. Event parameters for Octa2 [a].

Compound	I_1 (pA)	I_2 (pA)	T_1 (ms)	T_2 (ms)	A_1	A_2	A_2/A_1	W_1	W_2
Octa2	-	-67	-	0.16	-	4790	-	-	8.8
Octa2:Cu(II) 1:2	-24	-77	0.06	0.46	940	2354	2.5	6.8	9.5
Octa2:Cu(II) 1:8	-23	-78	0.05	0.35	1128	2047	1.8	13.9	7.1
Octa2:Mg(II) 1:16	-	-64	-	0.18	-	6026	-	-	6.7
Octa2:Mn(II) 1:16	-	-66	-	0.18	-	4308	-	-	8.2
Octa2:Zn(II) 1:16	-23	-72	0.05	0.38	717	5973	8.3	6.9	16.4

[a] **I_1**, **I_2**, **T_1**, and **T_2** represent the intensities and the durations of the current blockades of the respective event populations presented in Figure 3.16. **A_1** and **A_2** are the number of events forming the populations and **W_1** and **W_2** represent their width at half the maximum height. (The error is estimated to be ±1 pA for **I** and ±10 % for **T**.)

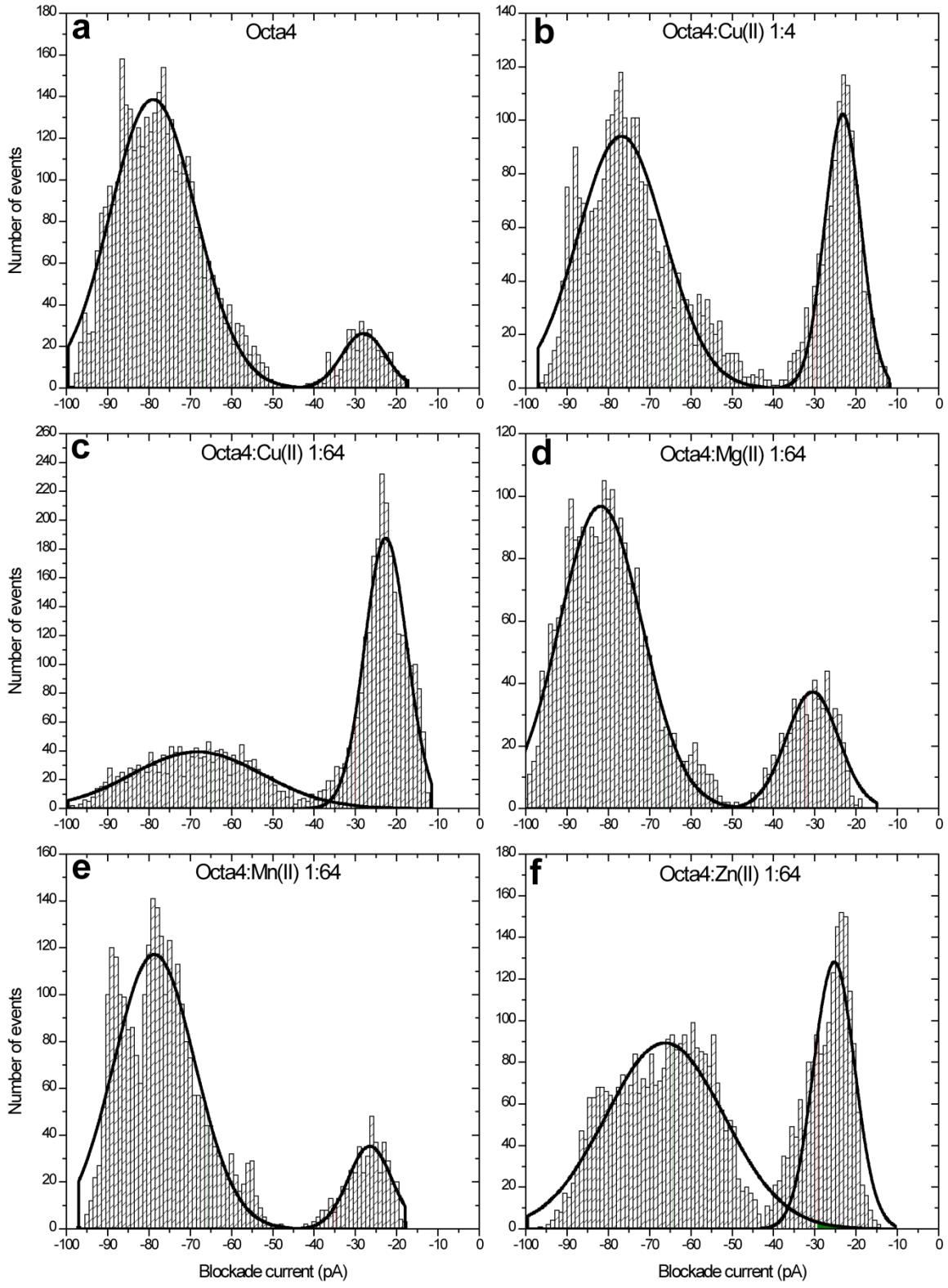

Figure 3.17. Blockade current histogram for (*a*) Octa 4, (*b*) with Cu(II) 4x, (*c*) with Cu(II) 64x, (*d*) with Mg(II) 64x, (*e*) with Mn(II) 64x, and (*f*) with Zn(II) 64x.

Table 3.8. Event parameters for Octa4 [a].

Compound	I_1 (pA)	I_2 (pA)	T_1 (ms)	T_2 (ms)	A_1	A_2	A_2/A_1	W_1	W_2
Octa4	-28	-79	0.04	0.58	344	3554	10.3	10.3	20.8
Octa4:Cu(II) 1:4	-20	-77	0.15	0.30	1092	1964	1.8	12.1	27.1
Octa4:Cu(II) 1:64	-22	-68	0.19	0.20	2441	1454	0.6	10.1	31.4
Octa4:Mg(II) 1:64	-30	-82	0.06	0.49	572	2415	4.2	12.5	20.1
Octa4:Mn(II) 1:64	-26	-79	0.06	0.49	455	2829	6.2	10.4	19.6
Octa4:Zn(II) 1:64	-25	-66	0.09	0.34	1735	2954	1.7	9.8	28.6

[a] **I_1**, **I_2**, **T_1**, and **T_2** represent the intensities and the durations of the current blockades of the respective event populations presented in Figure 3.17. **A_1** and **A_2** are the number of events forming the populations and **W_1** and **W_2** represent their width at half the maximum height. (the error is estimated to be ±1 pA for **I** and ±10 % for **T**.)

0.04 ms to about 0.19 ms. Most significant and in contrast to Octa2, the value of $\mathbf{T}_2$ decreases from about 0.6 ms to about 0.3 ms in the presence of Cu(II). As with Octa2, the addition of Mg(II) or Mn(II) causes only small changes, so the binding must be weak. Zn(II) clearly binds to Octa4 because the translocation peak broadens and the proportion of bumping events increases; however, as with Octa2, this binding is weaker (compare Zn(II) 64x with Cu(II) 64x in Figure 3.17).

In the absence of metal ions, PrP106–126 yields both translocation and bumping events with an $\mathbf{A}_2/\mathbf{A}_1$ ratio of about 4 (Figure 3.18 and Table 3.9). Upon addition of Cu(II) (1x) the ratio decreases to about 0.3 and with an excess of Cu(II) the translocation peak all but disappears. Thus, Cu(II) binds tightly to PrP106–126 and the complex is unable to translocate freely. Mg(II) and Mn(II) appear to bind weakly because there is some broadening of the bumping peak and $\mathbf{T}_1$ decreases significantly. In contrast, Zn(II) behaves similarly to Cu(II) and very few translocation events are observed at high concentrations.

The results presented above clearly indicate that metal ion binding to all three prion peptides induced significant changes in peptide conformation which in turn are reflected in their interaction parameters with the α-hemolysin pore.

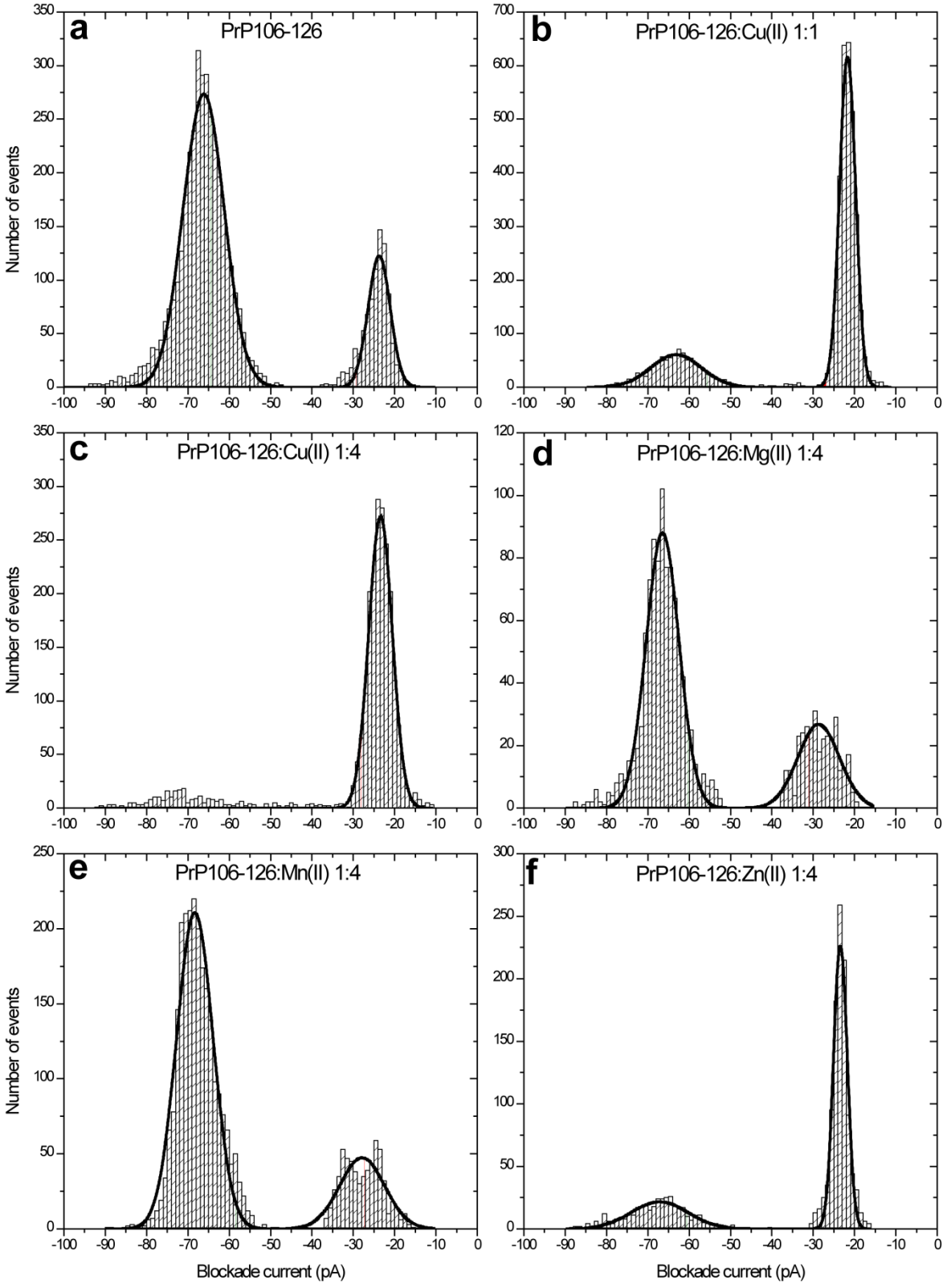

Figure 3.18. Blockade current histograms for (a) PrP106–126, (b) with Cu(II) 1x, (c) with Cu(II) 4x, (d) with Mg(II) 4x, (e) with Mn(II) 4x, and (f) with Zn(II) 4x.

Table 3.9. Event parameters for PrP106-126 [a].

Compound	I_1 (pA)	I_2 (pA)	T_1 (ms)	T_2 (ms)	A_1	A_2	A_2/A_1	W_1	W_2
PrP106-126	-24	-66	0.17	0.17	898	3625	4.0	5.1	9.8
PrP106-126:Cu(II) 1:1	-22	-63	0.17	0.11	3062	985	0.3	3.6	12.1
PrP106-126:Cu(II) 1:4	-23	-	0.15	-	1957	-	-	5.4	-
PrP106-126:Mg(II) 1:4	-29	-66	0.08	0.18	325	944	2.9	9.9	7.8
PrP106-126:Mn(II) 1:4	-28	-68	0.09	0.18	618	2403	3.9	10.8	8.7
PrP106-126:Zn(II) 1:4	-23	-67	0.16	0.15	1033	385	0.4	2.9	13.7

[a] $\mathbf{I}_1$, $\mathbf{I}_2$, $\mathbf{T}_1$, and $\mathbf{T}_2$ represent the intensities and the durations of the current blockades of the respective event populations presented in Figure 3.18. $\mathbf{A}_1$ and $\mathbf{A}_2$ are the number of events forming the populations and $\mathbf{W}_1$ and $\mathbf{W}_2$ represent their width at half the maximum height. (The error is estimated to be ±1 pA for **I** and ±10 % for **T**.)

3.4 Analysis of protein molecules using solid-state nanopores

3.4.1 Introduction

Bacterial toxins, such as α-hemolysin from *S. aureus*, have proven to be very useful tools for the analysis of single molecules and have laid the foundation of the nanopore analysis field (Kasianowicz *et al.*, 1996; Branton *et al.*, 2008; Howorka and Siwy, 2009). To improve the versatility and stability of nanopore sensing with natural pores, artificial pores or solid-state pores were developed in synthetic silicon nitride (Si_xN_y) membranes (Li *et al.*, 2001; Dekker, 2007). While the detection principle continued to rely on the blockade current and blockade duration determined by the interaction of the analyte with the nanopore, the solid-state nanopores held the promise of controllable dimensions, adjustable surface properties and high stability over a wide range of experimental conditions (temperature, pH, applied potentials, solvents and electrolyte concentration) that would normally destroy lipid bilayer assemblies. In practice, working with solid-state nanopores proved challenging and several authors reported irreversible clogging due to the analytes adhering to the inside walls of the pores (Li *et al.*, 2003; Han *et al.*, 2006; Han *et al.*, 2008; Niedzwiecki *et al.*, 2010; Yusko *et al.*, 2011).

The interaction of proteins with Si_xN_y nanopores was investigated. For example, it was shown that bovine serum albumin (BSA) and fibrinogen could be distinguished on the basis of the event parameters and translocation of BSA to the *trans* side of the pore was confirmed by an immunosorbent assay (Fologea *et al.*, 2007). Others have used synthetic pores to investigate antibody/protein interactions with the goal of developing ultra-sensitive bioassays (Han *et al.*, 2008; Sexton *et al.*, 2007). Although several protein molecules of different dimensions have been analyzed with Si_xN_y nanopores, contradictory results regarding the folding state of the proteins during translocation have been obtained. Based on the excluded volume and blockade duration, Talaga and Li reported that the majority of β-lactoglobulin molecules tested were linearized or looped during translocation by the high electrical forces acting on them (Talaga and Li, 2009). On the other hand, the results of Firnkes and coworkers showed no evidence of such an effect with their model protein, avidin (Firnkes *et al.*, 2010).

To shed more light on the folding state of protein molecules during translocation, a detailed analysis of three negatively-charged proteins of increasing sizes (HPr, calmodulin, CaM, and maltose binding protein, MBP) interacting with two Si_xN_y nanopores with diameters of 7 nm

and 5 nm was conducted. The reason for choosing proteins with net negative charges was that their electrostatic interaction with the negatively-charged walls of the Si_xN_y nanopores would be inhibited thereby reducing permanent pore blockages. The pI of each protein had to be taken into consideration as well as the pH of the buffer used to avoid changes in the net charge of the proteins. Furthermore, it was advisable to use a series of proteins with different dimensions to determine if their size difference would be reflected in their interaction parameters with the nanopores which in turn would indicate if the molecules were translocating folded or unfolded. The properties of the pores are presented in Table 3.10 and the properties of the proteins are presented in Table 3.11.

3.4.2 Analysis of maltose binding protein, calmodulin and HPr with Si_xN_y nanopores

3.4.2.1 The 7 nm pore

Before addition of protein, the current-voltage curve (*I/V* curve) was measured to ensure linearity and that there were no leaks (Figure 3.19). MBP was added to the *cis* chamber and current blockades (events) were observed only when the electrode in the *trans* chamber was positively biased, which correlated with the negatively charged protein molecule being transported by the applied potential. Typical event profiles are shown in Figure 3.20. The magnitude and duration of the blockade currents were measured and plotted as histograms versus the total number of events recorded. The peak values of the current distributions were calculated with a Gaussian function and the blockade duration histograms were fitted with an exponential decay function of first order with the standard functions from Origin 7.0. In order to be able to compare the results of the same protein interacting with pores of different diameters it was convenient to convert the blockade current values to the percentage block (% block) of the respective open pore current measured at the beginning of each experiment.

As shown in Figure 3.21a, b and c and Table 3.12, the majority of the events fall into a single population of blockade currents with % peak values of 21.9% at 50 mV, 10.7% at 100 mV and 5.8% at 200 mV potential. Small populations of events (<25% of the total) were also seen at 34.0%, 29.4% and 17–30% for 50 mV, 100 mV and 200 mV respectively. The number of events in the second population at 200 mV was too small and the values too spread out, to allow meaningful analysis. The blockade times, for both populations, show a single exponential

Table 3.10. Parameters of the solid-state nanopores.

Pore diameter (nm)	Conductance (nS)[a]	Pore volume (nm^3)[b]
7	22.4	576.9
5	14.4	294.3

[a] measured from the slope of the I/V curve.
[b] calculated based on the physical characteristics of the pore.

Table 3.11. Physical and chemical characteristics of the proteins.

Protein	Characteristic							
	Net Charge	**Charge Density[a]**	**M.W. (kDa)**	**No. of residues**	**pI[b]**	**Dimensions (nm)[c]**	**Volume (nm^3)[d]**	**Volume (nm^3)[e]**
HPr	-2	-0.023	9.1	85	5.5	2.1x2.7x3.8	11.27	40.4
Calmodulin	-25	-0.169	16.9	148	3.9	2.3x3.0x6.5	23.47	78.8
MBP	-8	-0.021	40.8	370	5.2	3.0x4.0x6.5	40.82	107.5

[a] Calculated from the net charge divided by the number of amino acids.
[b] Taken from references (14-16).
[c] Taken from references (17-19).
[d] Calculated based on dimensions considering an ellipsoidal shape (without 0.7 nm water shell).
[e] Calculated based on dimensions considering an ellipsoidal shape (with 0.7 nm water shell).

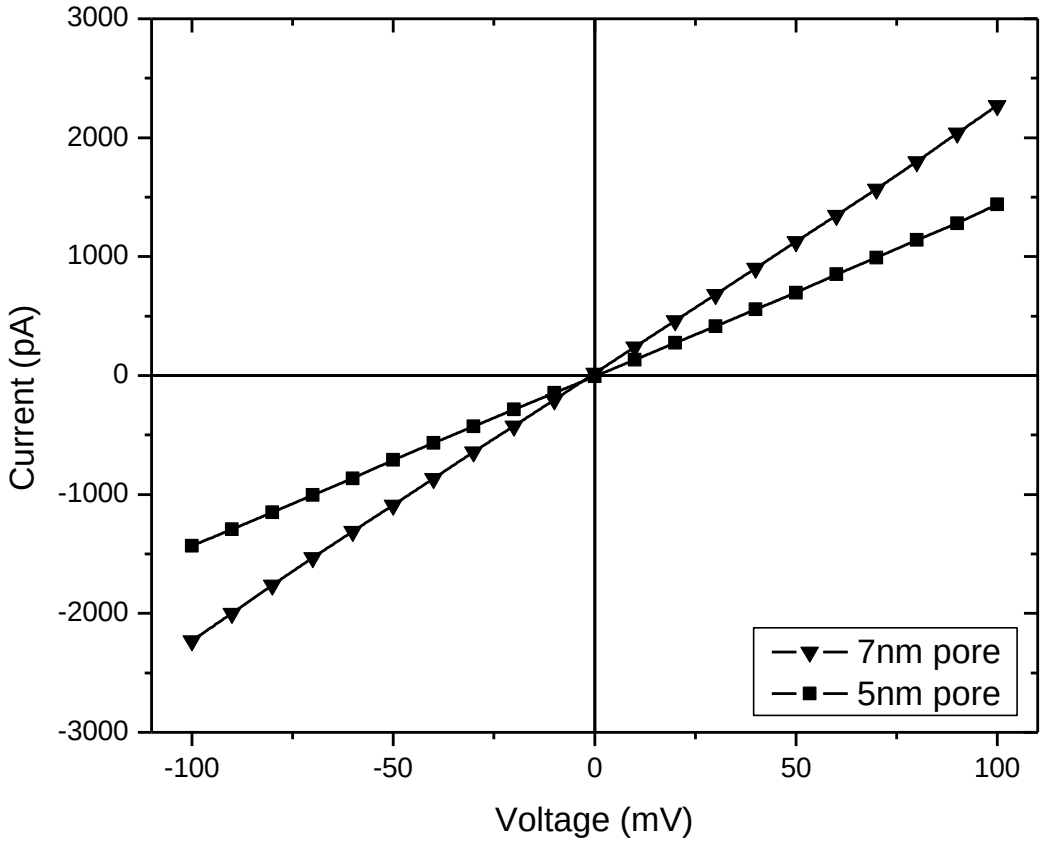

Figure 3.19. Current-voltage curves for the 7 nm (triangles) and 5 nm (squares) pores recorded at 1 M KCl, 10 mM Tris-HCl, pH 7.3.

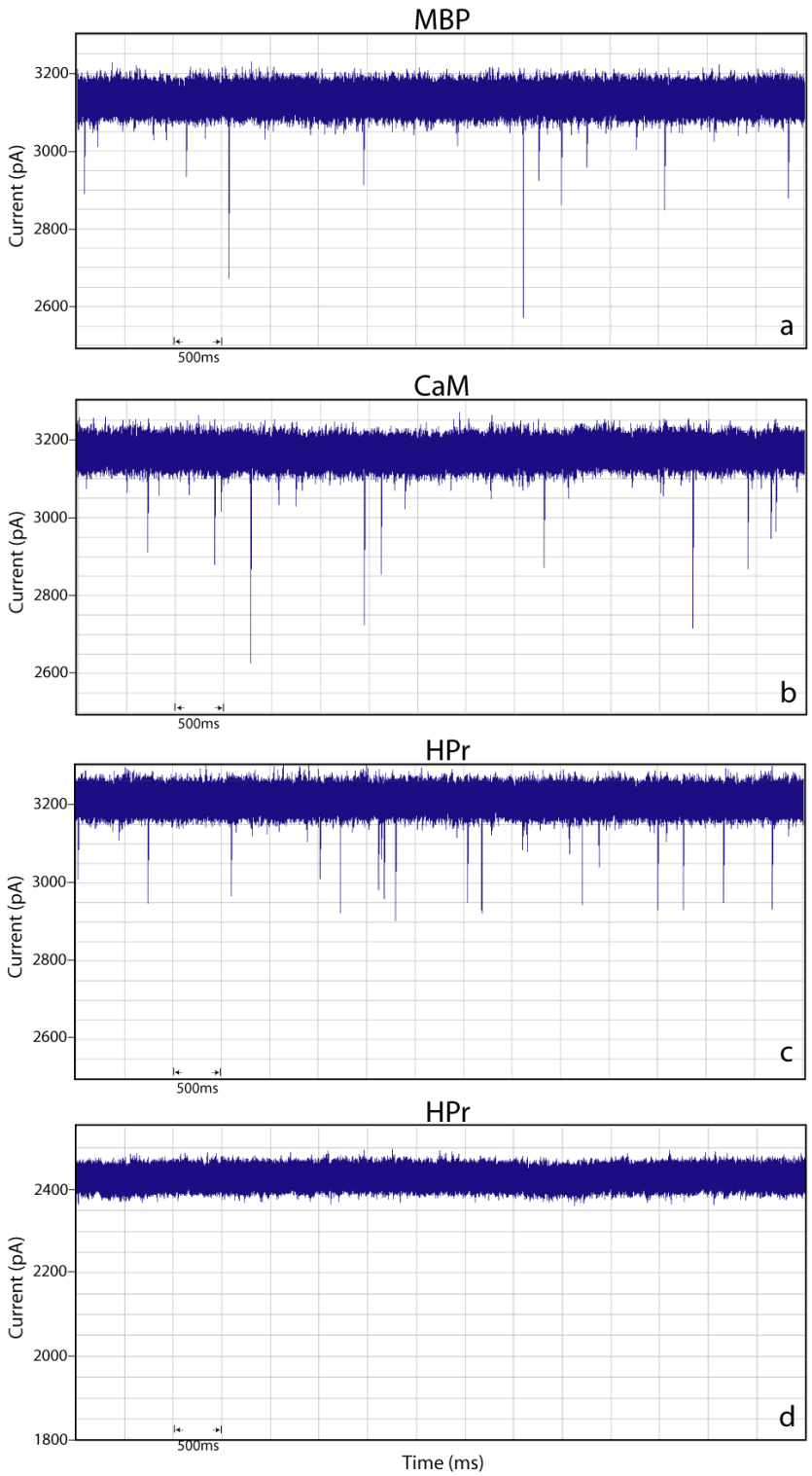

Figure 3.20. Current traces through the 7 nm pore for (a) MBP, (b) CaM and (c-d) HPr under an applied voltage of 100 mV in 1 M KCl, 10 mM Tris-HCl (a-c) and 2 M KCl, 10 mM Tris-HCl, 8 M urea (d). Current blockades generated by unfolded HPr molecules cannot be resolved from the noise (d). Note the drop in the pore conductance due to the presence of 8 M urea in d).

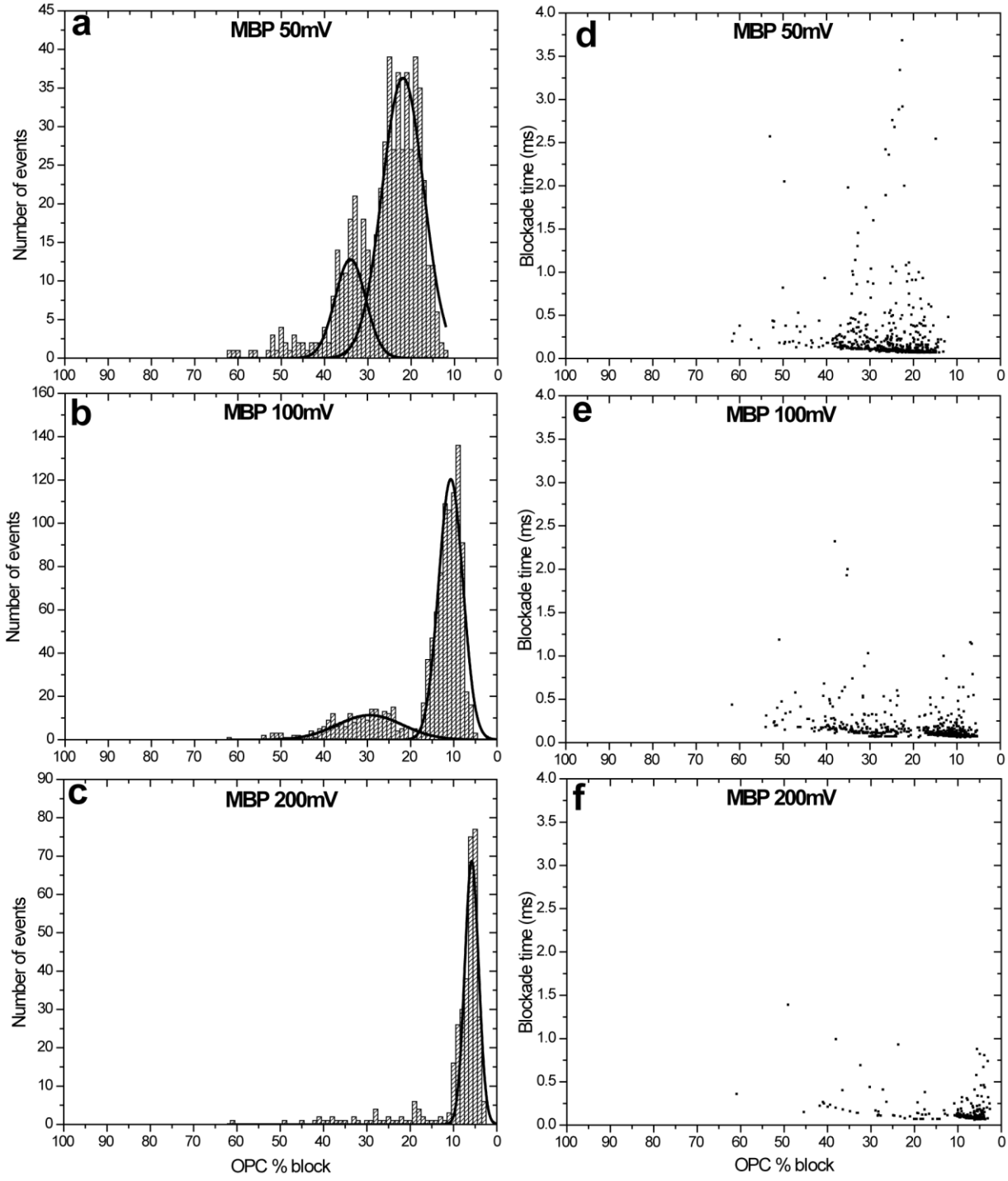

Figure 3.21. % blockade current histograms and scatter plots for MBP interactions with the 7 nm pore under applied potentials of 50, 100, and 200 mV.

Table 3.12. Event parameters for MBP interactions with the 7 nm pore [a].

Voltage (mV)	OPC (pA)	% block (1)	% block (2)	T_1 (ms)	T_2 (ms)	A_1	A_2	W_1	W_2
50	1600	21.9	34.0	0.059	0.099	410	155	9.5	7.0
100	3150	10.7	29.4	0.040	0.089	843	222	5.4	15.1
200	6350	5.8	19.0	0.049		349		3.0	

[a] **OPC**, open pore current; **%block**, percentage block; **T**, blockade time; **A**, number of events under curve; **W**, peak width at half height. The subscripts 1 and 2 refer to the respective population of events. (The error is estimated to be ±1% for **%block** and ±10% for **T**).

distribution with very fast durations of <0.1 ms (Table 3.12). As will be discussed below, these results are difficult to reconcile with translocation because the event durations are roughly constant and the % block is not constant with increasing voltage; i.e. they are consistent with bumping events in which the protein approaches the pore but then diffuses away.

Plotting the % block peak values against the blockade times as two-dimensional scatter plots enhances the visualization of the protein interactions with the nanopore. Each point in the plot correlates the blockade duration with the % block determined by the interaction of a single molecule with the Si_xN_y nanopore. In this way it is possible to observe the blockade durations of the events which form the blockade current populations. For MBP, the scatter plots (Figure 3.21d, e and f) show that most of the events from both populations have blockade durations faster than 0.25 ms, indicating one type of interaction between the protein molecules and the pore.

The histograms of % block and the scatter plots for CaM are shown in Figure 3.22 and the corresponding event parameters are summarized in Table 3.13. Again, the event profiles are dominated by populations at low % block (13.2, 7.3 and 4.4% for 50 mV, 100 mV and 200 mV, respectively). Because the % block decreases with increasing voltage, these events are consistent with bumping into the pore before diffusing away. At 100 and 200 mV, there is a second population of events with a % block of about 13%, which can also be seen in the scatter plots of Figures 3.22e and f. The event duration decreases with increasing voltage which, as well, is consistent with translocation. It should be noted that the single broad peak recorded at 50 mV with a % block of 13.2% may include both bumping and translocation events which cannot be distinguished in the scatter plot of Figure 3.22d.

In contrast with MBP and CaM, HPr's interaction with the 7 nm Si_xN_y pore reveals very narrow and well defined populations of events. The current blockade events are grouped in a single population for the experiments at 50 and 100 mV potential whereas two populations of events are apparent for the 200 mV experiment (Figure 3.23a, b and c). The % block of this population (7.2–7.5%) does not change with voltage and the blockade duration decreases from 0.28 to 0.11 ms as the voltage increases, indicating that these are translocation events (Table 3.14). Similarly to CaM, a second population of events with short duration, 0.05 ms, and small % block, 4%, becomes apparent at higher voltages which is consistent with bumping events.

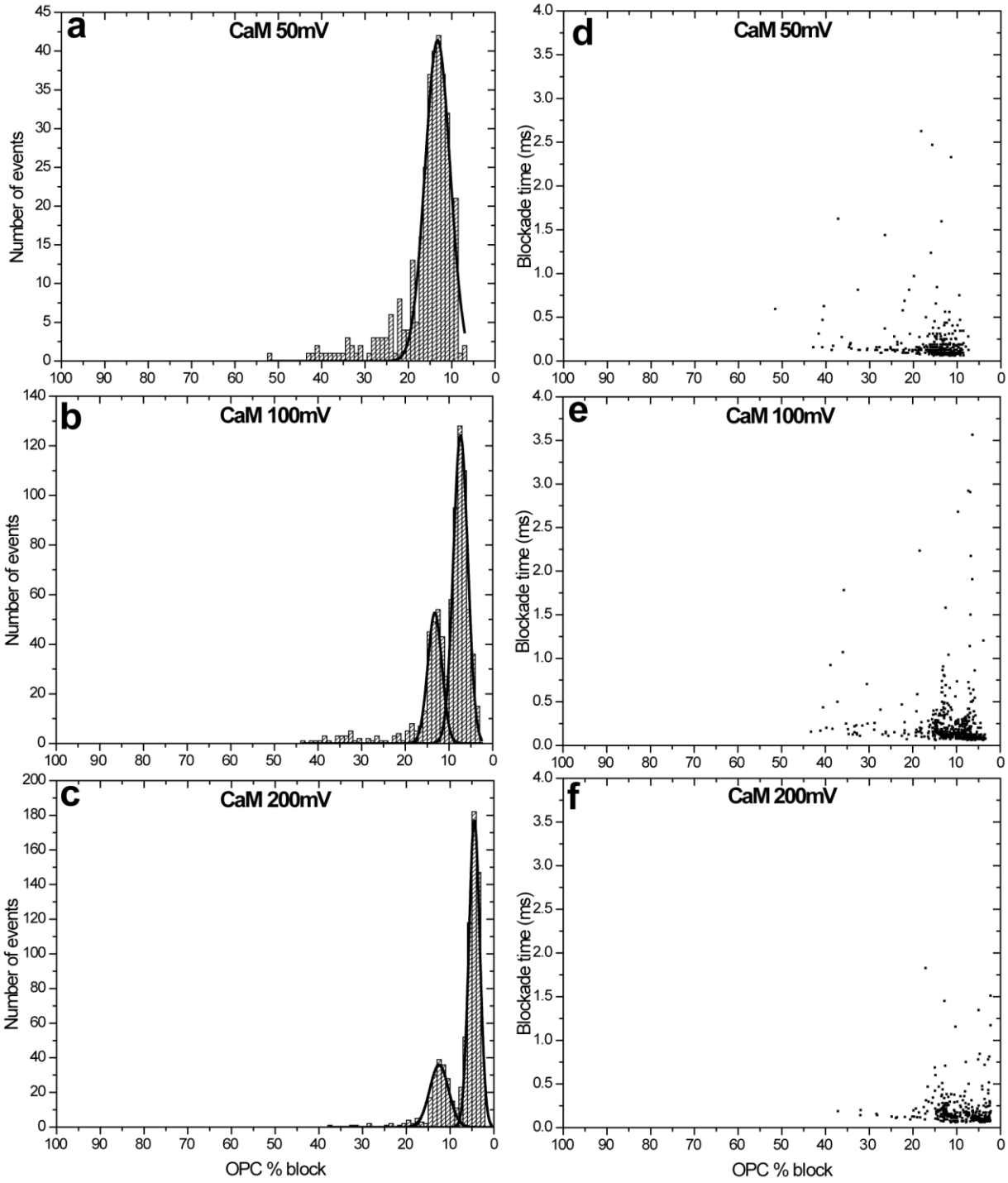

Figure 3.22. % blockade current histograms and scatter plots for MBP interactions with the 7 nm pore under applied potentials of 50, 100, and 200 mV.

Table 3.13. Event parameters for CaM interactions with the 7 nm pore [a].

Voltage (mV)	OPC (pA)	% block (1)	% block (2)	T_1 (ms)	T_2 (ms)	A_1	A_2	W_1	W_2
50	1600	13.2		0.14		345		5.7	
100	3150	7.3	13.2	0.076	0.12	496	297	3.2	3.1
200	6350	4.4	12.5	0.032	0.096	545	217	2.4	4.2

[a] **OPC**, open pore current; **%block**, percentage block; **T**, blockade time; **A**, number of events under curve; **W**, peak width at half height. The subscripts 1 and 2 refer to the respective population of events. (The error is estimated to be ±1% for **%block** and ±10% for **T**).

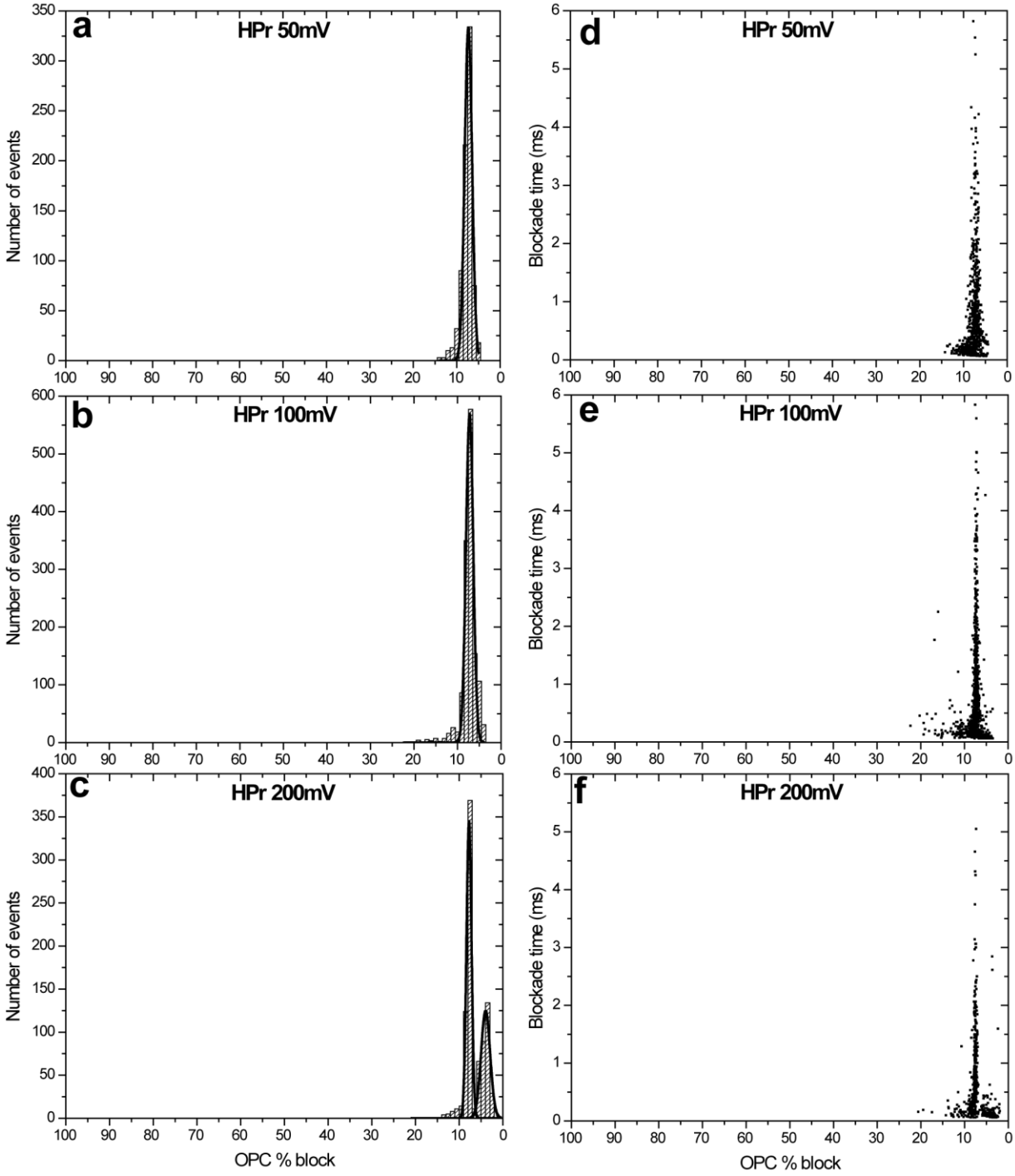

Figure 3.23. % blockade current histograms and scatter plots for HPr interactions with the 7 nm pore under applied potentials of 50, 100, and 200 mV.

Table 3.14. Event parameters for HPr interactions with the 7 nm pore [a]

Voltage (mV)	OPC (pA)	% block (1)	% block (2)	T_1 (ms)	T_2 (ms)	A_1	A_2	W_1	W_2
50	1600	7.3		0.28		797		1.7	
100	3150	7.2		0.12		1396		1.6	
200	6350	3.9	7.5	0.048	0.11	322	546	2.0	1.1

[a] **OPC**, open pore current; **%block**, percentage block; **T**, blockade time; **A**, number of events under curve; **W**, peak width at half height. The subscripts 1 and 2 refer to the respective population of events. (The error is estimated to be ±1% for **%block** and ±10% for **T**).

3.4.2.2 The 5 nm pore

Originally it was intended for MBP, CaM and HPr molecules to be tested on a 5 nm pore as well. Unfortunately, after analyzing MBP and HPr, the nanopore became permanently blocked and unusable for further experimentation. Even though the pore presented a good ohmic behavior and correct open pore currents, it tended to become blocked when voltages higher than 150 mV were tested. As a consequence, the highest voltage used in these experiments was 150 mV.

Analysis of MBP reveals two populations of events at all voltages; a sharp peak at low % block and a broader peak at higher % block (Figure 3.24 and Table 3.15). For both populations the % block decreases with increasing voltage and the scatter plots show very fast interaction times ($\boldsymbol{T} < 0.25$ ms) for the majority of events (Figure 3.24d, e and f). From the above, it appears unlikely that MBP can translocate.

HPr generates histograms very similar to those for CaM when analyzed on the 7 nm pore. There is one broad population of events for the 50 mV experiment and two populations of events for the 100 and 150 mV experiments (Figures 3.25a, b and c). The two-dimensional scatter plots indicate a significant number of interactions with durations longer than 0.25 ms (Figures 3.7d, e and f). The smaller population of events at 100 and 200 mV are consistent with translocation because the % blocks are similar and the event durations decrease with increasing voltage (Table 3.16). As was mentioned with CaM above, the single peak for HPr at 50 mV may include both bumping and translocation events which cannot be separated.

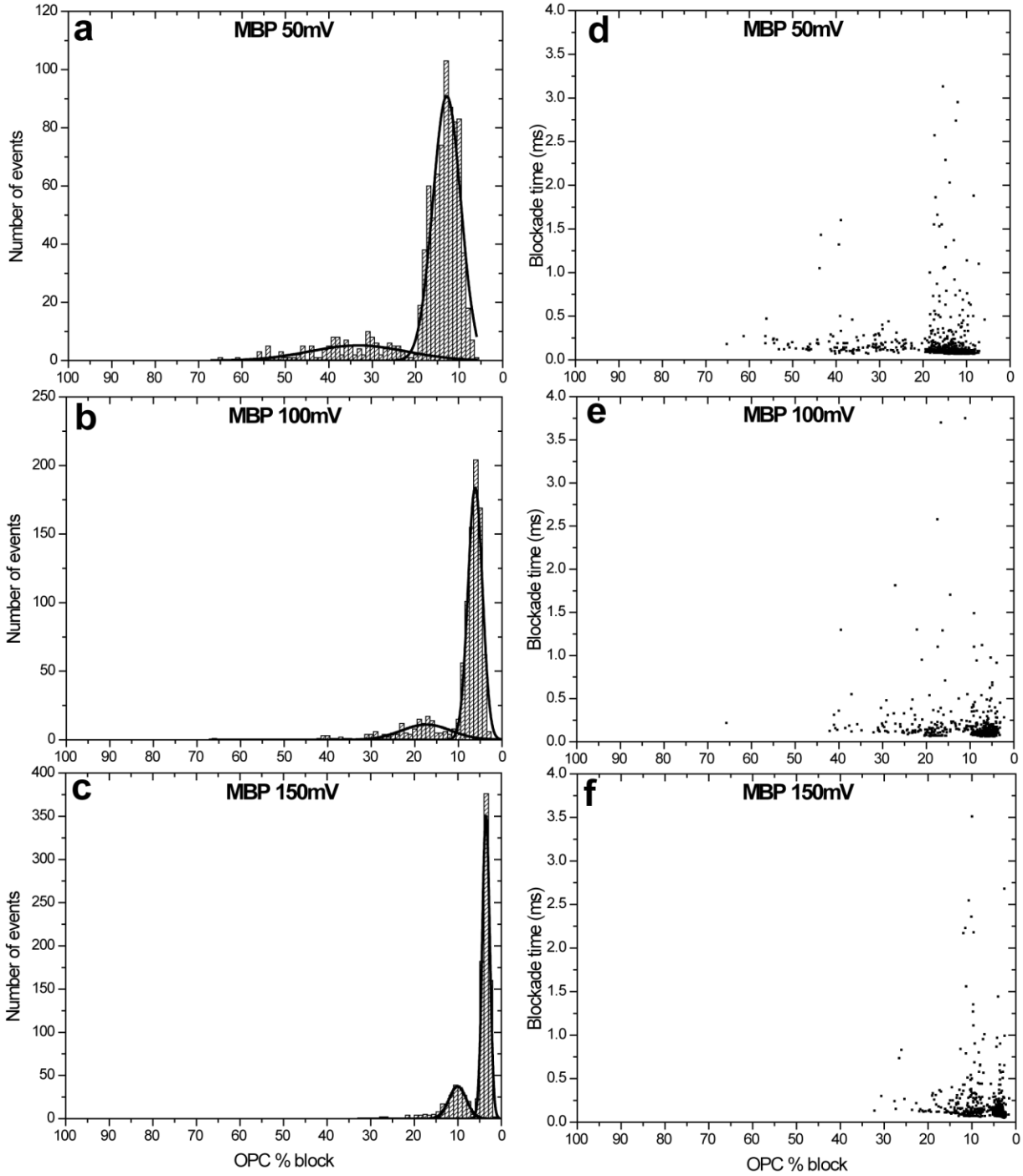

Figure 3.24. % blockade current histograms and scatter plots for MBP interactions with the 5 nm pore under applied potentials of 50, 100, and 150 mV.

Table 3.15. Event parameters for MBP interactions with the 5 nm pore [a].

Voltage (mV)	OPC (pA)	% block (1)	% block (2)	T_1 (ms)	T_2 (ms)	A_1	A_2	W_1	W_2
50	1286	12.9	33.3	0.045	0.085	724	130	6.3	22.2
100	2572	6.1	17.4	0.034	0.064	767	161	3.0	11.3
150	3858	3.5	10.1	0.038	0.086	737	236	1.6	3.9

[a] **OPC**, open pore current; **%block**, percentage block; **T**, blockade time; **A**, number of events under curve; **W**, peak width at half height. The subscripts 1 and 2 refer to the respective population of events. (The error is estimated to be ±1% for **%block** and ±10% for **T**).

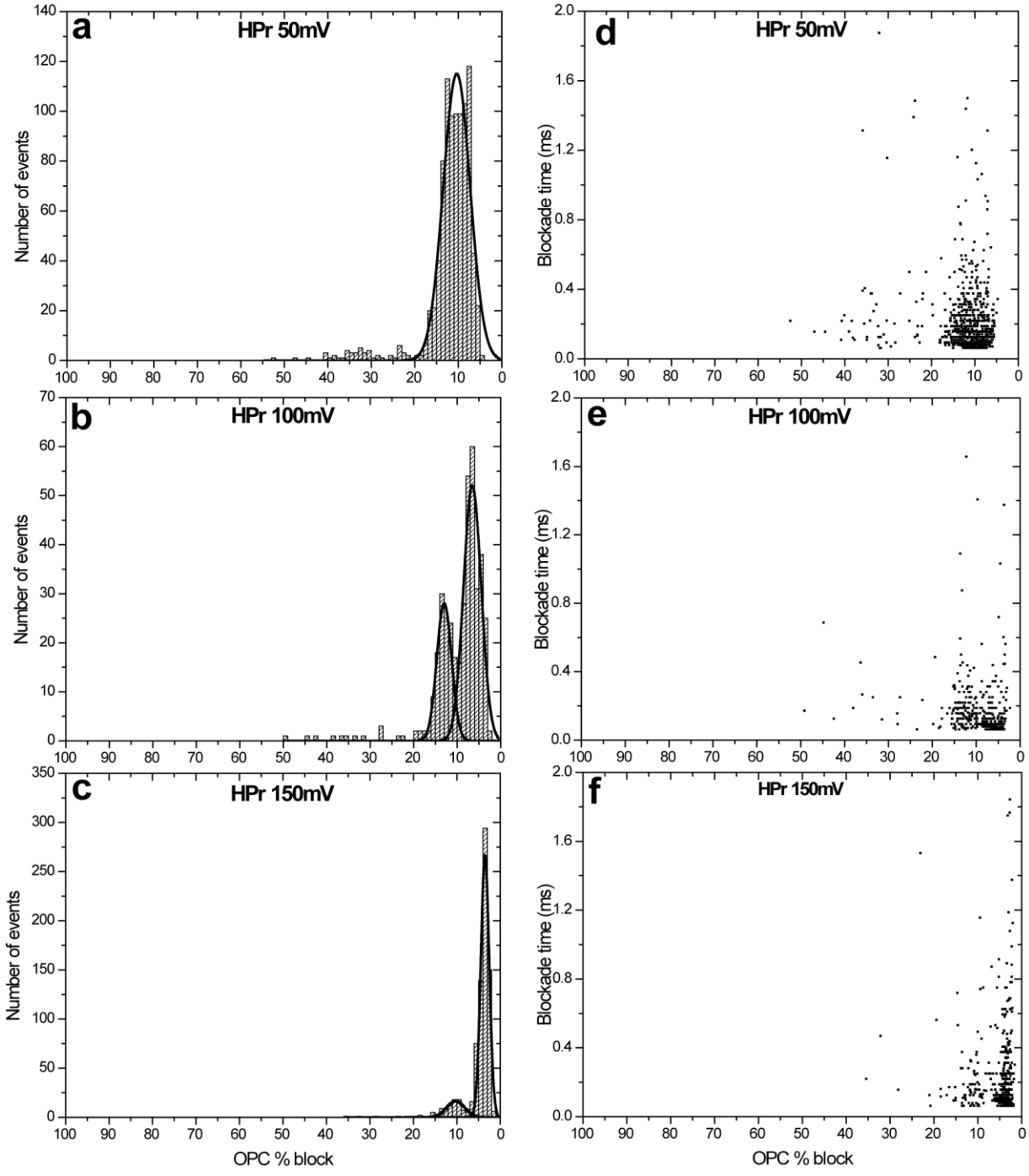

Figure 3.25. % blockade current histograms and scatter plots for HPr interactions with the 5 nm pore under applied potentials of 50, 100, and 150 mV.

Table 3.16. Event parameters for HPr interactions with the 5 nm pore [a].

Voltage (mV)	OPC (pA)	% block (1)	% block (2)	T_1 (ms)	T_2 (ms)	A_1	A_2	W_1	W_2
50	1240	10.4		0.12		869		6.1	
100	2480	6.5	12.9	0.049	0.083	254	144	3.9	3.2
150	3720	3.5	10.3	0.069	0.055	679	96	1.8	4.1

[a] **OPC**, open pore current; **%block**, percentage block; **T**, blockade time; **A**, number of events under curve; **W**, peak width at half height. The subscripts 1 and 2 refer to the respective population of events. (The error is estimated to be ±1% for **%block** and ±10% for **T**).

3.4.3 Analysis of bPrP(25-242) interaction with monoclonal antibody M2188

Antibodies that selectively bind one of the two forms of the prion protein PrP^{C} or PrP^{Sc} have been recently developed (Korth *et al.*, 1997; Paramithiotis *et al.*, 2003; Curin Serbec *et al.*, 2004; Zou *et al.*, 2004; Andrievskaia *et al.*, 2006; Polymenidou *et al.*, 2008). This selectivity resides in the fact that different epitopes are exposed in the two prion isoforms. More specifically, Andrievskaia and coworkers have generated a PrP^{C}-specific monoclonal antibody (M2188) which binds the SRPLIHFG epitope (positions 146-153) (Andrievskaia *et al.*, 2006). With a molecular weight of 150 kDa, the M2188 antibody has the classic Y-shape of the IgG2a class of antibodies. The largest dimension of the antibody is its height of 14.5 nm followed by its width of 8.5 nm and its thickness of 4 nm (Silverton *et al.*, 1977). As presented in Table 3.17, we have calculated a hydrated volume of 436 nm^3 assuming a 0.7 nm thick water shell.

So far, the detection of the bPrP/M2188 complex formation has been successfully tested only in patch-clamp experiments utilizing the α-hemolysin pore (Madampage *et al.*, 2010). Since solid-state nanopores will provide the sensitivity of the portable prion detector, the next step in my project was to investigate if the prion/antibody complex formation could be detected with this type of nanopore.

Recombinant bovine prion protein encompassing residues 25-242 (bPrP25-242) with a carboxy-terminal His5 tag and the M2188 antibody were tested on two solid-state nanopores with diameters of 11 nm and 19 nm respectively. The 11 nm pore was chosen because its diameter is larger than bPrP but smaller than M2188 and it should permit the transit of the prion protein but not of the antibody. Upon binding of M2188 to bPrP25-242, the translocation peak of the prion protein should disappear which, in turn, would report the formation of the prion/antibody complex. On the other hand, the interactions of bPrP and M2188 with the 19 nm pore should result in translocations since the pore's diameter should accommodate the transit of both molecules. In this case, the complex formation would be indicated either by an increase in the blockade current determined by the complex translocation or a complete lack of translocations if the complex is unable to transit the pore. Regardless of the outcome of the interaction with the nanopore, the complex formation should still be detectable.

All protein molecules tested on the two nanopores had positive net charges as opposed to the ones presented in section 3.4.2 and possessed a higher risk of clogging the pores by adhering to their negatively-charged surface. Preliminary testing determined that the M2188 antibody had a

positive net charge as current blockades were witnessed only when the antibody was added to the positively-biased chamber. All chemical and physical characteristics of the proteins are presented in Table 3.17.

Before the experiments were started, the conductivity of each pore was tested. While the 11 nm pore presented stable conductance values at all applied voltages, the conductance of the 19 nm pore frequently oscillated between the correct value and a lower value at voltages above 80 mV. For this reason, the experiments performed on the 19 nm pore were recorded only at an applied potential of 80 mV. The conductance values of both pores stayed constant during the individual experiments. The initial conductance values and volumes of the two pores are listed in Table 3.18 and the *I/V* curves are presented in Figure 3.26.

3.4.3.1 The 11 nm pore

All % block distributions were plotted against the number of events per minute in order to obtain a more detailed picture of the interaction of bPrP, M2188 antibody and bPrP/M2188 complex with the nanopore and to facilitate the visual observation of the applied voltage effect on the event frequency.

First, the current blockade histograms of bPrP interaction with the 11 nm pore revealed two distinct populations of events for all applied voltages tested (Figure 3.27a, d and g). The first population had % blockade peak values ranging from 2.3 % to 2.9 % and the second population had values between 4.1 % and 4.5 % (Table 3.19). Plotting the % block values against the number of events per minute allows the observation that the number of events per minute increases with the applied potential indicative of an electrophoretically-driven process. At the same time, the proportion of events forming the higher blockade population increases and both populations of events shift slightly to lower % blockade values as the applied potential is increased. The single-exponential fit of the blockade duration distribution generated by the events of the higher blockade population indicate values of 0.162 ms, 0.033 ms and 0.078 ms as the voltage was increased from 75 mV to 100 mV and to 150 mV respectively (Figure 3.27b, e and h). At the same time the blockade durations of the lower blockade population were faster and stayed mostly constant with the increasing voltage (Figure 3.27c, f and i). All calculated parameters are presented in Table 3.19. The two-dimensional scatter plots maintain good

Table 3.17. Physical and chemical characteristics of the proteins.

Protein	Characteristic							
	Net Charge	**Charge Density[a]**	**M.W. (kDa)**	**No. of residues**	**pI[b]**	**Dimensions (nm)[c]**	**Volume (nm^3)[d]**	**Volume (nm^3)[e]**
bPrP	+8	+0.036	25.0	223	9.7	4.4x2.8x2.7	17.4	54.3
RNase A	+4	+0.032	13.7	124	9.5	3.8x2.8x2.8	15.6	49.0
M2188	+		150.0			14.5x8.5x4.0	211.0	436.0

[a] calculated from the net charge divided by the number of amino acids.
[b] calculated with Innovagen Peptide Property Calculator (Lund, Sweden).
[c] taken from references (Joseph-McCarthy *et al.*, 1996; Lopez-Garcia *et al.*, 2000).
[d] calculated based on dimensions considering an ellipsoidal shape (without 0.7 nm water shell).
[e] calculated based on dimensions considering an ellipsoidal shape (with 0.7 nm water shell).

Table 3.18. Parameters of the solid-state nanopores.

Pore diameter (nm)	Conductance (nS)[a]	Pore volume (nm^3)[b]
11	57.8	1424.8
19	129.7	4250.8

[a] measured from the slope of the I/V curve.
[b] calculated based on the physical characteristics of the pore.

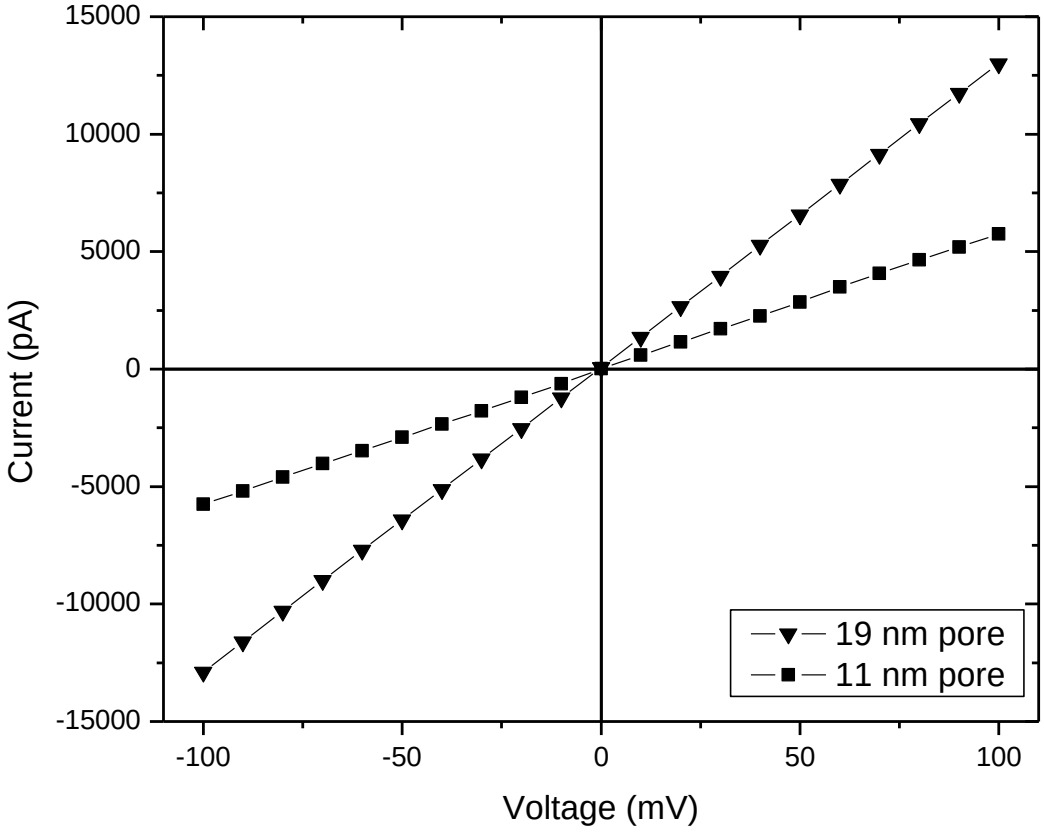

Figure 3.26. Current-voltage curves for the 19 nm (triangles) and 11 nm (squares) pores recorded at 1 M KCl, 10 mM Tris-HCl, pH 7.8.

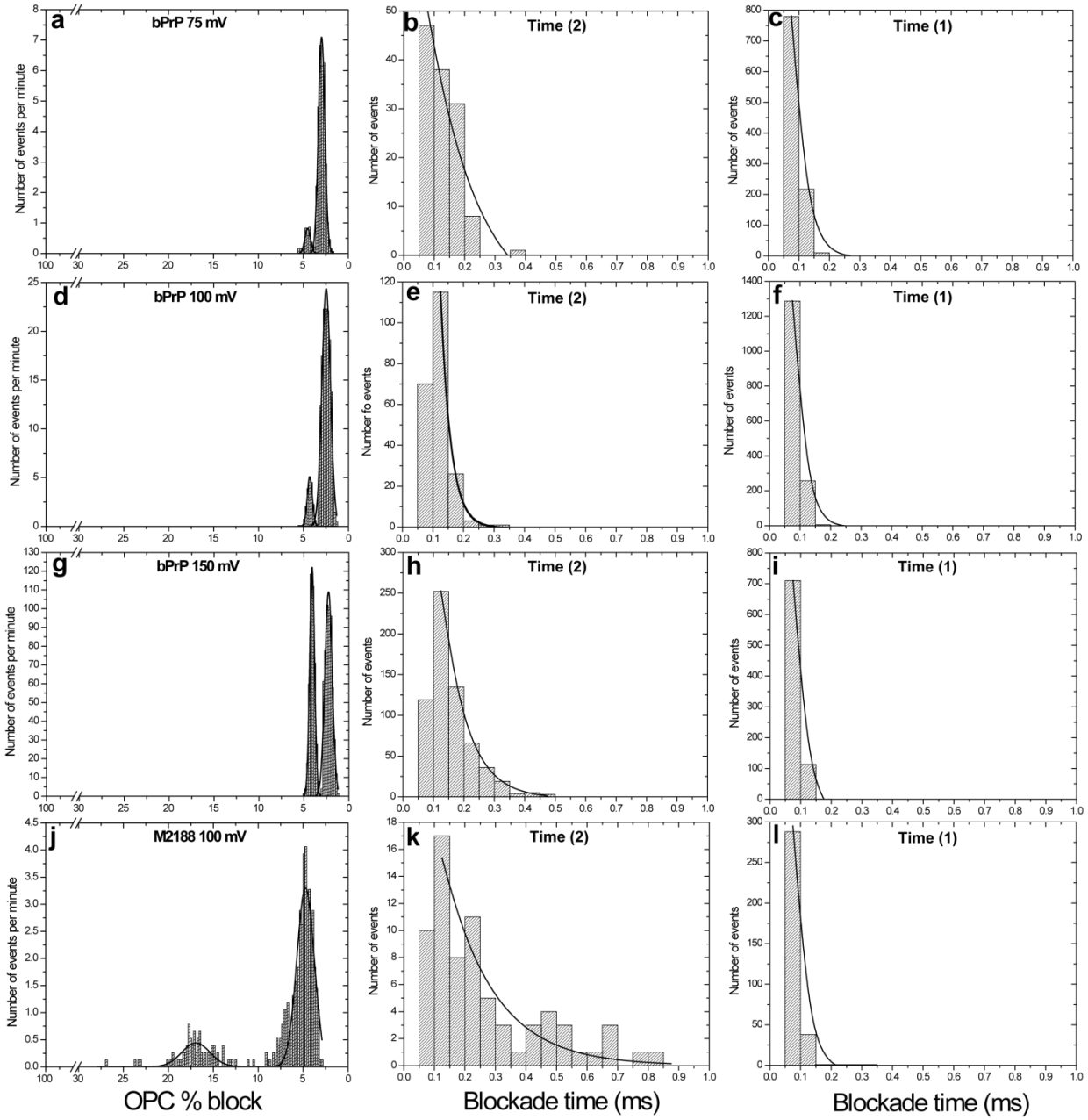

Figure 3.27. % blockade current histograms and blockade time histograms for bPrP interactions with the 11 nm pore under applied potentials of 75, 100, and 150 mV (panels a-i) and for M2188 under an applied potential of 100 mV (panel j-l).

Table 3.19. Event parameters for bPrP and M2188 interactions with the 11 nm pore [a].

Protein	Voltage (mV)	OPC (pA)	% block (1)	% block (2)	T_1 (ms)	T_2 (ms)	A_1	A_2	W_1	W_2
bPrP	**75**	4350	2.9	4.5	0.036	0.162	31.5	3.0	0.7	0.6
bPrP	**100**	5750	2.5	4.3	0.030	0.033	144.5	18.0	0.9	0.6
bPrP	**150**	8675	2.3	4.1	0.030	0.078	559.5	415.5	0.8	0.5
M2188	**100**	5475	4.7	16.9	0.034	0.161	40.0	8.5	1.9	3.1

[a] **OPC**, open pore current; **%block**, percentage block; **T**, blockade time; **A**, number of events under curve; **W**, peak width at half height. The subscripts 1 and 2 refer to the respective population of events. (The error is estimated to be ±1% for **%block** and ±10% for **T**).

separation between the two populations of events and confirm that the events forming the lower % blockade population are faster than those belonging to the higher % blockade population (Figure 3.28a, b and d) (Table 3.19). This is consistent with the time values listed in Table 3.19 which suggest the existence of two types of interactions between bPrP and the pore: translocation and bumping.

Second, the interaction of the M2188 antibody with the 11 nm pore could only be studied under 100 mV applied potential before the nanopore became irreversibly blocked and ceased to function. The % blockage and blockade time histograms of this experiment are shown in Figure 3.27j, k and l and reveal the presence of two populations of events. A peak value of 4.7 % for the lower population and 16.9 % for the peak of the higher population are reported in Table 3.19. The high % block population is formed of events with long interactions with the pore (0.161 ms) while the low % block population contains events with much shorter interaction times (0.034 ms). These results are also reflected in the scatter plot which shows a very compact cluster of events with fast times for the low % block population and a more spread-out cluster of events with slower interaction times for the high % block population (Figure 3.28c).

Third, to detect a possible dose-dependent effect of the specific protein/antibody binding, two bPrP/M2188 molar ratios were tested. The % block histograms of bPrP/M2188 at 1:1 ratio are presented in Figure 3.29d, e and f and at 2:1 ratio in Figure 3.29a, b and c. The corresponding parameters are summarized in Table 3.20 and Table 3.21. For all three applied voltages the histograms of both protein/antibody ratios look similar for the same applied voltage. The events are grouped in two well-represented populations for the 75 mV and 100 mV experiments while at 150 mV the higher blockade populations have very few events detected. At the same time the lower blockade populations become narrower with the increasing voltage indicating that there is less variation in the orientation of the molecules as they interact with the pore. On one hand, both bPrP/M2188 ratios and the M2188 antibody alone have similar % block values ranging from 4.0 % to 5.9 % for the low % block population and from 14.9 % block to 17.5 % for the high % block population (Table 3.19 and Table 3.20). On the other hand, there are more events generated per minute by bPrP/M2188 1:1 than by bPrP/M2188 2:1 and in both cases more than the events generated by M2188 alone. Similarly to the bPrP results, the % block values decrease slightly with the increasing voltage. Generally, the low % block populations have faster blockade times than the high % block populations pointing towards bumping for the former and

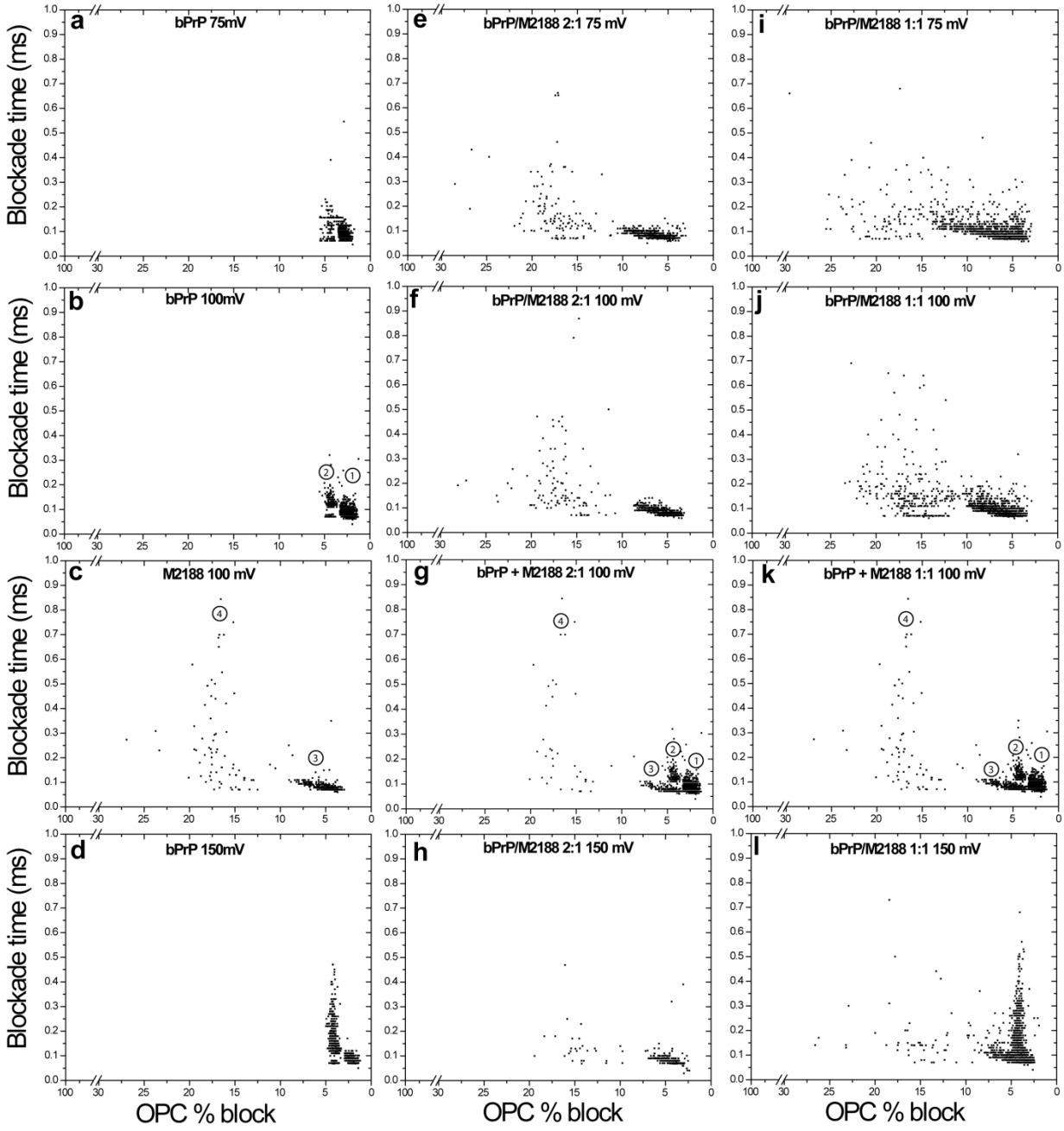

Figure 3.28. Scatter plots for bPrP, bPrP/M2188 2:1, bPrP/M2188 1:1 interactions with the 11 nm pore under applied potentials of 50, 100, and 150 mV. Panels c, g and k show scatter plots of M2188, bPrP+M2188 2:1 and bPrP+M2188 1:1 under 100 mV applied potential.

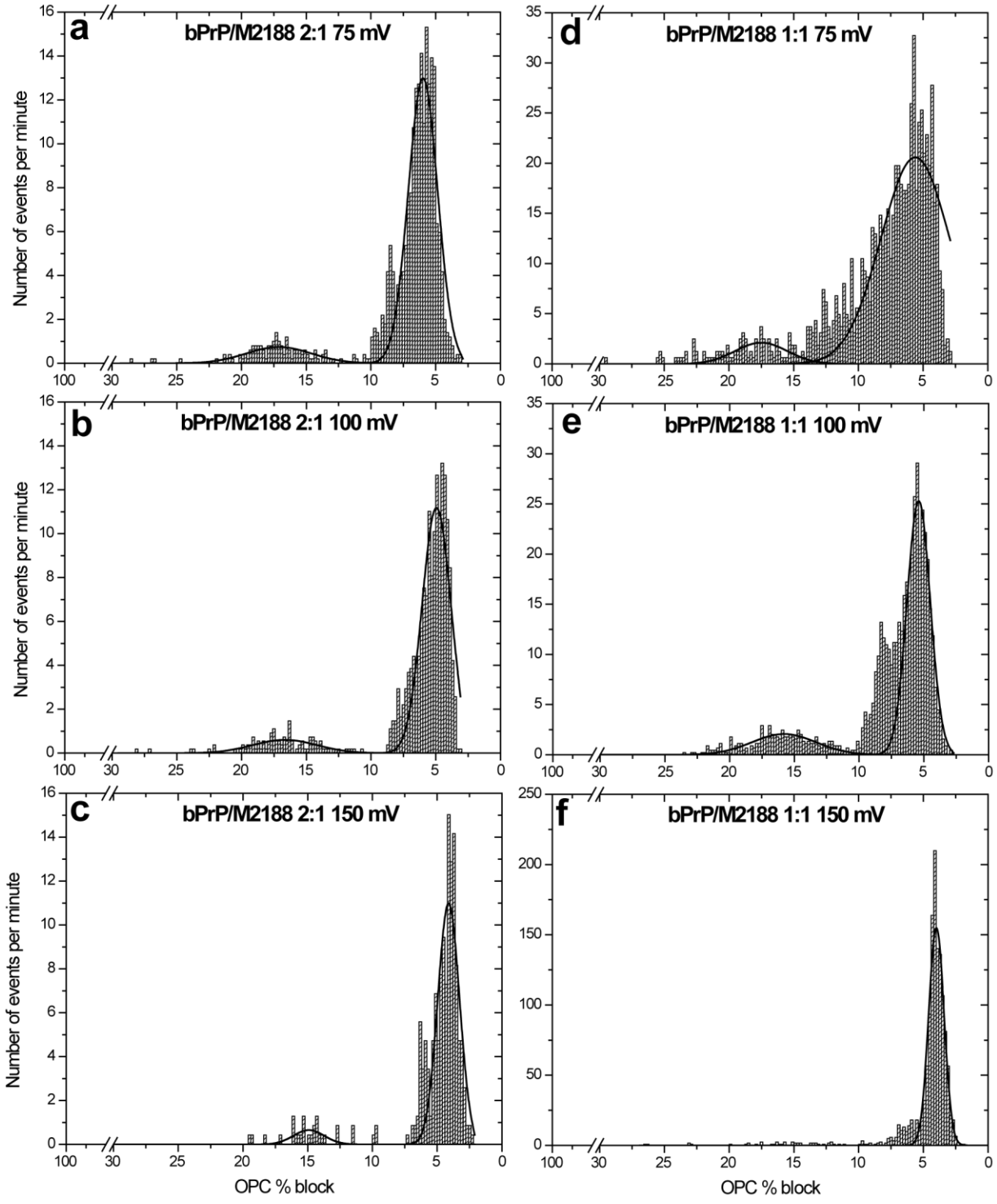

Figure 3.29. % blockade current histograms for bPrP/M2188 2:1 and bPrP/M2188 1:1 interactions with the 11 nm pore under applied potentials of 75, 100, and 150 mV.

Table 3.20. Event parameters for bPrP/M2188 1:1 interactions with the 11 nm pore [a].

Voltage (mV)	OPC (pA)	% block (1)	% block (2)	T_1 (ms)	T_2 (ms)	A_1	A_2	W_1	W_2
75	4350	5.6	17.5	0.066	0.094	687.0	53.5	5.3	4.0
100	5750	5.4	15.8	0.036	0.088	284.5	64.0	1.7	4.9
150	8675	4.0	-	0.081	-	1146.5	-	1.0	-

[a] **OPC**, open pore current; **%block**, percentage block; **T**, blockade time; **A**, number of events under curve; **W**, peak width at half height. The subscripts 1 and 2 refer to the respective population of events. (The error is estimated to be ±1% for **%block** and ±10% for **T**).

Table 3.21. Event parameters for bPrP/M2188 2:1 interactions with the 11 nm pore [a].

Voltage (mV)	OPC (pA)	% block (1)	% block (2)	T_1 (ms)	T_2 (ms)	A_1	A_2	W_1	W_2
75	4150	5.9	17.1	0.019	0.087	184.0	23.0	2.1	5.0
100	5475	4.9	16.7	0.022	0.093	155.0	18.5	2.1	4.9
150	8375	4.1	14.9	0.021	0.050	115.5	9.5	1.6	2.3

[a] **OPC**, open pore current; **%block**, percentage block; **T**, blockade time; **A**, number of events under curve; **W**, peak width at half height. The subscripts 1 and 2 refer to the respective population of events. (The error is estimated to be ±1% for **%block** and ±10% for **T**)

translocation or intercalation for the latter as presented in section 4.7.1 of the Discussion. As the voltage increases, the $\mathbf{T_2}$ values stay roughly constant for both bPrP/M2188 ratios with the exception of bPrP/M2188 2:1 at 150 mV where the very few recorded events did not allow a proper calculation of the blockade time. The $\mathbf{T_1}$ values stay around 0.020 ms for bPrP/M2188 2:1 and vary irregularly for bPrP/M2188 1:1. The irregularities in blockade duration values and the different frequency of events generated for the two protein/antibody ratios indicate original interaction patterns with the pore for each of the two sets of experiments. Furthermore, the scatter plots show narrower time distribution clusters for bPrP/M2188 2:1 (Figure 3.28e, f and h) as compared to bPrP/M2188 1:1 (Figure 3.28i, j and l). A unique scatter plot is generated at 150 mV by bPrP/M2188 1:1 (Figure 3.28i) where the low blockade population has a large extra cluster of events with longer duration values that is not present in any of the other scatter plots regardless of the antigen/antibody ratio. This indicates a special phenomenon taking place at this particular applied voltage that could clearly be observed in the scatter plot and not in the % block histogram.

A plot of the sum of the individual scatter plots of bPrP and M2188 at 100 mV applied potential against the adjusted frequency of events for bPrP:M2188 ratios of 2:1 and 1:1 was performed to provide a point of reference for the comparison with the experimentally-recorded bPrP/M2188 1:1 and 2:1 scatter plots at the same potential (Figure 3.28g and k). A crucial point for data interpretation was to know how the scatter plots would look if no interaction between bPrP and M2188 would take place. In other words we were interested to determine whether the bPrP/M2188 1:1 and bPrP/M2188 2:1 histograms were generated by the protein-antibody complex or by the individual unbound species. While the % block histograms in Figure 3.29 show some degree of interaction between bPrP and M2188, the scatter plots give a clearer indication of complex formation. In the resulting scatter plots four well-defined event clusters are visible in contrast to only two clusters observed for bPrP/M2188 1:1 and 2:1 (Figure 3.28g, k and f, j respectively).

3.4.3.2 The 19 nm pore

The same molecules analyzed on the 11 nm pore were also analyzed on a pore with a diameter of 19 nm under an applied potential of 80 mV. RNase A was added to the group to serve as a negative control since it does not have binding affinity for the M2188 antibody. As far as the protein/antibody complex formation was concerned, only the 2:1 ratio was tested during the bPrP/M2188 and RNase A/M2188 experiments to facilitate the interpretation of the results by having only one molecular species in solution as discussed in section 4.7.1. Similarly to the 11 nm pore analysis, the % block histograms were plotted against the number of events per minute in order to enable a visual comparison of the event frequency generated by the different molecules tested.

The % block histograms show single populations of events for both bPrP and RNase A molecules with peak values of 1.18 % and 0.84 % respectively (Figure 3.30a and d). Although both populations have very similar widths at half the peak hight: 0.37 for bPrP and 0.36 for RNase A, the number of events per minute generated by bPrP was slightly higher than that of RNase A (Table 3.22). The molecules also generated sharp two-dimensional scatter plots with blockade time values of 0.149 ms for bPrP and 0.111 ms for RNase A (Figure 3.31a and d). All numeric values with statistical parameters are presented in Table 3.22.

The interaction of the M2188 antibody with the 19 nm pore resulted in a % block histogram with two populations of events: a sharper peak situated at 1.82 % block and a broader peak positioned at 4.02 % block (Figure 3.30c). The blockade times show single exponential distributions with values of 0.030 ms and 0.093 ms respectively. The scatter plot in Figure 3.31c shows the events arranged in two clusters with the vast majority of blockade times around a value of 0.100 ms. In the same plot a few longer-lived events can be visualized for both clusters. The antibody generated the least number of events per minute of all molecules tested (Table 3.22).

RNase A incubated for one hour with the M2188 antibody at a molar ratio of 2:1 reveals a three peak histogram with % block values of 0.90 %, 1.83 % and 3.99 % and blockade times of 0.071 ms, 0.060 ms and 0.055 ms respectively (Figure 3.30b and Table 3.22). The scatter plot in Figure 3.31b shows a first cluster of events similar in shape to the one belonging to RNase A from Figure 3.31a while the rest of the events are distributed in a second cluster stretching across a broader % block range at blockade times below 0.100 ms. The similarity in % block

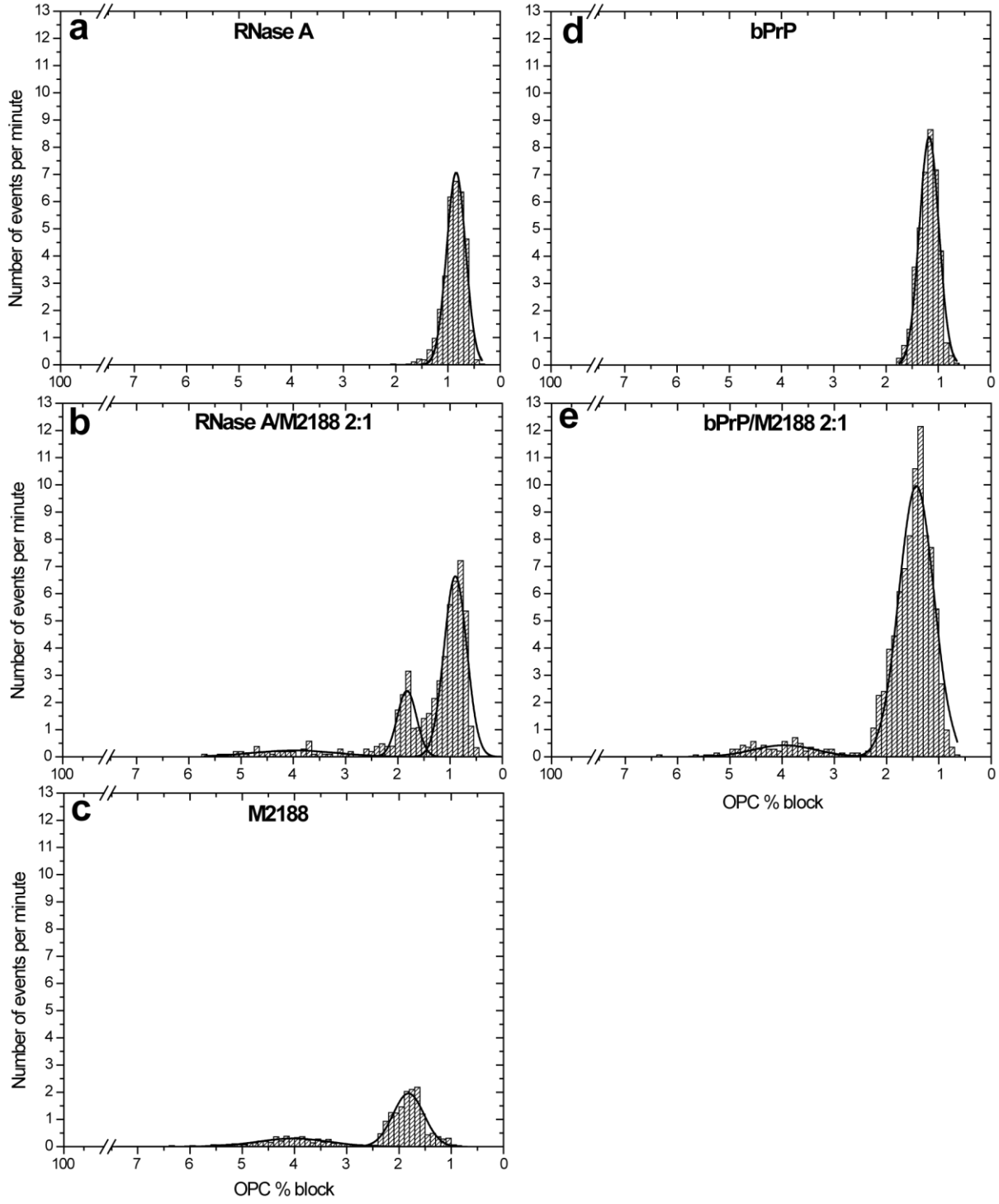

Figure 3.30. % block current histograms for RNase A, bPrP, RNase A/M2188 2:1, bPrP/M2188 2:1 and M2188 interactions with the 19 nm pore under an applied potential of 80 mV. All histograms are presented on the same scale for an easy visual comparison of the event frequencies.

Table 3.22. Event parameters for RNase A, bPrP, RNase A/M2188 2:1, bPrP/M2188 2:1 and M2188 interactions with the 19 nm pore under an applied potential of 80 mV[a].

Protein	% block (1)	% block (2)	% block (3)	T_1 (ms)	T_2 (ms)	T_3 (ms)	A_1	A_2	A_3	W_1	W_2	W_3
RNase A	0.84	-	-	0.111	-	-	32.1	-	-	0.36	-	-
bPrP	1.18	-	-	0.149	-	-	39.2	-	-	0.37	-	-
M2188	1.82	4.02	-	0.030	0.093	-	14.6	5.1	-	0.58	1.36	-
RNase A/M2188 2:1	0.90	1.83	3.99	0.071	0.060	0.055	36.1	11.2	4.8	0.42	0.32	1.65
bPrP/M2188 2:1	1.43	3.96	-	0.033	0.089	-	83.3	6.4	-	0.65	1.19	-

[a] **%block**, percentage block; **T**, blockade time; **A**, number of events per minute; **W**, peak width at half height. The subscripts 1, 2 and 3 refer to the respective population of events. (The error is estimated to be ±1% for **%block** and ±10% for **T**).

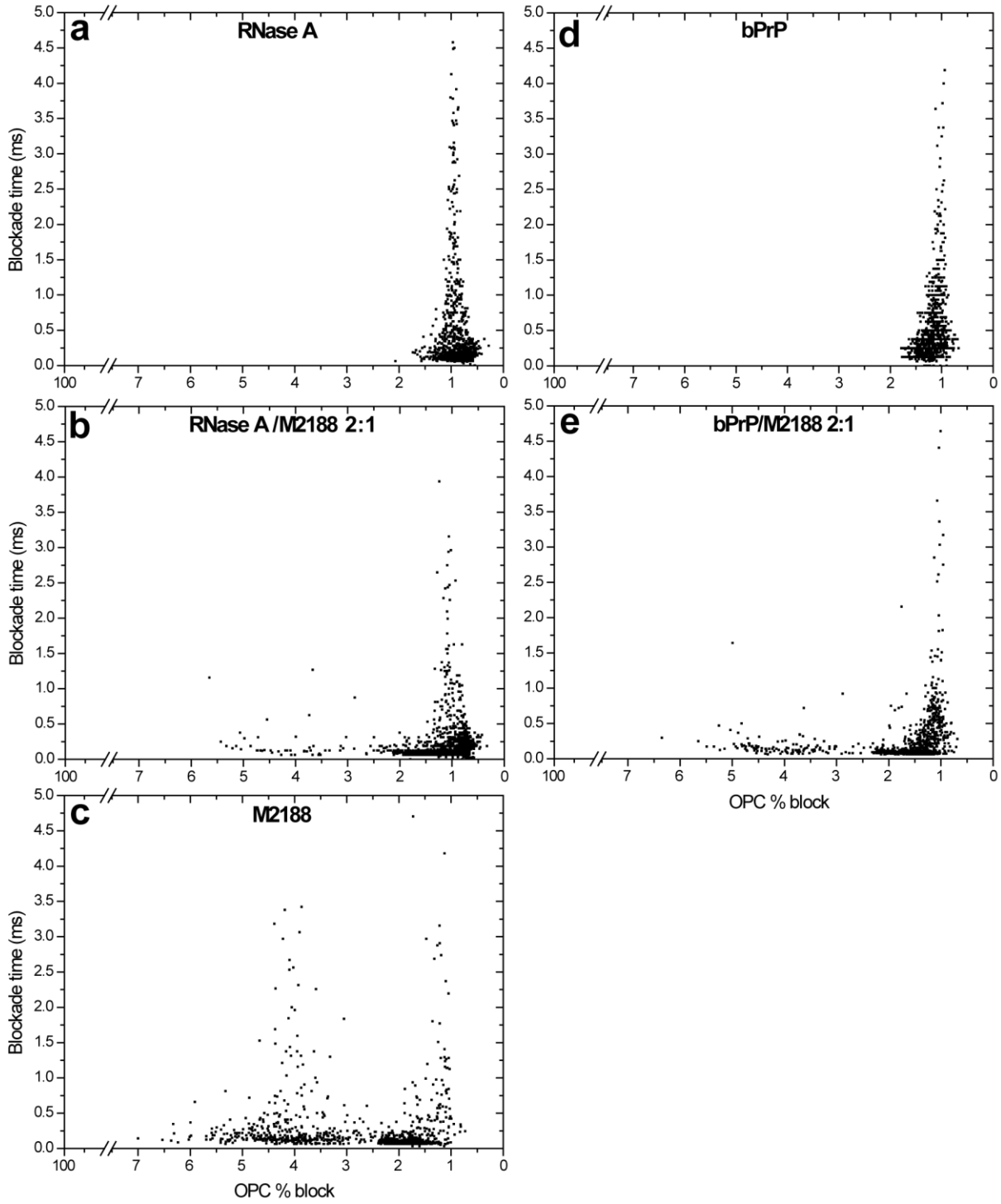

Figure 3.31. Scatter plots for RNase A, bPrP, RNase A/M2188 2:1, bPrP/M2188 2:1 and M2188 interactions with the 19 nm pore under an applied potential of 80 mV.

values of the first population of RNase A/M2188 2:1 with RNase A experiments as well as between the second and third populations of RNase A/M2188 2:1 with the two populations of M2188 strongly indicate that RNase A did not bind the M2188 antibody (Figure 3.30). This outcome is also observed, although less pronounced, in the scatter plots of Figure 3.31.

bPrP incubated with M2188 for the same amount of time and at the same molar ratio as the RNase A/M2188 experiment generates a two peak histogram with the first peak centered at 1.43 % block and the second at 4.02 % block (Figure 3.30e). The blockade times are 0.033 ms and 0.089 ms for the first and second peak respectively (Table 3.22). It must be noted here that the position and blockade time value of the second peak are extremely similar to those belonging to the second peak of M2188 (Table 3.22). The scatter plot for this molecule is presented in Figure 3.31e and is dominated by a first cluster of events similar to the one recorded for bPrP tested alone while the rest of the events are distributed along fast durations in a cluster similar in shape to the second cluster of M2188 from Figure 3.14c. Compared to bPrP and M2188 experiments there is an increase in the number of events forming the histograms as well as in the width of the first population most probably determined by the superposition of the bPrP population over the first antibody population.

Because the first population of M2188 and the population of bPrP have very close % block values, the two populations are superimposed and cannot be separately identified in the histogram.

4.0 DISCUSSION

4.1 Analysis of wild type and mutant HPr with aerolysin pores

It is clear that the two distinct populations of events in the current blockade histograms indicate two different types of interactions between the HPr proteins and the aerolysin pore. From a theoretical point of view, it is possible that both event populations could be determined by different non-translocational events. However, as for previous peptide analysis with nanopores, the simplest interpretation is that the first population of events (smaller blockade current values) is assigned to molecules that bump into the pore, diffusing away afterwards, while the second population of events (larger blockade current values) corresponds to molecules that translocate the pore. Considering that the dimensions of HPr (21 Å x 27 Å x 38 Å) are larger than the diameter of aerolysin (~14 Å), it is obvious that the protein can not translocate in its folded conformation. HPr's structural conformation and behavior in solution under an applied electric field within the confinement of the nanopore is unknown, but it is known that small globular proteins with low activation free energy of unfolding such as HPr (~5 kcal/mol) can unfold and refold spontaneously even without additional factors or assistance (Nicholson and Scholtz, 1996; Stefureac *et al.*, 2008; Movileanu, 2009).

It is important to know that the current blockade value is a measure of the pore volume from which ions are excluded as the protein molecules translocate. Thus, the current blockade depends on the dimensions of the molecule traversing the pore. Consequently, a big molecule will determine a larger current blockade than a small one. In other words, a folded molecule will exclude more ions from the nanopore than an unfolded molecule. As far as the translocation time is concerned, an unfolded structure will need a longer time to translocate than the folded structure if no interactions between the protein and the amino acids lining the inside walls of the pore occur.

On one hand, the results indicate that wtHPr translocates the aerolysin pore in a more folded conformation than the T34N mutant, determining a larger current blockade (-43 pA) and a faster translocation time (0.19 ms). Furthermore, the disrupted structure of T34N allows the

mutant to unfold to a greater extent than the wild type protein, generating a smaller current blockade (-39 pA) and a longer translocation time (0.23 ms). The difference in the number of translocations between wtHPr and T34N mutant most probably is a consequence of the mutant's disrupted structure which makes the molecule more prone for bumping than translocation. Since both wtHPr and T34N have no net charge, they are mostly diffusion-driven towards the nanopore and thus a disrupted structure is more difficult to orient for translocation than a compact structure. On the other hand, the similar $\mathbf{I}_1$ values recorded for all three HPr variants represent a good indication that the first populations of events are determined by collisions with the pore.

The S46D mutant has a structure very similar to that of the wtHPr which is confirmed by comparable $\mathbf{I}_2$ values, yet it generated the highest number of translocations of all three molecules. This is likely due to the net negative charge that this molecule carries which facilitates its electrophoretic rather than diffusional transport to the pore. The long translocation time of S46D (similar to T34N) as opposed to the wtHPr may seem surprising at first but it is to be expected if we consider aerolysin's preference for cation transport (aerolysin has a net charge of -52e) (Pastoriza-Gallego *et al.*, 2011). The results for S46D show that the protein is transported towards the pore entrance faster than the wtHPr and T34N, while its transit through aerolysin is retarded by the repulsive interactions between the protein and the amino acid side chains lining the inside walls of the pore.

To determine the effect that the pore structure exerts on the interaction parameters of the proteins, the aerolysin results must be discussed in comparison to the results previously obtained with the α-hemolysin pore which are presented in Figure 4.1 and summarized in Table 4.1 for easier reference. It can be observed clearly that the proteins interact with the two nanopores very differently (Figure 3.3 and Table 3.1; Figure 4.1 and Table 4.1). First, for aerolysin all three proteins generated fewer events at high blockade currents, suggesting that it is more difficult to translocate through the aerolysin pore compared to α-hemolysin. Second, for α-hemolysin the value of $\mathbf{I}_2$ was lowest for S46D whereas for aerolysin the lowest value is for T34N. Third, the peak widths at half height are much less variable for aerolysin compared to α-hemolysin. Fourth, the translocation times through α-hemolysin were faster than through aerolysin, correlating well with the preference of the pores for anions or cations respectively.

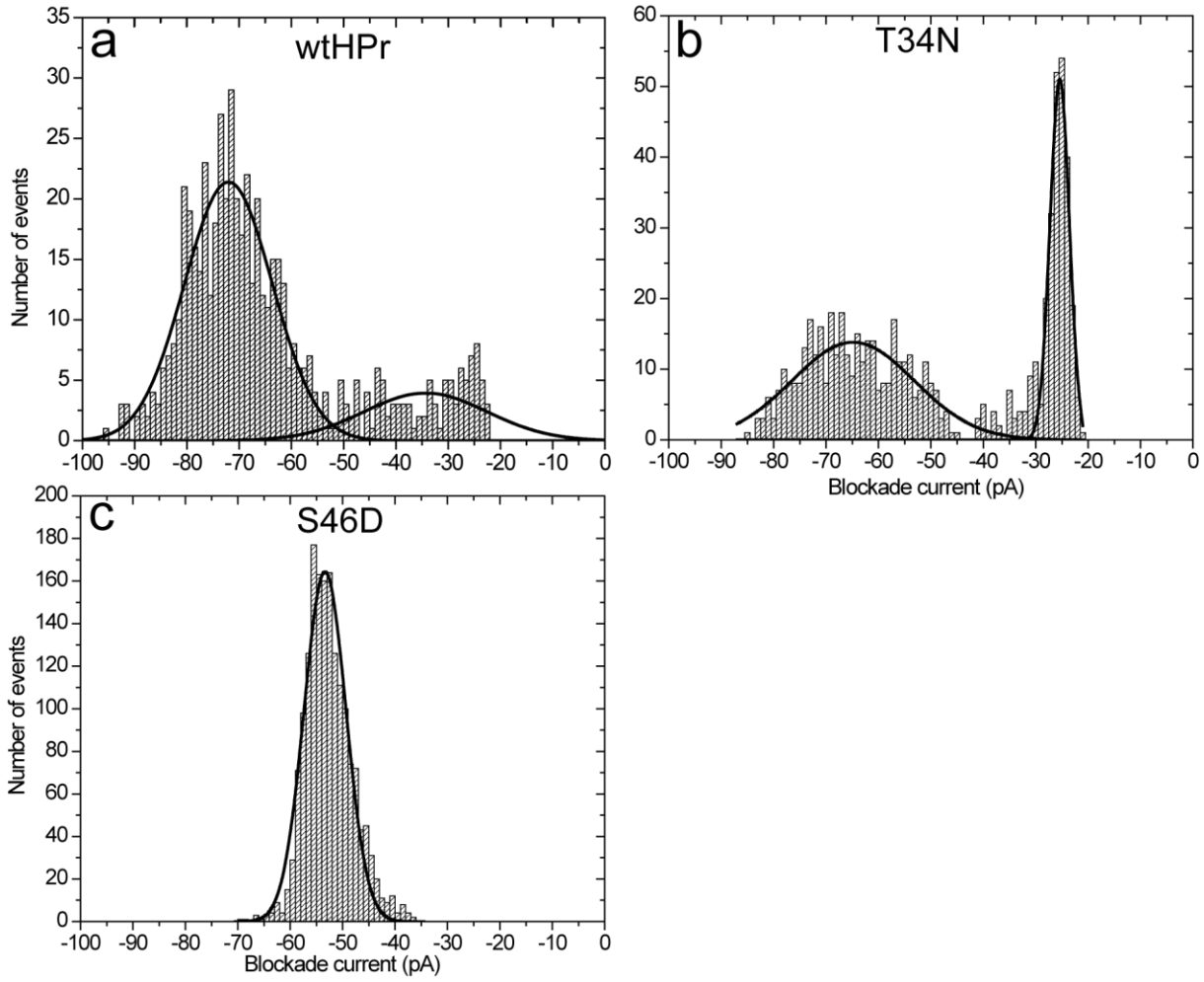

Figure 4.1. Histograms of the blockade current values determined by the interactions of wtHPr, T34N and S46D mutants with α-hemolysin. The peak current values were obtained by fitting the event populations with the Gaussian function.

Table 4.1. Interaction parameters of the wtHPr together with the T34N and S46D mutants with the α-hemolysin pores[a].

Compound	I_1 (pA)	I_2 (pA)	T_1 (ms)	T_2 (ms)	A_1	A_2	A_2/A_1	W_1	W_2
wtHPr	-34	-72	0.65	0.10	116	454	3.9	23.5	16.7
T34N	-25	-65	0.80	0.14	234	403	1.7	3.4	23.3
S46D		-53		0.11		1701			8.0

[a] $\mathbf{I}_1$, $\mathbf{I}_2$, $\mathbf{T}_1$ and $\mathbf{T}_2$ represent the intensities and the durations of the current blockades of the respective event populations presented in Figure 2. The number of events ($\mathbf{A}_1$ and $\mathbf{A}_2$) forming the populations and their widths at half their heights ($\mathbf{W}_1$ and $\mathbf{W}_2$) are also presented here. (The error is estimated to be ±1 pA for **I** and ±10% for **T**).

The reduction in the proportion of translocation events for aerolysin compared to α-hemolysin was also observed for a series of α-helical peptides and is attributed to the presence of the vestibule domain of α-hemolysin which is absent in aerolysin (Stefureac *et al.*, 2006). Upon entering the vestibule, a more hydrophobic environment is created which favours the unfolding of the protein and its subsequent translocation. This process is enhanced when a protein is driven into the vestibule by a negative charge as is the case with S46D. In comparison, for translocation through aerolysin a protein would have to interact in a rather precise orientation to allow simultaneous unfolding and translocation (Figure 4.2). Thus for aerolysin the proportion of translocation events is reduced.

In conclusion, we have shown that small proteins can translocate aerolysin pores by unfolding and single mutations are sufficient to alter the event profile. Either the mutants must unfold differently or they must interact with the pore differently from the wtHPr. More importantly, the anatomy and net charge of the pores are crucial factors which affect the translocation parameters of the analytes.

The ultimate goal of the nanopore technology is to be able to provide sequence and structure information for single molecules. Sequencing of proteins may be very challenging because single amino acids cannot be detected directly. However, single amino acid substitutions do cause structural changes which are readily detected by this technology.

4.2 Analysis of insulin with α-hemolysin pores in the presence of TCEP

The size of the monomeric insulin molecule (31 Å x 18 Å x 27 Å) is too large to permit its transit through the α-hemolysin nanopore (limiting diameter of 15 Å) and unlike HPr, insulin cannot unfold to translocate due to the presence of the disulfide bonds which enforce its quaternary structure. As a result, insulin can only collide with the *cis* end of the nanopore and then diffuses away. These collisions are responsible for generating the events forming the low current blockade population with faster blockade durations in Figure 3.5a. However, the extended amino acid strands of chain B or the short α-helical segments of chain A may also partially and temporarily enter the nanopore without translocating, giving rise to larger current blockades than the simple collisions. This type of interaction supports the wide distribution of events obtained for the insulin experiments.

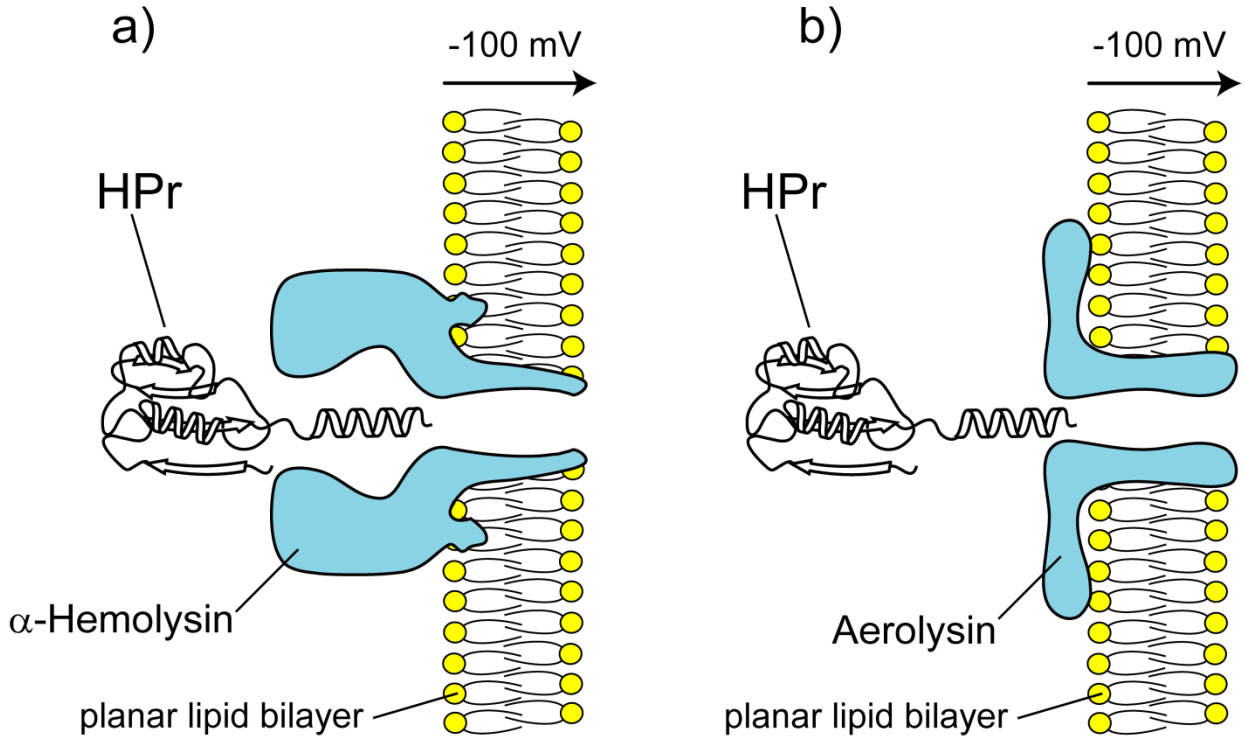

Figure 4.2. Cartoon of α-hemolysin (panel a) and aerolysin (panel b) nanopores inserted into lipid bilayers with HPr proteins unfolding for translocation. The funnel-shaped vestibule domain of α-hemolysin facilitates the unfolding and translocation process. Molecules must adopt precise orientations to transit the aerolysin pore.

The net separation of the peaks in Figure 3.5b is an indication of the fact that the disulphide bonds have been cleaved by TCEP. After TCEP's reducing action, the two component peptide chains of insulin are separated and can translocate easier than the bulky insulin which explains the increase in the number of events as opposed to the low total number of events generated by the large insulin molecule. The complete separation of the two insulin strands by TCEP was also confirmed in an SDS-PAGE experiment (Figure 4.3). Due to its small size (2.5 kD), chain A was difficult to capture on the gel but it is visible both as a cleavage product of insulin and better as a pure solution used as a control.

Our previous experiments with α-helical peptides of different lengths indicated blockade current values ranging from -62 pA to -78 pA for α-helices of 14 to 26 amino acids (Stefureac *et al.*, 2006). Since insulin's chain A is 21 amino acids long with two short helices at the ends and chain B is 30 amino acids long with a three-turn central helix, it was initially expected that upon disulphide bond cleavage of insulin two translocation peaks (one for each insulin chain) would become visible. As it can be seen in Figure 3.5b this was not confirmed. There were two possible explanations for this situation. On one hand, the low aqueous solubility of chain B can cause its precipitation and so, the only molecule transiting the pore following disulfide bond cleavage would be chain A. On the other hand, the two separated chains may adopt different structures in solution but might cause similar blockade current values. For this scenario two superimposed translocation populations would be generated and impossible to distinguish.

To elucidate this issue, the two insulin chains were analyzed separately. The low number of translocation events generated by chain B and the similar $\mathbf{I}_2$ values of chain A and of the cleaved insulin (75 pA and 76 pA respectively) both supported the former explanation and proved that chain A translocation was in fact responsible for the second peak of the cleaved insulin histogram (Figure 3.5b, Table 3.2). Furthermore, the blockade current values were in the range expected for α-helical peptides of this length (Stefureac *et al.*, 2006).

The nanopore analysis of the two individual insulin chains also suggested that minor modifications in their net charges determined major differences in their blockade durations. The insulin chains used for the control experiments were ordered from Sigma-Aldrich and contained the thiol groups (-SH) of the cysteines oxidized to sulfonic groups ($-SO_3^-$). This modified the net charge of the chains from -2e to -6e for chain A and from 0 to -2e for chain B compared to the chains resulting from TCEP cleavage of insulin. The increase in electronegativity of chainA

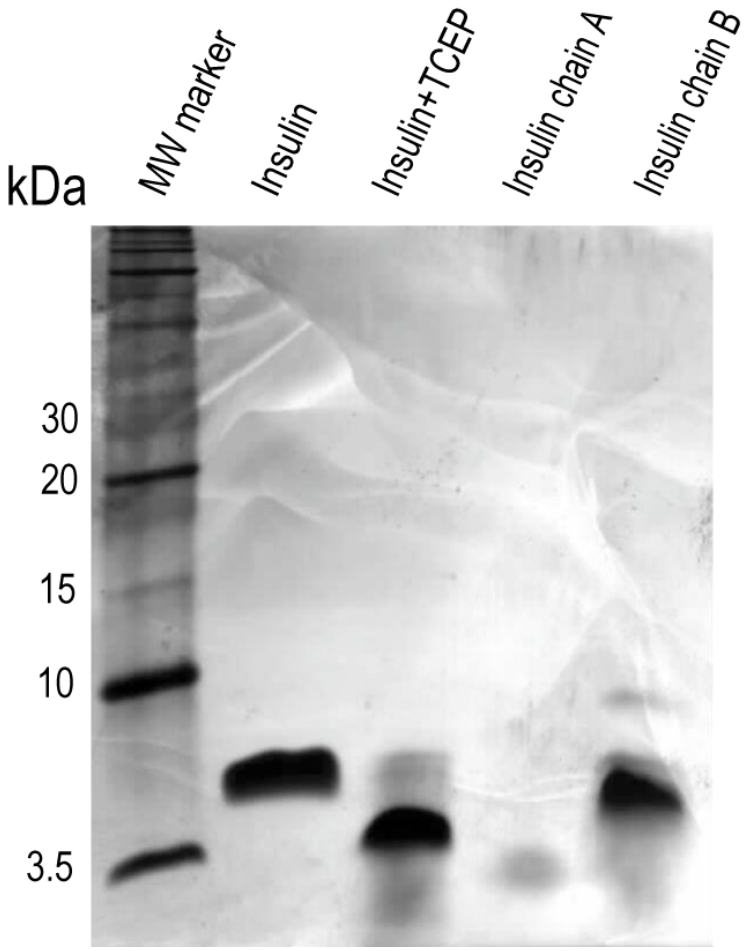

Figure 4.3. SDS-PAGE gel confirming the separation of the two insulin chains by the reducing agent TCEP. Separate samples of insulin chain A and chain B served as controls.

explains its fast translocation time (0.08 ms) compared to the translocation time of the TCEP cleaved chain (0.27 ms) (Table 3.2) as the molecules are dragged through the nanopore by the electric field faster. Although the control chain B is negatively-charged, its tendency for aggregation likely account for the small number of translocations present in the current blockade histogram as well as the long $\mathbf{T}_1$ and $\mathbf{T}_2$ values.

In conclusion, the experiments presented above showed that protein structural modifications determined by the cleavage of disulphide bonds can be studied with the nanopore method of analysis and changes in the net charge of polypeptides are reflected in their translocation parameters.

4.3 The alternating current effect on peptide interaction with α-hemolysin

As a starting point to understand the alternating current results, previous work on the electric dichroism of proteins and DNA has demonstrated that an electric field of 10 kV/cm is sufficient to align polarized molecules (Ding *et al.*, 1972; Hogan *et al.*, 1978; Antosiewicz and Porschke, 1995). In our work, the α-hemolysin pore has dimensions at the opening to the pore of about 2 nm so that an applied AC voltage of 200 mV results in a transient field of at least 100 kV/cm in this region. As well, the correlation times of molecules of this size are estimated to be about 600 MHz (Larsen et al, 2003). Thus, it is entirely reasonable that the motion of peptides can be modified by the fields used in this work. A simple working hypothesis for the behaviour of the A10 peptide can be constructed as follows (Figure 3.7B). In the absence of an AC voltage, the peptide, due to its dipole moment, is oriented in the DC electric field such that the axis of the peptide is aligned with the axis of the lumen of the pore. Thus, translocation is favored. In an AC field, the peptide may rotate so that it can no longer enter the constriction of the pore and a bumping event will be the result. As the AC frequency increases, there is an increased probability that the peptide will adopt an orientation that is incompatible with translocation. The translocation time of the peptide is in the ms range so that rotation of the peptide may occur many times as it approaches the lumen of the pore.

For CY12(-)T2 there are two translocation peaks in the absence of the AC field. We propose that the peak at -53 pA is due to a linear conformation of the peptide which has no formal dipole. Thus, it is not affected by the AC field and maintains its position at all AC frequencies. In contrast the peak at – 47 pA is due to a conformation which has a dipole and thus, in an AC

field, translocation events are less favored. It should be noted that even DNA which has no permanent dipole can be oriented in electric fields due to anisotropic ion flow which, in turn, creates an asymmetric ion atmosphere around the DNA (Tsoulou *et al.*, 2001). However, anisotropic ion flow requires μs (i.e kHz frequencies) to become established and so the MHz frequencies of these studies are probably too fast to induce a dipole moment in the peptides.

In summary, we have shown that nanopore analysis can be performed in the presence of an applied MHz AC field. Translocation of peptides with a permanent dipole moment is inhibited whereas peptides with no dipole moment are less affected. These results have important implications for understanding the transportation of polymers through pores and may allow the development of biosensors which can discriminate different molecules based on differences in dipole moment.

4.4 Nanopore analysis of the folding of Zn-fingers

The folded structures of Zif268 and FSD-1 have dimensions of about 2 nm x 2 nm x 1.2 nm which is larger than the 1.5 nm diameter of the α-hemolysin pore and, thus, translocation should be inhibited. Conversely, in the absence of metal ions the Zif268 peptide is unfolded and can freely translocate the α-hemolysin pore. (Figure 4.4). That is why the folded finger only gives rise to bumping events whereas in the unfolded state translocation events predominate. Although smaller than HPr in size, the folded finger cannot be unfolded by the applied electric potential to translocate because its free energy of unfolding is larger than that of HPr (16 kcal/mol versus 5 kcal/mol respectively) (Krizek *et al.*, 1993). Thus, the Zn-finger motif is more tightly-folded and cannot thread through the pore. Similarly, the large maltose binding protein from *E. coli* (370 amino acids) only translocates after denaturation with guanadinium hydrochloride (Oukhaled *et al.*, 2007).

Previous studies with FSD-1 have shown that the folding is weakly cooperative with a melting temperature of 42 ^{o}C (Dahiyat and Mayo, 1997). Thus at 20 ^{o}C it should be mostly folded and generate a high number of bumping events. This hypothesis is indeed experimentally confirmed (Figure 3.9d).

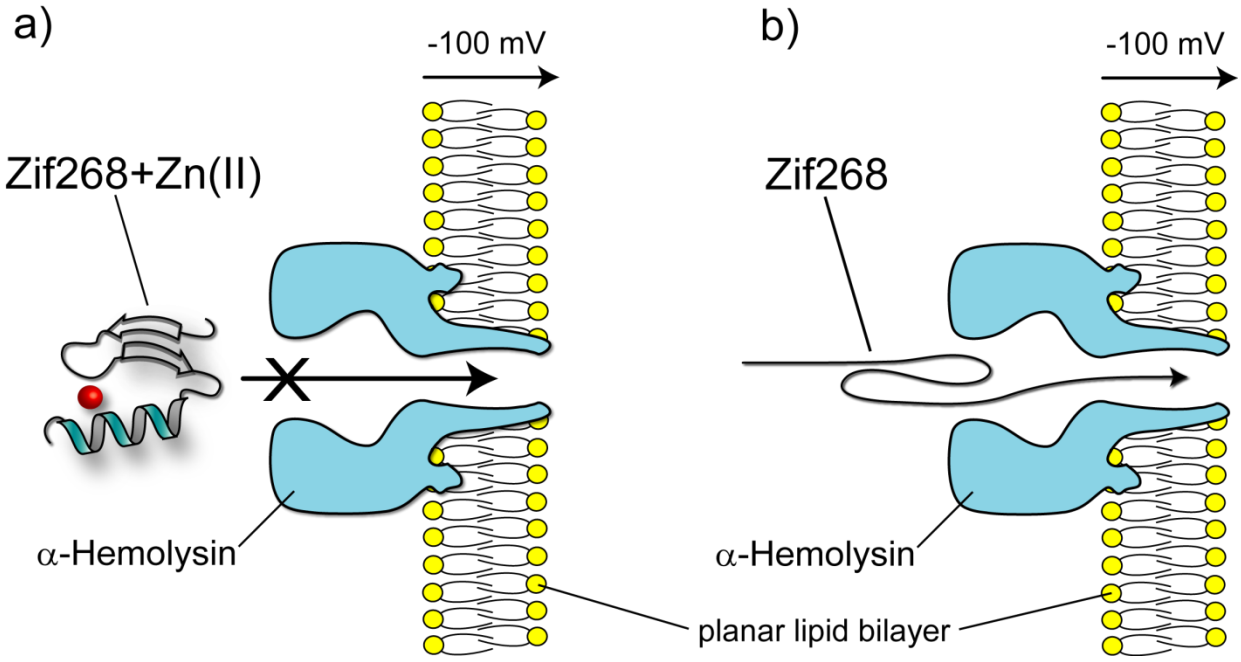

Figure 4.4. Cartoon illustrating the conformational effect of metal ion binding to a Zn-finger peptide as detected by nanopore sensing. Upon Zn(II) binding, Zif268 adopts the Zn-finger structural motif which is too large to translocate the α-hemolysin nanopore inserted into a lipid bilayer (panel a). In the absence of Zn(II), Zif268 is unfolded and is able to transit the nanopore (panel b).

The high affinity for Zn(II) of Zif268 is highlighted in the two control experiments conducted in the presence of Mg(II) and Co(II) by a low bumping-to-translocation event ratio similar to that of Zif268 in the absence of Zn(II).

One limitation of this method is that it is very difficult to estimate the metal ion dissociation constant (K_d) because the relationship between number of events and concentration of a particular conformation is unknown. For example the rate of diffusion to the pore will be different for folded and unfolded molecules which will alter their effective concentrations. As well, even in the absence of Zn(II) the unfolded peptide gives rise to a significant number of bumping events which cannot be distinguished from bumping events by folded molecules.

In conclusion, we have demonstrated that the Zn(II)-induced folding of a small protein can be studied by nanopore analysis. These studies highlight the advantages of using a single molecule technique for investigating protein folding. Finally, similar techniques may be applicable to other small proteins such as calmodulin, α-synuclein or prions whose folding is influenced by metal ions (Chiti and Dobson, 2006; Binolfi *et al.*, 2006).

4.5 Nanopore analysis of the interaction of metal ions with prion peptides

Nanopore analysis has obvious advantages for studying conformational changes because each molecule in the sample is interrogated individually. Thus, several conformations in the same sample can be analyzed simultaneously as long as each gives rise to distinct event parameters, namely the blockade current (**I**), width at half height (**W**), and blockade time (**T**). In general, small changes to the value of **I** are difficult to interpret because it is a measure of the number of ions occluded from the pore. Thus, it depends not only on the conformation of the molecule but also on the number of ions carried by the molecule. The value of **W** is a measure of the conformational flexibility of the molecule. For example, the PrP106–126–Cu(II) complex (Figure 3.15) gives a very sharp bumping peak, suggesting that the complex adopts a single, rigid structure. On the other hand, the bumping peak for Octa2 broadens with increasing Cu(II), suggesting that multiple conformations can exist.

The value of 1/**T** can be interpreted as the dissociation rate constant, k_{off} (Gu *et al.* 2001), for the interaction of the molecule with the pore. For example, $\mathbf{T}_1$ for Octa2 increases significantly on binding Cu(II) so that the dissociation of the complex from the vicinity of the pore is much slower, which could be caused by a change in the rate of diffusion or in the

interaction with the pore. Since there is no evidence for significant aggregation that would change the rate of diffusion, it would appear that the metal complex binds more tightly to the pore. Comparison of the $\mathbf{T}_2$ values for Octa2 and Octa4 is also instructive. For Octa2, $\mathbf{T}_2$ increases on binding Cu(II); for Octa4, $\mathbf{T}_2$ decreases on complex formation. One interpretation is that the individual octarepeats in Octa2 and Octa4 adopt different conformations that present different functional groups for interaction with the pore.

In the present case, the major change upon addition of divalent metal ions was in the ratio of bumping to translocation events as was seen previously with Zn fingers (Stefureac *et al.* 2008). Peptides or proteins with tightly bound metal ions may be unable to sufficiently unfold to thread through the pore. For Octa2, the addition of excess Cu(II) causes the appearance of bumping events, but translocations still predominate. Thus, it seems likely that the folded Octa2–Cu(II) complex is not sufficiently bulky to prevent passage through the pore. This view is supported by the observation that the translocation parameters are different in the presence of Cu(II); $\mathbf{T}_2$ increases several fold and $\mathbf{I}_2$ increases by more than 10 pA (Table 3.6). In principle, the values of $\mathbf{A}_1$ and $\mathbf{A}_2$ could be used to calculate an equilibrium constant, but in practice this becomes difficult when the complex also translocates and the peaks overlap. We have shown previously that both folded α-helical or β-sheet hairpins can translocate readily (Madampage, 2011). The proposed structure of the Octa2–Cu(II) complex consists of a simple, linear, two-stranded fold around the Cu(II) ions and thus translocation is not unexpected (Millhauser, 2004; Gaggelli *et al.*, 2006). Similar observations can be made for the Octa4–Cu(II) complex, since even at the highest Cu(II) concentration a significant proportion of translocation events were still observed (Table 3.7). Alternatively, the binding of Cu(II) is not tight enough to maintain the folded conformation during interaction with the pore. On the other hand, the behaviour of PrP106–126 is different, since the majority of the complex with both Zn(II) and Cu(II) cannot translocate. A previous NMR and EPR study proposed that the Cu(II) complex involved the imadazole and ionized amide groups of His111 together with functional groups from both the N- and C-termini to give an overall double fold that may indeed be too large to translocate (Gaggelli *et al.*, 2005). In contrast, they found no interaction with Zn(II), but the experiments were performed at pH 5.7 (in contrast to pH 7.8), which may be too low for Zn(II) to deprotonate the amide group. They also reported a complex with Mn(II), although we could find no evidence for this in our experiments with PrP106–126.

In order to test if metal ion binding to the full prion protein can be detected by this methodology, a nanopore sensing investigation of the effect of metal ions on full-length recombinant bovine PrP^{C} (BrecPrP) was conducted in our lab by Claudia Madampage (Stefureac *et al.*, 2010). The results indicated that BrecPrP formed complexes both with Cu(II) and Zn(II). Moreover, the formation of these metal complexes was readily reversed by the addition of EDTA which acts as a metal ion scavenger.

In conclusion, we have demonstrated that nanopore analysis can be useful for interpreting conformational changes of peptides caused by the concentration-dependent binding of metal ions. Since these experiments can be performed at very low peptide concentrations, aggregation or precipitation of the peptides is much less likely to occur and does not interfere. This set of experiments together with the detection of metal ion binding to full-length BrecPrP suggested that nanopore sensing could be used to study drugs or peptides binding to PrP^{C} that may cause conformational changes leading to the prevention of conversion to PrP^{Sc}. Similarly, if the PrP is bound to an antibody, then translocation will be inhibited so that antibody discrimination of PrP^{C} and PrP^{Sc} or other conformations can be analyzed and the nanopore analysis method could be further developed into a real-time live prion detector.

4.6 Analysis of protein molecules using solid-state nanopores

4.6.1 Working with the solid-state nanopores

Despite the high expectations, working with the solid-state pores proved to be a difficult and often frustrating task. During the experimentation it was found that the operating life of the Si_xN_y pores ranged between 2-7 days depending on the applied potentials used and on the net charge of the molecules analyzed. Applied potentials above 200 mV and molecules with net positive charges proved to shorten the life span of the pores which usually became partially and irreversibly blocked prohibiting the detection of new analytes. Initially, it was suspected that one of the positively-charged protein molecules might have plugged the pore by adhering to its negatively-charged walls and so reversal of the applied potential temporarily solved the problem. Unfortunately, this behaviour became more and more frequent from that moment on until it finally resulted in a permanent block of the nanopore.

To correct this problem and revive the nanopores several approaches have been tested. Unmounting and recleaning with Piranha solution ($3H_2SO_4$:$1H_2O_2$) followed by remounting on the experimental setup did not prove successful. Soaking in a concentrated ethanol solution overnight as well as in acidic (pH 2.0-5.4) buffer solutions failed to unblock the nanopores. Furthermore, the addition of a 1 mg/mL solution of proteinase K in the presence of 3 mM Ca^{2+} in a pH 10.0 buffer that was expected to digest the eventual protein molecule blocking the pore was unsuccessful. The pH 10.0 value was chosen to render proteinase K negatively charged and thus to avoid its own binding to the nanopore walls which in turn would have caused permanent blockage of the nanopores. Ultimately, treatment of the blocked nanopores with oxygen plasma (100 W) for 30-45 seconds failed as well. Regardless of the above efforts, the blocked state of the solid-state nanopores could not be reversed so that they proved to be essentially single-use devices.

4.6.2 Solid-state nanopore analysis of maltose binding protein, calmodulin and HPr

Theoretically, the drop in blockade current generated by a molecule passing through an electrolyte-filled pore should be proportional to the volume of the electrolyte being displaced by the translocating molecule (Coulter, 1953). Thus, it is expected that the translocation of a molecule with a given folded structure on a given pore will generate the same % block at all applied voltages. Another strong indication for translocation driven by electrophoresis is that the blockade durations should decrease with increasing voltages. In contrast, non-translocational interactions or bumping with the nanopore may result in % blocks that will vary widely with the applied voltages. Intuitively, a large molecule will displace a larger volume of electrolyte from the pore than a smaller molecule and so it will generate a larger blockade current. Based on this principle of detection it is possible to distinguish the translocation of different molecules and even identify particular levels of folding of the same molecule. Therefore, it is important to calculate the volumes of the molecules to be analyzed as well as the volumes of the pores to be used for the analysis. These volumes are summarized in Tables 3.10 and 3.11. The minimum % block for a particular molecule can be calculated based on these numbers once the open pore currents have been identified. The actual % block is expected to be larger than this value due to the hydration shell around the protein which has been estimated to be between 0.5 and 1.0 nm (Ebbinghaus *et al.*, 2007). Since the hydration shell

carries bound ions of both charges, it will reduce the effective current and increase the effective volume of the protein. We have chosen an intermediate value of 0.7 nm for the increased radius of the hydration shell (Table 3.11) and used this to estimate the % current block.

4.6.2.1 Translocation or bumping

For MBP, the distinguishable populations give % blocks which decrease with increasing voltage and event durations which are roughly constant. Thus, there is no evidence for translocation through either pore at any voltage. The largest dimension of the folded, MBP molecule is 6.5 nm (assuming no water shell) and so it presumably bumps into the conical entrance of the pore before quickly diffusing away. The two distinct populations of events at 50 and 100 mV may correspond to interaction of the protein with the pore in different orientations.

For CaM with the 7 nm pore, a population could be distinguished with a constant % block of about 13% and decreasing event durations as the voltage was increased. The % block can also be calculated from the volume of the pore which is occluded by the protein (DeBlois and Bean, 1970). The calculated % block of 13.6% is in good agreement with the measured value. These putative translocation events represent 37% and 28% of the total at 100 and 200 mV respectively. Presumably, translocations also occur at 50 mV but they cannot be distinguished from the bumping events having the same parameters.

For HPr with the 7 nm pore, the majority of the events are consistent with translocation since the % block is constant at about 7.3% and the event duration decreases as the voltage increases. The expected % block is estimated to be about 7.0%, or about half that of CaM which is twice the volume, again in excellent agreement with the measured values. For the 5 nm pore, a small population of events was also consistent with translocation with a % block of about 11% and an estimated block of about 13%.

4.6.2.2 Folded or unfolded protein translocations

The second question to be answered regards the folding state of the translocating proteins. Translocation of completely unfolded protein molecules longer than 15 nm (the pore thickness) should generate similar % block values at the same applied voltage. As previously reported, for a completely unfolded linear peptide, on average each amino acid contributes 0.38 nm to the

length of the polypeptide chain which equals about 39 amino acids that can fit inside the 15 nm thick pore (Talaga and Li, 2009). The maximum volume of electrolyte displaced by the unfolded protein segment residing inside the nanopores is smaller than the volume displaced by the same protein when folded. Figure 4.5 illustrates the dimensions of completely unfolded MBP, CaM and HPr as they relate to the length of the nanopores. Thus, for a linear unfolded protein the % block would be expected to be similar for CaM and HPr. However, the magnitude of the % block for translocating CaM is about twice that for HPr and in both cases it agrees well with the calculated values expected for folded molecules.

Experiments performed with HPr in the presence of denaturants with the 7 nm pore further confirm that the translocation events witnessed for CaM and HPr are indeed generated by the passing of folded protein molecules. The conformational state of HPr in a buffer solution containing 8 M urea is completely unfolded (Talaga and Li, 2009). Based on the excluded volume, the % block generated by the passage of such a molecule should have a value of about 0.95 % which translates into a blockade current of 23 pA. Because the noise (width) of the open pore current trace is roughly 100 pA, such small current blockades cannot be resolved. The current trace for this experiment (Figure 3.20d) shows no current blockades although HPr was present but in an unfolded conformation.

In conclusion, the evidence presented above indicates that protein molecules which have dimensions similar to, or larger than the pore do not translocate. However, smaller proteins can apparently translocate and do so in a folded conformation.

4.6.3 Analysis of bPrP(25-242) interaction with monoclonal antibody M2188

The experiments performed with MBP, CaM and HPr have confirmed that solid-state pores are sensitive enough to distinguish between protein molecules of different dimensions and most importantly have shown that these molecules translocate the solid-state pores in a folded conformation. These results represent crucial preliminary steps towards the development of the prion detector and indicate that the prion protein together with aggregates of different sizes could be individually identified from a mixture in solution in a similar way.

To interpret the results obtained during the study of bPrP and M2188 antibody with the 11 nm and 19 nm pores, the same principles of analysis as presented in Chapter 4.6 were used. The basic rules taking into account the applied voltage, the volume of the nanopore and of the

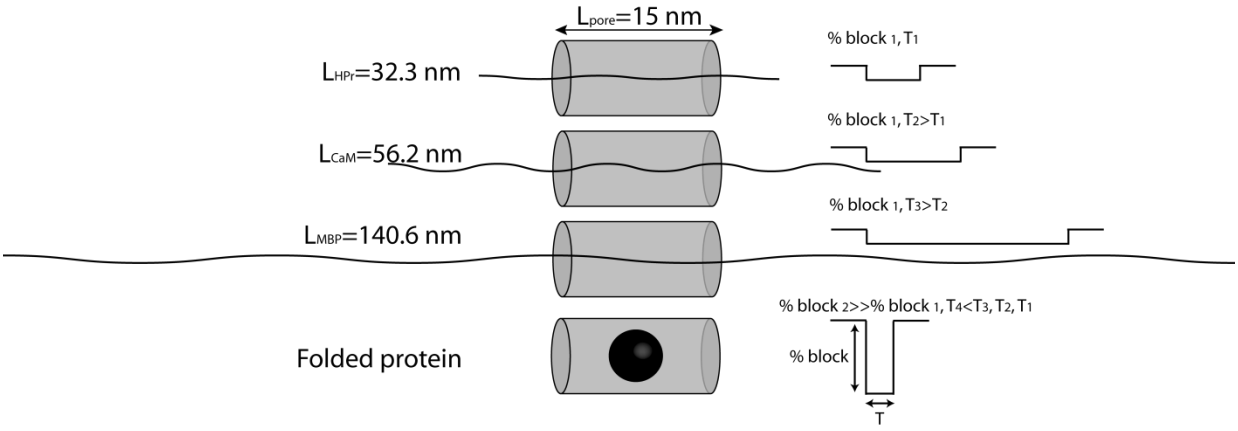

Figure 4.5. Cartoon comparing the translocation signatures of completely unfolded proteins versus a folded protein through a solid-state nanopore. If the completely unfolded proteins are longer than the pore, the % block should stay the same while the blockade time should increase proportional to their length (% $block_1$ stays constant for all unfolded proteins and $\mathbf{T}_1<\mathbf{T}_2<\mathbf{T}_3$). However, this is not observed. Translocation of a folded protein will determine a much larger % block and a more rapid blockade time than the unfolded proteins (% $block_2$>>% $block_1$ and $\mathbf{T}_4<\mathbf{T}_3$, $\mathbf{T}_2$, $\mathbf{T}_1$).

molecule tested and their effect on the magnitude and duration of the open pore current blockade are essential in understanding the intimacy of the protein/pore and protein/protein interaction process.

4.6.3.1 The 11 nm pore

The presence of the two well-defined populations of events for bPrP interaction with the 11 nm pore was unexpected since the recombinant bPrP used in this study is a globular protein with dimensions of 4.4 x 2.8 x 2.7 nm and a volume of 54.3 nm^3 if a 0.7 nm-thick water shell is taken into account (Table 3.17). Considering the largest dimension of bPrP molecule is 4.4 nm and the pore diameter is 11 nm it was expected for this molecule to freely translocate generating only one population of events. As Figure 3.27 shows, this was not the case. However, similar results were obtained by Talaga and Li for the interaction of β-lactoglobulin with an 8 nm Si_xN_y pore (Talaga and Li, 2009). The presence of two populations of events could have been caused by an irregular morphology of the pore entrance that appeared during pore fabrication and/or by electrostatic interactions between the positively charged bPrP molecules and the negatively charged walls of the pore (Talaga and Li, 2009; Niedzwiecki 2011).

From a theoretical point of view, a molecule such as bPrP should generate a % block of about 3.8 % during translocation through the 11 nm pore. This value is very similar to the values of 4.1 %, 4.3 % and 4.5 % observed for the higher % blockade populations under 150 mV, 100 mV and 75 mV potentials respectively (Table 3.19) pointing out that the events forming this population may constitute translocations. The fact that the number of events forming this population increase with the increasing voltage while the blockade duration values decrease with increasing voltage represents the final proof that these populations of events are generated by translocating bPrP molecules. This is not observed for the lower % blockade populations which have roughly constant and generally much faster blockade durations indicative of non-translocational interactions with the nanopore or bumpings.

For the M2188 antibody, it is difficult to establish if the higher % block population is formed by translocating or non-translocating molecules since only one voltage was investigated. One thing that can be stated is that depending on its hydration level, M2188 could cause % block values from 14.8 % (unhydrated) to 30.6 % (0.7 nm hydration shell) and above

while translocating the pore. The observed % block value of 16.9 % shown in Table 3.19 for the second population of events is well within this range and could be attributed to translocations but the largest dimension of M2188 (14.5 nm) compared to the pore diameter of 11 nm makes this outcome very unlikely. Considering the Y-shaped structure of the antibody, the large current blockades generated by this molecule most probably belong to a type of non-translocational interaction called intercalation. In this type of interaction, one arm of the antibody molecule that fits the pore diameter enters the pore to a point where its incipient translocation is stopped by the bulk of the molecule left outside the pore. Since it cannot continue the translocation the antibody diffuses backwards and exits the pore on the same side it entered. Such interactions have durations that usually increase with the applied potential as decribed by Christensen *et al.* for the interaction of multiply-branched peptides with the α-hemolysin pore (Christensen *et al.*, 2011). Similarly, since the % blockade value for the first population of events (4.7 %) is much smaller than expected for a translocating molecule and the blockade time is very fast (0.030 ms) it can be concluded that the molecules are neither entering nor translocating the nanopore but only bump into it and then diffuse away.

To interpret and understand the interaction with the pore of the two protein/antibody complexes all the experimental results have to be taken into account. The first observation that can be made is that the % block histograms of the M2188 antibody and of the two bPrP/M2188 experiments are very similar in terms of peak % block values but different in the number of events detected per minute (Figure 3.27 and Figure 3.29). It must be mentioned here that each M2188 antibody can bind a maximum of two bPrP molecules. Assuming all bPrP molecules are bound to the antibody it means that for a bPrP/M2188 molar ratio of 1:1 in solution there is a mixture of three molecular species: free antibody, antibody with one bPrP molecule bound and antibody with two bPrP molecules bound (Figure 4.6). In contrast, at a molar ratio of 2:1 bPrP/M2188 there is only one molecular species in solution both binding sites of the antibody being occupied by bPrP molecules. The presence of the different species accounts for the broader distribution of the % block populations for bPrP/M2188 1:1 (Figure 3.29d, e and f) as opposed to the narrower peaks of the bPrP/M2188 2:1 experiment (Figure 3.29a, b, and c). The scatter plots also show more variation of the event distribution within the clusters for bPrP/M2188 1:1 than for bPrP/M2188 2:1 (Figure 3.28) which are very similar to the scatter plot of M2188 alone from Figure 3.28c. There is, however, one notable exception for

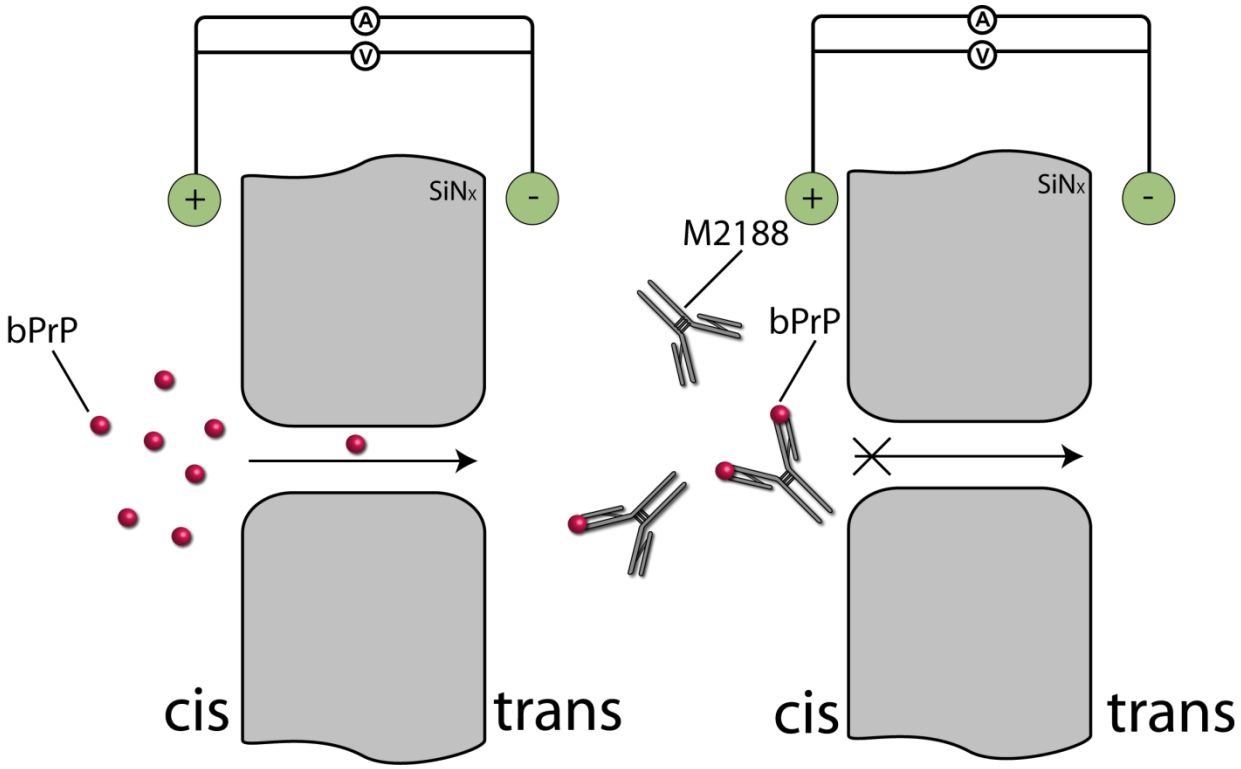

Figure 4.6. Cartoon of the interaction of bPrP, M2188 and bPrP/M2188 1:1 with the 11 nm solid-state nanopore. Free bPrP molecules are able to pass through the nanopore while neither the free M2188 antibody nor the antibody-bound bPrP molecules are able to do so due to the large volume of M2188. (Drawn approximately to scale).

bPrP/M2188 1:1 at an applied potential of 150 mV. Although the % blockade is very similar for the two bPrP/M2188 ratio experiments, bPrP/M2188 1:1 has generated more events and had a narrower population than bPrP/M2188 2:1 under 150 mV potential (Figure 3.29f). An even bigger discrepancy between this result and the other bPrP/M2188 results is observed in the scatter plot (Figure 3.28i) which shows a well-represented cluster of events with longer blockade times similar to the translocation cluster of bPrP (Figure 3.28c). Unfortunately, no definite conclusion could be drawn from this experiment since a repeat experiment was impossible after the nanopore became unusable.

The three different molecular species with different net charges present in solution for the case of the bPrP/M2188 1:1 experiment generate more events than the single molecular species of the bPrP/M2188 2:1 ratio experiment. Moreover, with each bPrP molecule binding the M2188 antibody the net charge of the complex increases by +8. The extra positive charges cause an increase in the number of events generated by the complex as opposed to the antibody alone.

The fact that both bPrP/M2188 ratios and M2188 have similar % block values is an indication that these molecules are unable to transit the nanopore. The bPrP molecules are 10 x smaller than the antibody and their binding to M2188 will not significantly affect the % block values of the antibody unless the complex is able to translocate. As observed in our experiments, complex formation identification is still possible without translocation, based on the different event frequency generated due to the extra positive charges brought in by the bPrP molecules.

The heterogeneity of the solution, due to the presence of multiple species in the bPrP/M2188 1:1 case, accounts for the irregular variation of $\mathbf{T_1}$ as each species generates characteristic blockade time values (Table 3.20). Although the $\mathbf{T_1}$ values are inconclusive, the % block values experimentally obtained for these populations are much smaller that the minimal calculated value for a translocation. Based on this consideration it can be concluded that these events represent bumpings.

Interpretation of the $\mathbf{T_1}$ values for bPrP/M2188 2:1 is a much easier task since there is only one molecular species interacting with the pore. The values are very fast and stay constant for all three voltages which is a behavior normally associated with bumping events. The roughly constant $\mathbf{T_2}$ values of both bPrP/M2188 ratio experiments do not support translocations

especially when the antibody is much larger than the diameter of the nanopore.

A clearer proof of protein/antibody complex formation is brought by comparing the scatter plots of bPrP/M2188 1:1 and 2:1 experiments done at 100 mV (Figure 3.28f and j) with the summed-up scatter plots of the individual bPrP and M2188 experiments at the same ratio and voltage (Figure 3.28g and k). Obvious differences appear in the number and position of the event clusters. The summed up scatter plots shows the events grouped in four different clusters whereas the bPrP/M2188 2:1 and 1:1 experiments revealed only two clusters. In order to highlight them, the clusters have been numbered in Figure 3.28b, c and g, k. Clusters 1 and 2 belonged to bPrP while clusters 3 and 4 belonged to M2188. All the above mentioned differences strongly support the formation of the protein/antibody complex.

In conclusion, the results have proven that bPrP/M2188 interaction at 1:1 and 2:1 molar ratios could be detected and distinguished even in the absence of the translocation of the complex through the pore. Although the individual species present in solution could not be separately identified for bPrP/M2188 1:1 experiment, the differences in the % blockade histogram characteristics and scatter plots indicated their presence. Finally, in order for the small changes in volume caused by bPrP binding to M2188 antibody to be directly reflected in the % block histograms, a pore with a diameter large enough to allow the passage of the protein/antibody complex would be needed.

4.6.3.2 The 19 nm pore

The presence of narrow single populations of events recorded for RNase A and bPrP during their analysis with the 19 nm pore confirm our initial expectations of both molecules being able to translocate freely. Furthermore, considering that the calculated volume of the hydrated RNase A molecule (with a 0.7 nm water shell) is 49.0 nm^3 (Table 3.16), it should generate a 1.15% block of the open pore current upon complete translocation. At the same time, bPrP with its hydrated volume of 54.3 nm^3 should generate a % block of 1.28 % upon translocation through this nanopore. The calculated values agree with the experimentally recorded values within the error of the hydration shell. Even though voltage studies were not performed during this set of experiments, a very strong proof for translocation is the fact that RNase A, which is a smaller molecule than bPrP, generates a smaller % block and a faster interaction time with the nanopore than bPrP. This result may seem contradictory because of bPrP's ability to generate

more events per minute than RNase A. To explain why a larger molecule generates more events with longer durations, while a smaller molecule causes less events but of shorter durations, it is necessary to consider the net charge and the volume of the two molecules as well as the different dynamics outside and inside the nanopore. In the vicinity of the nanopore, bPrP with its net charge of +8 will be transported faster towards the pore than RNase A, which has a net charge of +4. Inside the confinement of the nanopore, the larger bPrP is slowed down by the opposing drag force which is higher than the drag force encountered by the smaller RNase A molecule (Pastoriza-Gallego *et al.*, 2011).

The M2188 antibody has an unhydrated volume of 211 nm^3 which should generate a minimum % block of 4.96 % when transiting the 19 nm pore. The event populations of Figure 3.30c have % block values of 1.82 % and 4.02 % which are well below the minimum calculated % block value for translocation. This result points towards non-translocational interaction of M2188 with the 19 nm nanopore which was unexpected since the diameter of this pore should have been large enough to accommodate the transit of the antibody. The very fast blockade time of the low % block event population clearly indicates bumping of M2188 molecules into the pore whereas the high % block population is most probably formed by intercalation events similar to the ones detected for M2188 interaction with the 11 nm nanopore. The low frequency of events indicates a lower positive net charge for the antibody as compared to either bPrP or RNase A, a behavior also observed in the experiments performed on the 11 nm pore.

Assuming that RNase A and M2188 formed a complex together, there would have not been a population generated by translocating RNase A molecules. In this situation the % block histogram would have contained only two populations of events corresponding to the bumping and intercalation events of the antibody carrying the RNase A molecules with % block values similar to those of M2188. Since this was not observed, the presence of the three peaks clearly indicates that RNase A did not bind the M2188 antibody. Further support for the absence of binding is apparent by comparing the % block histograms in panels a, b and c of Figure 3.30 where it is possible to identify the population situated at 0.90 % as being caused by RNase A molecules, the population at 1.83 % corresponding to the bumping population of M2188 and the population at 3.98 % corresponding to the intercalation peak of M2188. A similar identification was also possible in the scatter plots of Figure 3.31a, b and c. From Table 3.22 it can be observed that there is very little variation in the number of events forming each

population. This variation could be caused by reciprocal pore access hindering of RNase A and M2188 molecules present together in solution due to the difference in size and charge even though the molecules do not bind to each other. In other words, the two molecules have different dynamics when present together in solution than when analyzed individually which affects their access time and interaction time with the nanopore.

A similar analysis was performed for the bPrP/M2188 2:1 experiment which was compared to the histograms of the individual bPrP and M2188 experiments. In contrast to the RNase A/M2188 2:1 experiment, here the peak % block values of the first population of events in Figure 3.30e is significantly different from the ones of M2188 and bPrP from Figure 3.30c and d suggesting the presence of a new molecular species in solution. Furthermore, the frequency of events belonging to the first population is 83.3 events per minute which is more than the sum of the event frequencies of the respective bPrP and M2188 populations, a fact that also supports the binding of bPrP to the antibody (Table 3.22). This change is also reflected in the width of the first population which increases accordingly. At the same time the second population does not change position or blockade duration but gains events indicating that intercalation continues to happen for this molecule at a higher rate. As it was reported in the experiments performed on the 11 nm pore, bPrP is not large enough to cause a change in the % block value of the intercalation peak of the complex but apparently affects the % block values of the bumping peak. On the other hand, the blockade time values of both bPrP/M2188 2:1 and M2188 populations are not significantly different (Table 3.22) which does not support bPrP/M2188 complex formation and suggests that the first population of M2188 may in fact be overlapping the event population of bPrP. Consequently, a definite decision in favor or against bPrP/M2188 complex formation cannot be made with this nanopore.

In conclusion, the experiments performed on the 11 nm pore are the first in the literature to report the detection of prion/antibody complex formation with Si_xN_y nanopores with diameters that allow the passage of the prion protein but not of the prion/antibody complex. The experiments performed on the 19 nm pore underline the importance of choosing a suitable pore size for the molecules that need to be analyzed in order to avoid inconclusive results. These results lay the foundation for the further development of the nanopore prion detector, although stable pores with larger diameters will be needed for the nanopore analysis of larger prion aggregates.

4.7 Future directions

The experiments conducted in this thesis have demonstrated that nanopore sensing can be used to study protein folding and protein-protein interaction in solution with single-molecule sensitivity. The method was able to detect conformational changes within proteins caused by point mutations, disulfide bond cleavage and binding of metal ions as well as the formation of prion-antibody complexes. These discoveries present nanopore sensing as the perfect technique to be developed into an electrophoretic prion detector that will enable real-time detection and discrimination between the normal and the infective prion proteins..

The novel AC nanopore sensing experiments of peptides with α-hemolysin show promise for the development of biosensors capable of distinguishing molecules based on differences in dipole moments. A systematical analysis of a series of α-helical peptides of increasing dipole moments is needed in order to determine the way in which the dipole moment governs their dynamics in solution and how different AC frequencies and amplitudes affect their interaction with the α-hemolysin nanopore. It would also be of interest to compare the AC behavior of the CY12(-)T1 peptide (which possesses a dipole moment) with that of CY12(-)T2. Moreover, AC field studies of peptides and proteins should be also conducted with solid-state nanopores of different dimensions. With a large solid-state nanopore in a DC field for example, two conformations of the same protein are expected to give very similar values for **I** and **T**. However, in an AC field the translocation of the conformation with the lower dipole moment will be less restrained and will enable its identification from the mix.

The solid-state nanopore experiments performed with HPr, CaM and MBP on pores of different diameters were able to distinguish between the individual proteins based on their interaction parameters with the pores. The parameters correlated well with the dimensions of the proteins showing that MBP, which is bigger than the pores, did not translocate while the smaller CaM and HPr were able to translocate in a folded conformation. However, other proteins with smaller free energies of unfolding or different structural features may behave differently. As well, other types of pores with different surface properties or different topologies may facilitate protein unfolding. The analysis of a broader panel of proteins with different types of pores is needed to fully understand protein translocation through solid-state

pores, especially since our work disagrees with the results obtained by Talaga and Li (Talaga and Li, 2009).

The experiments conducted with the prion protein have demonstrated that sensing with Si_xN_y nanopores was able to detect the formation of complexes between bPrP and the specific monoclonal antibody M2188 provided the appropriate nanopore diameter is used. This finding represents a fundamental step towards the development of an *in vivo* and real-time diagnosis of prion diseases. The prion detector will rely on solid-state nanopores engineered with specific antibodies and will be able to physically detect prion particles interacting with the antibody-coated nanopores by monitoring the blockade current and duration. Every time a prion protein will bind the antibody there will be a permanent current blockade of certain amplitude. The number of current blockades will correlate with the number of prion proteins bound, while the amplitude will indicate the degree of aggregation of each prion particle.

Although techniques based on PMCA with improved detection limits are available, they are expensive, laborious and require long times to diagnose the disease. The advantages of the nanopore prion detector are three-fold: speed of detection – the results would be available within a few hours, high specificity – conferred by bPrP specific antibodies and sensitivity – provided by the nanopore which in principle can detect a single molecule. Thus, such a real-time prion detector will be of great benefit for both the beef industry and human health by being able to detect, monitor and prevent future prion infections.

At the present time the analysis of recombinant PrP^C fibrillar aggregates of different sizes using solid-state nanopores would be the next step to take. It is expected that aggregated prion molecules will cause larger current blockades than single PrP^C molecules and so the two forms can be readily distinguished. Furthemore, the identification of the monomeric PrP^{Sc} immediately after PrP^C conversion will help elucidate the conversion mechanism and potentially identify where on the prion protein the misfolding process begins. The nanopore analysis of different species of PrP^{Sc} will prove useful to further understand the species barrier concept.

Finally, nanopore sensing could be applied for the study and detection of other proteins involved in neurodegeneration with important diagnostic applications. Molecules such as α-synuclein (Parkinson's) and β-amyloid (Alzheimer's) both form aggregates and could also be of medical interest.

5.0 REFERENCES

Abbondanzieri, E.A., Greenleaf, W.J., Shaevitz, J.W., Landick, R., and Block, S.M. (2005). Direct observation of base-pair stepping by RNA polymerase. Nature *438*, 460-465.

Adams, M.J., Blundell, T.L., Dodson, E.J., Dodson, G.G., Vijayan, M., Baker, E.N., Harding, M.M., Hodgkin, D.C., Rimmer, B., and Sheat, S. (1969). Structure of Rhombohedral 2 Zinc Insulin Crystals. Nature *224*, 491-495.

Aguzzi, A., and Calella, A.M. (2009). Prions: protein aggregation and infectious diseases. Physiol Rev *89*, 1105-1152.

Aguzzi, A., and Polymenidou, M. (2004). Mammalian prion biology: one century of evolving concepts. Cell *116*, 313-327.

Aguzzi, A., Sigurdson, C., and Heikenwaelder, M. (2008). Molecular mechanisms of prion pathogenesis. Annu Rev Pathol *3*, 11-40.

Akeson, M., Branton, D., Kasianowicz, J.J., Brandin, E., and Deamer, D.W. (1999). Microsecond time-scale discrimination among polycytidylic acid, polyadenylic acid, and polyuridylic acid as homopolymers or as segments within single RNA molecules. Biophys J *77*, 3227-3233.

Alper, T., Haig, D.A., and Clarke, M.C. (1966). The exceptionally small size of the scrapie agent. Biochem Biophys Res Commun *22*, 278-284.

Alper, T., Haig, D.A., and Clarke, M.C. (1978). The scrapie agent: evidence against its dependence for replication on intrinsic nucleic acid. J Gen Virol *41*, 503-516.

Anderson, B., Weigel, N., Kundig, W., and Roseman, S. (1971). Sugar transport. 3. Purification and properties of a phosphocarrier protein (HPr) of the phosphoenolpyruvate-dependent phosphotransferase system of Escherichia coli. J Biol Chem *246*, 7023-7033.

Andrievskaia, O., McRae, H., Elmgren, C., Huang, H., Balachandran, A., and Nielsen, K. (2006). Generation of antibodies against bovine recombinant prion protein in various strains of mice. Clin Vaccine Immunol *13*, 98-105.

Angers, R.C., Kang, H.E., Napier, D., Browning, S., Seward, T., Mathiason, C., Balachandran, A., McKenzie, D., Castilla, J., Soto, C., *et al.* (2010). Prion strain mutation determined by prion protein conformational compatibility and primary structure. Science *328*, 1154-1158.

Antosiewicz, J., and Porschke, D. (1995). Electrostatics of hemoglobins from measurements of the electric dichroism and computer simulations. Biophys J *68*, 655-664.

Apel, P.Y., Korchev, Y.E., Siwy, Z., Spohr, R., and Yoshida, M. (2001). Diode-like single-ion track membrane prepared by electro-stopping. Nuclear Instruments and Methods in Physics Research Section B: Beam Interactions with Materials and Atoms *184*, 337-346.

Astier, Y., Braha, O., and Bayley, H. (2006). Toward single molecule DNA sequencing: direct identification of ribonucleoside and deoxyribonucleoside 5'-monophosphates by using an engineered protein nanopore equipped with a molecular adapter. J Am Chem Soc *128*, 1705-1710.

Atarashi, R., Satoh, K., Sano, K., Fuse, T., Yamaguchi, N., Ishibashi, D., Matsubara, T., Nakagaki, T., Yamanaka, H., Shirabe, S., *et al.* (2011). Ultrasensitive human prion detection in cerebrospinal fluid by real-time quaking-induced conversion. Nat Med *17*, 175-178.

Atarashi, R., Wilham, J.M., Christensen, L., Hughson, A.G., Moore, R.A., Johnson, L.M., Onwubiko, H.A., Priola, S.A., and Caughey, B. (2008). Simplified ultrasensitive prion detection by recombinant PrP conversion with shaking. Nat Methods *5*, 211-212.

Bartz, J.C., Kincaid, A.E., and Bessen, R.A. (2002). Retrograde transport of transmissible mink encephalopathy within descending motor tracts. J Virol *76*, 5759-5768.

Bashford, C.L., Alder, G.M., Fulford, L.G., Korchev, Y.E., Kovacs, E., MacKinnon, A., Pederzolli, C., and Pasternak, C.A. (1996). Pore formation by S. aureus alpha-toxin in liposomes and planar lipid bilayers: effects of nonelectrolytes. J Membr Biol *150*, 37-45.

Bashford, C.L., Alder, G.M., Graham, J.M., Menestrina, G., and Pasternak, C.A. (1988). Ion modulation of membrane permeability: effect of cations on intact cells and on cells and phospholipid bilayers treated with pore-forming agents. J Membr Biol *103*, 79-94.

Basu, S., Mohan, M.L., Luo, X., Kundu, B., Kong, Q., and Singh, N. (2007). Modulation of proteinase K-resistant prion protein in cells and infectious brain homogenate by redox iron: implications for prion replication and disease pathogenesis. Mol Biol Cell *18*, 3302-3312.

Bayley, H. (1995). Pore-forming proteins with built-in triggers and switches. Bioorg. Chem. *23*, 340-354.

Bechtluft, P., van Leeuwen, R.G., Tyreman, M., Tomkiewicz, D., Nouwen, N., Tepper, H.L., Driessen, A.J., and Tans, S.J. (2007). Direct observation of chaperone-induced changes in a protein folding pathway. Science *318*, 1458-1461.

Bellon, A., Seyfert-Brandt, W., Lang, W., Baron, H., Groner, A., and Vey, M. (2003). Improved conformation-dependent immunoassay: suitability for human prion detection with enhanced sensitivity. J Gen Virol *84*, 1921-1925.

Bencsik, A., Debeer, S., Petit, T., and Baron, T. (2009). Possible case of maternal transmission of feline spongiform encephalopathy in a captive cheetah. PLoS One *4*, e6929.

Bennion, B.J., and Daggett, V. (2002). Protein conformation and diagnostic tests: the prion protein. Clin Chem *48*, 2105-2114.

Berg, J.M., and Godwin, H.A. (1997). Lessons from zinc-binding peptides. Annu Rev Biophys Biomol Struct *26*, 357-371.

Bernheimer, A.W., Avigad, L.S., and Avigad, G. (1975). Interactions between aerolysin, erythrocytes, and erythrocyte membranes. Infect Immun *11*, 1312-1319.

Bessen, R.A., and Marsh, R.F. (1992). Biochemical and physical properties of the prion protein from two strains of the transmissible mink encephalopathy agent. J Virol *66*, 2096-2101.

Bezrukov, S.M., and Kasianowicz, J.J. (1993). Current noise reveals protonation kinetics and number of ionizable sites in an open protein ion channel. Phys Rev Lett *70*, 2352-2355.

Bhakdi, S., Fussle, R., and Tranum-Jensen, J. (1981). Staphylococcal alpha-toxin: oligomerization of hydrophilic monomers to form amphiphilic hexamers induced through contact with deoxycholate detergent micelles. Proc Natl Acad Sci U S A *78*, 5475-5479.

Biffiger, K., Zwald, D., Kaufmann, L., Briner, A., Nayki, I., Purro, M., Bottcher, S., Struckmeyer, T., Schaller, O., Meyer, R., *et al.* (2002). Validation of a luminescence immunoassay for the detection of PrP(Sc) in brain homogenate. J Virol Methods *101*, 79-84.

Bikwemu, R., Wolfe, A.J., Xing, X., and Movileanu, L. (2010). Facilitated translocation of polypeptides through a single nanopore. J Phys Condens Matter *22*, 454117.

Binnig, G., Quate, C.F., and Gerber, C. (1986). Atomic Force Microscope. Physical Review Letters *56*, 930.

Binolfi, A., Rasia, R.M., Bertoncini, C.W., Ceolin, M., Zweckstetter, M., Griesinger, C., Jovin, T.M., and Fernandez, C.O. (2006). Interaction of alpha-synuclein with divalent metal ions reveals key differences: a link between structure, binding specificity and fibrillation enhancement. J Am Chem Soc *128*, 9893-9901.

Blundell, T.L., Cutfield, J.F., Dodson, G.G., Dodson, E., Hodgkin, D.C., and Mercola, D. (1971). The structure and biology of insulin. Biochem J *125*, 50P-51P.

Borchelt, D.R., Taraboulos, A., and Prusiner, S.B. (1992). Evidence for synthesis of scrapie prion proteins in the endocytic pathway. J Biol Chem *267*, 16188-16199.

Borsenberger, V., Mitchell, N., and Howorka, S. (2009). Chemically labeled nucleotides and oligonucleotides encode DNA for sensing with nanopores. J Am Chem Soc *131*, 7530-7531.

Brange, J., Andersen, L., Laursen, E.D., Meyn, G., and Rasmussen, E. (1997). Toward understanding insulin fibrillation. J Pharm Sci *86*, 517-525.

Branton, D., Deamer, D.W., Marziali, A., Bayley, H., Benner, S.A., Butler, T., Di Ventra, M., Garaj, S., Hibbs, A., Huang, X., *et al.* (2008). The potential and challenges of nanopore sequencing. Nat Biotechnol *26*, 1146-1153.

Brazier, M.W., Davies, P., Player, E., Marken, F., Viles, J.H., and Brown, D.R. (2008). Manganese binding to the prion protein. J Biol Chem *283*, 12831-12839.

Brion, L.P., Satlin, L.M., and Schwartz, G.J. (1990). Video fluorescence microscopy as a tool for the study of cellular heterogeneity in epithelia. Biotechniques *8*, 282-289.

Brown, D.R. (2000). Prion protein peptides: optimal toxicity and peptide blockade of toxicity. Mol Cell Neurosci *15*, 66-78.

Brown, D.R. (2011a). Metals in neurodegenerative disease. Metallomics *3*, 226-228.

Brown, D.R. (2011b). Prions and manganese: A maddening beast. Metallomics *3*, 229-238.

Brown, D.R., Besinger, A., Herms, J.W., and Kretzschmar, H.A. (1998a). Microglial expression of the prion protein. Neuroreport *9*, 1425-1429.

Brown, D.R., Clive, C., and Haswell, S.J. (2001a). Antioxidant activity related to copper binding of native prion protein. J Neurochem *76*, 69-76.

Brown, D.R., Hafiz, F., Glasssmith, L.L., Wong, B.S., Jones, I.M., Clive, C., and Haswell, S.J. (2000). Consequences of manganese replacement of copper for prion protein function and proteinase resistance. EMBO J *19*, 1180-1186.

Brown, D.R., Herms, J., and Kretzschmar, H.A. (1994). Mouse cortical cells lacking cellular PrP survive in culture with a neurotoxic PrP fragment. Neuroreport *5*, 2057-2060.

Brown, D.R., Qin, K., Herms, J.W., Madlung, A., Manson, J., Strome, R., Fraser, P.E., Kruck, T., von Bohlen, A., Schulz-Schaeffer, W., *et al.* (1997). The cellular prion protein binds copper in vivo. Nature *390*, 684-687.

Brown, D.R., Wong, B.S., Hafiz, F., Clive, C., Haswell, S.J., and Jones, I.M. (1999). Normal prion protein has an activity like that of superoxide dismutase. Biochem J *344 Pt 1*, 1-5.

Brown, P. (2001). Creutzfeldt-Jakob disease: blood infectivity and screening tests. Semin Hematol *38*, 2-6.

Brown, P., Cervenakova, L., and Diringer, H. (2001b). Blood infectivity and the prospects for a diagnostic screening test in Creutzfeldt-Jakob disease. J Lab Clin Med *137*, 5-13.

Brown, P., Rohwer, R.G., Dunstan, B.C., MacAuley, C., Gajdusek, D.C., and Drohan, W.N. (1998b). The distribution of infectivity in blood components and plasma derivatives in experimental models of transmissible spongiform encephalopathy. Transfusion *38*, 810-816.

Buckley, J.T., Halasa, L.N., Lund, K.D., and MacIntyre, S. (1981). Purification and some properties of the hemolytic toxin aerolysin. Can J Biochem *59*, 430-435.

Bueler, H., Fischer, M., Lang, Y., Bluethmann, H., Lipp, H.-P., DeArmond, S.J., Prusiner, S.B., Aguet, M., and Weissmann, C. (1992). Normal development and behaviour of mice lacking the neuronal cell-surface PrP protein. Nature *356*, 577-582.

Burns, C.S., Aronoff-Spencer, E., Legname, G., Prusiner, S.B., Antholine, W.E., Gerfen, G.J., Peisach, J., and Millhauser, G.L. (2003). Copper coordination in the full-length, recombinant prion protein. Biochemistry *42*, 6794-6803.

Burns, J.A., Butler, J.C., Moran, J., and Whitesides, G.M. (1991). Selective Reduction of Disulfides by Tris(2-carboxyethyl)phosphine. J Org Chem *56*, 2648-2650.

Bustamante, C., Chemla, Y.R., and Moffitt, J.R. (2008). High-resolution dual-trap optical tweezers with differential detection. In Single-molecule techniques: A laboratory manual, P.R. Selvin, and T. Ha, eds. (Cold Spring Harbor Laboratory Press), pp. 297-324.

Butler, T.Z., Gundlach, J.H., and Troll, M.A. (2006). Determination of RNA orientation during translocation through a biological nanopore. Biophys J *90*, 190-199.

Butler, T.Z., Pavlenok, M., Derrington, I.M., Niederweis, M., and Gundlach, J.H. (2008). Single-molecule DNA detection with an engineered MspA protein nanopore. Proc Natl Acad Sci U S A *105*, 20647-20652.

Calzolai, L., Lysek, D.A., Perez, D.R., Guntert, P., and Wuthrich, K. (2005). Prion protein NMR structures of chickens, turtles, and frogs. Proc Natl Acad Sci U S A *102*, 651-655.

Caughey, B. (1993). Scrapie associated PrP accumulation and its prevention: insights from cell culture. Br Med Bull *49*, 860-872.

Caughey, B., and Baron, G.S. (2006). Prions and their partners in crime. Nature *443*, 803-810.

Caughey, B., and Chesebro, B. (1997). Prion protein and the transmissible spongiform encephalopathies. Trends Cell Biol *7*, 56-62.

Caughey, B., Ernst, D., and Race, R.E. (1993). Congo red inhibition of scrapie agent replication. J Virol *67*, 6270-6272.

Caughey, B., and Raymond, G.J. (1993). Sulfated polyanion inhibition of scrapie-associated PrP accumulation in cultured cells. J Virol *67*, 643-650.

Caughey, B.W., Dong, A., Bhat, K.S., Ernst, D., Hayes, S.F., and Caughey, W.S. (1991). Secondary structure analysis of the scrapie-associated protein PrP 27-30 in water by infrared spectroscopy. Biochemistry *30*, 7672-7680.

Caughey, W.S., Raymond, L.D., Horiuchi, M., and Caughey, B. (1998). Inhibition of protease-resistant prion protein formation by porphyrins and phthalocyanines. Proc Natl Acad Sci U S A *95*, 12117-12122.

Cavanagh, J., Fairbrother, W.J., Palmer, A.G., Rance, M., and Skelton, M.J. (2007). Classical NMR spectroscopy. In Protein NMR spectroscopy: Principles and practice. (Academic Press), p. 21.

Chang, X., Jorgensen, A.M., Bardrum, P., and Led, J.J. (1997). Solution structures of the R6 human insulin hexamer. Biochemistry *36*, 9409-9422.

Charvin, G., Vologodskii, A., Bensimon, D., and Croquette, V. (2005). Braiding DNA: experiments, simulations, and models. Biophys J *88*, 4124-4136.

Chen, P., Mitsui, T., Farmer, D.B., Golovchenko, J., Gordon, R.G., and Branton, D. (2004). Atomic Layer Deposition to Fine-Tune the Surface Properties and Diameters of Fabricated Nanopores. Nano Letters *4*, 1333-1337.

Chiti, F., and Dobson, C.M. (2006). Protein misfolding, functional amyloid, and human disease. Annu Rev Biochem *75*, 333-366.

Christensen, C., Baran, C., Krasniqi, B., Stefureac, R.I., Nokhrin, S., and Lee, J.S. (2011). Effect of charge, topology and orientation of the electric field on the interaction of peptides with the alpha-hemolysin pore. J Pept Sci.

Chu, J., Gonzalez-Lopez, M., Cockroft, S.L., Amorin, M., and Ghadiri, M.R. (2010). Real-time monitoring of DNA polymerase function and stepwise single-nucleotide DNA strand translocation through a protein nanopore. Angew Chem Int Ed Engl *49*, 10106-10109.

Clarke, J., Wu, H.C., Jayasinghe, L., Patel, A., Reid, S., and Bayley, H. (2009). Continuous base identification for single-molecule nanopore DNA sequencing. Nat Nanotechnol *4*, 265-270.

Cockroft, S.L., Chu, J., Amorin, M., and Ghadiri, M.R. (2008). A single-molecule nanopore device detects DNA polymerase activity with single-nucleotide resolution. J Am Chem Soc *130*, 818-820.

Coitinho, A.S., Freitas, A.R., Lopes, M.H., Hajj, G.N., Roesler, R., Walz, R., Rossato, J.I., Cammarota, M., Izquierdo, I., Martins, V.R., *et al.* (2006). The interaction between prion protein and laminin modulates memory consolidation. Eur J Neurosci *24*, 3255-3264.

Collinge, J. (2010). Medicine. Prion strain mutation and selection. Science *328*, 1111-1112.

Collinge, J., and Clarke, A.R. (2007). A general model of prion strains and their pathogenicity. Science *318*, 930-936.

Collinge, J., and Rossor, M. (1996). A new variant of prion disease. Lancet *347*, 916-917.

Collinge, J., Whitfield, J., McKintosh, E., Beck, J., Mead, S., Thomas, D.J., and Alpers, M.P. (2006). Kuru in the 21st century--an acquired human prion disease with very long incubation periods. Lancet *367*, 2068-2074.

Collinge, J., Whittington, M.A., Sidle, K.C., Smith, C.J., Palmer, M.S., Clarke, A.R., and Jefferys, J.G. (1994). Prion protein is necessary for normal synaptic function. Nature *370*, 295-297.

Colquhoun, D., and Sigworth, F.J. (1995). Fitting and statistical analysis of single-channel records. In Single-channel recording, B. Sakmann, and E. Neher, eds. (New York: Plenum Press), pp. 483-585.

Coulter, W.H. (1953). US Pat., 2656508.

Curin Serbec, V., Bresjanac, M., Popovic, M., Pretnar Hartman, K., Galvani, V., Rupreht, R., Cernilec, M., Vranac, T., Hafner, I., and Jerala, R. (2004). Monoclonal antibody against a peptide of human prion protein discriminates between Creutzfeldt-Jacob's disease-affected and normal brain tissue. J Biol Chem *279*, 3694-3698.

Dahiyat, B.I., and Mayo, S.L. (1997). De novo protein design: fully automated sequence selection. Science *278*, 82-87.

Daiguji, H., Oka, Y., and Shirono, K. (2005). Nanofluidic diode and bipolar transistor. Nano Lett *5*, 2274-2280.

de Zoysa, R.S.S., Jayawardhana, D.A., Zhao, Q., Wang, D., Armstrong, D.W., and Guan, X. (2009). Slowing DNA Translocation through Nanopores Using a Solution Containing Organic Salts. The Journal of Physical Chemistry B *113*, 13332-13336.

DeBlois, R.W., and Bean, C.P. (1970). Counting and Sizing of Submicron Particles by the Resistive Pulse Technique, Vol 41 (AIP).

Dekker, C. (2007). Solid-state nanopores. Nat Nanotechnol *2*, 209-215.

Deleault, N.R., Lucassen, R.W., and Supattapone, S. (2003). RNA molecules stimulate prion protein conversion. Nature *425*, 717-720.

Deniz, A.A., Laurence, T.A., Beligere, G.S., Dahan, M., Martin, A.B., Chemla, D.S., Dawson, P.E., Schultz, P.G., and Weiss, S. (2000). Single-molecule protein folding: diffusion fluorescence resonance energy transfer studies of the denaturation of chymotrypsin inhibitor 2. Proc Natl Acad Sci U S A *97*, 5179-5184.

Derrington, I.M., Butler, T.Z., Collins, M.D., Manrao, E., Pavlenok, M., Niederweis, M., and Gundlach, J.H. (2010). Nanopore DNA sequencing with MspA. Proc Natl Acad Sci U S A *107*, 16060-16065.

Di Natale, G., Grasso, G., Impellizzeri, G., La Mendola, D., Micera, G., Mihala, N., Nagy, Z., Osz, K., Pappalardo, G., Rigo, V., *et al.* (2005). Copper(II) interaction with unstructured prion domain outside the octarepeat region: speciation, stability, and binding details of copper(II) complexes with PrP106-126 peptides. Inorg Chem *44*, 7214-7225.

Diez, M., Zimmermann, B., Borsch, M., Konig, M., Schweinberger, E., Steigmiller, S., Reuter, R., Felekyan, S., Kudryavtsev, V., Seidel, C.A.M., *et al.* (2004). Proton-powered subunit rotation in single membrane-bound F0F1-ATP synthase. Nat Struct Mol Biol *11*, 135-141.

Ding, D.W., Rill, R., and Van Holde, K.E. (1972). The dichroism of DNA in electric fields. Biopolymers *11*, 2109-2124.

Ebbinghaus, S., Kim, S.J., Heyden, M., Yu, X., Heugen, U., Gruebele, M., Leitner, D.M., and Havenith, M. (2007). An extended dynamical hydration shell around proteins. Proc Natl Acad Sci U S A *104*, 20749-20752.

Eiden, M., Hoffmann, C., Balkema-Buschmann, A., Muller, M., Baumgartner, K., and Groschup, M.H. (2010). Biochemical and immunohistochemical characterization of feline spongiform encephalopathy in a German captive cheetah. J Gen Virol *91*, 2874-2883.

Enari, M., Flechsig, E., and Weissmann, C. (2001). Scrapie prion protein accumulation by scrapie-infected neuroblastoma cells abrogated by exposure to a prion protein antibody. Proc Natl Acad Sci U S A *98*, 9295-9299.

Ervin, E.N., Kawano, R., White, R.J., and White, H.S. (2008). Simultaneous alternating and direct current readout of protein ion channel blocking events using glass nanopore membranes. Anal Chem *80*, 2069-2076.

Ervin, E.N., White, R.J., Owens, T.G., Tang, J.M., and White, H.S. (2007). AC conductance of transmembrane protein channels. The number of ionized residue mobile counterions at infinite dilution. J Phys Chem B *111*, 9165-9171.

Ervin, E.N., White, R.J., and White, H.S. (2009). Sensitivity and signal complexity as a function of the number of ion channels in a stochastic sensor. Anal Chem *81*, 533-537.

Evans, R.M., and Hollenberg, S.M. (1988). Zinc fingers: gilt by association. Cell *52*, 1-3.

Faller, M., Niederweis, M., and Schulz, G.E. (2004). The structure of a mycobacterial outer-membrane channel. Science *303*, 1189-1192.

Fichet, G., Comoy, E., Duval, C., Antloga, K., Dehen, C., Charbonnier, A., McDonnell, G., Brown, P., Lasmezas, C.I., and Deslys, J.P. (2004). Novel methods for disinfection of prion-contaminated medical devices. Lancet *364*, 521-526.

Fink, A.L. (2005). Natively unfolded proteins. Curr Opin Struct Biol *15*, 35-41.

Firnkes, M., Pedone, D., Knezevic, J., Doblinger, M., and Rant, U. (2010). Electrically facilitated translocations of proteins through silicon nitride nanopores: conjoint and competitive action of diffusion, electrophoresis, and electroosmosis. Nano Lett *10*, 2162-2167.

Fivaz, M., Velluz, M.C., and van der Goot, F.G. (1999). Dimer dissociation of the pore-forming toxin aerolysin precedes receptor binding. J Biol Chem *274*, 37705-37708.

Fleischer, R.L., and Price, P.B. (1963). Tracks of Charged Particles in High Polymers. Science *140*, 1221-1222.

Fologea, D., Brandin, E., Uplinger, J., Branton, D., and Li, J. (2007a). DNA conformation and base number simultaneously determined in a nanopore. Electrophoresis *28*, 3186-3192.

Fologea, D., Gershow, M., Ledden, B., McNabb, D.S., Golovchenko, J.A., and Li, J. (2005a). Detecting single stranded DNA with a solid state nanopore. Nano Lett *5*, 1905-1909.

Fologea, D., Ledden, B., McNabb, D.S., and Li, J. (2007b). Electrical characterization of protein molecules by a solid-state nanopore. Appl Phys Lett *91*, 539011-539013.

Fologea, D., Uplinger, J., Thomas, B., McNabb, D.S., and Li, J. (2005b). Slowing DNA translocation in a solid-state nanopore. Nano Lett *5*, 1734-1737.

Forloni, G., Angeretti, N., Chiesa, R., Monzani, E., Salmona, M., Bugiani, O., and Tagliavini, F. (1993). Neurotoxicity of a prion protein fragment. Nature *362*, 543-546.

Fraser, H., and Dickinson, A.G. (1973). Scrapie in mice. Agent-strain differences in the distribution and intensity of grey matter vacuolation. J Comp Pathol *83*, 29-40.

Friedler, A., Veprintsev, D.B., Hansson, L.O., and Fersht, A.R. (2003). Kinetic instability of p53 core domain mutants: implications for rescue by small molecules. J Biol Chem *278*, 24108-24112.

Fussle, R., Bhakdi, S., Sziegoleit, A., Tranum-Jensen, J., Kranz, T., and Wellensiek, H.J. (1981). On the mechanism of membrane damage by Staphylococcus aureus alpha-toxin. J Cell Biol *91*, 83-94.

Gabizon, R., Meiner, Z., Halimi, M., and Ben-Sasson, S.A. (1993). Heparin-like molecules bind differentially to prion-proteins and change their intracellular metabolic fate. J Cell Physiol *157*, 319-325.

Gaggelli, E., Bernardi, F., Molteni, E., Pogni, R., Valensin, D., Valensin, G., Remelli, M., Luczkowski, M., and Kozlowski, H. (2005). Interaction of the human prion PrP(106-126) sequence with copper(II), manganese(II), and zinc(II): NMR and EPR studies. J Am Chem Soc *127*, 996-1006.

Gaggelli, E., Kozlowski, H., Valensin, D., and Valensin, G. (2006). Copper homeostasis and neurodegenerative disorders (Alzheimer's, prion, and Parkinson's diseases and amyotrophic lateral sclerosis). Chem Rev *106*, 1995-2044.

Gajdusek, D.C., and Zigas, V. (1957). Degenerative disease of the central nervous system in New Guinea; the endemic occurrence of kuru in the native population. N Engl J Med *257*, 974-978.

Gambetti, P., Parchi, P., Petersen, R.B., Chen, S.G., and Lugaresi, E. (1995). Fatal familial insomnia and familial Creutzfeldt-Jakob disease: clinical, pathological and molecular features. Brain Pathol *5*, 43-51.

Garaj, S., Hubbard, W., Reina, A., Kong, J., Branton, D., and Golovchenko, J.A. (2010). Graphene as a subnanometre trans-electrode membrane. Nature *467*, 190-193.

Garalde, D.R., Simon, C.A., Dahl, J.M., Wang, H., Akeson, M., and Lieberman, K.R. (2011). Distinct complexes of DNA polymerase I (Klenow fragment) for base and sugar discrimination during nucleotide substrate selection. J Biol Chem *286*, 14480-14492.

Garland, W.J., and Buckley, J.T. (1988). The cytolytic toxin aerolysin must aggregate to disrupt erythrocytes, and aggregation is stimulated by human glycophorin. Infect Immun *56*, 1249-1253.

Ghetti, B., Dlouhy, S.R., Giaccone, G., Bugiani, O., Frangione, B., Farlow, M.R., and Tagliavini, F. (1995). Gerstmann-Straussler-Scheinker disease and the Indiana kindred. Brain Pathol *5*, 61-75.

Giese, A., Levin, J., Bertsch, U., and Kretzschmar, H. (2004). Effect of metal ions on de novo aggregation of full-length prion protein. Biochem Biophys Res Commun *320*, 1240-1246.

Gilch, S., Chitoor, N., Taguchi, Y., Stuart, M., Jewell, J.E., and Schatzl, H.M. (2011). Chronic wasting disease. Top Curr Chem *305*, 51-77.

Gilch, S., Wopfner, F., Renner-Muller, I., Kremmer, E., Bauer, C., Wolf, E., Brem, G., Groschup, M.H., and Schatzl, H.M. (2003). Polyclonal anti-PrP auto-antibodies induced with dimeric PrP interfere efficiently with PrPSc propagation in prion-infected cells. J Biol Chem *278*, 18524-18531.

Glatzel, M., Abela, E., Maissen, M., and Aguzzi, A. (2003). Extraneural pathologic prion protein in sporadic Creutzfeldt-Jakob disease. N Engl J Med *349*, 1812-1820.

Goldfarb, L.G., Brown, P., McCombie, W.R., Goldgaber, D., Swergold, G.D., Wills, P.R., Cervenakova, L., Baron, H., Gibbs, C.J., Jr., and Gajdusek, D.C. (1991). Transmissible familial Creutzfeldt-Jakob disease associated with five, seven, and eight extra octapeptide coding repeats in the PRNP gene. Proc Natl Acad Sci U S A *88*, 10926-10930.

Goodrich, C.P., Kirmizialtin, S., Huyghues-Despointes, B.M., Zhu, A., Scholtz, J.M., Makarov, D.E., and Movileanu, L. (2007). Single-molecule electrophoresis of beta-hairpin peptides by electrical recordings and Langevin dynamics simulations. J Phys Chem B *111*, 3332-3335.

Gore, J., Bryant, Z., Stone, M.D., Nollmann, M., Cozzarelli, N.R., and Bustamante, C. (2006). Mechanochemical analysis of DNA gyrase using rotor bead tracking. Nature *439*, 100-104.

Gouaux, J.E., Braha, O., Hobaugh, M.R., Song, L., Cheley, S., Shustak, C., and Bayley, H. (1994). Subunit stoichiometry of staphylococcal alpha-hemolysin in crystals and on membranes: a heptameric transmembrane pore. Proc Natl Acad Sci U S A *91*, 12828-12831.

Gracheva, M.E., Xiong, A., Aksimentiev, A., Schulten, K., Timp, G., and Leburton, J.-P. (2006). Simulation of the electric response of DNA translocation through a semiconductor nanopore–capacitor. Nanotechnology *17*, 622-633.

Grassi, J., Comoy, E., Simon, S., Creminon, C., Frobert, Y., Trapmann, S., Schimmel, H., Hawkins, S.A., Moynagh, J., Deslys, J.P., *et al.* (2001). Rapid test for the preclinical postmortem diagnosis of BSE in central nervous system tissue. Vet Rec *149*, 577-582.

Grasso, D., Milardi, D., La Rosa, C., and Rizzarelli, E. (2004). The different role of Cu++ and Zn++ ions in affecting the interaction of prion peptide PrP106-126 with model membranes. Chem Commun (Camb), 246-247.

Gross, J.E., and Miller, M.W. (2001). Chronic wasting disease in mule deer: disease dynamics and control. J. Wildlife. Manage. *65*, 205-215.

Gu, L.Q., Braha, O., Conlan, S., Cheley, S., and Bayley, H. (1999). Stochastic sensing of organic analytes by a pore-forming protein containing a molecular adapter. Nature *398*, 686-690.

Guan, X., Gu, L.Q., Cheley, S., Braha, O., and Bayley, H. (2005). Stochastic sensing of TNT with a genetically engineered pore. Chembiochem *6*, 1875-1881.

Gyarfas, B., Olasagasti, F., Benner, S., Garalde, D., Lieberman, K.R., and Akeson, M. (2009). Mapping the position of DNA polymerase-bound DNA templates in a nanopore at 5 A resolution. ACS Nano *3*, 1457-1466.

Ha, T. (2001). Single-molecule fluorescence resonance energy transfer. Methods *25*, 78-86.

Ha, T. (2004). Structural dynamics and processing of nucleic acids revealed by single-molecule spectroscopy. Biochemistry *43*, 4055-4063.

Ha, T., Enderle, T., Ogletree, D.F., Chemla, D.S., Selvin, P.R., and Weiss, S. (1996). Probing the interaction between two single molecules: fluorescence resonance energy transfer between a single donor and a single acceptor. Proc Natl Acad Sci U S A *93*, 6264-6268.

Hadlow, W.J., Kennedy, R.C., and Race, R.E. (1982). Natural infection of Suffolk sheep with scrapie virus. J Infect Dis *146*, 657-664.

Haik, S., and Brandel, J.P. (2011). Biochemical and strain properties of CJD prions: complexity versus simplicity. J Neurochem.

Hainfellner, J.A., Brantner-Inthaler, S., Cervenakova, L., Brown, P., Kitamoto, T., Tateishi, J., Diringer, H., Liberski, P.P., Regele, H., Feucht, M., *et al.* (1995). The original Gerstmann-Straussler-Scheinker family of Austria: divergent clinicopathological phenotypes but constant PrP genotype. Brain Pathol *5*, 201-211.

Halfmann, R., and Lindquist, S. (2010). Epigenetics in the extreme: prions and the inheritance of environmentally acquired traits. Science *330*, 629-632.

Hall, A.R., Scott, A., Rotem, D., Mehta, K.K., Bayley, H., and Dekker, C. (2010). Hybrid pore formation by directed insertion of alpha-haemolysin into solid-state nanopores. Nat Nanotechnol *5*, 874-877.

Halverson, K.M., Panchal, R.G., Nguyen, T.L., Gussio, R., Little, S.F., Misakian, M., Bavari, S., and Kasianowicz, J.J. (2005). Anthrax biosensor, protective antigen ion channel asymmetric blockade. J Biol Chem *280*, 34056-34062.

Han, A., Creus, M., Schürmann, G., Linder, V., Ward, T.R., de Rooij, N.F., and Staufer, U. (2008). Label-Free Detection of Single Protein Molecules and Protein−Protein Interactions Using Synthetic Nanopores. Analytical Chemistry *80*, 4651-4658.

Han, A., Schürmann, G., Mondin, G., Bitterli, R.A., Hegelbach, N.G., Rooij, N.F.d., and Staufer, U. (2006). Sensing protein molecules using nanofabricated pores, Vol 88 (AIP).

Hartsough, G.R., and Burger, D. (1965). Encephalopathy of mink. I. Epizootiologic and clinical observations. J Infect Dis *115*, 387-392.

Hedlin, P.D., Cashman, N.R., Li, L., Gupta, J., Babiuk, L.A., Potter, A.A., Griebel, P., and Napper, S. (2010). Design and delivery of a cryptic PrP(C) epitope for induction of PrP(Sc)-specific antibody responses. Vaccine *28*, 981-988.

Hegde, R.S., Mastrianni, J.A., Scott, M.R., DeFea, K.A., Tremblay, P., Torchia, M., DeArmond, S.J., Prusiner, S.B., and Lingappa, V.R. (1998). A transmembrane form of the prion protein in neurodegenerative disease. Science *279*, 827-834.

Heinemann, S. (1995). Guide to data acquisition and analysis. In Single-channel recording, B. Sakmann, and E. Neher, eds. (New York: Plenum Press), pp. 53-90.

Henrickson, S.E., Misakian, M., Robertson, B., and Kasianowicz, J.J. (2000). Driven DNA transport into an asymmetric nanometer-scale pore. Phys Rev Lett *85*, 3057-3060.

Heppner, F.L., Musahl, C., Arrighi, I., Klein, M.A., Rulicke, T., Oesch, B., Zinkernagel, R.M., Kalinke, U., and Aguzzi, A. (2001). Prevention of scrapie pathogenesis by transgenic expression of anti-prion protein antibodies. Science *294*, 178-182.

Hill, A.F., Zeidler, M., Ironside, J., and Collinge, J. (1997). Diagnosis of new variant Creutzfeldt-Jakob disease by tonsil biopsy. Lancet *349*, 99-100.

Hilton, D.A., Fathers, E., Edwards, P., Ironside, J.W., and Zajicek, J. (1998). Prion immunoreactivity in appendix before clinical onset of variant Creutzfeldt-Jakob disease. Lancet *352*, 703-704.

Hogan, M., Dattagupta, N., and Crothers, D.M. (1978). Transient electric dichroism of rod-like DNA molecules. Proc Natl Acad Sci U S A *75*, 195-199.

Hong, D.P., Ahmad, A., and Fink, A.L. (2006). Fibrillation of human insulin A and B chains. Biochemistry *45*, 9342-9353.

Hope, J., Reekie, L.J., Hunter, N., Multhaup, G., Beyreuther, K., White, H., Scott, A.C., Stack, M.J., Dawson, M., and Wells, G.A. (1988). Fibrils from brains of cows with new cattle disease contain scrapie-associated protein. Nature *336*, 390-392.

Hornshaw, M.P., McDermott, J.R., Candy, J.M., and Lakey, J.H. (1995). Copper binding to the N-terminal tandem repeat region of mammalian and avian prion protein: structural studies using synthetic peptides. Biochem Biophys Res Commun *214*, 993-999.

Howard, S.P., and Buckley, J.T. (1985). Activation of the hole-forming toxin aerolysin by extracellular processing. J Bacteriol *163*, 336-340.

Howard, S.P., Garland, W.J., Green, M.J., and Buckley, J.T. (1987). Nucleotide sequence of the gene for the hole-forming toxin aerolysin of Aeromonas hydrophila. J Bacteriol *169*, 2869-2871.

Hsiao, K., Baker, H.F., Crow, T.J., Poulter, M., Owen, F., Terwilliger, J.D., Westaway, D., Ott, J., and Prusiner, S.B. (1989). Linkage of a prion protein missense variant to Gerstmann-Straussler syndrome. Nature *338*, 342-345.

Hua, Q.X., Gozani, S.N., Chance, R.E., Hoffmann, J.A., Frank, B.H., and Weiss, M.A. (1995). Structure of a protein in a kinetic trap. Nat Struct Biol *2*, 129-138.

Huang, Z., Prusiner, S.B., and Cohen, F.E. (1996). Structures of prion proteins and conformational models for prion diseases. Curr Top Microbiol Immunol *207*, 49-67.

Hunter, N., Goldmann, W., Foster, J.D., Cairns, D., and Smith, G. (1997). Natural scrapie and PrP genotype: case-control studies in British sheep. Vet Rec *141*, 137-140.

Hurt, N., Wang, H., Akeson, M., and Lieberman, K.R. (2009). Specific nucleotide binding and rebinding to individual DNA polymerase complexes captured on a nanopore. J Am Chem Soc *131*, 3772-3778.

Ingrosso, L., Ladogana, A., and Pocchiari, M. (1995). Congo red prolongs the incubation period in scrapie-infected hamsters. J Virol *69*, 506-508.

Jackson, G.S., Murray, I., Hosszu, L.L., Gibbs, N., Waltho, J.P., Clarke, A.R., and Collinge, J. (2001). Location and properties of metal-binding sites on the human prion protein. Proc Natl Acad Sci U S A *98*, 8531-8535.

Jaroslawski, S., Zadek, B., Ashcroft, F., Venien-Bryan, C., and Scheuring, S. (2007). Direct visualization of KirBac3.1 potassium channel gating by atomic force microscopy. J Mol Biol *374*, 500-505.

Jayawardhana, D.A., Crank, J.A., Zhao, Q., Armstrong, D.W., and Guan, X. (2009). Nanopore stochastic detection of a liquid explosive component and sensitizers using boromycin and an ionic liquid supporting electrolyte. Anal Chem *81*, 460-464.

Jia, Z., Quail, J.W., Waygood, E.B., and Delbaere, L.T. (1993). The 2.0-A resolution structure of Escherichia coli histidine-containing phosphocarrier protein HPr. A redetermination. Journal of Biological Chemistry *268*, 22490-22501.

Jobling, M.F., Huang, X., Stewart, L.R., Barnham, K.J., Curtain, C., Volitakis, I., Perugini, M., White, A.R., Cherny, R.A., Masters, C.L., *et al.* (2001). Copper and zinc binding modulates the aggregation and neurotoxic properties of the prion peptide PrP106-126. Biochemistry *40*, 8073-8084.

Joseph-McCarthy, D., Fedorov, A.A., and Almo, S.C. (1996). Comparison of experimental and computational functional group mapping of an RNase A structure: implications for computer-aided drug design. Protein Eng *9*, 773-780.

Kaim, W., and Schwederski, B. (1994). The "Zinc finger" and other gene regulatory zinc proteins. In Bioinorganic chemistry: Inorganic elements in the chemistry of life. (John Wiley and Sons), pp. 260-262.

Kasianowicz, J.J., and Bezrukov, S.M. (1995). Protonation dynamics of the alpha-toxin ion channel from spectral analysis of pH-dependent current fluctuations. Biophys J *69*, 94-105.

Kasianowicz, J.J., Brandin, E., Branton, D., and Deamer, D.W. (1996). Characterization of individual polynucleotide molecules using a membrane channel. Proc Natl Acad Sci U S A *93*, 13770-13773.

Kasianowicz, J.J., Burden, D.L., Han, L.C., Cheley, S., and Bayley, H. (1999). Genetically engineered metal ion binding sites on the outside of a Channel's transmembrane beta-barrel. Biophys J *76*, 837-845.

Keyser, U.F., Does, J.v.d., Dekker, C., and Dekker, N.H. (2006). Optical tweezers for force measurements on DNA in nanopores, Vol 77 (AIP).

Kim, C.L., Umetani, A., Matsui, T., Ishiguro, N., Shinagawa, M., and Horiuchi, M. (2004). Antigenic characterization of an abnormal isoform of prion protein using a new diverse panel of monoclonal antibodies. Virology *320*, 40-51.

Kim, M.J., McNally, B., Murata, K., and Meller, A. (2007). Characteristics of solid-state nanometer pores fabricated using a transmission electron microscope. Nanotechnology *18*, 205302.

Kim, M.J., Wanunu, M., Bell, D.C., and Meller, A. (2006). Rapid Fabrication of Uniformly Sized Nanopores and Nanopore Arrays for Parallel DNA Analysis. Advanced Materials *18*, 3149-3153.

Kimberlin, R.H., Cole, S., and Walker, C.A. (1987). Temporary and permanent modifications to a single strain of mouse scrapie on transmission to rats and hamsters. J Gen Virol *68 (Pt 7)*, 1875-1881.

Klatzo, I., Gajdusek, D.C., and Zigas, V. (1959). Pathology of Kuru. Lab Invest *8*, 799-847.

Klevit, R.E., and Waygood, E.B. (1986). Two-dimensional proton NMR studies of histidine-containing protein from Escherichia coli. 3. Secondary and tertiary structure as determined by NMR. Biochemistry *25*, 7774-7781.

Klewpatinond, M., Davies, P., Bowen, S., Brown, D.R., and Viles, J.H. (2008). Deconvoluting the Cu2+ binding modes of full-length prion protein. J Biol Chem *283*, 1870-1881.

Klewpatinond, M., and Viles, J.H. (2007). Fragment length influences affinity for Cu2+ and Ni2+ binding to His96 or His111 of the prion protein and spectroscopic evidence for a multiple histidine binding only at low pH. Biochem J *404*, 393-402.

Klitzman, R.L., Alpers, M.P., and Gajdusek, D.C. (1984). The Natural Incubation Period of Kuru and the Episodes of Transmission in Three Clusters of Patients. Neuroepidemiology *3*, 3-20.

Klug, A., and Rhodes, D. (1987). Zinc fingers: a novel protein fold for nucleic acid recognition. Cold Spring Harb Symp Quant Biol *52*, 473-482.

Koch, T.K., Berg, B.O., De Armond, S.J., and Gravina, R.F. (1985). Creutzfeldt-Jakob disease in a young adult with idiopathic hypopituitarism. Possible relation to the administration of cadaveric human growth hormone. N Engl J Med *313*, 731-733.

Kocisko, D.A., Come, J.H., Priola, S.A., Chesebro, B., Raymond, G.J., Lansbury, P.T., and Caughey, B. (1994). Cell-free formation of protease-resistant prion protein. Nature *370*, 471-474.

Korchev, Y.E., Bashford, C.L., Alder, G.M., Kasianowicz, J.J., and Pasternak, C.A. (1995). Low conductance states of a single ion channel are not 'closed'. J Membr Biol *147*, 233-239.

Korth, C., May, B.C., Cohen, F.E., and Prusiner, S.B. (2001). Acridine and phenothiazine derivatives as pharmacotherapeutics for prion disease. Proc Natl Acad Sci U S A *98*, 9836-9841.

Korth, C., Stierli, B., Streit, P., Moser, M., Schaller, O., Fischer, R., Schulz-Schaeffer, W., Kretzschmar, H., Raeber, A., Braun, U., *et al.* (1997). Prion (PrPSc)-specific epitope defined by a monoclonal antibody. Nature *390*, 74-77.

Krantz, B.A., Melnyk, R.A., Zhang, S., Juris, S.J., Lacy, D.B., Wu, Z., Finkelstein, A., and Collier, R.J. (2005). A phenylalanine clamp catalyzes protein translocation through the anthrax toxin pore. Science *309*, 777-781.

Krasemann, S., Zerr, I., Weber, T., Poser, S., Kretzschmar, H., Hunsmann, G., and Bodemer, W. (1995). Prion disease associated with a novel nine octapeptide repeat insertion in the PRNP gene. Brain Res Mol Brain Res *34*, 173-176.

Kretzschmar, H.A., Prusiner, S.B., Stowring, L.E., and DeArmond, S.J. (1986). Scrapie prion proteins are synthesized in neurons. Am J Pathol *122*, 1-5.

Krizek, B.A., Merkle, D.L., and Berg, J.M. (1993). Ligand variation and metal ion binding specificity in zinc finger peptides. Inorg Chem *32*, 937-940.

Kron, S.J., and Spudich, J.A. (1986). Fluorescent actin filaments move on myosin fixed to a glass surface. Proc Natl Acad Sci U S A *83*, 6272-6276.

Kundig, W., Roseman, S., and Ghosh, S. (1965). Phosphate bound to a histidine in a protein as an intermediate in a novel phosphotransferase system. Proc Natl Acad Sci U S A *52*, 1067-1074.

Kuwata, K., Kamatari, Y.O., Akasaka, K., and James, T.L. (2004). Slow conformational dynamics in the hamster prion protein. Biochemistry *43*, 4439-4446.

Lagerqvist, J., Zwolak, M., and Di Ventra, M. (2006). Fast DNA sequencing via transverse electronic transport. Nano Lett *6*, 779-782.

Lagerqvist, J., Zwolak, M., and Di Ventra, M. (2007). Influence of the environment and probes on rapid DNA sequencing via transverse electronic transport. Biophys J *93*, 2384-2390.

Lakhiari, H., and Muller, D. (2004). Insulin adsorption on coated silica based supports grafted with N-acetylglucosamine by liquid affinity chromatography. J Chromatogr B Analyt Technol Biomed Life Sci *808*, 35-41.

Lam, W.C., Seifert, J.M., Amberger, F., Graf, C., Auer, M., and Millar, D.P. (1998). Structural dynamics of HIV-1 Rev and its complexes with RRE and 5S RNA. Biochemistry *37*, 1800-1809.

Larsen, O.F.A., van Stokkum, I.H.M., Pandit, A., van Grondelle, R., and van Amerongen, H. (2003). Ultrafast Polarized Fluorescence Measurements on Tryptophan and a Tryptophan-Containing Peptide. The Journal of Physical Chemistry B *107*, 3080-3085.

Lathrop, D.K., Ervin, E.N., Barrall, G.A., Keehan, M.G., Kawano, R., Krupka, M.A., White, H.S., and Hibbs, A.H. (2010). Monitoring the escape of DNA from a nanopore using an alternating current signal. J Am Chem Soc *132*, 1878-1885.

Leach, S.P., Salman, M.D., and Hamar, D. (2006). Trace elements and prion diseases: a review of the interactions of copper, manganese and zinc with the prion protein. Anim Health Res Rev *7*, 97-105.

Lee, K.S., Magalhaes, A.C., Zanata, S.M., Brentani, R.R., Martins, V.R., and Prado, M.A. (2001). Internalization of mammalian fluorescent cellular prion protein and N-terminal deletion mutants in living cells. J Neurochem *79*, 79-87.

Leliveld, S.R., Dame, R.T., Wuite, G.J., Stitz, L., and Korth, C. (2006). The expanded octarepeat domain selectively binds prions and disrupts homomeric prion protein interactions. J Biol Chem *281*, 3268-3275.

Levenberg, K. (1944). A method for the solution of certain non-linear problems in least-squares. Quart Appl Math *2*, 164-168.

Lezmi, S., Bencsik, A., Monks, E., Petit, T., and Baron, T. (2003). First case of feline spongiform encephalopathy in a captive cheetah born in France: PrP(sc) analysis in various tissues revealed unexpected targeting of kidney and adrenal gland. Histochem Cell Biol *119*, 415-422.

Li, J., Gershow, M., Stein, D., Brandin, E., and Golovchenko, J.A. (2003). DNA molecules and configurations in a solid-state nanopore microscope. Nat Mater *2*, 611-615.

Li, J., Stein, D., McMullan, C., Branton, D., Aziz, M.J., and Golovchenko, J.A. (2001). Ion-beam sculpting at nanometre length scales. Nature *412*, 166-169.

Li, L., Napper, S., and Cashman, N.R. (2010). Immunotherapy for prion diseases: opportunities and obstacles. Immunotherapy *2*, 269-282.

Liang, X., and Chou, S.Y. (2008). Nanogap Detector Inside Nanofluidic Channel for Fast Real-Time Label-Free DNA Analysis. Nano Letters *8*, 1472-1476.

Liberski, P.P., Sikorska, B., Guiroy, D., and Bessen, R.A. (2009). Transmissible mink encephalopathy - review of the etiology of a rare prion disease. Folia Neuropathol *47*, 195-204.

Lieberman, K.R., Cherf, G.M., Doody, M.J., Olasagasti, F., Kolodji, Y., and Akeson, M. (2010). Processive replication of single DNA molecules in a nanopore catalyzed by phi29 DNA polymerase. J Am Chem Soc *132*, 17961-17972.

Ligios, C., Sigurdson, C.J., Santucciu, C., Carcassola, G., Manco, G., Basagni, M., Maestrale, C., Cancedda, M.G., Madau, L., and Aguzzi, A. (2005). PrPSc in mammary glands of sheep affected by scrapie and mastitis. Nat Med *11*, 1137-1138.

Lima, L.M., Cordeiro, Y., Tinoco, L.W., Marques, A.F., Oliveira, C.L., Sampath, S., Kodali, R., Choi, G., Foguel, D., Torriani, I., *et al.* (2006). Structural insights into the interaction between prion protein and nucleic acid. Biochemistry *45*, 9180-9187.

Lionnet, T., Allemand, J.F., Revyakin, A., Strick, T.R., Saleh, O.A., Bensimon, D., and Croquette, V. (2008). Single-molecules studies using magnetic traps. In Single-molecule techniques: A laboratory manual, P.R. Selvin, and T. Ha, eds. (New York: Cold Spring Harbor Laboratory Press), pp. 347-369.

López García, F., Zahn, R., Riek, R., and Wüthrich, K. (2000). NMR structure of the bovine prion protein. Proceedings of the National Academy of Sciences *97*, 8334-8339.

Lysek, D.A., Schorn, C., Nivon, L.G., Esteve-Moya, V., Christen, B., Calzolai, L., von Schroetter, C., Fiorito, F., Herrmann, T., Guntert, P., *et al.* (2005). Prion protein NMR structures of cats, dogs, pigs, and sheep. Proc Natl Acad Sci U S A *102*, 640-645.

Madampage, C.A. (2011). The first step towards the development of an electrophoretic prion detector. In Department of Biochemistry (University of Saskatchewan), pp. 85-93.

Madampage, C.A., Andrievskaia, O., and Lee, J.S. (2010). Nanopore detection of antibody prion interactions. Anal Biochem *396*, 36-41.

Magde, D., Elson, E., and Webb, W.W. (1972). Thermodynamic Fluctuations in a Reacting System—Measurement by Fluorescence Correlation Spectroscopy. Physical Review Letters *29*, 705.

Magri, G., Clerici, M., Dall'Ara, P., Biasin, M., Caramelli, M., Casalone, C., Giannino, M.L., Longhi, R., Piacentini, L., Della Bella, S., *et al.* (2005). Decrease in pathology and progression of scrapie after immunisation with synthetic prion protein peptides in hamsters. Vaccine *23*, 2862-2868.

Marc, D., Mercey, R., and Lantier, F. (2007). Scavenger, transducer, RNA chaperone? What ligands of the prion protein teach us about its function. Cell Mol Life Sci *64*, 815-829.

Marquardt, D.W. (1963). An algorithm for least-squares estimation of non-linear parameters J Soc Ind Appl Math *11*, 431-441.

Marsh, R.F. (1976). The subacute spongiform encephalopathies. Front Biol *44*, 359-380.

Marsh, R.F., and Bessen, R.A. (1994). Physicochemical and biological characterizations of distinct strains of the transmissible mink encephalopathy agent. Philos Trans R Soc Lond B Biol Sci *343*, 413-414.

Marsh, R.F., Bessen, R.A., Lehmann, S., and Hartsough, G.R. (1991). Epidemiological and experimental studies on a new incident of transmissible mink encephalopathy. J Gen Virol *72 (Pt 3)*, 589-594.

Martins, V.R., and Brentani, R.R. (2002). The biology of the cellular prion protein. Neurochem Int *41*, 353-355.

Mathe, J., Aksimentiev, A., Nelson, D.R., Schulten, K., and Meller, A. (2005). Orientation discrimination of single-stranded DNA inside the alpha-hemolysin membrane channel. Proc Natl Acad Sci U S A *102*, 12377-12382.

Mathe, J., Visram, H., Viasnoff, V., Rabin, Y., and Meller, A. (2004). Nanopore unzipping of individual DNA hairpin molecules. Biophys J *87*, 3205-3212.

McKinley, M.P., Bolton, D.C., and Prusiner, S.B. (1983). A protease-resistant protein is a structural component of the scrapie prion. Cell *35*, 57-62.

McNally, B., Singer, A., Yu, Z., Sun, Y., Weng, Z., and Meller, A. (2010). Optical recognition of converted DNA nucleotides for single-molecule DNA sequencing using nanopore arrays. Nano Lett *10*, 2237-2244.

McNally, B., Wanunu, M., and Meller, A. (2008). Electromechanical unzipping of individual DNA molecules using synthetic sub-2 nm pores. Nano Lett *8*, 3418-3422.

Medori, R., Montagna, P., Tritschler, H.J., LeBlanc, A., Cortelli, P., Tinuper, P., Lugaresi, E., and Gambetti, P. (1992). Fatal familial insomnia: a second kindred with mutation of prion protein gene at codon 178. Neurology *42*, 669-670.

Meller, A., Nivon, L., Brandin, E., Golovchenko, J., and Branton, D. (2000). Rapid nanopore discrimination between single polynucleotide molecules. Proc Natl Acad Sci U S A *97*, 1079-1084.

Meller, A., Nivon, L., and Branton, D. (2001). Voltage-driven DNA translocations through a nanopore. Phys Rev Lett *86*, 3435-3438.

Menestrina, G. (1986). Ionic channels formed by Staphylococcus aureus alpha-toxin: voltage-dependent inhibition by divalent and trivalent cations. J Membr Biol *90*, 177-190.

Meng, H., Detillieux, D., Baran, C., Krasniqi, B., Christensen, C., Madampage, C., Stefureac, R.I., and Lee, J.S. (2010). Nanopore analysis of tethered peptides. J Pept Sci *16*, 701-708.

Merchant, C.A., Healy, K., Wanunu, M., Ray, V., Peterman, N., Bartel, J., Fischbein, M.D., Venta, K., Luo, Z., Johnson, A.T., *et al.* (2010). DNA translocation through graphene nanopores. Nano Lett *10*, 2915-2921.

Merzlyak, P.G., Capistrano, M.F., Valeva, A., Kasianowicz, J.J., and Krasilnikov, O.V. (2005). Conductance and ion selectivity of a mesoscopic protein nanopore probed with cysteine scanning mutagenesis. Biophys J *89*, 3059-3070.

Meyer, R.K., McKinley, M.P., Bowman, K.A., Braunfeld, M.B., Barry, R.A., and Prusiner, S.B. (1986). Separation and properties of cellular and scrapie prion proteins. Proc Natl Acad Sci U S A *83*, 2310-2314.

Miller, M.W., Wild, M.A., and Williams, E.S. (1998). Epidemiology of chronic wasting disease in captive Rocky Mountain elk. J Wildl Dis *34*, 532-538.

Millhauser, G.L. (2004). Copper binding in the prion protein. Acc Chem Res *37*, 79-85.

Millhauser, G.L. (2007). Copper and the prion protein: methods, structures, function, and disease. Annu Rev Phys Chem *58*, 299-320.

Mirsaidov, U.M., Wang, D., Timp, W., and Timp, G. (2010). Molecular diagnostics for personal medicine using a nanopore. Wiley Interdiscip Rev Nanomed Nanobiotechnol *2*, 367-381.

Misakian, M., and Kasianowicz, J.J. (2003). Electrostatic influence on ion transport through the alphaHL channel. J Membr Biol *195*, 137-146.

Mitchell, N., and Howorka, S. (2008). Chemical tags facilitate the sensing of individual DNA strands with nanopores. Angew Chem Int Ed Engl *47*, 5565-5568.

Mitsui, T., Stein, D., Kim, Y.R., Hoogerheide, D., and Golovchenko, J.A. (2006). Nanoscale volcanoes: accretion of matter at ion-sculpted nanopores. Phys Rev Lett *96*, 036102.

Mohammad, M.M., and Movileanu, L. (2008). Excursion of a single polypeptide into a protein pore: simple physics, but complicated biology. Eur Biophys J *37*, 913-925.

Mohammad, M.M., Prakash, S., Matouschek, A., and Movileanu, L. (2008). Controlling a single protein in a nanopore through electrostatic traps. J Am Chem Soc *130*, 4081-4088.

Moniatte, M., van der Goot, F.G., Buckley, J.T., Pattus, F., and van Dorsselaer, A. (1996). Characterisation of the heptameric pore-forming complex of the Aeromonas toxin aerolysin using MALDI-TOF mass spectrometry. FEBS Lett *384*, 269-272.

Montagna, P. (2005). Fatal familial insomnia: a model disease in sleep physiopathology. Sleep Med Rev *9*, 339-353.

Montagna, P. (2011). Fatal familial insomnia and the role of the thalamus in sleep regulation. Handb Clin Neurol *99*, 981-996.

Mouillet-Richard, S., Ermonval, M., Chebassier, C., Laplanche, J.L., Lehmann, S., Launay, J.M., and Kellermann, O. (2000). Signal transduction through prion protein. Science *289*, 1925-1928.

Movileanu, L. (2008). Squeezing a single polypeptide through a nanopore. Soft Matter *4*, 925-931.

Movileanu, L. (2009). Interrogating single proteins through nanopores: challenges and opportunities. Trends Biotechnol *27*, 333-341.

Movileanu, L., Schmittschmitt, J.P., Scholtz, J.M., and Bayley, H. (2005). Interactions of peptides with a protein pore. Biophys J *89*, 1030-1045.

Moynagh, J., and Schimmel, H. (1999). Tests for BSE evaluated. Bovine spongiform encephalopathy. Nature *400*, 105.

Muller, D.J., Schoenenberger, C.A., Buldt, G., and Engel, A. (1996). Immuno-atomic force microscopy of purple membrane. Biophys J *70*, 1796-1802.

Muramoto, T., Scott, M., Cohen, F.E., and Prusiner, S.B. (1996). Recombinant scrapie-like prion protein of 106 amino acids is soluble. Proc Natl Acad Sci U S A *93*, 15457-15462.

Murayama, Y., Yoshioka, M., Yokoyama, T., Iwamaru, Y., Imamura, M., Masujin, K., Yoshiba, S., and Mohri, S. (2007). Efficient in vitro amplification of a mouse-adapted scrapie prion protein. Neurosci Lett *413*, 270-273.

Nadal, R.C., Davies, P., Brown, D.R., and Viles, J.H. (2009). Evaluation of copper2+ affinities for the prion protein. Biochemistry *48*, 8929-8931.

Nakane, J., Wiggin, M., and Marziali, A. (2004). A nanosensor for transmembrane capture and identification of single nucleic Acid molecules. Biophys J *87*, 615-621.

Nandi, P.K. (1997). Interaction of prion peptide HuPrP106-126 with nucleic acid. Arch Virol *142*, 2537-2545.

Napper, S., Anderson, J.W., Georges, F., Quail, J.W., Delbaere, L.T., and Waygood, E.B. (1996). Mutation of serine-46 to aspartate in the histidine-containing protein of Escherichia coli mimics the inactivation by phosphorylation of serine-46 in HPrs from gram-positive bacteria. Biochemistry *35*, 11260-11267.

Nevin, S., Mc, M.W., Behrman, S., and Jones, D.P. (1960). Subacute spongiform encephalopathy--a subacute form of encephalopathy attributable to vascular dysfunction (spongiform cerebral atrophy). Brain *83*, 519-564.

Nicholson, E.M., and Scholtz, J.M. (1996). Conformational stability of the Escherichia coli HPr protein: test of the linear extrapolation method and a thermodynamic characterization of cold denaturation. Biochemistry *35*, 11369-11378.

Niederweis, M., Ehrt, S., Heinz, C., Klocker, U., Karosi, S., Swiderek, K.M., Riley, L.W., and Benz, R. (1999). Cloning of the mspA gene encoding a porin from Mycobacterium smegmatis. Mol Microbiol *33*, 933-945.

Niedzwiecki, D.J., Grazul, J., and Movileanu, L. (2010). Single-Molecule Observation of Protein Adsorption onto an Inorganic Surface. Journal of the American Chemical Society *132*, 10816-10822.

Nishida, N., Tremblay, P., Sugimoto, T., Shigematsu, K., Shirabe, S., Petromilli, C., Erpel, S.P., Nakaoke, R., Atarashi, R., Houtani, T., *et al.* (1999). A mouse prion protein transgene rescues mice deficient for the prion protein gene from purkinje cell degeneration and demyelination. Lab Invest *79*, 689-697.

Nunziante, M., Kehler, C., Maas, E., Kassack, M.U., Groschup, M., and Schatzl, H.M. (2005). Charged bipolar suramin derivatives induce aggregation of the prion protein at the cell surface and inhibit PrPSc replication. J Cell Sci *118*, 4959-4973.

Oesch, B., Doherr, M., Heim, D., Fischer, K., Egli, S., Bolliger, S., Biffiger, K., Schaller, O., Vandevelde, M., and Moser, M. (2000). Application of Prionics Western blotting procedure to screen for BSE in cattle regularly slaughtered at Swiss abattoirs. Arch Virol Suppl, 189-195.

Okpara-Hofmann, J., Knoll, M., Durr, M., Schmitt, B., and Borneff-Lipp, M. (2005). Comparison of low-temperature hydrogen peroxide gas plasma sterilization for endoscopes using various Sterrad models. J Hosp Infect *59*, 280-285.

Olasagasti, F., Lieberman, K.R., Benner, S., Cherf, G.M., Dahl, J.M., Deamer, D.W., and Akeson, M. (2010). Replication of individual DNA molecules under electronic control using a protein nanopore. Nat Nanotechnol *5*, 798-806.

Orru, C.D., Wilham, J.M., Raymond, L.D., Kuhn, F., Schroeder, B., Raeber, A.J., and Caughey, B. (2011). Prion disease blood test using immunoprecipitation and improved quaking-induced conversion. MBio *2*, e00078-00011.

Oukhaled, A., Cressiot, B., Bacri, L., Pastoriza-Gallego, M., Betton, J.M., Bourhis, E., Jede, R., Gierak, J., Auvray, L., and Pelta, J. (2011). Dynamics of completely unfolded and native proteins through solid-state nanopores as a function of electric driving force. ACS Nano *5*, 3628-3638.

Oukhaled, G., Mathe, J., Biance, A.L., Bacri, L., Betton, J.M., Lairez, D., Pelta, J., and Auvray, L. (2007). Unfolding of proteins and long transient conformations detected by single nanopore recording. Phys Rev Lett *98*, 158101.

Owen, F., Poulter, M., Lofthouse, R., Collinge, J., Crow, T.J., Risby, D., Baker, H.F., Ridley, R.M., Hsiao, K., and Prusiner, S.B. (1989). Insertion in prion protein gene in familial Creutzfeldt-Jakob disease. Lancet *1*, 51-52.

Palmer, M.S., Dryden, A.J., Hughes, J.T., and Collinge, J. (1991). Homozygous prion protein genotype predisposes to sporadic Creutzfeldt-Jakob disease. Nature *352*, 340-342.

Pan, K.M., Baldwin, M., Nguyen, J., Gasset, M., Serban, A., Groth, D., Mehlhorn, I., Huang, Z., Fletterick, R.J., Cohen, F.E., *et al.* (1993). Conversion of alpha-helices into beta-sheets features in the formation of the scrapie prion proteins. Proc Natl Acad Sci U S A *90*, 10962-10966.

Pan, K.M., Stahl, N., and Prusiner, S.B. (1992). Purification and properties of the cellular prion protein from Syrian hamster brain. Protein Sci *1*, 1343-1352.

Paramithiotis, E., Pinard, M., Lawton, T., LaBoissiere, S., Leathers, V.L., Zou, W.Q., Estey, L.A., Lamontagne, J., Lehto, M.T., Kondejewski, L.H., *et al.* (2003). A prion protein epitope selective for the pathologically misfolded conformation. Nat Med *9*, 893-899.

Parchi, P., Castellani, R., Capellari, S., Ghetti, B., Young, K., Chen, S.G., Farlow, M., Dickson, D.W., Sima, A.A., Trojanowski, J.Q., *et al.* (1996). Molecular basis of phenotypic variability in sporadic Creutzfeldt-Jakob disease. Ann Neurol *39*, 767-778.

Parker, M.W., Buckley, J.T., Postma, J.P., Tucker, A.D., Leonard, K., Pattus, F., and Tsernoglou, D. (1994). Structure of the Aeromonas toxin proaerolysin in its water-soluble and membrane-channel states. Nature *367*, 292-295.

Parraga, G., Horvath, S.J., Eisen, A., Taylor, W.E., Hood, L., Young, E.T., and Klevit, R.E. (1988). Zinc-dependent structure of a single-finger domain of yeast ADR1. Science *241*, 1489-1492.

Pastoriza-Gallego, M., Gibrat, G., Thiebot, B., Betton, J.M., and Pelta, J. (2009). Polyelectrolyte and unfolded protein pore entrance depends on the pore geometry. Biochim Biophys Acta *1788*, 1377-1386.

Pastoriza-Gallego, M., Oukhaled, G., Mathe, J., Thiebot, B., Betton, J.M., Auvray, L., and Pelta, J. (2007). Urea denaturation of alpha-hemolysin pore inserted in planar lipid bilayer detected by single nanopore recording: loss of structural asymmetry. FEBS Lett *581*, 3371-3376.

Pastoriza-Gallego, M., Rabah, L., Gibrat, G., Thiebot, B., van der Goot, F.G., Auvray, L., Betton, J.M., and Pelta, J. (2011). Dynamics of unfolded protein transport through an aerolysin pore. J Am Chem Soc *133*, 2923-2931.

Pattison, I.H., and Millson, G.C. (1961). Scrapie produced experimentally in goats with special reference to the clinical syndrome. J Comp Pathol *71*, 101-109.

PClamp (2005). Users guide (2005) Axon Instruments Inc., (Foster City, CA).

Peden, A.H., Head, M.W., Ritchie, D.L., Bell, J.E., and Ironside, J.W. (2004). Preclinical vCJD after blood transfusion in a PRNP codon 129 heterozygous patient. Lancet *364*, 527-529.

Peretz, D., Williamson, R.A., Kaneko, K., Vergara, J., Leclerc, E., Schmitt-Ulms, G., Mehlhorn, I.R., Legname, G., Wormald, M.R., Rudd, P.M., *et al.* (2001). Antibodies inhibit prion propagation and clear cell cultures of prion infectivity. Nature *412*, 739-743.

Perrier, V., Kaneko, K., Safar, J., Vergara, J., Tremblay, P., DeArmond, S.J., Cohen, F.E., Prusiner, S.B., and Wallace, A.C. (2002). Dominant-negative inhibition of prion replication in transgenic mice. Proc Natl Acad Sci U S A *99*, 13079-13084.

Perutz, M.F., Pope, B.J., Owen, D., Wanker, E.E., and Scherzinger, E. (2002). Aggregation of proteins with expanded glutamine and alanine repeats of the glutamine-rich and asparagine-rich domains of Sup35 and of the amyloid beta-peptide of amyloid plaques. Proc Natl Acad Sci U S A *99*, 5596-5600.

Pilz, I., Kratky, O., Licht, A., and Sela, M. (1975). Shape and volume of fragments Fab' and (Fab')2 of anti-poly(D-alanyl) antibodies in the presence and absence of tetra-D-alanine as determined by small-angle x-ray scattering. Biochemistry *14*, 1326-1333.

Pilz, I., Schwarz, E., and Palm, W. (1976). Small-angle X-ray studies of the Fab and Fc fragments from the human immunoglobulin molecule Kol. Eur J Biochem *71*, 239-247.

Poli, G., Martino, P.A., Villa, S., Carcassola, G., Giannino, M.L., Dall'Ara, P., Pollera, C., Iussich, S., Tranquillo, V.M., Bareggi, S., *et al.* (2004). Evaluation of anti-prion activity of congo red and its derivatives in experimentally infected hamsters. Arzneimittelforschung *54*, 406-415.

Polymenidou, M., Moos, R., Scott, M., Sigurdson, C., Shi, Y.Z., Yajima, B., Hafner-Bratkovic, I., Jerala, R., Hornemann, S., Wuthrich, K., *et al.* (2008). The POM monoclonals: a comprehensive set of antibodies to non-overlapping prion protein epitopes. PLoS One *3*, e3872.

Prasad, L., Waygood, E.B., Lee, J.S., and Delbaere, L.T.J. (1998). The 2.5 Å resolution structure of the Jel42 Fab fragment/HPr complex. Journal of Molecular Biology *280*, 829-845.

Prusiner, S.B. (1982). Novel proteinaceous infectious particles cause scrapie. Science *216*, 136-144.

Prusiner, S.B. (1989). Creutzfeldt-Jakob disease and scrapie prions. Alzheimer Dis Assoc Disord *3*, 52-78.

Prusiner, S.B. (1991). Molecular biology of prion diseases. Science *252*, 1515-1522.

Prusiner, S.B. (1998). Prions. Proc Natl Acad Sci U S A *95*, 13363-13383.

Prusiner, S.B. (2001). Neurodegenerative Diseases and Prions. New England Journal of Medicine *344*, 1516-1526.

Prusiner, S.B., May, B.C., and Cohen, F.E. (2004). Therapeutic approaches to prion diseases. In Prion biology and diseases, S.B. Prusiner, ed. (Cold Spring Harbor Laboratory Press, USA), pp. 961-1014.

Prusiner, S.B., McKinley, M.P., Bowman, K.A., Bolton, D.C., Bendheim, P.E., Groth, D.F., and Glenner, G.G. (1983). Scrapie prions aggregate to form amyloid-like birefringent rods. Cell *35*, 349-358.

Pushie, M.J., and Vogel, H.J. (2009). A Potential Mechanism for Cu2+ Reduction, β-Cleavage, and β-Sheet Initiation Within The N-Terminal Domain of the Prion Protein: Insights from Density Functional Theory and Molecular Dynamics Calculations. Journal of Toxicology and Environmental Health, Part A *72*, 1040-1059.

Quaglio, E., Chiesa, R., and Harris, D.A. (2001). Copper converts the cellular prion protein into a protease-resistant species that is distinct from the scrapie isoform. J Biol Chem *276*, 11432-11438.

Rabbi, M., and Marszalek, P.E. (2008). Probing polysaccharide and protein mechanisms by atomic force microscopy. In Single-molecules techniques: A laboratory manual, P.R. Selvin, and T. Ha, eds. (New York: Cold Spring Harbor Laboratory Press), pp. 371-394.

Riek, R., Hornemann, S., Wider, G., Billeter, M., Glockshuber, R., and Wuthrich, K. (1996). NMR structure of the mouse prion protein domain PrP(121-321). Nature *382*, 180-182.

Rincon-Restrepo, M., Mikhailova, E., Bayley, H., and Maglia, G. (2011). Controlled translocation of individual DNA molecules through protein nanopores with engineered molecular brakes. Nano Lett *11*, 746-750.

Roos, R., Gajdusek, D.C., and Gibbs, C.J., Jr. (1973). The clinical characteristics of transmissible Creutzfeldt-Jakob disease. Brain *96*, 1-20.

Rossi, D., Cozzio, A., Flechsig, E., Klein, M.A., Rulicke, T., Aguzzi, A., and Weissmann, C. (2001). Onset of ataxia and Purkinje cell loss in PrP null mice inversely correlated with Dpl level in brain. EMBO J *20*, 694-702.

Saa, P., Castilla, J., and Soto, C. (2006). Presymptomatic detection of prions in blood. Science *313*, 92-94.

Saborio, G.P., Permanne, B., and Soto, C. (2001). Sensitive detection of pathological prion protein by cyclic amplification of protein misfolding. Nature *411*, 810-813.

Safar, J., Wille, H., Itri, V., Groth, D., Serban, H., Torchia, M., Cohen, F.E., and Prusiner, S.B. (1998). Eight prion strains have PrP(Sc) molecules with different conformations. Nat Med *4*, 1157-1165.

Safar, J.G., Scott, M., Monaghan, J., Deering, C., Didorenko, S., Vergara, J., Ball, H., Legname, G., Leclerc, E., Solforosi, L., *et al.* (2002). Measuring prions causing bovine spongiform encephalopathy or chronic wasting disease by immunoassays and transgenic mice. Nat Biotechnol *20*, 1147-1150.

Sakaguchi, S., Katamine, S., Nishida, N., Moriuchi, R., Shigematsu, K., Sugimoto, T., Nakatani, A., Kataoka, Y., Houtani, T., Shirabe, S., *et al.* (1996). Loss of cerebellar Purkinje cells in aged mice homozygous for a disrupted PrP gene. Nature *380*, 528-531.

Sako, Y., Minoghchi, S., and Yanagida, T. (2000). Single-molecule imaging of EGFR signalling on the surface of living cells. Nat Cell Biol *2*, 168-172.

Sako, Y., and Yanagida, T. (2003). Single-molecule visualization in cell biology. Nat Rev Mol Cell Biol *Suppl*, SS1-5.

Sakudo, A., Lee, D.C., Saeki, K., Nakamura, Y., Inoue, K., Matsumoto, Y., Itohara, S., and Onodera, T. (2003). Impairment of superoxide dismutase activation by N-terminally truncated prion protein (PrP) in PrP-deficient neuronal cell line. Biochem Biophys Res Commun *308*, 660-667.

Saleh, O.A., and Sohn, L.L. (2003). Direct detection of antibody-antigen binding using an on-chip artificial pore. Proc Natl Acad Sci U S A *100*, 820-824.

Sales, N., Rodolfo, K., Hassig, R., Faucheux, B., Di Giamberardino, L., and Moya, K.L. (1998). Cellular prion protein localization in rodent and primate brain. Eur J Neurosci *10*, 2464-2471.

Schaller, O., Fatzer, R., Stack, M., Clark, J., Cooley, W., Biffiger, K., Egli, S., Doherr, M., Vandevelde, M., Heim, D., *et al.* (1999). Validation of a western immunoblotting procedure for bovine PrP(Sc) detection and its use as a rapid surveillance method for the diagnosis of bovine spongiform encephalopathy (BSE). Acta Neuropathol *98*, 437-443.

Schmitt, A., Westner, I.M., Reznicek, L., Michels, W., Mitteregger, G., and Kretzschmar, H.A. (2010). Automated decontamination of surface-adherent prions. J Hosp Infect *76*, 74-79.

Schneider, G.F., Kowalczyk, S.W., Calado, V.E., Pandraud, G., Zandbergen, H.W., Vandersypen, L.M., and Dekker, C. (2010). DNA translocation through graphene nanopores. Nano Lett *10*, 3163-3167.

Schwarz, A., Kratke, O., Burwinkel, M., Riemer, C., Schultz, J., Henklein, P., Bamme, T., and Baier, M. (2003). Immunisation with a synthetic prion protein-derived peptide prolongs survival times of mice orally exposed to the scrapie agent. Neurosci Lett *350*, 187-189.

Selvin, P.R. (2000). The renaissance of fluorescence resonance energy transfer. Nat Struct Biol *7*, 730-734.

Sexton, L.T., Horne, L.P., Sherrill, S.A., Bishop, G.W., Baker, L.A., and Martin, C.R. (2007). Resistive-pulse studies of proteins and protein/antibody complexes using a conical nanotube sensor. J Am Chem Soc *129*, 13144-13152.

Sexton, L.T., Mukaibo, H., Katira, P., Hess, H., Sherrill, S.A., Horne, L.P., and Martin, C.R. (2010). An adsorption-based model for pulse duration in resistive-pulse protein sensing. J Am Chem Soc *132*, 6755-6763.

Shaked, G.M., Meiner, Z., Avraham, I., Taraboulos, A., and Gabizon, R. (2001). Reconstitution of prion infectivity from solubilized protease-resistant PrP and nonprotein components of prion rods. J Biol Chem *276*, 14324-14328.

Sharma, S., Georges, F., Delbaere, L.T., Lee, J.S., Klevit, R.E., and Waygood, E.B. (1991). Epitope mapping by mutagenesis distinguishes between the two tertiary structures of the histidine-containing protein HPr. Proc Natl Acad Sci U S A *88*, 4877-4881.

Sherman-Gold, R. (2008). The Axon guide - A guide to electrophysiology and biophysics laboratory techniques.

Shin, S.H., Luchian, T., Cheley, S., Braha, O., and Bayley, H. (2002). Kinetics of a reversible covalent-bond-forming reaction observed at the single-molecule level. Angew Chem Int Ed Engl *41*, 3707-3709; 3523.

Shyng, S.L., Moulder, K.L., Lesko, A., and Harris, D.A. (1995). The N-terminal domain of a glycolipid-anchored prion protein is essential for its endocytosis via clathrin-coated pits. J Biol Chem *270*, 14793-14800.

Sigalov, G., Comer, J., Timp, G., and Aksimentiev, A. (2008). Detection of DNA sequences using an alternating electric field in a nanopore capacitor. Nano Lett *8*, 56-63.

Silverton, E.W., Navia, M.A., and Davies, D.R. (1977). Three-dimensional structure of an intact human immunoglobulin. Proc Natl Acad Sci U S A *74*, 5140-5144.

Singer, S.J., Maher, P.A., and Yaffe, M.P. (1987). On the translocation of proteins across membranes. Proc Natl Acad Sci U S A *84*, 1015-1019.

Singh, A., Isaac, A.O., Luo, X., Mohan, M.L., Cohen, M.L., Chen, F., Kong, Q., Bartz, J., and Singh, N. (2009a). Abnormal brain iron homeostasis in human and animal prion disorders. PLoS Pathog *5*, e1000336.

Singh, A., Mohan, M.L., Isaac, A.O., Luo, X., Petrak, J., Vyoral, D., and Singh, N. (2009b). Prion protein modulates cellular iron uptake: a novel function with implications for prion disease pathogenesis. PLoS One *4*, e4468.

Singh, N., Das, D., Singh, A., and Mohan, M.L. (2010). Prion protein and metal interaction: physiological and pathological implications. Curr Issues Mol Biol *12*, 99-107.

Siwy, Z., Apel, P., Dobrev, D., Neumann, R., Spohr, R., Trautmann, C., and Voss, K. (2003a). Ion transport through asymmetric nanopores prepared by ion track etching. Nuclear Instruments and Methods in Physics Research Section B: Beam Interactions with Materials and Atoms *208*, 143-148.

Siwy, Z., Dobrev, D., Neumann, R., Trautmann, C., and Voss, K. (2003b). Electro-responsive asymmetric nanopores in polyimide with stable ion-current signal. Applied Physics A: Materials Science & Processing *76*, 781-785.

Siwy, Z., Gu, Y., Spohr, H.A., Baur, D., Wolf-Reber, A., Spohr, R., Apel, P., and Korchev, Y.E. (2002). Rectification and voltage gating of ion currents in a nanofabricated pore. Europhys. Lett. *60*, 349-355.

Siwy, Z., Trofin, L., Kohli, P., Baker, L.A., Trautmann, C., and Martin, C.R. (2005). Protein biosensors based on biofunctionalized conical gold nanotubes. J Am Chem Soc *127*, 5000-5001.

Siwy, Z.S. (2006). Ion-Current Rectification in Nanopores and Nanotubes with Broken Symmetry. Advanced Functional Materials *16*, 735-746.

Smallshaw, J.E., Brokx, S., Lee, J.S., and Waygood, E.B. (1998). Determination of the binding constants for three HPr-specific monoclonal antibodies and their Fab fragments. Journal of Molecular Biology *280*, 765-774.

Smeets, R.M., Keyser, U.F., Krapf, D., Wu, M.Y., Dekker, N.H., and Dekker, C. (2006a). Salt dependence of ion transport and DNA translocation through solid-state nanopores. Nano Lett *6*, 89-95.

Smeets, R.M.M., Keyser, U.F., Wu, M.Y., Dekker, N.H., and Dekker, C. (2006b). Nanobubbles in Solid-State Nanopores. Physical Review Letters *97*, 088101.

Solassol, J., Crozet, C., Perrier, V., Leclaire, J., Beranger, F., Caminade, A.M., Meunier, B., Dormont, D., Majoral, J.P., and Lehmann, S. (2004). Cationic phosphorus-containing dendrimers reduce prion replication both in cell culture and in mice infected with scrapie. J Gen Virol *85*, 1791-1799.

Song, L., Hobaugh, M.R., Shustak, C., Cheley, S., Bayley, H., and Gouaux, J.E. (1996). Structure of staphylococcal alpha-hemolysin, a heptameric transmembrane pore. Science *274*, 1859-1866.

Soto, C. (2004). Diagnosing prion diseases: needs, challenges and hopes. Nat Rev Microbiol *2*, 809-819.

Soto, C., Anderes, L., Suardi, S., Cardone, F., Castilla, J., Frossard, M.J., Peano, S., Saa, P., Limido, L., Carbonatto, M., *et al.* (2005). Pre-symptomatic detection of prions by cyclic amplification of protein misfolding. FEBS Lett *579*, 638-642.

Spudich, J.A., Rice, S.E., Rock, R.S., Purcell, T.J., and Warrick, H.M. (2008). Optical traps to study properties of molecular motors. In Single-molecule techniques: A laboratory manual., P.R. Selvin, and T. Ha, eds. (New York: Cold Spring Harbor Laboratory Press), pp. 279-296.

Stahl, C., Kubetzko, S., Kaps, I., Seeber, S., Engelhardt, H., and Niederweis, M. (2001). MspA provides the main hydrophilic pathway through the cell wall of Mycobacterium smegmatis. Mol Microbiol *40*, 451-464.

Stefureac, R., Long, Y.T., Kraatz, H.B., Howard, P., and Lee, J.S. (2006). Transport of alpha-helical peptides through alpha-hemolysin and aerolysin pores. Biochemistry *45*, 9172-9179.

Stefureac, R., Waldner, L., Howard, P., and Lee, J.S. (2008). Nanopore analysis of a small 86-residue protein. Small *4*, 59-63.

Stefureac, R.I., Madampage, C.A., Andrievskaia, O., and Lee, J.S. (2010a). Nanopore analysis of the interaction of metal ions with prion proteins and peptides. Biochem Cell Biol *88*, 347-358.

Stefureac, R.I., Trivedi, D., Marziali, A., and Lee, J.S. (2010b). Evidence that small proteins translocate through silicon nitride pores in a folded conformation. J Phys Condens Matter *22*, 454133.

Stein, D., Kruithof, M., and Dekker, C. (2004). Surface-charge-governed ion transport in nanofluidic channels. Phys Rev Lett *93*, 035901.

Stein, D., Li, J., and Golovchenko, J.A. (2002). Ion-beam sculpting time scales. Phys Rev Lett *89*, 276106.

Stevens, D.J., Walter, E.D., Rodriguez, A., Draper, D., Davies, P., Brown, D.R., and Millhauser, G.L. (2009). Early onset prion disease from octarepeat expansion correlates with copper binding properties. PLoS Pathog *5*, e1000390.

Stockel, J., Safar, J., Wallace, A.C., Cohen, F.E., and Prusiner, S.B. (1998). Prion protein selectively binds copper(II) ions. Biochemistry *37*, 7185-7193.

Stoddart, D., Heron, A.J., Mikhailova, E., Maglia, G., and Bayley, H. (2009). Single-nucleotide discrimination in immobilized DNA oligonucleotides with a biological nanopore. Proc Natl Acad Sci U S A *106*, 7702-7707.

Stoddart, D., Maglia, G., Mikhailova, E., Heron, A.J., and Bayley, H. (2010). Multiple base-recognition sites in a biological nanopore: two heads are better than one. Angew Chem Int Ed Engl *49*, 556-559.

Stoffler, D., Goldie, K.N., Feja, B., and Aebi, U. (1999). Calcium-mediated structural changes of native nuclear pore complexes monitored by time-lapse atomic force microscopy. J Mol Biol *287*, 741-752.

Storm, A.J., Chen, J.H., Ling, X.S., Zandbergen, H.W., and Dekker, C. (2003). Fabrication of solid-state nanopores with single-nanometre precision. Nat Mater *2*, 537-540.

Storm, A.J., Chen, J.H., Zandbergen, H.W., and Dekker, C. (2005a). Translocation of double-strand DNA through a silicon oxide nanopore. Phys Rev E Stat Nonlin Soft Matter Phys *71*, 051903.

Storm, A.J., Storm, C., Chen, J., Zandbergen, H., Joanny, J.F., and Dekker, C. (2005b). Fast DNA translocation through a solid-state nanopore. Nano Lett *5*, 1193-1197.

Strick, T.R., Allemand, J.F., Bensimon, D., Bensimon, A., and Croquette, V. (1996). The elasticity of a single supercoiled DNA molecule. Science *271*, 1835-1837.

Supattapone, S., Nguyen, H.O., Cohen, F.E., Prusiner, S.B., and Scott, M.R. (1999). Elimination of prions by branched polyamines and implications for therapeutics. Proc Natl Acad Sci U S A *96*, 14529-14534.

Supattapone, S., Wille, H., Uyechi, L., Safar, J., Tremblay, P., Szoka, F.C., Cohen, F.E., Prusiner, S.B., and Scott, M.R. (2001). Branched polyamines cure prion-infected neuroblastoma cells. J Virol *75*, 3453-3461.

Sutherland, T.C., Long, Y.-T., Stefureac, R.-I., Bediako-Amoa, I., Kraatz, H.-B., and Lee, J.S. (2004). Structure of Peptides Investigated by Nanopore Analysis. Nano Letters *4*, 1273-1277.

Tabard-Cossa, V., and *et al.* (2007). Noise analysis and reduction in solid-state nanopores. Nanotechnology *18*, 305505.

Tagliavini, F., McArthur, R.A., Canciani, B., Giaccone, G., Porro, M., Bugiani, M., Lievens, P.M., Bugiani, O., Peri, E., Dall'Ara, P., *et al.* (1997). Effectiveness of anthracycline against experimental prion disease in Syrian hamsters. Science *276*, 1119-1122.

Tahiri-Alaoui, A., Bouchard, M., Zurdo, J., and James, W. (2003). Competing intrachain interactions regulate the formation of beta-sheet fibrils in bovine PrP peptides. Protein Sci *12*, 600-608.

Talaga, D.S., and Li, J. (2009). Single-molecule protein unfolding in solid state nanopores. J Am Chem Soc *131*, 9287-9297.

Taylor, D.M., McConnell, I., and Fraser, H. (1996). Scrapie infection can be established readily through skin scarification in immunocompetent but not immunodeficient mice. J Gen Virol *77 (Pt 7)*, 1595-1599.

Telling, G.C., Scott, M., Mastrianni, J., Gabizon, R., Torchia, M., Cohen, F.E., DeArmond, S.J., and Prusiner, S.B. (1995). Prion propagation in mice expressing human and chimeric PrP transgenes implicates the interaction of cellular PrP with another protein. Cell *83*, 79-90.

Thackray, A.M., Knight, R., Haswell, S.J., Bujdoso, R., and Brown, D.R. (2002). Metal imbalance and compromised antioxidant function are early changes in prion disease. Biochem J *362*, 253-258.

Thompsett, A.R., and Brown, D.R. (2007). Dual polarisation interferometry analysis of copper binding to the prion protein: evidence for two folding states. Biochim Biophys Acta *1774*, 920-927.

Thorne, L., and Terry, L.A. (2008). In vitro amplification of PrPSc derived from the brain and blood of sheep infected with scrapie. J Gen Virol *89*, 3177-3184.

Tobler, I., Gaus, S.E., Deboer, T., Achermann, P., Fischer, M., Rulicke, T., Moser, M., Oesch, B., McBride, P.A., and Manson, J.C. (1996). Altered circadian activity rhythms and sleep in mice devoid of prion protein. Nature *380*, 639-642.

Todorova-Balvay, D., Simon, S., Creminon, C., Grassi, J., Srikrishnan, T., and Vijayalakshmi, M.A. (2005). Copper binding to prion octarepeat peptides, a combined metal chelate affinity and immunochemical approaches. J Chromatogr B Analyt Technol Biomed Life Sci *818*, 75-82.

Tropini, C., and Marziali, A. (2007). Multi-nanopore force spectroscopy for DNA analysis. Biophys J *92*, 1632-1637.

Tsoulou, E., Kalfas, C.A., and Sideris, E.G. (2001). Probing irradiated DNA with the perturbed angular correlation method. Radiat Res *156*, 181-185.

Tsutsui, M., Taniguchi, M., and Kawai, T. (2009). Transverse field effects on DNA-sized particle dynamics. Nano Lett *9*, 1659-1662.

Umehara, S., Karhanek, M., Davis, R.W., and Pourmand, N. (2009). Label-free biosensing with functionalized nanopipette probes. Proc Natl Acad Sci U S A *106*, 4611-4616.

Uram, J.D., Ke, K., Hunt, A.J., and Mayer, M. (2006). Submicrometer pore-based characterization and quantification of antibody-virus interactions. Small *2*, 967-972.

Uversky, V.N. (2002). Natively unfolded proteins: a point where biology waits for physics. Protein Sci *11*, 739-756.

Uversky, V.N., Oldfield, C.J., and Dunker, A.K. (2008). Intrinsically disordered proteins in human diseases: introducing the D2 concept. Annu Rev Biophys *37*, 215-246.

van der Goot, F.G., Ausio, J., Wong, K.R., Pattus, F., and Buckley, J.T. (1993). Dimerization stabilizes the pore-forming toxin aerolysin in solution. J Biol Chem *268*, 18272-18279.

van Holde, K., and Zlatanova, J. (2006). Scanning chromatin: a new paradigm? J Biol Chem *281*, 12197-12200.

Varela-Nallar, L., Gonzalez, A., and Inestrosa, N.C. (2006). Role of copper in prion diseases: deleterious or beneficial? Curr Pharm Des *12*, 2587-2595.

Vassallo, N., and Herms, J. (2003). Cellular prion protein function in copper homeostasis and redox signalling at the synapse. J Neurochem *86*, 538-544.

Venkatesan, B., Polans, J., Comer, J., Sridhar, S., Wendell, D., Aksimentiev, A., and Bashir, R. (2011). Lipid bilayer coated Al₂O₃ nanopore sensors: towards a hybrid biological solid-state nanopore. Biomedical Microdevices *13*, 671-682.

Vercoutere, W., Winters-Hilt, S., Olsen, H., Deamer, D., Haussler, D., and Akeson, M. (2001). Rapid discrimination among individual DNA hairpin molecules at single-nucleotide resolution using an ion channel. Nat Biotechnol *19*, 248-252.

Vercoutere, W.A., Winters-Hilt, S., DeGuzman, V.S., Deamer, D., Ridino, S.E., Rodgers, J.T., Olsen, H.E., Marziali, A., and Akeson, M. (2003). Discrimination among individual Watson-Crick base pairs at the termini of single DNA hairpin molecules. Nucleic Acids Res *31*, 1311-1318.

Viles, J.H., Cohen, F.E., Prusiner, S.B., Goodin, D.B., Wright, P.E., and Dyson, H.J. (1999). Copper binding to the prion protein: Structural implications of four identical cooperative binding sites. Proceedings of the National Academy of Sciences *96*, 2042-2047.

Viles, J.H., Donne, D., Kroon, G., Prusiner, S.B., Cohen, F.E., Dyson, H.J., and Wright, P.E. (2001). Local Structural Plasticity of the Prion Protein. Analysis of NMR Relaxation Dynamics†. Biochemistry *40*, 2743-2753.

Viles, J.H., Klewpatinond, M., and Nadal, R.C. (2008). Copper and the structural biology of the prion protein. Biochem Soc Trans *36*, 1288-1292.

Vucetic, S., Brown, C.J., Dunker, A.K., and Obradovic, Z. (2003). Flavors of protein disorder. Proteins *52*, 573-584.

Wallace, E.V., Stoddart, D., Heron, A.J., Mikhailova, E., Maglia, G., Donohoe, T.J., and Bayley, H. (2010). Identification of epigenetic DNA modifications with a protein nanopore. Chem Commun (Camb) *46*, 8195-8197.

Walsh, P., Simonetti, K., and Sharpe, S. (2009). Core structure of amyloid fibrils formed by residues 106-126 of the human prion protein. Structure *17*, 417-426.

Walter, E.D., Chattopadhyay, M., and Millhauser, G.L. (2006). The affinity of copper binding to the prion protein octarepeat domain: evidence for negative cooperativity. Biochemistry *45*, 13083-13092.

Walter, E.D., Stevens, D.J., Spevacek, A.R., Visconte, M.P., Dei Rossi, A., and Millhauser, G.L. (2009). Copper binding extrinsic to the octarepeat region in the prion protein. Curr Protein Pept Sci *10*, 529-535.

Walter, E.D., Stevens, D.J., Visconte, M.P., and Millhauser, G.L. (2007). The prion protein is a combined zinc and copper binding protein: Zn2+ alters the distribution of Cu2+ coordination modes. J Am Chem Soc *129*, 15440-15441.

Walter, N.G., Huang, C.Y., Manzo, A.J., and Sobhy, M.A. (2008). Do-it-yourself guide: how to use the modern single-molecule toolkit. Nat Methods *5*, 475-489.

Wang, D., Zhao, Q., de Zoysa, R.S.S., and Guan, X. (2009). Detection of nerve agent hydrolytes in an engineered nanopore. Sens. Actuators, B *139*, 440-446.

Wang, H.Y., Ying, Y.L., Li, Y., Kraatz, H.B., and Long, Y.T. (2011). Nanopore Analysis of beta-Amyloid Peptide Aggregation Transition Induced by Small Molecules. Anal Chem.

Wanunu, M., Chakrabarti, B., Mathe, J., Nelson, D.R., and Meller, A. (2008). Orientation-dependent interactions of DNA with an alpha-hemolysin channel. Phys Rev E Stat Nonlin Soft Matter Phys *77*, 031904.

Wanunu, M., and Meller, A. (2007). Chemically modified solid-state nanopores. Nano Lett *7*, 1580-1585.

Waygood, E.B., Erickson, E., El-Kabbani, O.A.L., and Delbaere, L.T.J. (1985). Characterization of phosphorylated histidine-containing protein (HPr) of the bacterial phosphoenolpyruvate/sugar phosphotransferase system. Biochemistry *24*, 6938-6945.

Waygood, E.B., and Steeves, T. (1980). Enzyme I of the phosphoenolpyruvate: sugar phosphotransferase system of Escherichia coli. Purification to homogeneity and some properties. Can J Biochem *58*, 40-48.

Weissmann, C. (1996). The Ninth Datta Lecture. Molecular biology of transmissible spongiform encephalopathies. FEBS Lett *389*, 3-11.

Wells, G.A., Scott, A.C., Johnson, C.T., Gunning, R.F., Hancock, R.D., Jeffrey, M., Dawson, M., and Bradley, R. (1987). A novel progressive spongiform encephalopathy in cattle. Vet Rec *121*, 419-420.

Wells, M.A., Jackson, G.S., Jones, S., Hosszu, L.L., Craven, C.J., Clarke, A.R., Collinge, J., and Waltho, J.P. (2006). A reassessment of copper(II) binding in the full-length prion protein. Biochem J *399*, 435-444.

Westaway, D., Zuliani, V., Cooper, C.M., Da Costa, M., Neuman, S., Jenny, A.L., Detwiler, L., and Prusiner, S.B. (1994). Homozygosity for prion protein alleles encoding glutamine-171 renders sheep susceptible to natural scrapie. Genes Dev *8*, 959-969.

Wharton, J.E., Jin, P., Sexton, L.T., Horne, L.P., Sherrill, S.A., Mino, W.K., and Martin, C.R. (2007). A method for reproducibly preparing synthetic nanopores for resistive-pulse biosensors. Small *3*, 1424-1430.

White, A.R., Enever, P., Tayebi, M., Mushens, R., Linehan, J., Brandner, S., Anstee, D., Collinge, J., and Hawke, S. (2003). Monoclonal antibodies inhibit prion replication and delay the development of prion disease. Nature *422*, 80-83.

Whittal, R.M., Ball, H.L., Cohen, F.E., Burlingame, A.L., Prusiner, S.B., and Baldwin, M.A. (2000). Copper binding to octarepeat peptides of the prion protein monitored by mass spectrometry. Protein Sci *9*, 332-343.

Wild, M.A., Spraker, T.R., Sigurdson, C.J., O'Rourke, K.I., and Miller, M.W. (2002). Preclinical diagnosis of chronic wasting disease in captive mule deer (Odocoileus hemionus) and white-tailed deer (Odocoileus virginianus) using tonsillar biopsy. J Gen Virol *83*, 2629-2634.

Wilesmith, J.W., Ryan, J.B., and Atkinson, M.J. (1991). Bovine spongiform encephalopathy: epidemiological studies on the origin. Vet Rec *128*, 199-203.

Wilk, S.J., Petrossian, L., Goryll, M., Tang, J.M., Eisenberg, R.S., Saraniti, M., Goodnick, S.M., and Thornton, T.J. (2006). Silicon-Based Ion Channel Platforms
Nonequilibrium Carrier Dynamics in Semiconductors. M. Saraniti, and U. Ravaioli, eds. (Springer Berlin Heidelberg), pp. 201-204.

Will, R., and Zeidler, M. (1996). Diagnosing Creutzfeldt-Jakob disease. BMJ *313*, 833-834.

Wille, H., Michelitsch, M.D., Guenebaut, V., Supattapone, S., Serban, A., Cohen, F.E., Agard, D.A., and Prusiner, S.B. (2002). Structural studies of the scrapie prion protein by electron crystallography. Proc Natl Acad Sci U S A *99*, 3563-3568.

Williams, E.S., and Young, S. (1980). Chronic wasting disease of captive mule deer: a spongiform encephalopathy. J Wildl Dis *16*, 89-98.

Williams, M.C., and Rouzina, I. (2002). Force spectroscopy of single DNA and RNA molecules. Curr Opin Struct Biol *12*, 330-336.

Wilmsen, H.U., Buckley, J.T., and Pattus, F. (1991). Site-directed mutagenesis at histidines of aerolysin from Aeromonas hydrophila: a lipid planar bilayer study. Mol Microbiol *5*, 2745-2751.

Wilmsen, H.U., Leonard, K.R., Tichelaar, W., Buckley, J.T., and Pattus, F. (1992). The aerolysin membrane channel is formed by heptamerization of the monomer. EMBO J *11*, 2457-2463.

Wilmsen, H.U., Pattus, F., and Buckley, J.T. (1990). Aerolysin, a hemolysin from Aeromonas hydrophila, forms voltage-gated channels in planar lipid bilayers. J Membr Biol *115*, 71-81.

Wilson, N.A., Abu-Shumays, R., Gyarfas, B., Wang, H., Lieberman, K.R., Akeson, M., and Dunbar, W.B. (2009). Electronic control of DNA polymerase binding and unbinding to single DNA molecules. ACS Nano *3*, 995-1003.

Winklhofer, K.F., and Tatzelt, J. (2000). Cationic lipopolyamines induce degradation of PrPSc in scrapie-infected mouse neuroblastoma cells. Biol Chem *381*, 463-469.

Winters-Hilt, S., Vercoutere, W., DeGuzman, V.S., Deamer, D., Akeson, M., and Haussler, D. (2003). Highly accurate classification of Watson-Crick basepairs on termini of single DNA molecules. Biophys J *84*, 967-976.

Wolfe, A.J., Mohammad, M.M., Cheley, S., Bayley, H., and Movileanu, L. (2007). Catalyzing the translocation of polypeptides through attractive interactions. J Am Chem Soc *129*, 14034-14041.

Wolfe, L.L., Conner, M.M., Baker, T.H., Dreitz, V.J., Burnham, K.P., Williams, E.S., Hobbs, N.T., and Miller, M.W. (2002). Evaluation of antemortem sampling to estimate chronic wasting disease prevalence in free-ranging mule deer. J Wildlife Manage *66*, 564-573.

Wong, C., Xiong, L.W., Horiuchi, M., Raymond, L., Wehrly, K., Chesebro, B., and Caughey, B. (2001). Sulfated glycans and elevated temperature stimulate PrP(Sc)-dependent cell-free formation of protease-resistant prion protein. EMBO J *20*, 377-386.

Wood, J.L., McGill, I.S., Done, S.H., and Bradley, R. (1997). Neuropathology of scrapie: a study of the distribution patterns of brain lesions in 222 cases of natural scrapie in sheep, 1982-1991. Vet Rec *140*, 167-174.

Xu, Y., Oyola, R., and Gai, F. (2003). Infrared study of the stability and folding kinetics of a 15-residue beta-hairpin. J Am Chem Soc *125*, 15388-15394.

Yusko, E.C., Johnson, J.M., Majd, S., Prangkio, P., Rollings, R.C., Li, J., Yang, J., and Mayer, M. (2011). Controlling protein translocation through nanopores with bio-inspired fluid walls. Nat Nanotechnol *6*, 253-260.

Zahn, R., Liu, A., Luhrs, T., Riek, R., von Schroetter, C., Lopez Garcia, F., Billeter, M., Calzolai, L., Wider, G., and Wuthrich, K. (2000). NMR solution structure of the human prion protein. Proc Natl Acad Sci U S A *97*, 145-150.

Zanusso, G., Ferrari, S., Cardone, F., Zampieri, P., Gelati, M., Fiorini, M., Farinazzo, A., Gardiman, M., Cavallaro, T., Bentivoglio, M., *et al.* (2003). Detection of pathologic prion protein in the olfactory epithelium in sporadic Creutzfeldt-Jakob disease. N Engl J Med *348*, 711-719.

Zhao, Q., Comer, J., Dimitrov, V., Yemenicioglu, S., Aksimentiev, A., and Timp, G. (2008a). Stretching and unzipping nucleic acid hairpins using a synthetic nanopore. Nucleic Acids Res *36*, 1532-1541.

Zhao, Q., de Zoysa, R.S.S., Wang, D., Jayawardhana, D.A., and Guan, X. (2009a). Real-Time Monitoring of Peptide Cleavage Using a Nanopore Probe. Journal of the American Chemical Society *131*, 6324-6325.

Zhao, Q., Jayawardhana, D.A., and Guan, X. (2008b). Stochastic Study of the Effect of Ionic Strength on Noncovalent Interactions in Protein Pores. Biophysical Journal *94*, 1267-1275.

Zhao, Q., Jayawardhana, D.A., Wang, D., and Guan, X. (2009b). Study of Peptide Transport through Engineered Protein Channels. The Journal of Physical Chemistry B *113*, 3572-3578.

Zhao, Q., Sigalov, G., Dimitrov, V., Dorvel, B., Mirsaidov, U., Sligar, S., Aksimentiev, A., and Timp, G. (2007). Detecting SNPs using a synthetic nanopore. Nano Lett *7*, 1680-1685.

Zhu, F., Davies, P., Thompsett, A.R., Kelly, S.M., Tranter, G.E., Hecht, L., Isaacs, N.W., Brown, D.R., and Barron, L.D. (2008). Raman optical activity and circular dichroism reveal dramatic differences in the influence of divalent copper and manganese ions on prion protein folding. Biochemistry *47*, 2510-2517.

Zhuang, X., Bartley, L.E., Babcock, H.P., Russell, R., Ha, T., Herschlag, D., and Chu, S. (2000). A Single-Molecule Study of RNA Catalysis and Folding. Science *288*, 2048-2051.

Ziegler, J., Sticht, H., Marx, U.C., Muller, W., Rosch, P., and Schwarzinger, S. (2003). CD and NMR studies of prion protein (PrP) helix 1. Novel implications for its role in the PrPC-->PrPSc conversion process. J Biol Chem *278*, 50175-50181.

Zou, W.Q., Zheng, J., Gray, D.M., Gambetti, P., and Chen, S.G. (2004). Antibody to DNA detects scrapie but not normal prion protein. Proc Natl Acad Sci U S A *101*, 1380-1385.

Zuegg, J., and Gready, J.E. (2000). Molecular dynamics simulation of human prion protein including both N-linked oligosaccharides and the GPI anchor. Glycobiology *10*, 959-974.

Zwolak, M., and Di Ventra, M. (2005). Electronic signature of DNA nucleotides via transverse transport. Nano Lett *5*, 421-424.